Development of Data-Efficient Machine Learning Approaches for the Modeling and Design in Electromagnetic Compatibility and Radio-Frequency Engineering

Dissertation (cumulative) approved by the
Doctoral Degree Committee of
Hamburg University of Technology
in pursuit of the academic degree of

Doktor-Ingenieur (Dr.-Ing.)

written by
Youcef Hassab

from
Oran, Algeria

2026

1. Reviewer:
Prof. Dr. sc. techn. Christian Schuster

2. Reviewer:
Prof. Dr.-Ing. habil. Alexander Kölpin

3. Reviewer:
Prof. Dr.-Ing. habil. Fabian Lurz

Chairman of the examination committee:
Prof. Dr.-Ing. habil. Gerhard Bauch

Day of the oral examination:
3rd of June, 2026

DOI: https://doi.org/10.15480/882.17406
ORCID: orcid.org/0009-0004-8219-5637

Summary

Machine learning (ML)-based modeling and design in electromagnetic compatibility (EMC) and related disciplines is shaped by the interplay of four main aspects: ML tools, available data, data acquisition and the engineers who guide their application. Recent advances have shown that ML methods can help accelerate simulations, improve design space exploration and speed up the modeling and design processes. Nevertheless, the wide adoption of ML in EMC is limited by recurring challenges, including the interpretability of models, the handling of high-dimensional design spaces, the data-efficiency of ML algorithms and the complexity of data acquisition.

This thesis investigates these challenges through a set of targeted studies at the intersection of ML, EMC and related disciplines. On the level of ML tools, methods such as time series classification (TSC) and adapted autoencoders (AEs) are explored for their potential to provide accurate models while retaining physically meaningful representations. Strategies for enhancing interpretability of ML models are considered, with the goal of linking model decisions to underlying electromagnetic behavior. On the level of data and its acquisition, emphasis is placed on improving data-efficiency and enabling reuse of existing datasets. Furthermore, contributions are made to the development of sharable datasets and validation frameworks, supporting reproducibility and collaborative progress within the community. The study is completed by providing a set of recommendations to help guide future research of ML integration in EMC engineering and related domains.

The proposed solutions have shown potential in addressing many challenges: Embedding physical insight into ML workflows consistently improved performance and reliability. The integration of data-efficient strategies, e.g., transfer learning (TL), effectively reduced the dependence on costly simulations and measurements. The implemented feature importance evaluation, e.g., using Gaussian process regression (GPR), helped with the interpretability of models and results. ML has shown considerable potential in reshaping and enhancing modeling, design and validation in EMC and related domains. While current solutions remain partial and problem-specific, the trajectory of progress in other fields, combined with the results presented here, suggests that focused research and collaborative data-sharing initiatives can bring scalable, interpretable and widely adoptable ML-based approaches for EMC.

Contents

List of Figures

List of Tables

List of Acronyms

AE autoencoder

AI artificial intelligence

ANN artificial neural network

BioEM bioelectromagnetics

BO Bayesian optimization

CI confidence interval

CIM contour integral method

CNN convolutional neural network

decap decoupling capacitor

EMC electromagnetic compatibility

EMF electromagnetic field

EMI electromagnetic interference

EV electric vehicle

FDTD finite-difference time-domain

FEM finite element method

FMCW frequency-modulated continuous wave

FNN feedforward neural network

FSV feature selective validation

FW full-wave

GA genetic algorithm

GAN generative adversarial network

GP Gaussian process

GPR Gaussian process regression

HFSS high-frequency structure simulator

HGR hand gesture recognition

IEEE Institute of Electrical and Electronics Engineers

ISI inter symbol interference

LHS latin hypercube sampling

MAE mean absolute error

MaV maximum value

ML machine learning

MoM method of moments

MRI magnetic resonance imaging

MSE mean squared error

NEC numerical electromagnetics code

nMAE normalized mean absolute error

nRMSE normalized root mean squared error

PB physics-based

PCB printed circuit board

PDN power delivery network

PEEC partial element equivalent circuit

PI power integrity

PPV proportion of positive values

PSO particle swarm optimization

RF radio-frequency

RMSE root mean squared error

SAR specific absorption rate

SI signal integrity

SVM support vector machine

TI target impedance

TL transfer learning

TSC time series classification

TUHH Hamburg University of Technology

Chapter 1

Introduction

Electromagnetic compatibility (EMC) engineering focuses on ensuring that electrical and electronic systems operate reliably within their electromagnetic environment. The goal is achieved by controlling the generation, propagation and reception of unintended electromagnetic emissions, as undesired emissions can lead to electromagnetic interference (EMI). Multiple disciplines are closely related to EMC, such as signal integrity (SI), power integrity (PI), bioelectromagnetics (BioEM) and radio-frequency (RF) engineering [**1**]. Depending on the scenarios, these fields must be taken into consideration when addressing EMC-related challenges. SI engineering aims at preserving the quality of signal transmission by minimizing reflections, losses and crosstalk. PI engineering ensures stable power delivery to components, in the presence of ground bounce and simultaneous switching noise. RF engineering contributes to understanding and managing electromagnetic fields at high frequencies, which is essential for the mitigation of radiated emissions. Beyond ensuring functional reliability, EMC also involves the protection of biological tissues from harmful electromagnetic exposure. The interaction of electromagnetic fields with biological tissue, studied under the field BioEM, is a critical consideration. The compliance with safety regulations is a key part of EMC assessments. This often involves rigorous testing and certification procedures, such as electromagnetic field (EMF) measurements around electronic devices. This helps estimate potential EMI and ensure compliance of devices. EMC is gaining an increasing importance in electrical engineering due to the extensive use of connected systems. Moreover, modern electronic systems, high-speed links and wireless technologies keep growing in complexity.

To illustrate the increasing complexity of modern electrical systems, consider the example of modern electric vehicles (EVs), see Fig. 1.1. EVs integrate many interconnected electrical and electronic subsystems operating at various voltage and frequency ranges, e.g., power and propulsion units, vehicle control, communication systems and user interfaces. These components are densely packed and must work in harmony to ensure reliable operation.

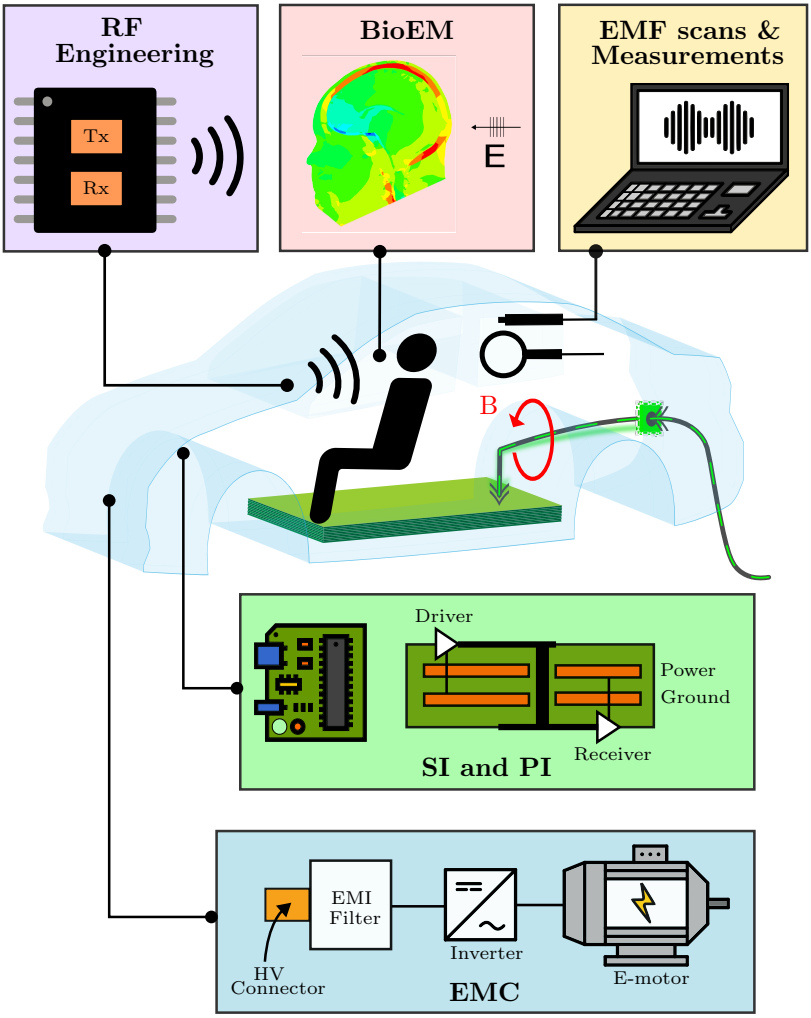

Figure 1.1: Aspects of electromagnetic compatibility (EMC) and related fields involved in electric vehicles (EVs). EVs represent a pertinent example of the rising complexity of electrical systems. Multiple subsystems are densely integrated in an EV. EMC considerations are an important aspect of the design process. Adapted from [1] © 2025 Institute of Electrical and Electronics Engineers (IEEE).

Achieving this level of integration requires careful consideration of EMC during the design process. Modern EVs, with their different processing units, incorporate a considerable amount of chips. Both SI and PI considerations are essential to ensure proper signal transmission and a stable power supply to the components. RF engineering also plays a role, for example in radar-based gesture recognition systems operating in the GHz range, introducing further EMC challenges. Beyond functionality, the safety of the passengers must be ensured. The interaction of the generated electromagnetic fields with the human body must remain within determined exposure limits [2]. EMF measurements and scans are essential tools to assess the electromagnetic behavior of the subsystems and ensure conformity with safety regulations.

The increasing complexity of modern electrical systems demands efficient approaches to modeling and design. Modeling refers to the creation of analytical or data-driven models that enable an accurate prediction of a system's behavior. In the context of EMC, design is the process of implementation of practical measures to ensure compatibility and compliance with EMI standards and regulations. Machine learning (ML) has become one of the most intensively researched fields in recent years. It deals with developing algorithms and computer programs that improve through experience gained from data [3]. Some ML applications in the EMC field have been pursued in the hope of providing more efficient alternatives to conventional methods [4].

The evolution of ML-based modeling and design for EMC is part of a broader technological journey. It is driven by advances in computational electromagnetics, data science and artificial intelligence (AI), see Fig. 1.2. This journey began in 1865 with the publication of Maxwell's equations, which laid the foundation for classical electromagnetism. A century later, significant progress in numerical methods enabled the practical solution of Maxwell's equations. The finite-difference time-domain (FDTD) method was introduced for time-domain simulations [5]. The method of moments (MoM) and finite element method (FEM) were developed for solving electromagnetic integral and differential equations, respectively [6]. These techniques became pillars of computational electromagnetics. They allowed the simulation of wave propagation and interaction with complex structures to simplify EMC analysis. By the 1980s, software tools such as numerical electromagnetics code (NEC) and high-frequency structure simulator (HFSS) emerged [7, 8]. This helped bring full-wave (FW) solvers to engineering practice and made detailed electromagnetic simulations widely accessible. It resulted in field visualization and EMC analysis with unprecedented accuracy. The era of physics-based (PB) modeling would change EMC engineering workflows. This shift was helped by the increasing computational power, availability of better hardware and

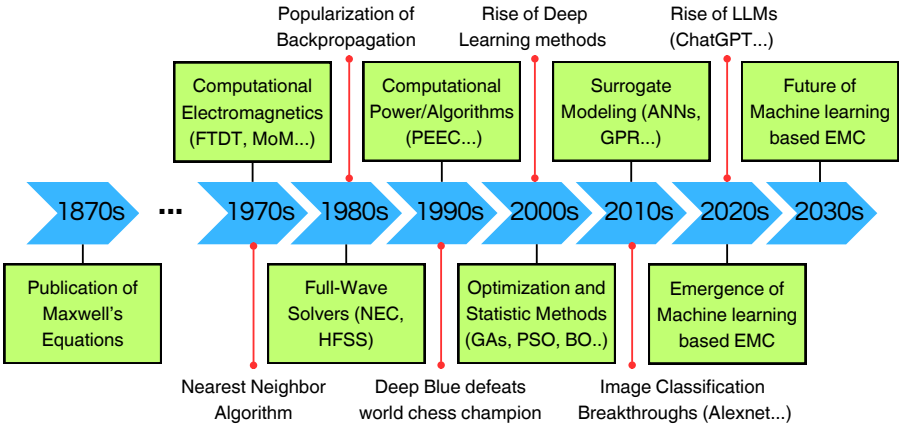

Figure 1.2: Timeline of machine learning (ML)-based electromagnetic compatibility (EMC) engineering. The application of ML-tools for the modeling and design in EMC has gained traction in the 2010s. Adapted from **[1]** © 2025 IEEE.

more established algorithms in the 1990s, e.g., parallel computing and partial element equivalent circuit (PEEC) [9]. The transition from physical to virtual prototyping, from reliance on intuition and experience to quantitative data, from isolated problems to system-level analysis, from trial and error to optimization allowed for major breakthroughs. The ability to efficiently simulate and visualize complex systems once thought of as impossible, have become commodity and standard practice in the 2000s. In addition, the use of computer-assisted optimization and statistical tools, e.g., genetic algorithms (GAs), Bayesian optimization (BO) and particle swarm optimization (PSO), had gained traction [10].

In parallel, the fields of AI and ML have experienced bursts of rapid advancements. This lead to major breakthroughs and the development of powerful tools for tasks such as image classification and natural language processing. As problems in the EMC domain continued to grow in complexity, conventional PB methods reached their limits in terms of accuracy or computational efficiency for some applications. Motivated by the success of data-driven approaches in other domains, the application of ML and AI techniques to EMC modeling and design began gaining momentum in the 2010s. In particular, surrogate modeling approaches have attracted increasing attention, e.g., using artificial neural networks (ANNs) or Gaussian process regression (GPR).

1.1 State of the Art

Many applications of ML in the EMC domain focus on reducing the time and computational cost associated with electromagnetic simulations, e.g., using surrogate models [**1**]. Recent advances in surrogate modeling for EMC include the use of minimal data from expensive 3D simulations to construct accurate models across wide frequency ranges [11, 12]. ML methods that offer sensitivity analysis have been investigated. They provide valuable design insights for applications such as automotive EMC and shielding cable emission modeling [11, 13]. Hybrid techniques that combine PB and data-driven models have also been developed. For instance, ANNs and generative adversarial networks (GANs) have been integrated into PEEC modeling to account for uncertainty [14, 15]. ML techniques have been applied to optimize EMI mitigation and filter design, leading to improvements in performance [12, 16, 17]. Other studies have addressed specific challenges in EMC, including the assessment of shielding effectiveness [18], enhancing electromagnetic susceptibility testing procedures [19], and predicting lightning-induced currents [20].

In the SI domain, ML has been used to characterize eye diagrams, e.g., vector machine regression to determine the eye-opening [21]. Researchers have also investigated the prediction of performance metrics such as inter symbol interference (ISI) and crosstalk using approaches based on weighted power sums [22, 23, 24]. The reconstruction of S-parameters using periodic Gaussian process (GP) kernels is another area of growing interest [25]. Optimization of high-speed links has been addressed using techniques such as BO for the equalization [26, 27] and deep neural networks for direct interconnect optimization [28, 29]. SI-compliant printed circuit board (PCB) design using ML has been explored, e.g., using ANNs and decision trees [30, 31, 32].

In the PI domain, research has explored the application of ML to improve the overall design process. This includes classifying power delivery networks (PDNs) with regard to the target impedance (TI) using ANNs or support vector machines (SVMs) [33]. Additional work has focused on using ML to gain insights into electromagnetic behavior during the design phase of PCBs [34, 35, 36]. Methods for optimizing the placement of decoupling capacitors (decaps) to reduce the PCB-based PDN impedance have been studied using various ML algorithms [37, 38, 39]. Optimization and modeling of PDNs have also been pursued using reinforcement learning, PSO and GAs [40, 41, 42].

In the field of BioEM, ML has been applied to estimate electrical tissue properties [43], predict specific absorption rate (SAR) and exposure levels to ensure compliance with safety limits [44, 45] and accelerate design and simulation tasks [46]. Many studies have shown that ML methods can effectively predict power absorption in magnetic resonance imaging (MRI), contributing

to the development of enhanced safety protocols [47, 48].

In RF engineering, ML has been investigated for the optimization of components and circuits to speed up design processes [49, 50, 51]. Inverse design, where design parameters are derived from specified design constraints, has been an area of research [52, 53]. Radar sensing represents a major application domain for ML solutions, e.g., vehicle detection [54], vital sign monitoring [55] and recognition of hand gestures [56]. ML methods have also supported improvements in RF measurements and EMF techniques. Research has focused on accurate field interpolation using limited sampling points [57, 58, 59]. Furthermore, accurate modeling of radiation sources using data from EMF scans has been the objective of several studies [60, 61]. Additional work has focused on solving EMC problems using a reduced number of EMF scans [58, 62].

1.2 Problem Statement

ML-based modeling and design involves the interplay between ML tools, data, data acquisition and engineers involved in the process, see Fig. 1.3. A closer examination of recent publications on ML in EMC and related fields reveals a set of recurring limitations and challenges facing the wide adoption of ML.

In the context of ML tools, a common challenge is the limited interpretability of results and the lack of insight in how ML models make decisions. From an engineering perspective, these aspects are important for gaining physical insight and improving decision-making in design-related tasks. Another major challenge is the handling of high-dimensional input spaces. Furthermore, because the relationships between inputs and outputs are often complex and not directly observable, many ML models require large amounts of data to generalize effectively. Data acquisition, which includes all activities related to collecting data for training and testing ML tools, is often time-consuming and resource-intensive. In particular, simulations and measurements can involve significant effort. If data generation is inefficient, the benefits of ML solutions may be outweighed by the costs of acquisition. The availability of high-quality and relevant datasets is critical for the development and evaluation of ML tools in EMC. Accessible datasets also enable the reuse of existing data, which can help optimize the learning process and reduce the need for new data. However, access to such datasets is still limited. The storage, organization and management of data to support meaningful search, retrieval and use remain important challenges that need to be addressed. Moreover, the considered problems and models are mostly simplified with a significant gap to real-world applications. The presented solutions are generally valid for very specific design spaces and defined scenarios.

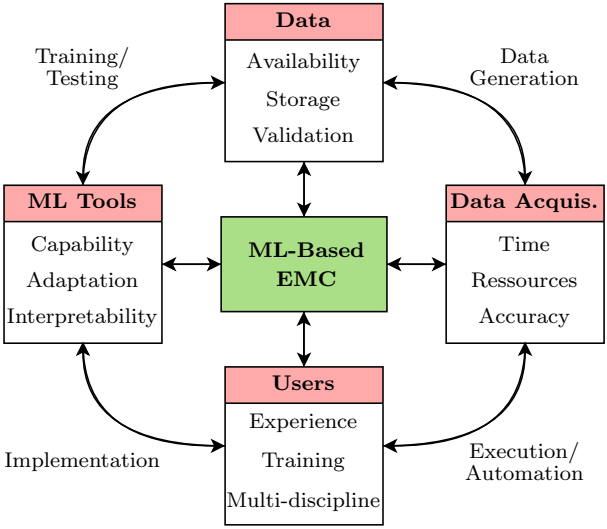

Figure 1.3: Diagram highlighting the most important aspects of machine learning (ML)-based electromagnetic compatibility (EMC) modeling and design. Adapted from [1] © 2025 IEEE.

1.3 Scope of the Thesis

The main objective of this thesis is to investigate and address key challenges associated with the aspects of ML tools, data and data acquisition processes that currently hinder the broader adoption of ML in the field of EMC. In particular, ML-based solutions are explored with the goal of enhancing the efficiency of modeling and design in EMC and the closely related domains of SI, PI, BioEM and RF engineering, see Fig. 1.4. Emphasis is placed on the development of solutions and the deployment of ML algorithms to address domain-specific problems while tackling common ML challenges: The important aspects of interpretability of models and high-dimensionality of datasets are considered. A major line of investigation concerns methods aimed at improving data-efficiency. These methods include approaches that enable the effective reuse of datasets. In turn, these methods thereby contribute to more resource-efficient modeling and design processes. In addition, contributions are made toward the buildup of sharable databases, with the aim of facilitating collaboration and accelerating progress within the research community. Finally, this thesis outlines recommendations for the future integration of ML in EMC, offering guidance on how the field may continue to evolve and mature.

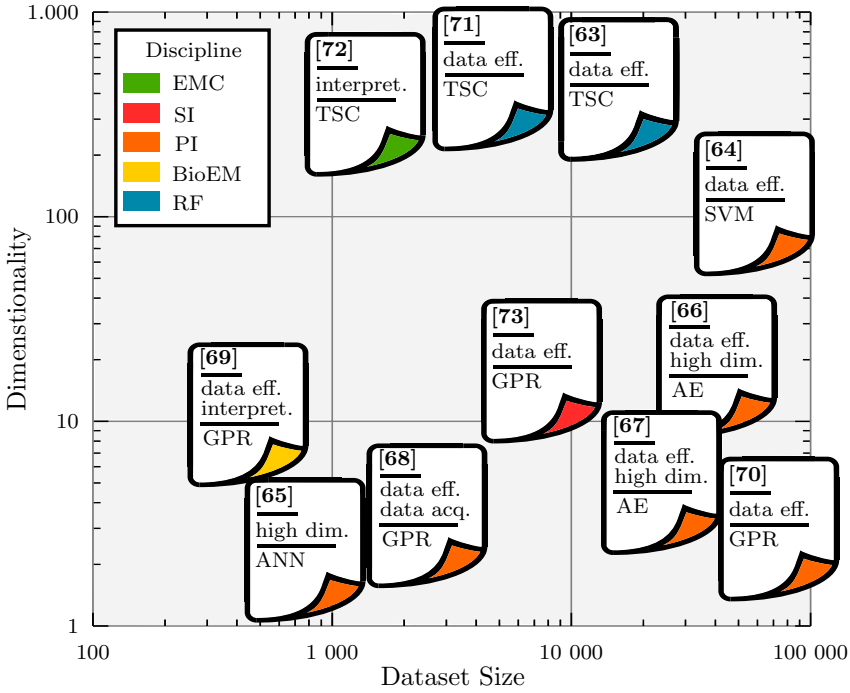

Figure 1.4: Publications of the author handling machine learning (ML) in electromagnetic compatibility (EMC) and related disciplines sorted by the number of dimensions, size of datasets and methods used.

The authors's publications used within this thesis, referenced in **bold**, cover a range of scenarios that differ in terms of complexity, dimensionality, size of used datasets and addressed challenges, see Fig. 1.4. Additionally, this thesis incorporates results from the master's thesis entitled "Characterization of PCB-based Interconnects Using Latent Space Mapping of Autoencoders", supervised by the author and written by Jan Heßling, in Section 3.5.

The remainder of this thesis is structured as follows: Chapter 2 gives a short theoretical background on used ML-tools and concepts in this thesis. Chapter 3 summarizes the results of the published papers on the application and development of ML approaches for efficient engineering in EMC and related fields. Chapter 4 presents a discussion and synthesis of the key findings and an outlook for the future. Chapter 5 provides a conclusion to the thesis. Full reprinted articles and their references are found under "Publications".

Chapter 2

Brief Introduction to Machine Learning Tools and Concepts

In this chapter, a concise theoretical background on the ML tools and concepts used throughout this thesis is provided. This review offers the necessary context for understanding the ML techniques investigated in the next chapters.

2.1 Artificial Neural Networks

Artificial neural networks (ANNs) are computational models inspired by the structure and function of biological neural networks **[67]**. They are first trained on data to then be used to predict an output vector $\boldsymbol{O} = [O_1, \ldots, O_N]$ for a previously unseen input vector $\boldsymbol{I} = [I_1, \ldots, I_N]$. ANNs are capable of learning complex relationships between inputs and outputs, allowing them to model a system's behavior. An ANN is composed of multiple layers of interconnected neurons, organized into an input layer, one or more hidden layers and an output layer, as illustrated in Fig. 2.1a. The neurons of the input layer are connected to the components of the input vector. The neurons of the output layer generate the elements of the output vector. Each neuron processes its inputs and produces an output a according to:

$$a = f(\boldsymbol{w}^{\mathrm{T}}\boldsymbol{x} + b), \tag{2.1}$$

where $\boldsymbol{w}$ is a vector of weights, b is a bias term, $\boldsymbol{x}$ is the vector of inputs from the connected neurons and f is an activation function that shapes the output, as shown in Fig. 2.1b. During training, the weights $\boldsymbol{w}$ are adjusted to minimize a chosen error function. The function quantifies the difference between the network's predicted outputs and the expected true values. This optimization is typically performed using backpropagation algorithms, such as the Adam optimizer [74]. Before training, several hyperparameters must be defined. These include, e.g., the number of hidden layers, the number of neurons per layer and the choice of activation function.

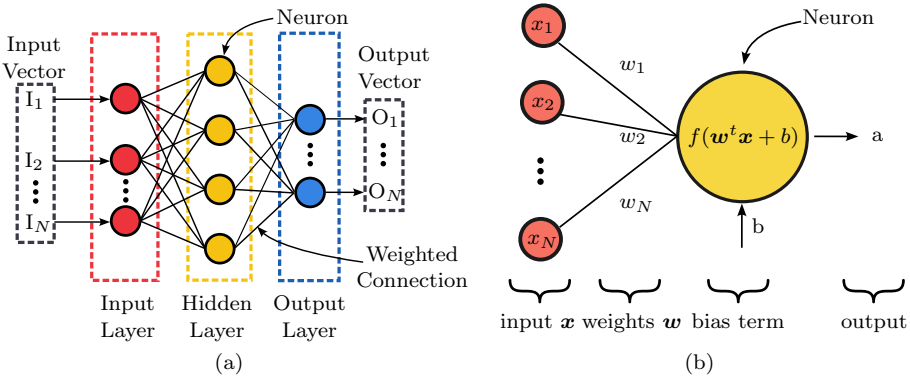

Figure 2.1: An overview of the (a) structure of an artificial neural network (ANN) with three layers and the (b) structure of single connected neuron from the hidden layer, is presented. Reprinted from [**67**].

2.2 Autoencoders

Autoencoders (AEs) are a type of ANNs that can learn compact and efficient representations of data [**67**]. They consist of three primary components: an encoder, a latent space and a decoder, as illustrated in Fig. 2.2. The encoder, denoted by the function E_θ, maps an input x to a lower-dimensional representation $z = E_\theta(x)$ within the latent space. The decoder, represented by the function D_ϕ, reconstructs an output $x' = D_\phi(z)$ from this latent representation z. Both encoder and decoder are ANNs, commonly implemented as feed-forward neural networks (FNNs) or convolutional neural networks (CNNs). During training, the sets of network weights (θ, ϕ) are optimized to produce reconstructions x' that closely match the original inputs x. This is typically achieved by minimizing a loss function that quantifies the reconstruction error over a set of N training samples x_i and their reconstructions x'_i. A common choice for the loss function L_{AE} is based on the mean squared error (MSE):

$$L_{AE}(\theta, \phi) = \frac{1}{N} \sum_{i=1}^{N} (x_i - x'_i)^2. \tag{2.2}$$

The latent space representation contains the most important features of the input data in a compressed form. One interesting property of AEs is regularity: Samples that are similar in the original input space tend to remain close in the latent space. This enables advanced data analysis and similarity detection.

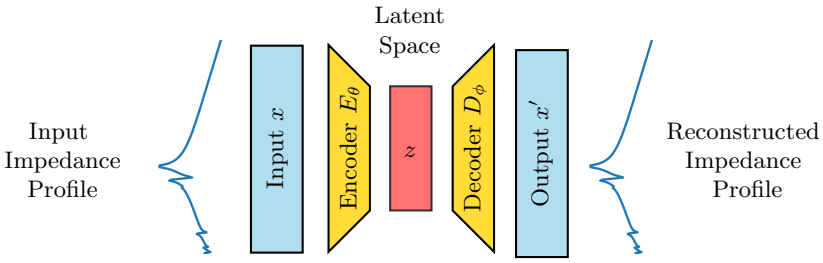

Figure 2.2: A regular autoencoder (AE) network can be trained to be able to reconstruct an input, e.g., an impedance profile, passing by the encoder, latent space and the decoder. Reprinted from **[67]**.

2.3 Gaussian Process Regression

Gaussian process regression (GPR) is a probabilistic regression method used to approximate an unknown target function $y = f(x)$ based on a given dataset of inputs and outputs $D_t = (X_t, Y_t) = [(x_1, y_1), \cdots, (x_t, y_t)]$, see Fig. 2.3 **[69]**. One of the main advantages of GPR is its effectiveness with limited datasets, as well as the ability to provide uncertainty estimates on the provided predictions [75]. The approach defines a probability distribution over all functions that could fit the observed data. As additional data points are included, initial assumptions about these functions are updated, resulting in an improved distribution over plausible functions. To represent this distribution, a GP is defined over the function values at certain input points $f(x_1), f(x_2), \cdots f(x_t)$. GPR assumes that these values are jointly Gaussian (normal) distributed:

$$f(x) \sim GP(\mu(X_t), K(X_t, X_t)). \tag{2.3}$$

Here, $\mu(X_t)$ denotes the mean function and $K(X_t, X_t)$ is the covariance function. The covariance is determined by a kernel function that includes assumptions about the smoothness and structure of the function y to be approximated. For EMC-related problems, a common choice is the Matérn 5/2 kernel [76], which is given for one-dimensional input points x_i and x_j by:

$$k_{\text{Matérn}}(x_i, x_j) = \left(1 + \frac{\sqrt{5}d}{\theta_l} + \frac{5d^2}{3\theta_l^2}\right) \exp\left(-\frac{\sqrt{5}d}{\theta_l}\right). \tag{2.4}$$

In this expression, d is the Euclidean distance between inputs and θ_l is a length-scale hyperparameter. The parameter defines how input proximity

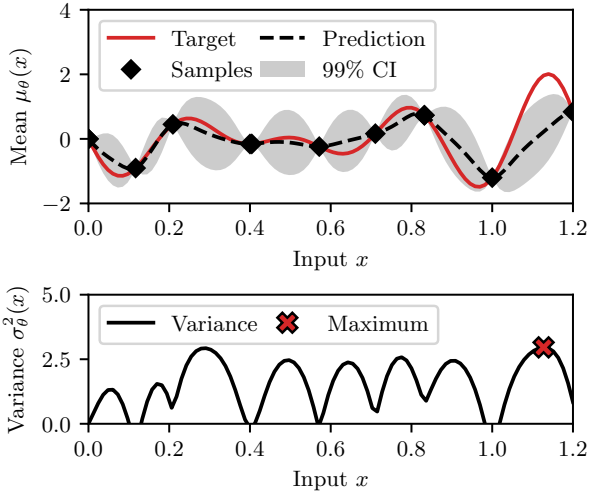

Figure 2.3: Gaussian process regression (GPR) is applied to approximate a 1D target function based on the training samples. The resulting variance provides insights into the uncertainty inherent in the GPR predictions. Reprinted from **[69]** © 2024 IEEE.

affects output correlation: closer points in input space lead to more correlated predictions. The kernel's hyperparameters θ_l are optimized using the available data to model the patterns in the data effectively. Since the function values are assumed to follow a joint Gaussian distribution, the conditional probability distribution at a new test point x can be derived from the known and available data points $Y_t = f(x_1), f(x_2), \cdots f(x_t)$. This process, known as conditioning, yields both the predictive mean and variance at any test point x [75]:

$$\mu_\theta(x) = K(x, X_t)K^{-1}(X_t, X_t)Y_t, \tag{2.5}$$

$$\sigma^2_\theta(x) = k - K(x, X_t)K^{-1}(X_t, X_t)K(X_t, x). \tag{2.6}$$

The function $\mu_\theta(x)$ gives the expected output at x and $\sigma^2_\theta(x)$ gives the uncertainty of the expectation. Fig. 2.3 illustrates an example of GPR approximating a one-dimensional target function. The predicted mean closely tracks the actual function near training data points. A 99 % confidence interval (CI), derived using the predicted variances, shows increasing uncertainty as test points move further from the training samples [77].

2.4 Active Learning

Active learning is a type of semi-supervised ML techniques [**70**]. In supervised learning approaches, the algorithms rely fully on datasets where all samples are labeled. In contrast, active learning uses a combination of labeled and unlabeled datasets. In active learning, the algorithm identifies which unlabeled samples should be labeled, iteratively. The objective is to maximize the information gain while minimizing the number of labeled samples required for training [78]. This becomes particularly useful in scenarios where labeling is resource-intensive, e.g., FW simulations of complex PCB structures. The general idea of active learning is illustrated in Fig. 2.4. Initially, an ML model is trained using a limited set of labeled data. The trained model then evaluates a larger pool of unlabeled samples and makes predictions. Based on these predictions, an acquisition function is used to select one or more data points for labeling. Once labeled, these new samples are added to the training set and the model is retrained to improve its predictions. GPR is well suited for integration into active learning strategies due to its ability to produce prediction uncertainty [79]. This uncertainty in the predictions, quantified by the variance, can be used to guide the selection of new samples for labeling. For instance, a sample that shows the highest uncertainty can be labeled to reduce the overall model uncertainty. Fig. 2.3 illustrates the predictive variance of a GPR model over a defined design space. The location associated with the highest uncertainty, indicated by a red cross, can be selected for labeling to improve the accuracy.

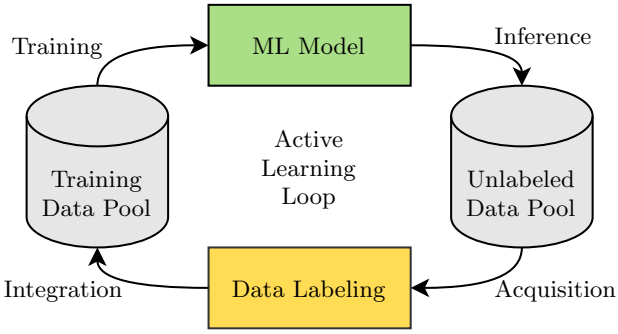

Figure 2.4: Diagram of the pool-based active learning cycle. Samples from the unlabeled data pool are iteratively selected for labeling and added to the training data. The machine learning (ML) model is trained on all labeled data each iteration. Adapted from [**70**].

2.5 Transfer Learning

Transfer learning (TL) is a method in ML where a model trained on one task is reused to address a different but related task [80]. The main idea is to use knowledge gained from solving the original task to accelerate and improve learning for the new task [**67**].

As illustrated in Fig. 2.5, the process generally involves two stages. The first stage, referred to as pre-training, involves training a model on a large dataset to learn a particular task. Once trained, the model can be stored and reused. This eliminates the need to repeat an extensive training process for every new task. In the second stage, known as fine-tuning, the pre-trained model is updated using fewer data from the new targeted task. This retraining step adjusts the model to the new task and enhances its performance. This approach is particularly useful when labeled data for the new task is limited or expensive to obtain, as is often the case in simulation-heavy tasks, e.g., EMC analysis or PCB design. By reusing previously acquired knowledge, a model benefits from an initialization of weights, allowing it to converge faster and with fewer resources for a new task. When applied effectively, TL may improve data-efficiency, reduce training time of ML models and lower computational cost. In engineering practice, it can also reduce the need for redundant simulations by reusing insights and knowledge acquired from one topology, frequency-band, or configuration to another. For example, let's assume an ML was model trained to predict the resonance frequency of a certain PCB topology from design parameters. The trained model can be reused by TL and fine-tuned to find the resonance frequency of another PCB design with a different topology and amount of layers [81].

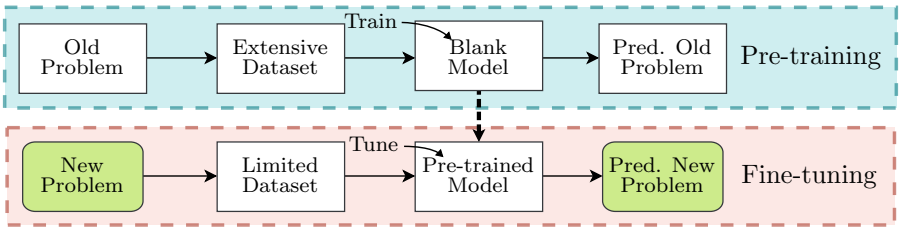

Figure 2.5: Diagram of the transfer learning (TL) approach. The pre-training stage involves the training of a model on older available datasets from scratch. The fine-tuning stage involves the retraining of the same model using new data samples from the new problem. Reprinted from [**67**].

2.6 Time Series Classification

A time series is a series of data points collected or recorded at determined points in time. Each observation in a time series represents the value of a variable at a specific point in time. TSC is a type of supervised ML in which labeled time series are assigned to predefined classes based on their structure and patterns. The goal in TSC is to build a model based on training data that can accurately predict the class of new, unseen time series.

There are many deep learning architectures specifically developed for TSC, e.g., *Rocket* [82, 83]. *Rocket* works by first transforming time series data with the help of a large number k of randomly generated convolutional kernels, as depicted in Fig. 2.6 **[72]**. Each one-dimensional kernel w is created with randomly assigned parameters: length l, dilation d and bias b [82]. The convolution operation on a time series sample X, at position i, is defined by [84]:

$$X_i * w = \left(\sum_{j=0}^{l-1} X_{i+(j \cdot d)} \cdot w_j \right) + b. \tag{2.7}$$

From the resulting feature maps, *Rocket* extracts two statistics per kernel multiplication result: the maximum value (MaV), corresponding to global max pooling and the proportion of positive values (PPV). Each time series sample is represented by $2 \times k$ features, the two extracted values per kernel operation. A classifier, e.g., a logistic regression model, is then used as a last step for the classification of the time series.

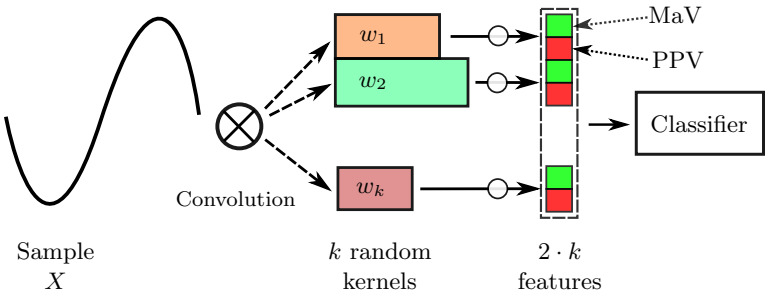

Figure 2.6: Depiction of simplified *Rocket* architecture [82]. A convolution operation is performed between random kernels and a time series sample. The maximum value (MaV) and proportion of positive values (PPV) are extracted from each resulting feature of the convolution operations. Reprinted from **[72]** © 2024 IEEE.

2.7 Regression Error Metrics

Regression is a type of statistical analysis used to model the relationship between input variables and a continuous output variable. To evaluate how well a regression model predicts continuous outputs, regression metrics are used. They represent quantitative measures used to compare a model's predicted values y' to actual values y in order to assess accuracy. These metrics are likewise useful for the comparison of functions, curves and continuous outputs, e.g., simulated and measured data. In this work, multiple metrics are used, including the root mean squared error (RMSE), mean absolute error (MAE) and coefficient of determination (R^2):

$$\mathrm{RMSE} = \sqrt{\frac{1}{n}\sum_{i=1}^{n}(y_i - y_i')^2}, \tag{2.8}$$

$$\mathrm{MAE} = \frac{1}{n}\sum_{i=1}^{n}|y_i - y_i'|, \tag{2.9}$$

$$R^2 = 1 - \frac{\sum_{i=1}^{n}(y_i - y_i')^2}{\sum_{i=1}^{n}(y_i - \bar{y})^2}, \tag{2.10}$$

where i is an index of a test set containing n samples and $\bar{y}$ is the mean of the true outputs y_i. Additionally, the normalized mean absolute error (nMAE) and normalized root mean squared error (nRMSE) represent percentage errors relative to the average values of outputs. They are helpful in making the comparison between different cases and variables more substantial:

$$\mathrm{nRMSE} = \frac{\mathrm{RMSE}}{\bar{y}}, \tag{2.11}$$

$$\mathrm{nMAE} = \frac{\mathrm{MAE}}{\bar{y}}. \tag{2.12}$$

These metrics provide complementary insights: RMSE and nRMSE penalize larger deviations more strongly. They are useful for detecting large prediction errors. The MAE and nMAE offer an intuitive measure of the average deviation in the same units as the predicted output. The R^2 score quantifies how well the model captures the variance of the data. Values close to 1 indicate high correlation between predicted and true outputs.

Chapter 3

Developing Machine Learning Solutions for Efficient Engineering

In this chapter, the development and application of ML-based solutions for EMC and related fields is showcased. The used study cases are drawn from the listed published articles and serve to illustrate how various ML techniques have been adapted and successfully applied to address practical challenges. Each application is briefly presented to highlight the core idea, methodology and results. The full technical details and implementation specifics are found in the attached publications.

3.1 Prediction of Specific Absorption Rate

The specific absorption rate (SAR) is a key metric for assessing human exposure to electromagnetic fields. It is defined as the power absorbed per mass of biological tissue, and can be calculated using the electric field, the electric properties and mass density of the tissue. Accurate SAR estimation is challenging due to the complex interactions between electromagnetic waves and biological tissues. Biological tissues naturally vary in electrical properties, such as permittivity ε_t and conductivity κ_t, across individuals. FW simulations are commonly used to estimate electric field distributions and SAR, but they are computationally demanding. Single simulations of a human head model usually take from few minutes to few days on commercial computers depending on resources and complexity [85]. ML tools such as ANNs have been successfully used for the prediction of SAR levels in human head tissues to replace electromagnetic simulations [47, 86, 87]. However, the proposed approaches need a large volume of samples for the training of the models and offer very little room for the interpretation of results.

The following scenario is considered: A human head model, including variations of the permittivity and the conductivity in 5 different tissues, is exposed to an external electromagnetic wave, see Fig. 3.1 [**69**]. The electromagnetic

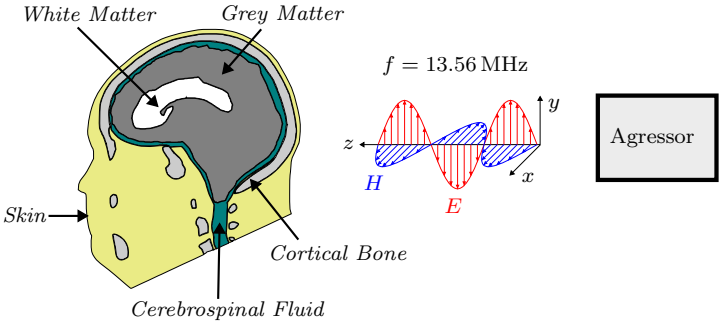

Figure 3.1: Illustration of a human head model with varying electrical properties of the tissues exposed to a plane electromagnetic wave. Adapted from [**69**] © 2024 IEEE.

wave is normal to the coronal plane and has a frequency of 13.56 MHz, typical for brain implants. In this application, GPR is embedded in an active sampling loop for the prediction of the SAR. The main target behind the use of GPR in an active learning loop is the increase of the data-efficiency and reduction of the number of expensive simulations needed in comparison to ANNs. Moreover, GPR allows more insight into the physics of the problem. The GPR models provide a prediction of the SAR depending on the inputs: The five tissues' conductivity and permittivity inside realistic ranges known as variation space. At the start of the process, no data is available for the training. The active learning loop guides the simulation process to sample points from the variation space to improve the predictions. After each iteration, a new simulation is performed and the resulting sample including the inputs and outputs (resulting SAR in the tissues) is added to the training set. The prediction accuracy of the GPR model increases iteratively.

For 50 points from the variation space, the predicted SAR in the Cortical Bone tissue using 20 training samples is compared with the simulations, see Fig. 3.2. The predicted SAR fits the values from the simulations. The GPR model can accurately predict the SAR for any combination of conductivity and permittivity while providing a CI around the predictions.

The maximum SAR exposure in the human head model over the variation space is very important to compare with safety limits [2]. Using the implemented GPR in an active learning loop allows finding the maximum SAR over all the tissues during the training iterations. The maximum SAR is found after 17 iterations only, see Fig. 3.3. In comparison, finding the maximum by randomly sampling the variation space takes much longer. In other words,

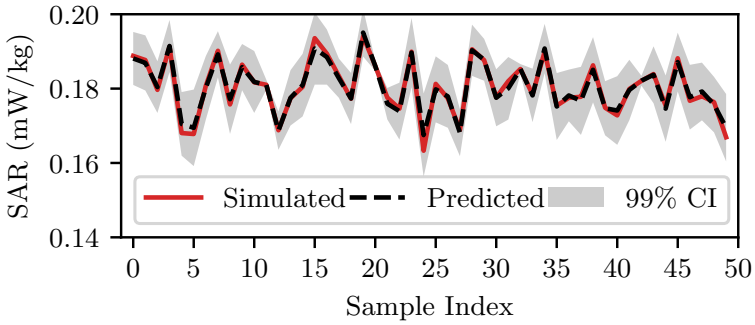

Figure 3.2: Predicted average specific absorption rate (SAR) by the trained Gaussian process regression (GPR) models inside the Cortical Bone compared to simulated values for 50 points of the variation space. Reprinted from [**69**] © 2024 IEEE.

the GPR allows the fast identification of the worst case (highest) exposure using a reduced number of simulations. Moreover, in comparison to ANNs, the GPR model natively enables the extraction of feature importance. The latter give insight on the most important input features affecting the SAR. The extracted feature importance from the trained model is given, see Fig. 3.4. The variation in the conductivity of the different tissues has more impact on the resulting SAR values than the variation in the permittivity of the tissues. From a physical perspective, this is an expected behavior for the SAR as the conductivity directly impacts the heat losses and the absorbed power. For the frequency of 13.56 MHz, the polarization losses are negligible, hence a much lower dependency of the SAR on the permittivity is observed.

In conclusion, GPR models demonstrated generalization capabilities and enabled fast predictions of the SAR. The ML models offer a promising alternative to reduce the computational cost of FW simulations and accelerate the design process in BioEM and EMC applications. Its built-in uncertainty estimation enables the identification of worst-case exposure scenarios within defined CIs, thus eliminating the need for dense sampling of a variation or design space. This facilitates, e.g., rapid safety assessments prior to production. By using an active learning loop, the number of required training data is reduced: Samples are iteratively added until a specified confidence level is reached. Additionally, a sensitivity analysis, obtained without extra computational cost, provides insights into the most influential parameters.

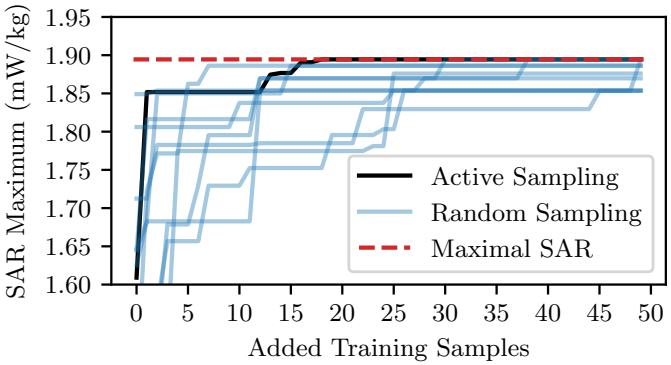

Figure 3.3: Specific absorption rate (SAR) maximum found using active sampling compared with 10 random sampling runs. The global maximum is found in 17 iterations. Reprinted from **[69]** © 2024 IEEE.

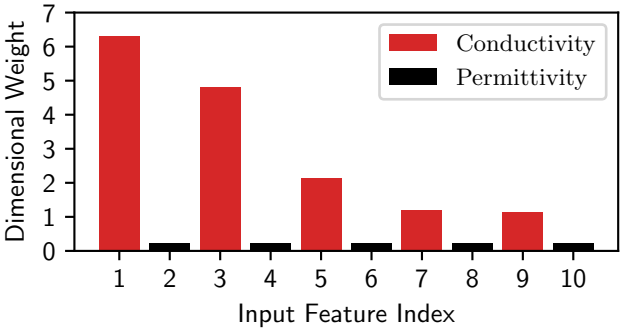

Figure 3.4: Sensitivity of the output (specific absorption rate) to variations in the input parameters. The sensitivity is calculated using the length-scales of the Gaussian process (GP) kernel. The conductivity of the tissues show more impact on the SAR than permittivity. Reprinted from **[69]** © 2024 IEEE.

3.2 Large-Scale Validation of Simulated Datasets

In EMC engineering, simulation and measurement play a crucial role. Particularly in SI and PI, they are heavily used in the design and verification of PCBs. Engineers frequently simulate electrical behavior using models that range from simplified PB representations to highly detailed FW solvers. One fundamental challenge in this context is ensuring the validity and reliability of simulation data. As a standard practice, engineers compare simulation results against one another or against measurement data to validate the accuracy of models. However, such validation is often based on subjective visual inspection of results: An engineer judges the similarity between two sets of curves, e.g., broadband S-parameters, based on experience and intuition [88]. This human validation process has several drawbacks including subjectivity: Different engineers may interpret the same data differently due to variations in experience, domain-knowledge and other cognitive biases. As data volumes grow, particularly in workflows that involve large datasets, e.g., ML applications, manual validation becomes impractical and time-consuming. To address these limitations, the EMC community has developed quantitative validation tools such as the feature selective validation (FSV) method [89, 90]. The FSV method attempts to emulate expert judgment using analytical comparisons of features in the data. However, FSV does not always align well with expert opinion. Especially on edge cases, it may yield inconsistent results depending on the dataset and metric configuration [91, 92]. As such, there is a clear need for a validation method that:

- Replicates human expert judgment more accurately than conventional error or correlation metrics.
- Reduces subjectivity by learning from multiple experts and averaging their insights to capture domain-knowledge.
- Scales to large datasets and supports automation.
- Is flexible and generalizable across different data representations, e.g., broadband S-parameters, impedance, admittance and domains, e.g., SI, PI, EMC and beyond.

To address these needs, a novel ML-based framework that uses supervised TSC to automate the validation process is proposed, see Fig. 3.5. The core idea is to train a time series classifier that mimics the visual assessment behavior of domain experts by learning directly from labeled examples **[72]**. This approach takes advantage of recent advances in deep learning for time

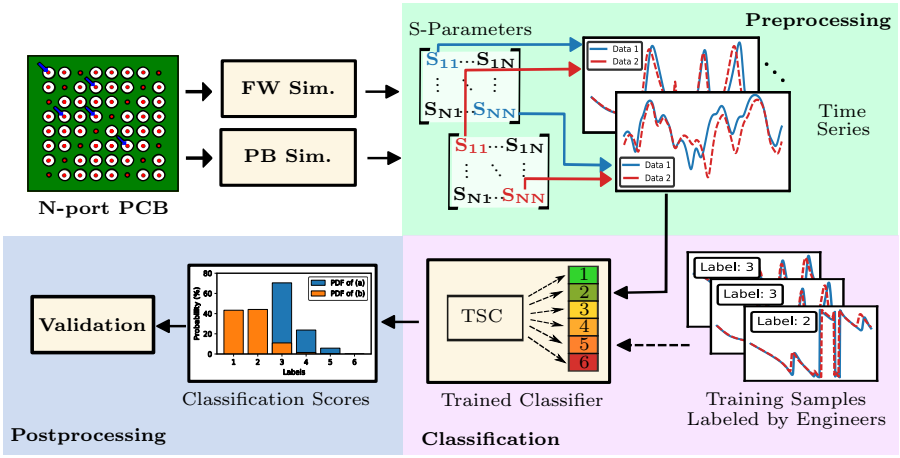

Figure 3.5: Block diagram of the proposed data validation framework. The three main blocks of the pipeline are the preprocessing, classification and postprocessing. Adapted from **[72]** © 2024 IEEE.

series. Convolutional and kernel-based TSC models can learn subtle patterns and relationships that align with human intuition [83]. The considered application example consists of the validation of simulated PCB structures using a PB model [93] against a commercial FW solver [94]. The proposed framework consists of three main stages: Preprocessing, where time series are constructed from simulated S-, Z- and Y-parameters (magnitude, real, imaginary, phase, etc.) in pairs of PB and FW simulation results. Classification, where trained *Rocket* models [82] are used to classify these time series into one of six agreement scores (where $1 \Rightarrow$ perfect match, $6 \Rightarrow$ no visible agreement). Postprocessing, where classification uncertainty is estimated and confidence-aware validation of large datasets is enabled. The proposed method can be integrated into data-driven processes and ML-based workflows.

For the training and testing processes, eight different PCB structures have been simulated using both PB and commercial FW tools. Over 1600 time series samples are generated, representing various network parameters across different structures and frequency domains. To train the models, the generated samples are visually assessed by six electrical engineers with a background in EMC according to a visual assessment scale [95], see Table 3.1. Each curve pair is labeled with a score from "1" to "6". The labeling distributions and behaviors vary across users, confirming the subjectivity of manual validation.

Table 3.1: Six-points visual assessment scale for the determination of the degree of agreement of two curves. Reprinted from [**72**] © 2024 IEEE.

Characteristics	**Quality**	**Description**	**Score**
Many similarities	Perfect match	Excellent	1
	Minor variations	Very good	2
Some similarities	Good agreement	Good	3
	Reasonable agreement	Fair	4
Many dissimilarities	Minor agreement	Poor	5
	No visible agreement	Very Poor	6

The performance of the ML-based classification has been tested on the generated datasets. When evaluated on labels averaged from six expert users, the model achieved an accuracy of 74.5 %. It outperforms all individual human raters in terms of alignment with the group consensus (average rating). In comparison, the best-performing human annotator reached a lower accuracy of approximately 68.8 %. Moreover, 96.6 % of predictions were either correct or within one score point of the expert-assigned label. This indicates that errors of more than one scale point are rare. These results confirm that the classifier closely matches expert opinion and maintains a high level of consistency.

For instance, two pairs of curves have been presented to the trained *Rocket* model for classification, see Fig. 3.6 (a) and Fig. 3.6 (b). The assessed labels are compared with the FSV method and the expert human visual assessment, see Fig. 3.6 (c). The *Rocket* model is able to correctly classify the pairs and match the visual assessment score in milliseconds. Moreover, the model also provides classification probabilities allowing uncertainty quantification. This enables the detection of low-confidence predictions or the assisted validation: Port-pairs with uncertain predictions can be flagged for manual review. An example that shows how this feature facilitates semi-automated review, optimizing the validation process of large datasets, is shown in [**72**].

In conclusion, the trained ML models, when applied to SI/PI datasets labeled by domain experts, outperform individual engineers in reproducing a group-average validation score. This method presents a promising framework for automated and scalable data validation: It effectively captures the visual assessment score given by experts, while offering rapid prediction and integrated uncertainty estimation. This is particularly relevant in ML workflows, where large volumes of simulation and measurement data must be validated. The proposed framework is flexible and can be adapted to other domains by incorporating domain-specific datasets labeled by domain experts.

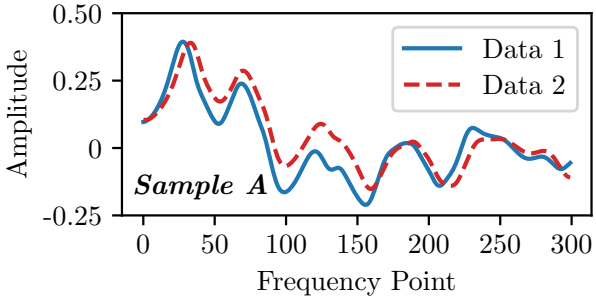

(a)

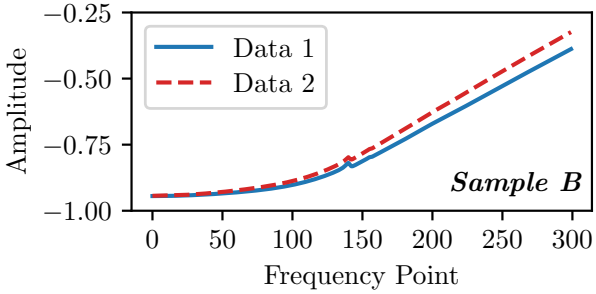

(b)

Test Sample	FSV	*Rocket*	Visual
Sample A	4	3	3
Sample B	1	2	2

(c)

Figure 3.6: Two time series input pairs (a) *Sample A* and (b) *Sample B* are fed to the trained *Rocket* model for classification. (c) *Sample A* and *Sample B* have been assigned a score of "3" and "2", respectively, matching the visual assessment. Adapted from **[72]** © 2024 IEEE.

3.3 Modeling of Power Delivery Network Features

The efficient design of PCB-based PDNs is a central challenge in high-speed digital systems. This is due to the rising integration density and operating frequency of the systems. Ensuring that the PDN impedance remains within specification usually requires computationally expensive simulations. The simulations are key to obtain information on the electromagnetic behavior of the PDN impedance. The information is necessary for many iterative PDN design processes using both ML or conventional methods [39, 96]. In the following application, key-features of the PDN impedance are predicted using ML tools. These key-features, conventionally extracted using FW simulations, give insight on the PDN impedance necessary for the design process. While ML models such as ANNs have already shown promise in predicting PDN key-features, they often require a large amount of training data. This can in turn become a bottleneck due to the simulation burden [34]. This issue is addressed here through a data-efficient ML framework. The approach combines transfer and active learning to minimize data requirements by smartly selecting training points while reusing existing data [**68**].

The proposed framework uses GPR as a main modeling tool embedded in an active learning loop, see Fig. 3.7. For a new PCB case and design space, training begins either from scratch or with a small set of available data. Then, the GPR model makes initial predictions and calculates uncertainty for each point in the design space. The point with the highest uncertainty is selected for simulation and added to the training set. This iterative process continues, improving the accuracy of the model gradually.

Instead of predicting the full impedance profile, the framework focuses on predicting a set of six key-features relevant to PDN design [34], see Fig. 3.8:

- The resonance frequency of the board f_r,
- the overshoot at the resonance frequency ΔZ_r,
- the frequency of the first local maximum f_m,
- the overshoot at the first local maximum ΔZ_m,
- the maximum overshoot ΔZ_o, and
- the first frequency span Δf_s.

These key-features are necessary for many PDN optimization techniques and predicting them directly can reduce both computation time and complexity in ML modeling.

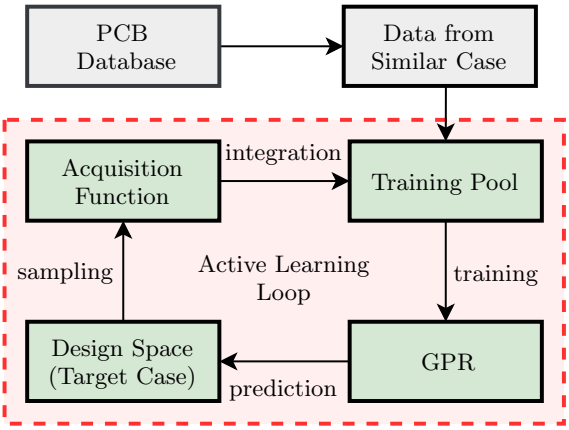

Figure 3.7: Diagram of the proposed data-efficient machine learning (ML) approach for key-feature prediction. The approach combines an active learning loop and data-reuse through transfer learning (TL). Adapted from [**68**] © 2024 IEEE.

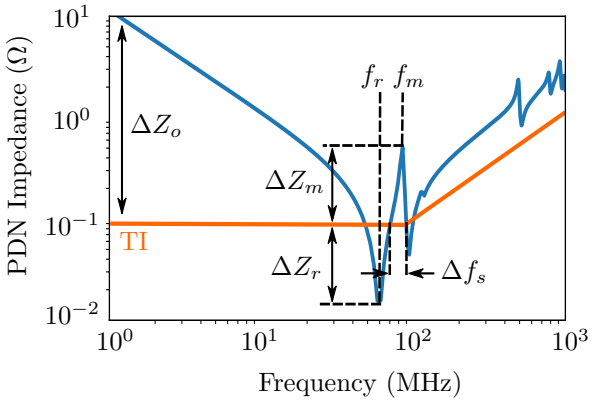

Figure 3.8: Defined key-features of the power delivery network (PDN) impedance. Many PDN optimization techniques rely on information of some distinct features of the PDN and the target impedance (TI). These key-features are predicted using machine learning (ML) tools to replace simulations. Adapted from [**68**] © 2024 IEEE.

To investigate the proposed approach, a 4-layer PCB structure including power and ground planes (ground, power, power, ground) is considered **[70]**, see Fig. 3.9. An array composed of a single central power via surrounded by two ground vias is placed in the middle of the board. Key geometrical and material parameters (inputs) X-width, Y-width, dielectric height and relative permittivity are varied within a defined design space. The self-impedance as seen from the power via is computed using a hybrid modeling approach: A contour integral method (CIM) for plane impedance and a PB via model for vertical structures [97]. A total of 2000 samples are generated via latin hypercube sampling (LHS) to cover the defined design space. These samples constitute the main dataset for training and evaluating the GPR model.

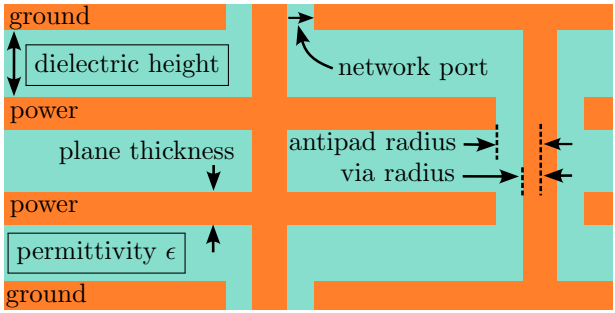

(a)

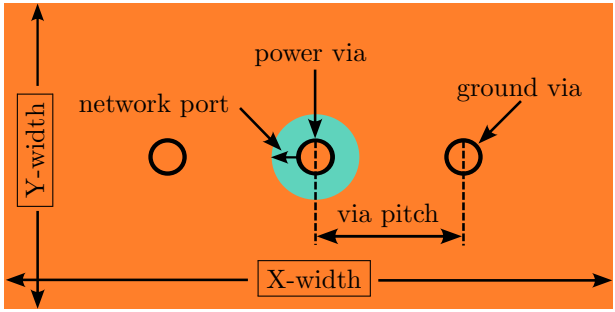

(b)

Figure 3.9: Geometrical depiction of the investigated case as seen from the (a) side of the board and the (b) top of board. Variable design parameters are framed. The conductor (orange) and dielectric (turquoise) are marked. Adapted from **[68]** © 2024 IEEE.

First, GPR models are evaluated using active learning only, i.e., they are implemented without data-reuse by TL. Several features, particularly those associated with board resonance (e.g., f_r, ΔZ_r, Δf_s), are predicted with high accuracy. The nRMSE for these features amounts to approximately 3 %. For the resonance frequency f_r, the RMSE and nRMSE amount to 1.8 MHz and 2.04 %, respectively. However, predictions for features involving overshoots at less stable frequencies (e.g., ΔZ_m and ΔZ_o) were less accurate. This is likely due to their higher variability and sensitivity to noise in the data.

To further enhance data-efficiency, TL is explored by dividing the design space into subspaces depending on the two parameters: X-width and Y-width, see Fig. 3.10. For example, subspace "*Sub 0*" is designated as the target problem, while data from subspaces "*Sub 4*" and "*Sub 8*" (which differ in geometric parameters) are used as prior knowledge. A GPR model is trained for the active prediction of the PCB resonance frequency f_r in "*Sub 0*" while using initial data from "*Sub 4*" or "*Sub 8*". The reuse of data from these subspaces provides a performance boost in early iterations reflected by a lower RMSE, see Fig. 3.11. In particular, closer subspaces (e.g., "*Sub 4*") lead to faster convergence of the prediction error compared to more distant ones (e.g., "*Sub 8*"). Dividing the design space including the dielectric height as an additional parameter, similar trends are observed.

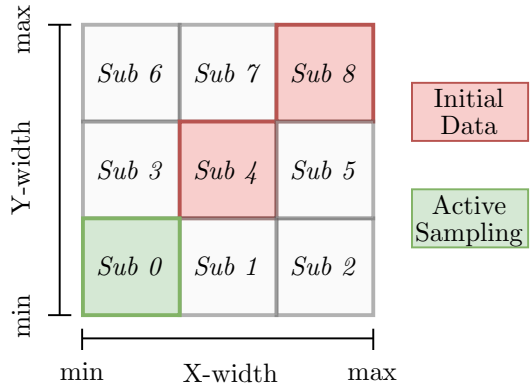

Figure 3.10: The design space is divided into nine subspaces depending on the X-Width and Y-Width of the board. Initial data is provided from "*Sub 8*" or "*Sub 4*" while further data points are actively sampled from "*Sub 0*". Adapted from **[68]** © 2024 IEEE.

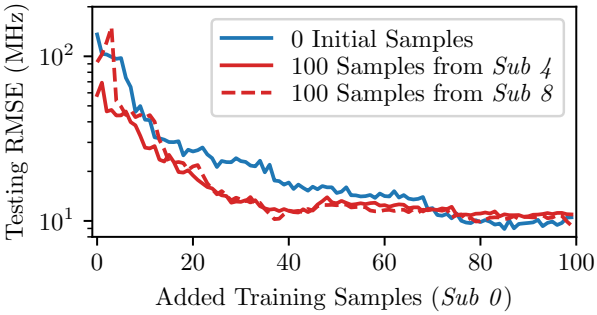

Figure 3.11: Prediction accuracy of the resonance frequency f_r in "*Sub 0*" using initial transfer learning (TL) data from "*Sub 8*" or "*Sub 4*". Adapted from **[68]** © 2024 IEEE.

In conclusion, the practicality of GPR-based regression embedded in transfer and active learning loops for efficiently predicting critical PDN impedance features is demonstrated. The proposed approach shows potential in reducing reliance on FW simulations while maintaining acceptable prediction accuracy. TL has shown benefits in increasing data-efficiency in the prediction of the resonance frequency, when data from related design configurations is reused.

3.4 Radar-Based Hand Gesture Recognition

Hand gesture recognition (HGR) is an emerging application domain for radar sensing. Radar-based HGR enables touchless interaction for consumer electronics, automotive interfaces and assistive technologies. Compared to optical sensors, radars offer more robustness to lighting conditions, privacy preservation and even penetration through certain materials [98]. However, high-accuracy gesture recognition in real-world environments remains challenging. This is partially due to gesture signal variability caused by differences in subjects, gesture execution speed and environmental clutter. There is a need for compact, data-efficient and real-time-capable solutions that can operate robustly across a range of practical scenarios without extensive calibration. Since hand gestures are very complex in nature, conventional signal processing methods do not represent reliable techniques for the classification of gestures. In an attempt to tackle these issues, a frequency-modulated continuous wave (FMCW) radar-based HGR system that leverages advanced signal preprocessing and deep learning for reliable classification is proposed **[71]**. The proposed

system uses TSC on preprocessed time series and augmented datasets. The main target of the application is the accurate recognition of micro gestures, i.e., finger movement, and macro gestures, i.e., full hand movement, from different locations surrounding an FMCW radar, see Fig. 3.12.

A comprehensive dataset of ten different defined gesture classes (e.g., swipe, push, pull) was recorded, see Fig. 3.13. The gestures were performed by multiple subjects from varying conditions and positions. Each gesture instance was captured as a sequence of range-Doppler frames. A preprocessing scheme is applied to transform the recorded gestures to 4-channel time series, see Fig. 3.14. The channels describe the change of range relative to the radar, angles to the radar and magnitude of the reflected signals by the subjects, respectively [**63**]. To build an HGR system capable of recognizing performed gestures, an ML-based TSC model is trained on the dataset of recorded gestures. *InceptionTime* architecture has been chosen for the modeling, as it has shown state-of-the-art classification accuracy on benchmark datasets [99]. The trained model has been evaluated on unseen test gestures and reached a prediction accuracy of 90.79 %. The model showcased a good classification ability on gestures performed from multiple ranges and angles, see Fig. 3.15. Since each subject performs gestures differently, including speed of execution, hand size and height, the models need to be trained on a very large amount of data samples to be able to generalize well. The recording and collection of samples is a time-consuming and costly operation. A physically-interpretable

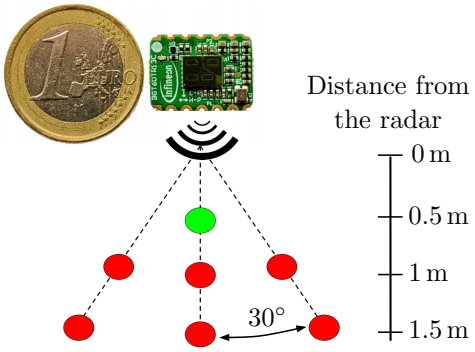

Figure 3.12: Diagram of the radar device and recording positions. The micro gestures are recorded from the position marked in green only. Adapted from [**71**] © 2023 IEEE.

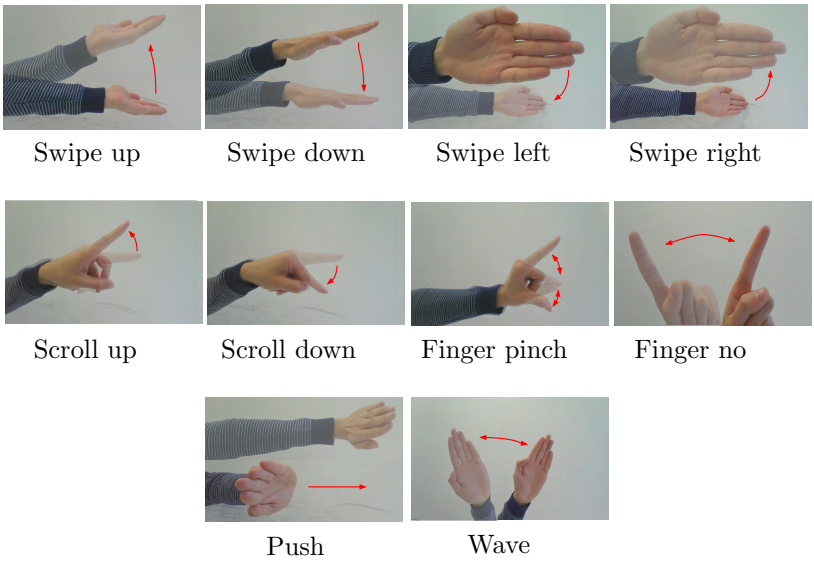

Figure 3.13: Graphical representation of the ten defined gestures for the radar hand gesture recognition (HGR) system. Reprinted from [**71**] © 2023 IEEE.

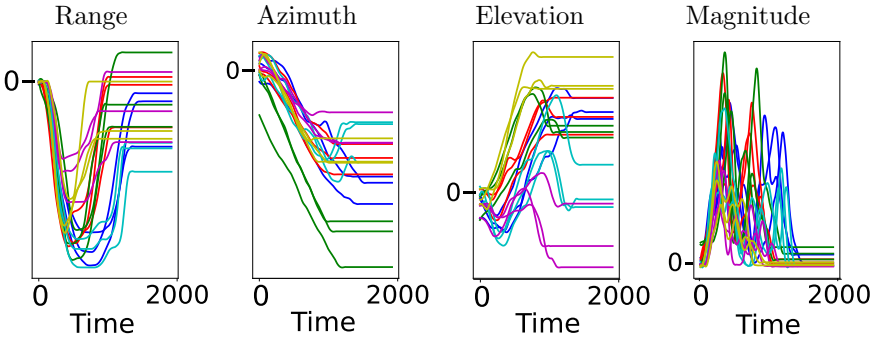

Figure 3.14: Plot of the four time series channels of a "push" gesture recorded for multiple subjects. Reprinted from [**71**] © 2023 IEEE.

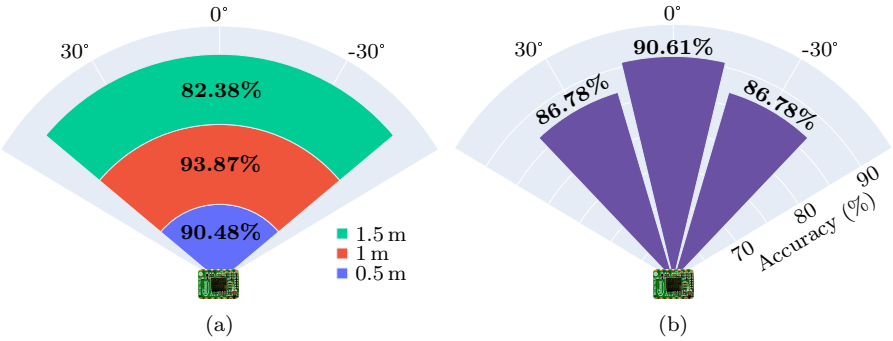

Figure 3.15: Prediction accuracy of the trained *InceptionTime* models on (a) gestures performed from multiple ranges and (b) gestures performed from multiple angles. Adapted from **[68]** © 2024 IEEE.

data augmentation technique is proposed to create synthetic samples from real recorded samples. The synthetic samples are added to existing datasets to increase the size and variety of datasets and enhance the performance. The proposed strategy applies transformations to radar time series data that correspond to realistic physical changes, see Fig. 3.16:

- Amplitude Scaling: Emulates variations in radar cross-section and range attenuation.
- Time Warping: Emulates faster or slower gesture execution while maintaining Doppler-time relationships.
- Slope Scaling: Models change in angle of gesture performance.

Each transformation is applied in a parameter-controlled way to ensure the augmented samples remain plausible radar observations. This contrasts with generic augmentations, which can distort motion patterns in physically meaningless ways. The model trained on augmented datasets achieved a prediction accuracy higher than 95 %. This marks an increase of approximately 5 percentage points in the accuracy when compared with the original non-augmented model. Moreover, the physically-interpretable proposed augmentation method outperforms other generic augmentation methods compared, e.g., sub-optimal warped time-series generator (SPAWNER) [100], weighted discriminative time warping barycenter averaging (wDBA) [101], random guided warping (RGW) and discriminative guided warping (DGW) [102]. An interesting area of application of the proposed augmentation technique is the improvement of accuracy

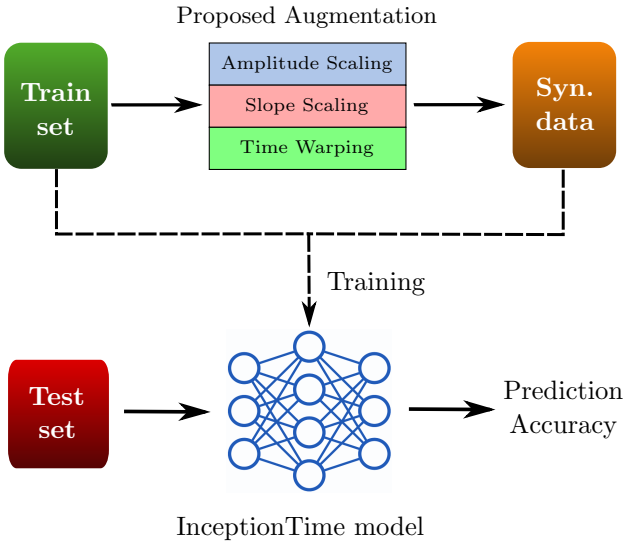

Figure 3.16: Framework of data augmentation for radar-based hand gesture recognition (HGR). The synthetic samples are added to existing training sets. Adapted from [71] © 2023 IEEE.

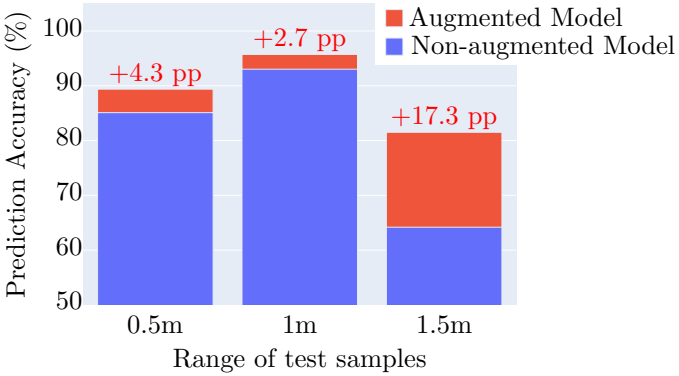

Figure 3.17: Prediction accuracy of the augmented and non-augmented 1 m models on test data from different ranges. Reprinted from [71] © 2023 IEEE.

for ranges and angles where no data has been recorded. For example, an ML model trained on available samples from the 1 m range only is considered. Targeted data augmentation can help create synthetic samples that emulate recordings from 0.5 m and 1.5 m ranges by proper choice of parameters. The model trained on augmented datasets provides a clear increase in performance in the prediction of gestures from the 0.5 m and 1.5 m ranges, see Fig. 3.17.

In conclusion, TSC models have been used in combination with a lightweight time series preprocessing scheme that simplifies very complex raw radar data of recorded hand gestures. The model trained on datasets containing micro and macro gestures from three different ranges and three different angles has shown a prediction accuracy higher than 90 %. A physically-interpretable data augmentation scheme has been proposed to successfully improve the accuracy of classification. This enables improved recognition performance, particularly in multi-range and subject-independent scenarios, by generating realistic variations that match physical radar behavior. The technique is useful in scenarios where the data is expensive to generate.

3.5 Impedance Profile Prediction for Modeling Power Delivery Networks

Modern PDN design is increasingly complex due to higher switching speeds, higher integration densities and lower supply voltages as mentioned in Section 3.3. This rises the requirement of even lower PDN impedances [103]. Achieving these low impedances often involves iterative placement of decoupling capacitors, guided by electromagnetic analysis [34]. FW simulations are time-intensive and represent a major bottleneck, especially when exploring large design spaces or multi-port configurations **[65]**. In the following, a data-efficient ML framework for the modeling of full self-impedance and transfer-impedance profiles of PDNs is proposed **[66]**. The full impedance profiles offer a more sophisticated knowledge on the electromagnetic behavior than distinct key-features. The approach enables the rapid modeling of N-port PDNs to speed-up the design process, see Fig. 3.18.

For this purpose, a two-stage architecture combining AEs with FNNs, denoted as FNN-AE, is used [36,**67**]. The main idea is to exploit the ability of AEs to learn a compact latent space representation of high-dimensional impedance profiles, and then train an FNN to predict this latent space representation from PCB design parameters. Stage 1 involves the training of an AE to reconstruct impedance magnitude profiles. In stage 2, the encoder is replaced by an FNN that maps design parameters (e.g., via radius, pitch,

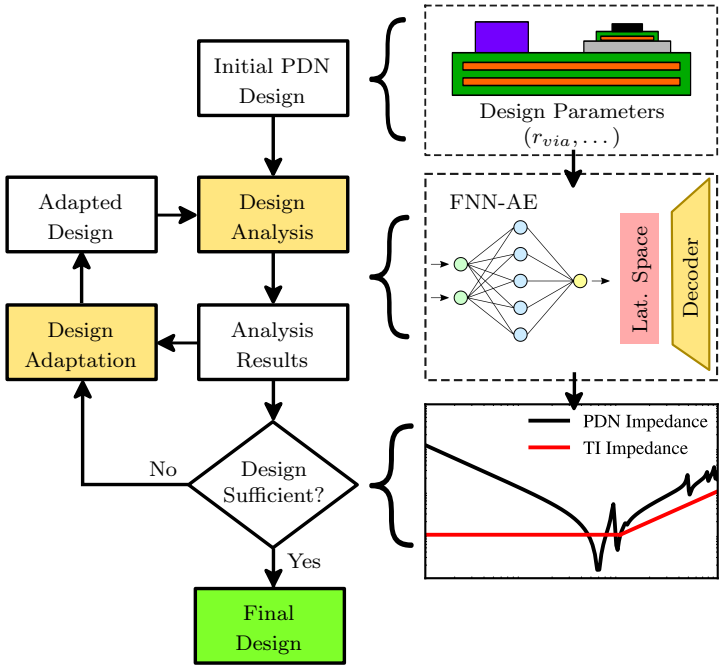

Figure 3.18: Flowchart of a power delivery network (PDN) design process: Starting from an initial design, the PDN is optimized in an iterative process where the design is alternately analyzed and adapted until target criteria are met. In the proposed approach, a combination of feedforward neural network (FNN) and autoencoders (AEs) predicts the self- and transfer-impedances from design parameters. Reprinted from **[66]**.

dielectric height, etc.) to the latent space. The trained decoder from Stage 1 then reconstructs the impedance profile from this predicted latent representation. This approach allows the FNN-AE to predict an entire impedance profile directly from design parameters. Moreover, TL is applied to increase data-efficiency: A model pre-trained on large datasets from previous PCB cases can be fine-tuned using a small number of samples from a new design, see Fig. 3.19. To evaluate this approach, six two-port PCB benchmark cases were defined, covering a range of complexities:

- *Case I*: 4-layer rectangular PCB, single via array and 4 variables.
- *Case II*: 8-layer rectangular PCB, two via arrays placed randomly and 8 variables.
- *Case III*: 4-layer irregular polygonal PCB, single via array with variable extensions and 4 variables.
- *Case IV*: 4-layer rectangular PCB, two identical via arrays with broad parameter variation and 13 variables.
- *Case V*: 2-layer rectangular PCB, mixed via array types and 4 variables.
- *Case VI*: 14-layer rectangular PCB, two identical via arrays and 13 variables.

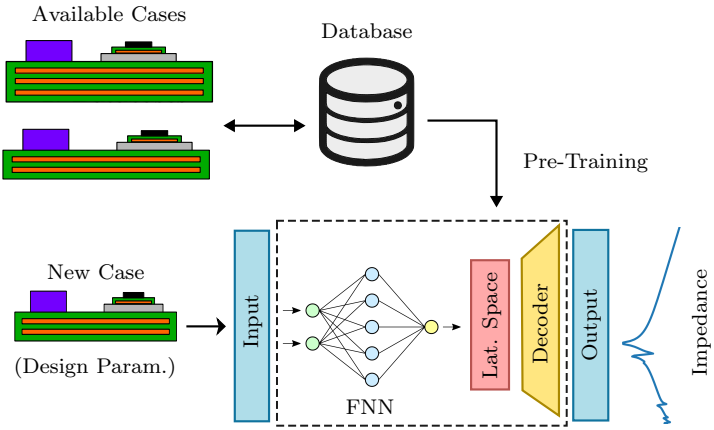

Figure 3.19: Architecture of the FNN-AE for impedance prediction. A feedforward neural network (FNN) is combined with the latent space and decoder parts of a trained autoencoder (AE). Previous datasets are reused in the process. Reprinted from [**66**].

These designs include variations in geometry, material properties, via configurations and position. The cases reflect reasonable PDN diversity while keeping simulation tractable. Datasets were generated using a PB cavity model method combining parallel-plane impedance CIM with PB via models [93]. In total, 55 500 samples were generated, showing variability in resonance amplitudes, frequencies and number of peaks in the impedance profiles. The prediction performance of the proposed FNN-AE models was evaluated on the six defined benchmark PCB cases. More than 15 preprocessed parameters based on design parameters (e.g., PCB size, via radius, pitch, dielectric height, via positions etc.) are used as inputs. Both self-impedance (Z_{11}) and transfer-impedance (Z_{12}) profiles were predicted for each case and compared to simulated results, see Fig. 3.20. The simulated and predicted impedance profiles show good agreement. The unified model trained on all cases achieved an nMAE below 20 % for every test case, confirming that a single network can generalize across diverse PCB designs. The impedance profiles are predicted in less than 50 ms. Accurate predictions were achieved with as few as 150 training samples for a new case. Using TL further reduced the required number of new samples by up to 80 % for some cases compared to training from scratch without data-reuse.

One of the most significant advantages of the proposed FNN-AE framework is its ability to model N-port PDNs using training data derived exclusively from simpler 2-port systems. This capability addresses a critical bottleneck in PDN design workflows: As the number of ports increases, the computational cost of dataset generation increases rapidly. The reason is that each simulation must compute all self-impedances and transfer-impedances for the N by N impedance matrix. For example, a 10-port system requires 100 impedance profiles per sample, compared to only 4 for a 2-port system. This makes brute-force dataset generation for training time-consuming in many practical scenarios. Next, a 10-port PCB sample created by sampling geometric and material parameters from the design space of *Case IV* (2-port) is considered. However, the PCB differs in its port configuration: Five via arrays are placed at random locations on the PCB area. Additional four via arrays are placed in proximity to form a dense cluster, One last via array is positioned near an edge of the board, see Fig. 3.21. The FNN-AE used for this task had been trained exclusively on the 55 500 samples from the six benchmark cases (all 2-port configurations) described earlier. No impedance data from 10-port systems was used during training or fine-tuning. For evaluation, the model predicted all self- and transfer-impedance profiles for the 10-port PCB directly from its design parameters. The self-impedance predictions were particularly accurate and the transfer-impedance predictions aligned closely with simulated curves, see Fig. 3.22 and Fig. 3.23.

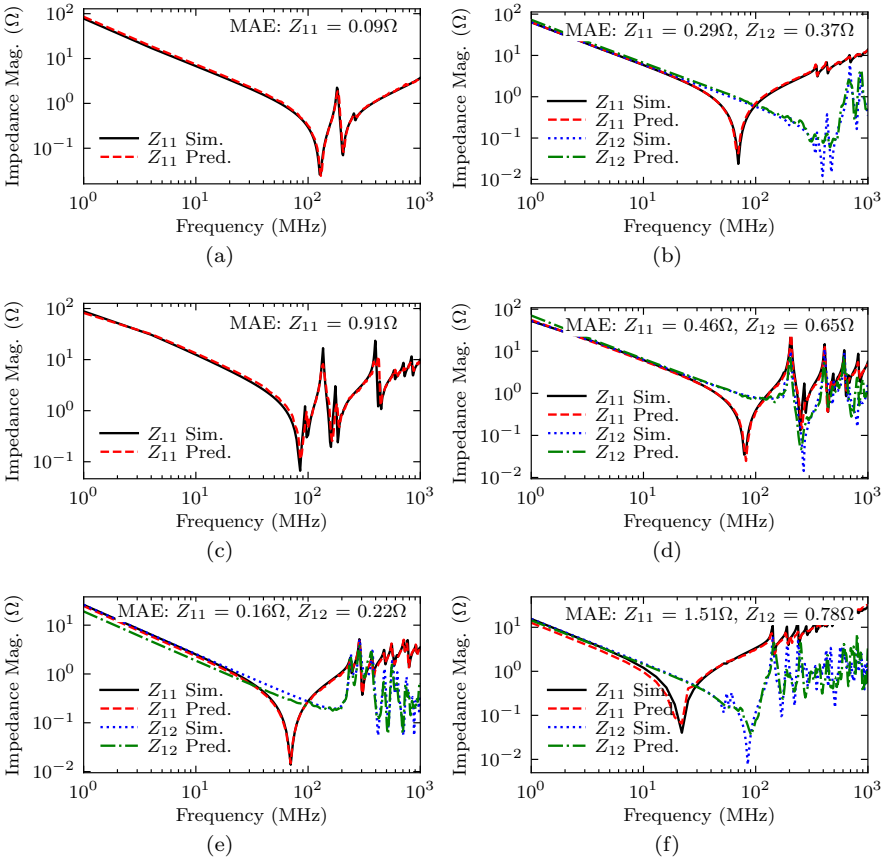

Figure 3.20: Simulated and predicted self- and transfer-impedances are compared for samples from (a) *Case I*, (b) *Case II*, (c) *Case III*, (d) *Case IV*, (e) *Case V* and (f) *Case VI*. The mean absolute error (MAE) between the simulated and predicted profiles is given at the top of each plot. Reprinted from **[66]**.

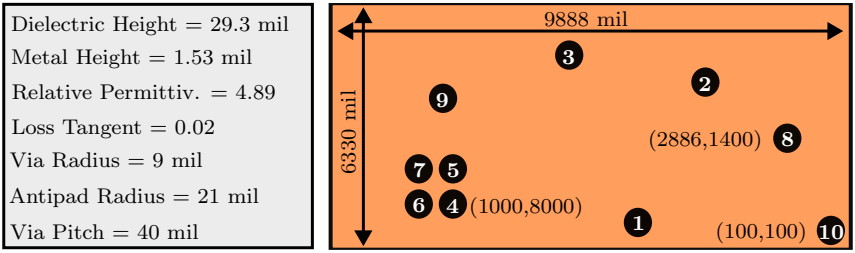

Figure 3.21: Top view of considered 10-port example sampled from the design space of *Case IV*. The ten defined ports are numbered from "1" to "10" while the design parameters are given. Adapted from **[66]**.

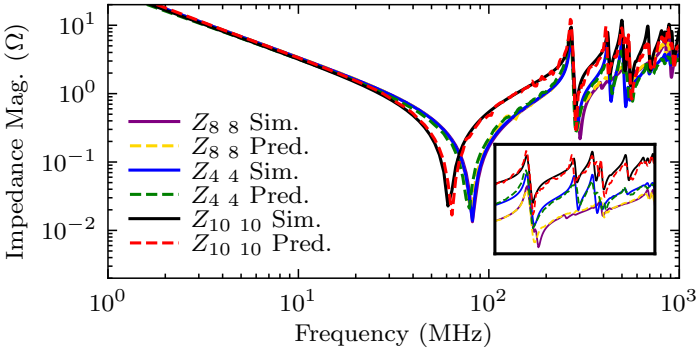

Figure 3.22: Simulated and predicted self-impedances $Z_{8\ 8}$, $Z_{4\ 4}$ and $Z_{10\ 10}$ with a zoom window. Reprinted from **[66]**.

In conclusion, the proposed FNN-AE approach enables fast, accurate and data-efficient prediction of broadband self- and transfer-impedance profiles for PCB-based PDNs. By using TL and physics-informed feature engineering, it minimizes the need for costly simulations while maintaining high fidelity. The ability to generalize from simpler 2-port cases to complex N-port boards further enhances practical applicability of this method. With growing availability of high-quality datasets, this method could become an integral part of PDN design workflows: The approach can help accelerate the decoupling process and reduce design time using the fast predictions instead of slow simulations.

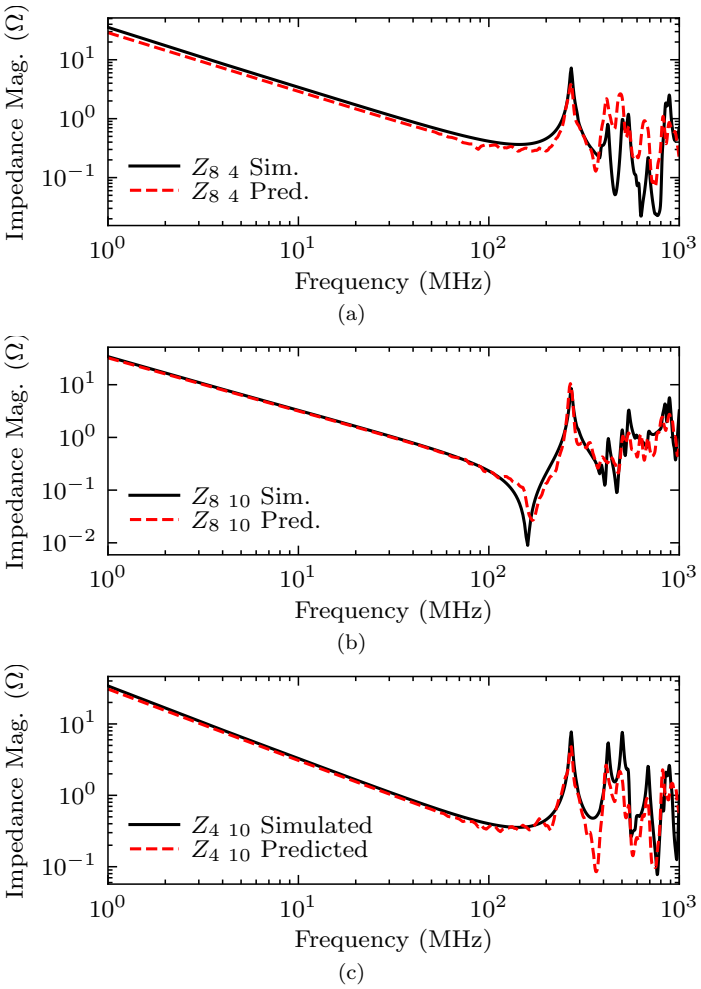

Figure 3.23: Transfer-impedance modeling of the 10-port sample. Simulated and predicted (a) transfer-impedance $Z_{8\ 4}$, (b) transfer-impedance $Z_{8\ 10}$ and (c) transfer-impedance $Z_{4\ 10}$, are shown. Reprinted from **[66]**.

Chapter 4

Lessons Learned from Machine Learning for Engineering

In this chapter, a discussion on the key findings of the application of ML solutions for EMC is provided. A set of recommendations for aspects of ML for EMC are synthesized in an effort to guide future research.

4.1 Discussion of Results and Key Findings

The presented study cases in Chapter 3 demonstrate the potential of ML approaches for EMC engineering and related fields such as SI, PI, BioEM and RF engineering. Some studies focused on improving parts of the modeling and design processes to provide alternatives to conventional tools: The investigated and proposed modeling approaches for PDN key-features and impedance profiles demonstrated capabilities in speeding up important parts of the design workflow [**67**]. The targeted bottleneck in these studies is the time-consuming and expensive PDN impedance analysis conventionally achieved by FW simulations. Efforts to tackle the issue are reflected by the continuous work based on a proof-of-concept for the simple ML-based prediction of key-features [34], to an increase of the data-efficiency and applicability of the method [**68**,**70**], an extension to full profile prediction of self-impedances [**67**] and transfer-impedances [**72**]. These incremental improvements point out a latent potential of ML in providing solutions to faced challenges, uncovered through sustained research efforts. The fast prediction of SAR in human head models demonstrated capabilities to speed up the modeling process of complex EMC systems [**69**]. Here too, the conventional modeling process based on FW simulations represents a major bottleneck. Other studies focused on providing ML solutions for problems that are hardly tractable and solved using conventional tools. The proposed ML-based data validation workflow allows the fast automated validation of large datasets [**72**]. Conventional methods of validation of data based on manual human assessment or analytical methods

such as FSV are either slow, inconsistent or non-integrable into automated workflows. Using TSC algorithms, radar-based HGR systems were designed for reliable function in complex multi-distance, multi-angle and multi-gesture scenarios [**71**]. Considering the complexity of hand gestures and recorded radar signals, conventional signal processing methods fall short. The latter applications point out a latent potential of ML algorithms to provide solutions hardly reachable by conventional methods.

Beyond the potential of ML in providing robust solutions for EMC engineering and beyond, the works presented reflect several recurring insights in the application of ML. First, data-efficiency is critical: ML approaches proved effective when strategies to maximize the value of limited data were included (e.g., PB augmentation, transfer or active learning). The complex nature of modern electrical and electronic systems leads to data acquisition processes that are expensive and time-intensive. The benefits offered by ML methods can be overshadowed if large amounts of data are needed for the training and testing of ML models. For the showcased human head models and PCBs, FW simulations for data-acquisition required a couple of minutes to several hours per sample depending on the complexity [**67**,**69**]. In other words, the expense of collecting large datasets hinders faster processes and the speed-up promised by ML. Second, reuse of data from previously generated datasets impacts data-efficiency positively. Less training and testing data samples needed renders ML algorithms more attractive and practical for real engineering problems. For the prediction of PDN impedances, data-reuse using a TL approach reduced the amount of needed samples by up to 80% for some example cases [**66**]. Third, including domain-knowledge and engineering expertise is critical for the successful implementation of ML algorithms. On the one hand, the inclusion of domain-knowledge is crucial for fundamental stages of ML workflows, e.g., data preprocessing and model training. For many applications, a domain-agnostic implementation of ML tools does not result in sufficient performance or adequate solutions. As an example: The PB preprocessing of input data to create meaningful features increased the performance in the classification of the TI of PCB-based PDNs by more than 20 percentage points [**64**]. On the other hand, domain-knowledge enables the development of solutions to enhance ML implementation in engineering. As an example: The proposed PB data augmentation improved the performance of HGR systems in new and unseen scenarios in comparision to domain-agnostic data augmentation methods [**71**]. In another example: Data labeled by experts enabled the training of ML models capable of autonomous qualitative data validation [**72**]. Fourth, interpretability and physical-grounding consistently emerged as central for the adoption of ML in engineering. Models that provide traceability to underlying electromagnetic phenomena or uncertainty

estimates are more readily integrated into engineering workflows, e.g., uncertainty estimations provided by TSC algorithm *Rocket* allowed the integration in automated data validation frameworks [**72**]. Fifth, generalization beyond simplified cases remains a challenge. Most studies addressed defined design spaces. Extending these methods to broader, real-world scenarios will require larger, sharable and standardized datasets. Sixth, the ML tools at disposition of engineers are improving, unlocking new possibilities and directly impacting the performance and application of ML solutions. The *Rocket* algorithm used for the validation of data by the classification of time series showcased an accuracy 10 percentage points higher than *InceptionTime* [**72**]. *Rocket* is a successor to *InceptionTime*, the algorithm used for the classification of hand gestures in [**71**]. Seventh, expertise and understanding of ML algorithms and their working principles enables advanced applications to provide adequate solutions to engineering problems. For the prediction of full impedance profiles, a hybrid model consisting of AEs and FNNs components embedded in an advanced two-stage training phase has been used [**67**]. This kind of implementations requires advanced knowledge of tools and programming experience.

4.2 Outlook for the Future

The reviewed research and presented works illustrate a certain trajectory: ML in EMC is maturing into a set of structured tools that, when combined with physical insight and collaborative data initiatives, can provide scalable and reliable solutions for EMC engineering and beyond. A vision for the future of ML-based engineering and a transition from purely experimental add-ons to usable tools on real problems is provided in the next sections [**1**].

4.2.1 The exploration and expansion phases

In recent years, research on ML-based modeling and design has largely been driven by an exploration mindset, see Fig. 4.1. During this stage, ML tools have been preliminarily implemented and tested across a wide range of applications with varying levels of complexity. This exploration phase has been crucial for building expertise and for gaining insights into the limitations and applicability of ML in EMC engineering. As a result, the field has now entered an expansion phase, in which ML tools are increasingly applied to support modeling and design tasks. Some tools are offering alternatives to PB and conventional approaches in selected parts of the modeling and design processes. Ongoing research continues to extend the integration of ML.

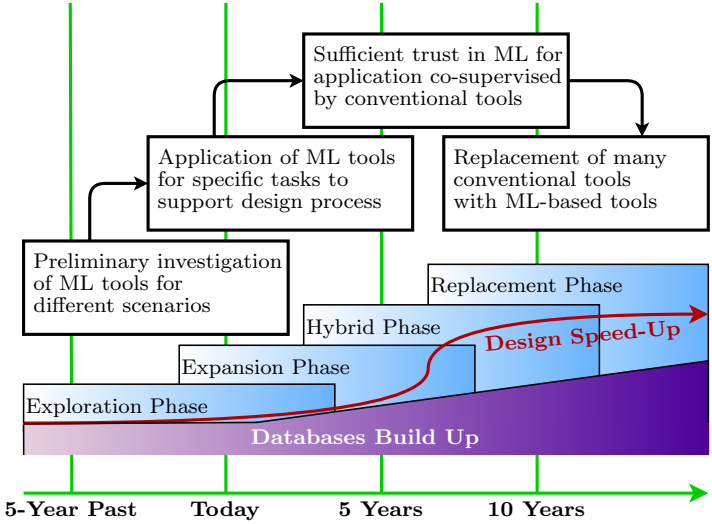

Figure 4.1: Time horizon and implementation phases of machine learning (ML) for the modeling and design in electromagnetic compatibility (EMC) domain. Adapted from [1] © 2025 IEEE.

4.2.2 The hybrid phase

Based on the exploration and expansion phases, a shift toward a hybrid application of ML and PB tools is expected, see Fig. 4.1. During this stage, sufficient trust in ML tools will be reached to use them in close supervision with conventional approaches. The increasing trust is mainly due to the growing experience in the handling of ML-based methods together with their improving performance. Additionally, design workflows are expected to be substantially accelerated, because ML models will begin to partially replace traditional simulation tools, such as PB simulations. Initially, the integration of ML into design loops will proceed in parallel with parametric investigations using simulation models. Active learning strategies or BO may be used to enhance optimization efficiency and the exploration of large design spaces. Training surrogate models in parallel with parametric simulation runs and measurements will further support optimization. As model adaptation to specific problems improves, the number of simulations and measurements required to achieve high surrogate accuracy will be significantly reduced. A major step forward is expected once data from previous design cycles can be systematically reused to improve the training of models for new problems.

4.2.3 The replacement phase

Since more data will be generated and stored with time, the databases of available datasets will continue to grow. With widely available datasets and increasing trust and performance of ML tools, models that generalize on past problems to provide consistent solutions for new design problems can be trained. Over time, ML-based tools may partially replace many conventional tools and overcome the reliance on PB methods for many applications. This replacement phase will pave the way for a future where AI and ML play a central role in the modeling and design for EMC and beyond.

The surrogate models trained on a vast amount of available data will allow the prediction of relevant outputs. For example, the radiation pattern of a device will be predicted in shorter times using available data and few new generated samples. Real-time EMC compliance prediction during the design phase will be possible with ML models trained on large datasets of EMC test results and simulation data to enable rapid prototyping. The automated early recognition of failures and the prediction of EMI hotspots during the design stages will reduce the need for design respins. Generative algorithms will enable the fast creation of optimized layouts, e.g., for PCBs, antennas and enclosures, to minimize EMI while maximizing the performance.

4.3 Recommendations for the Future

Machine learning (ML) based modeling and design is the result of the interaction between computational tools, available data, data acquisition and the engineers involved. To support the successful implementation and wider adoption of ML approaches, a set of recommendations is provided for each of these aspects in the following sections [**1**]. A brief summary of the provided recommendations is depicted in Fig. 4.2.

4.3.1 Machine learning tools

The surge of interest in ML has resulted in the recent development of more performant and varied tools. However, significant drawbacks still exist, necessitating either the development of novel tools or the adaptation of existing ones. A primary drawback is the lack of interpretability and limited insight into the tools' decision-making processes. From an engineering perspective, these aspects are critical for deriving physical knowledge and enhancing decision-making in design problems. The investigation of interpretable tools and algorithms should be pursued. ML tools can be used in combination with

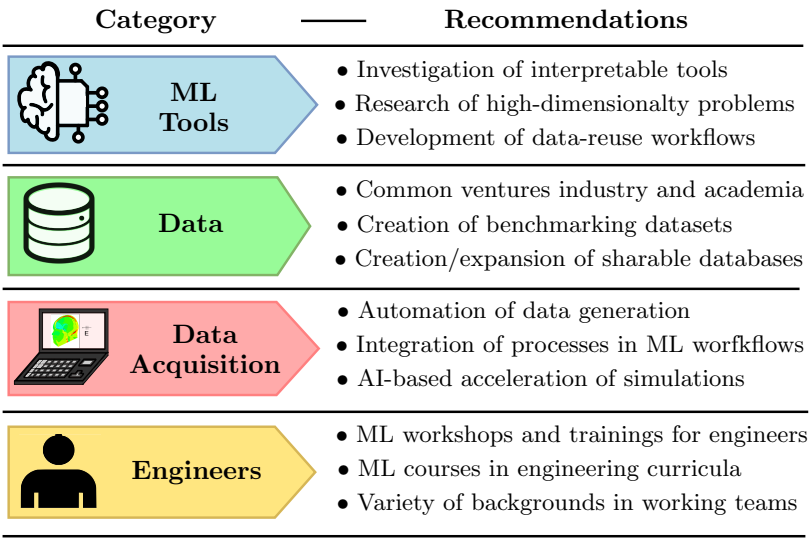

Figure 4.2: Set of recommendations to overcome the limitations and challenges facing a wider adoption of machine learning (ML) in electromagnetic compatibility (EMC). Adapted from [**1**] © 2025 IEEE.

other data-driven algorithms for feature importance analysis, e.g., variance-based sensitivity analysis [104]. A further challenge is the capability of tools to effectively handle high-dimensional parameter spaces. Therefore, efforts should be made to develop ML algorithms be able to handle higher dimensional spaces. This can be partially achieved by focusing on the adaptation of ML tools and their integration into frameworks informed by domain-specific knowledge. Given that the relationship between model inputs and outputs is often complex, many algorithms require substantial volumes of data to achieve robust generalization. Pursuing increased data-efficiency within algorithms and the development of methodologies for reusing data is essential. In the presented works, existing ML tools have been adapted and combined to solve complex problems, e.g., a hybrid FNN-AE has been constructed for the prediction of broadband PDN impedance profiles from design parameters [**72**]. The interpretability of ML tools has been investigated through the extraction of feature importance, e.g., to find the most impactful parameters on the SAR in human head models [**69**] and allow for uncertainty-aware validation of data [**72**]. To address the problem of dimensionality, feature reduction techniques based on domain-knowledge have been proposed, e.g., to reduce the number of needed input dimensions for the modeling of PCB-based PDNs [**65**].

4.3.2 Data availability

Having access to high-quality and relevant datasets plays an important role in the development and investigation of ML tools for EMC. The availability of data enables researchers to investigate and develop ML-based solutions and workflows. For ML-based workflows, the availability of data allows the reuse of existing datasets. This helps the training and implementation processes and lessens the need to generate new data from scratch. However, obtaining valuable datasets remains a significant challenge that poses an obstacle to the advancement of ML solutions within the EMC field. To overcome these barriers, joint initiatives focusing on data sharing and collaborative problem-solving should be pursued. Creating accessible benchmarking datasets and scenarios that accurately reflect real-world EMC problems is essential. These resources would enable meaningful comparisons of ML tools and their performance in practical applications. Addressing the storage and management of datasets is also important to ensure that data can be found, retrieved and used effectively. In addition, establishing standards for data preprocessing and formatting should facilitate the reuse of data. Many datasets used in the published works are made freely available to researchers, e.g., PCB use cases for PI applications [**66**] and SI applications [**73**]. The PCB cases have been generated balancing physical realism with computational tractability. The datasets offer benchmark cases with an increasing number of varied parameters that are simplified but retain the core physical mechanisms important for SI and PI analysis. The datasets can be accessed on the SI/PI-Database at https://www.tet.tuhh.de/en/si-pi-database. The SI/PI-Database is a collection of PCB-based structures that showcase various electromagnetic aspects relevant to SI and PI applications [105, 106]. Moreover, the proposed large-scale data validation should help ensure the quality of the datasets [**72**]. This work contributes thus to the qualitative data generation, validation, preservation and sharing efforts to help accelerate research in this area.

4.3.3 Data acquisition

Data acquisition involves all aspects of the collection of data for the development and use of ML tools. The processes of simulation and measurement, heavily used in EMC engineering, are frequently characterized by high demands on resources and time. Therefore, inefficient data generation can negate the advantages offered by ML methodologies. Thus it is crucial to enhance the efficiency of these processes through techniques such as data-efficient algorithms, data reuse and other techniques that can reduce the needed number of samples for the implementation. For successful ML-based modeling and

design, a shift in data acquisition methodology is recommended: Significant acceleration can be achieved by automating simulation and measurement processes and reducing human intervention. The conventional approaches treat data acquisition as a distinct, preliminary phase within an ML workflow. In contrast, future methodologies should integrate it as a component within ML workflows. These workflows should be equipped with smart sampling strategies, e.g., active learning, to generate data incrementally based on need. The collection of data, guided by ML tools, is performed via automated simulation of selected samples or targeted measurements. These aspects have been investigated and solutions have been proposed in different published works: Data reuse through TL to decrease the number of needed training samples in ML workflows, e.g., for PDN impedance profile prediction [**66**,**67**]. Active learning for the automation of dataset generation and the increase of data-efficiency, e.g., for the prediction of SAR in human head models [**69**] and PDN key-features [**68**,**70**]. Reduction of data generation expense through the use of domain-knowledge and targeted data augmentation, e.g., for the development of radar-based HGR systems [**71**].

4.3.4 Engineers

The engineers responsible for the research and implementation of ML algorithms constitute an important resource. The needed skill set involves a combination of engineering domain expertise, foundational knowledge in data science and ML and coding proficiency. A noticeable increase in the proficiency of researchers using ML tools is evident, with many recent publications featuring adapted and advanced algorithms tailored to domain-specific challenges. However, greater effort and investment in the training of both current and future engineers are needed. The development of specialized pedagogical programs that integrate ML theory with domain-specific engineering applications is crucial. Academic institutions should systematically incorporate ML coursework into engineering curricula. Furthermore, cross-disciplinary collaboration between data scientists and engineers must be actively promoted through collaborative projects, dedicated workshops and interdisciplinary conferences. Assembling research teams with diverse academic and professional backgrounds is essential to foster knowledge exchange and accelerate the maturation of ML applications within EMC. In the published works, the importance of domain-knowledge and cross-disciplinary assets has been highlighted, e.g., time series preprocessing based on domain-knowledge for robust HGR systems [**63**] and PB preprocessing to enable the prediction of TI violations in PCB-based PDNs [**64**].

Chapter 5

Conclusion

The investigations presented in this thesis underline the potential of ML to transform the modeling and design in EMC and the related disciplines of SI, PI, BioEM and RF engineering. A unifying theme across all studies is the ability of ML methods in solving encountered challenges in EMC, providing careful adaptation to the underlying engineering problems. ML tools are most effective when they integrate domain-knowledge and expertise: Embedding domain-knowledge in preprocessing, training or evaluation stages consistently improved the performance and reliability of the models.

However, some recurring challenges hinder the wide adoption of ML methods in modeling and design in EMC. The presented works further emphasized some limitations facing the adoption of ML and avenues to be pursued: Data-efficient approaches and solutions based on the reuse of available datasets are key for the success of ML. High-quality datasets are as important as model development itself. The generation, storage and accessibility of high-quality, domain-relevant datasets must therefore be considered a priority. Scalable models to different scenarios are needed to move from problem-specific and partial to practical solutions.

The presented application cases in this work have demonstrated the ability of the proposed methods to tackle the issues efficiently. To give a few examples: Dimensionality reduction and latent representations enabled the handling of high-dimensional design spaces. Adapted AEs demonstrated that complex input-output relations can be compressed into informative features, which in turn can support more efficient design space exploration and similarity detection. The introduction of techniques to increase data-efficiency, e.g., transfer and active learning, have helped reduce the amount of needed samples for training of ML algorithms. Feature importance evaluation performed using GPR has helped with the interpretation of models and results.

Within this context, contributions have been made by the author to the broad field of ML in EMC and related disciplines. The main contributions of this thesis are summarized in the following points:

- It has been shown that despite the differences in the considered application domains, a common set of challenges facing the disciplines exist. With regard to the use of ML, the challenges include the cost of data acquisition, high-dimensional design spaces, lack of interpretability of models and requirements on training data.

- Different ML-based approaches have been proposed to tackle these common challenges. The methods have proven to be successful in mitigating many issues when applied across a wide range of applications, e.g., the use of transfer and active learning to decrease the amount of needed training samples for SAR and impedance modeling.

- The potential of ML in providing alternatives to improve conventional modeling and design processes has been investigated. The proposed solutions based on domain knowledge have been thoroughly investigated and the performances noted, e.g., ML-based data comparison has shown better performances than human subjects in large-scale data validation.

- A vision for the future of ML in EMC and related disciplines has been provided. The presented vision has been accompanied by a series of recommendations based on the author's experience. The recommendations are an attempt at guiding future research towards the most pressing issues to unlock the full potential and enable a wider adoption of ML.

Overall, EMC engineering can benefit greatly from the integration of ML. Recent work, including the studies presented here, demonstrates encouraging progress in enhancing and accelerating modeling and design. Nonetheless, simplified models, partial solutions and limited data availability still dominate the field. Advances in computational capabilities and the growing experience of engineers with ML tools are contributing to progressive trends. Still, widespread adoption will require further progress in handling high-dimensional problems, increasing data-efficiency and building shared infrastructures for dataset generation and storage. The trajectory of ML in other domains, such as computer vision and natural language processing, shows the potential impact of sustained research in this area. By transferring and adapting such innovations to EMC while embedding physical knowledge into the methods, the community can move toward scalable, automated and accurate tools for modeling and design. The potential benefits justify continued investment and focused research, to the benefit of EMC as a discipline and its applications in an increasingly complex technological environment.

Bibliography

[1] Y. Hassab, M. Schierholz, L. P. P. B. Bohl, H. Esmaeili, T. Hillebrecht, C. Yang, J. Hessling, and C. Schuster, "Developments in Machine Learning based Modeling and Design for Electromagnetic Compatibility," *IEEE Electromagnetic Compatibility Magazine*, vol. 14, no. 4, pp. 69–80, Dec. 2025.

[2] "IEEE Standard for Safety Levels with Respect to Human Exposure to Electric, Magnetic, and Electromagnetic Fields, 0 Hz to 300 GHz," *IEEE Std C95.1-2019*, Oct. 2019.

[3] T. M. Mitchell, *Machine Learning*. New York, NY, USA: McGraw-Hill, 1997.

[4] R. Jhaveri, R. A., R. Kadiyala, R. Raut, and R. K. D, "A Review on Machine Learning Strategies for Real-World Engineering Applications," *Mobile Information Systems*, vol. 2022, Aug. 2022.

[5] K. Yee, "Numerical Solution of Initial Boundary Value Problems Involving Maxwell's Equations in Isotropic Media," *IEEE Transactions on Antennas and Propagation*, vol. 14, no. 3, pp. 302–307, May 1966.

[6] S. Xin-Qing and S. Wei, *Essentials of Computational Electromagnetics*. Hoboken, NJ, USA: John Wiley & Sons, Ltd, 2012.

[7] G. Burke, E. Miller, and A. Poggio, "The Numerical Electromagnetics Code (NEC) - A Brief History," in *IEEE Antennas and Propagation Society Symposium*, Monterey, CA, Jun 2004.

[8] Z. Cendes, "The Development of HFSS," in *USNC-URSI Radio Science Meeting*, Fajardo, Puerto Rico, USA, Jan. 2016.

[9] A. Ruehli, "Partial Element Equivalent Circuit (PEEC) Method and Its Application in the Frequency and Time Domain," in *Proceedings of Symposium on Electromagnetic Compatibility*, Santa Clara, CA, USA, Sep. 1996.

[10] T. El-Ghazali, *Metaheuristics: From Design to Implementation*. Hoboken, NJ, USA: John Wiley & Sons, Ltd, 2009.

[11] K. Patra, S. Cheruvalath, S. Dhar, B. P. Nayak, A. Gupta, and J. Hansen, "Surrogate Modeling for Predicting Shielded Cable Emissions," *IEEE Transactions on Electromagnetic Compatibility*, vol. 65, no. 1, pp. 249–256, Feb. 2023.

[12] R. S. Rezende, J. Hansen, A. Piwonski, and R. Schuhmann, "Wideband Kriging for Multiobjective Optimization of a High-Voltage EMI Filter," *IEEE Transactions on Electromagnetic Compatibility*, vol. 66, no. 4, pp. 1116–1124, Dec. 2024.

[13] A. Bingler, S. Bilicz, and M. Csornyei, "Polynomial Chaos Kriging Metamodel for Automotive EMC Simulations," in *International Symposium on Electromagnetic Compatibility – EMC Europe*, Gothenburg, Sweden, Sep. 2022.

[14] Y. Ping, Y. Zhang, and L. Jiang, "Uncertainty Quantification in PEEC Method: A Physics-Informed Neural Networks-Based Polynomial Chaos Expansion," *IEEE Transactions on Electromagnetic Compatibility*, vol. 66, no. 6, pp. 2095–2101, Dec. 2024.

[15] Y. Ping, Y. Zhang, and L. Jiang, "Uncertainty Quantification for PEEC Based on Wasserstein Generative Adversarial Network," *IEEE Transactions on Electromagnetic Compatibility*, vol. 66, no. 6, pp. 2048–2055, Dec. 2024.

[16] M. Gonzalez-Atienza, D. Vanoost, M. Verbeke, and D. Pissoort, "An Optimized Adaptive Bayesian Algorithm for Mitigating EMI-Induced Errors in Dynamic Electromagnetic Environments," *IEEE Transactions on Electromagnetic Compatibility*, vol. 66, no. 6, pp. 2085–2094, Dec. 2024.

[17] C.-P. Huang, Y.-H. Ma, Q. Q. Liu, W.-S. Zhao, B. You, X. Wang, C.-H. Yu, and D.-W. Wang, "PPO Algorithm-Assisted Design of Absorptive Common-Mode Suppression Filters," *IEEE Transactions on Electromagnetic Compatibility*, vol. 66, no. 6, pp. 2039–2047, Dec. 2024.

[18] R. Choupanzadeh and A. Zadehgol, "A Deep Neural Network Modeling Methodology for Efficient EMC Assessment of Shielding Enclosures Using MECA-Generated RCS Training Data," *IEEE Transactions on Electromagnetic Compatibility*, vol. 65, no. 6, pp. 1782–1792, Dec. 2023.

[19] T. Xu, Y. Chen, M. Zhao, Y. Wang, and X. Zhang, "Adaptive EMS Test Design Method on UAV Data Link Based on Bayesian Optimization," *IEEE Transactions on Electromagnetic Compatibility*, vol. 65, no. 3, pp. 716–724, Dec. 2023.

[20] P. Monferran, C. Guille-Escuret, C. Guiffaut, and A. Reineix, "Prediction of Lightning Currents on Fastening Assemblies of an Aircraft Fuel Tank With Machine Learning Methods," *IEEE Transactions on Electromagnetic Compatibility*, vol. 65, no. 3, pp. 812–822, Dec. 2023.

[21] M. Telescu, R. Trinchero, N. Soleimani, N. Tanguy, and I. S. Stievano, "Stochastic Time-Domain Mapping for Comprehensive Uncertainty Assessment in Eye Diagrams," *IEEE Transactions on Electromagnetic Compatibility*, vol. 65, no. 6, pp. 1930–1938, Dec. 2023.

[22] K. Scharff, C. M. Schierholz, C. Yang, and C. Schuster, "ANN Performance for the Prediction of High-Speed Digital Interconnects and Multiple PCBs," in *Proceedings of 2020 IEEE 29th Conference on Electrical Performance of Electronic Packaging and Systems (EPEPS)*, San Jose, CA, USA, Oct. 2020.

[23] M. A. Dolatsara, J. A. Hejase, W. D. Becker, J. Kim, S. K. Lim, and M. Swaminathan, "Worst-Case Eye Analysis of High-Speed Channels Based on Bayesian Optimization," *IEEE Transactions on Electromagnetic Compatibility*, vol. 63, no. 1, pp. 246–258, Feb. 2021.

[24] D. Shi, N. Sun, Y. Liu, C. Lian, X. Chen, X. Zhou, X. Liu, Q. Liu, and J. Zhou, "Fast Calculation Method for Crosstalk of High-Density Printed Circuit Board by Using Machine Learning," *IEEE Transactions on Electromagnetic Compatibility*, vol. 66, no. 3, pp. 971–982, Dec. 2024.

[25] F. Garbuglia, D. Spina, T. Reuschel, C. Schuster, D. Deschrijver, and T. Dhaene, "Modeling S-Parameters of Interconnects using Periodic Gaussian Process Kernels," in *2023 IEEE 27th Workshop on Signal and Power Integrity (SPI)*, Aveiro, Portugal, May 2023.

[26] M. A. Dolatsara, "Equalization Optimization for SerDes Channels with Constrained Bayesian Optimization," in *2022 IEEE International Symposium on Electromagnetic Compatibility and Signal/Power Integrity (EMCSI)*, Spokane, WA, USA, Aug. 2022.

[27] L. P. P. B. Bohl, K. Scharff, X. Duan, D. Kaller, and C. Schuster, "Bayesian Optimization of First-Order Continuous-Time Linear Equalization in High-Speed Links Including Crosstalk," in *IEEE 27th Workshop on Signal and Power Integrity (SPI)*, Aveiro, Portugal, May 2023.

[28] Q. Chen, L. Zhang, H. Ma, D. Li, Y. Li, E.-X. Liu, and E.-P. Li, "Deep Neural Network-Based Surrogate-Assisted Inverse Optimization for High-Speed Interconnects," *IEEE Transactions on Electromagnetic Compatibility*, vol. 66, no. 6, pp. 2019–2026, Dec. 2024.

[29] O. Akinwande, S. Erdogan, R. Kumar, and M. Swaminathan, "Surrogate Modeling With Complex-Valued Neural Nets for Signal Integrity Applications," *IEEE Transactions on Microwave Theory and Techniques*, vol. 72, no. 1, pp. 478–489, Jan. 2024.

[30] E. Ecik, W. John, J. Withöft, R. Brüning, and J. Götze, "A Statistically Evaluated Decision Tree Approach for SI-Compliant PCB Design," in *2024 International Symposium on Electromagnetic Compatibility – EMC Europe*, Bruges, Belgium, Sep. 2024.

[31] J. Withöft, W. John, E. Ecik, and J. Götze, "AI-Based SI-Compliant PCB Design Support for DDR Technology Enhanced by Transfer Learning," in *2023 International Symposium on Electromagnetic Compatibility – EMC Europe*, Krakow, Poland, Sep. 2023.

[32] J. Withöft, W. John, E. Ecik, R. Brüning, and J. Götze, "Machine Learning Methods for Elaborating the Feasible Region for Signal Integrity Analysis in Differential Pair PCB Structures," in *2024 International Symposium on Electromagnetic Compatibility – EMC Europe*, Bruges, Belgium, Sep. 2024.

[33] M. Schierholz, K. Scharff, and C. Schuster, "Evaluation of Neural Networks to Predict Target Impedance Violations of Power Delivery Networks," in *IEEE 28th Conference on Electrical Performance of Electronic Packaging and Systems (EPEPS)*, Montreal, QC, Canada, Oct. 2019.

[34] M. Schierholz, I. Erdin, J. Balachandran, and C. Schuster, "Data-Efficient Supervised Machine Learning Technique for Practical PCB Noise Decoupling," in *DesignCon 2023*, Santa Clara, CA, USA, Feb. 2023.

[35] W. Zhang, F. Feng, J. Jin, and Q.-J. Zhang, "Parallel Multiphysics Optimization for Microwave Devices Exploiting Neural Network Surrogate," *IEEE Microwave and Wireless Components Letters*, vol. 31, no. 4, pp. 341–344, Apr. 2021.

[36] Z. Nezhi, M. Stiemer, M. Schierholz, and C. Schuster, "Dimensional Reduction by Auto-Encoders in Machine Learning Based Power Integrity

Analysis," in *2024 IEEE 28th Workshop on Signal and Power Integrity (SPI)*, Lisbon, Portugal, May 2024.

[37] I. Erdin and R. Achar, "Decoupling Capacitor Placement on Resonant Parallel-Plates Via Driving Point Impedance," *IEEE Transactions on Microwave Theory and Techniques*, vol. 67, no. 6, pp. 2162–2171, Jun. 2019.

[38] Z. Xu, Z. Wang, C. Hwang, H. Delingette, and J. Fan, "Jitter-Aware Economic PDN Optimization With a Genetic Algorithm," *IEEE Transactions on Microwave Theory and Techniques*, vol. 69, no. 8, pp. 3715 – 3725, Aug. 2021.

[39] H. Park, J. Park, S. Kim, K. Cho, D. Lho, S. Jeong, S. Park, G. Park, B. Sim, S. Kim, Y. Kim, and J. Kim, "Deep Reinforcement Learning-Based Optimal Decoupling Capacitor Design Method for Silicon Interposer-Based 2.5-D/3-D ICs," *IEEE Transactions on Components, Packaging and Manufacturing Technology*, vol. 10, no. 3, pp. 467–478, Mar. 2020.

[40] X.-P. Zhou, D.-W. Wang, W.-S. Zhao, P. Zhang, and J.-H. Pan, "Modeling of Through-Silicon Capacitor and Its Applications for the Optimization of Power Distribution Network in 3-D Integrated Circuits," *IEEE Transactions on Signal and Power Integrity*, vol. 3, pp. 199–211, Nov. 2024.

[41] H. Vaghasiya, A. Jain, and J. N. Tripathi, "A Radial Basis Function Network-Based Surrogate-Assisted Swarm Intelligence Approach for Fast Optimization of Power Delivery Networks," *IEEE Transactions on Signal and Power Integrity*, vol. 1, pp. 140–149, Oct. 2022.

[42] J. Juang, L. Zhang, H. Manoharan, F. De Paulis, and C. Hwang, "Augmented Genetic Algorithm for Decoupling Capacitor Optimization in Power Distribution Network Design Through Improved Population Generation," *IEEE Transactions on Signal and Power Integrity*, vol. 3, pp. 186–198, Nov. 2024.

[43] E. A. Rashed, Y. Diao, and A. Hirata, "Learning-Based Estimation of Dielectric Properties and Tissue Density in Head Models for Personalized Radio-Frequency Dosimetry," *Physics in Medicine and Biology*, vol. 65, no. 6, Mar. 2020.

[44] H. Esmaeili, C. Yang, and C. Schuster, "Efficient Iterative Data Generation Using Evaluation of Prioritized Input Parameters in ANNs for SAR

Prediction in Human Head Models at 13.56 MHz," *IEEE Transactions on Electromagnetic Compatibility*, vol. 66, no. 6, pp. 1947–1957, Dec. 2024.

[45] H. Esmaeili, C. Yang, and C. Schuster, "SAR Prediction for Human Head Models Considering Dependencies on Incident Angle of Exposure Using Parameter Prioritization in ANNs," in *2024 IEEE MTT-S International Microwave Biomedical Conference (IMBioC)*, Montreal, QC, Canada, Jun. 2024.

[46] C. Zheng, X. Chen, B. T. Nguyen, P. Sanpitak, J. Vu, U. Bagci, and L. Golestanirad, "Predicting RF Heating of Conductive Leads During Magnetic Resonance Imaging at 1.5 T: A Machine Learning Approach," in *Annual International Conference of the IEEE Engineering in Medicine and Biology Society.*, Guadalajara, Jalisco, Mexico, Nov. 2021.

[47] J. Vu, T. Nguyen, B. Bhusal, J. Baraboo, J. Rosenow, U. Bagci, G. Bright, and L. Golestanirad, "Machine Learning-Based Prediction of MRI-Induced Power Absorption in the Tissue in Patients With Simplified Deep Brain Stimulation Lead Models," *IEEE Transactions on Electromagnetic Compatibility*, vol. 63, no. 5, pp. 1757–1766, Oct. 2021.

[48] J. Chang, Q. Lan, R. Guo, J. Zheng, R. Romero, W. Kainz, S. A. Long, and J. Chen, "MRI RF-Induced Heating Prediction of Complex-Shaped Passive Implantable Medical Devices Using Mesh-Based Convolutional Neural Network," *IEEE Transactions on Microwave Theory and Techniques*, vol. 71, no. 5, pp. 2207–2214, Dec. 2023.

[49] S. Koziel and A. Pietrenko-Dabrowska, "Rapid Surrogate-Aided Multicriterial Optimization of Compact Microwave Passives Employing Machine Learning and ANNs," *IEEE Transactions on Microwave Theory and Techniques*, vol. 72, no. 8, pp. 4475–4488, Aug. 2024.

[50] B. Liu, L. Xue, H. Fan, Y. Ding, M. Imran, and T. Wu, "An Efficient and General Automated Power Amplifier Design Method Based on Surrogate Model Assisted Hybrid Optimization Technique," *IEEE Transactions on Microwave Theory and Techniques*, vol. 73, no. 2, pp. 926–937, Feb. 2025.

[51] Z. Zhou, Z. Wei, J. Ren, Y.-X. Sun, Y. Yin, G. F. Pedersen, and M. Shen, "Bayesian-Inspired Sampling for Efficient Machine-Learning-Assisted Microwave Component Design," *IEEE Transactions on Microwave Theory and Techniques*, vol. 72, no. 2, pp. 996–1007, Feb. 2024.

[52] Y.-H. Liu, J.-C. Liang, B.-Z. Wang, and R. Wang, "Inverse Design Method for Electromagnetic Periodic Structures Based on Physics-Informed Neural Network With Embedded Analytical Models," *IEEE Transactions on Microwave Theory and Techniques*, vol. 73, no. 2, pp. 844–853, Feb. 2025.

[53] Z. Zhou, Z. Wei, J. Ren, Y. Yin, J. Li, and T.-T. Chan, "End-to-End Machine-Learning Framework for Electromagnetic Inverse Design: From Practical Constraints to Optimized Structures," *IEEE Transactions on Microwave Theory and Techniques*, Jul. 2025.

[54] A. N. Sayed, H. Abedi, O. M. Ramahi, and G. Shaker, "Enhanced UAV Detection and Classification Using Machine Learning and MIMO Radars," *IEEE Transactions on Microwave Theory and Techniques*, vol. 72, no. 11, pp. 6716–6727, Nov. 2024.

[55] J. B. Yip, S. Griesshammer, H. Leutheuser, R. Richer, H. Lu, A. Koelpin, B. M. Eskofier, C. Ostgathe, and T. Steigleder, "Continuous-Wave Radar and Motion-Derived Biomarkers for Non-Contact Vital Status Classification in End-of-Life Care: A Clinically Validated Machine Learning Approach," *IEEE Journal of Biomedical and Health Informatics*, Aug. 2025.

[56] W. Kim, J. Byung Park, S. Ahmed, and S. Ho Cho, "FMCW Radar-Based In-Air Alphanumeric Gesture Recognition With Machine Learning," *IEEE Transactions on Instrumentation and Measurement*, vol. 74, May 2025.

[57] L. Zhang, Y.-R. Feng, B. Pu, X.-D. Cai, D. Li, X.-C. Wei, B. Mutnury, J. Fan, H. Chen, J. L. Drewniak *et al.*, "A Novel Machine-Learning-Based Batch Selection Method in Sparse Near-Field Scanning," *IEEE Transactions on Microwave Theory and Techniques*, vol. 70, no. 11, pp. 5019–5028, Nov. 2022.

[58] C. Bujard, E. Neufeld, M. Douglas, J. Wiart, and N. Kuster, "A Gaussian Process Based Approach for Validation of Multi-Variable Measurement Systems: Application to SAR Measurement Systems," *IEEE Access*, vol. 12, pp. 60 404–60 424, Apr. 2024.

[59] E. K. Cho and E. Simsek, "Enhancing the Resolution of Local Near-Field Probing Measurements With Machine Learning," *IEEE Transactions on Microwave Theory and Techniques*, vol. 72, no. 3, pp. 1515–1519, Mar. 2024.

[60] J. Wen, X.-C. Wei, Y.-L. Zhang, and T.-H. Song, "Near-Field Prediction in Complex Environment Based on Phaseless Scanned Fields and Machine Learning," *IEEE Transactions on Electromagnetic Compatibility*, vol. 63, no. 2, pp. 571–579, Apr. 2021.

[61] Z. Gao, Y.-X. Liu, X.-C. Li, Z.-M. Wu, Z. Li, and T. Tan, "An Equivalent Radiation Source Reconstruction Method Based on Enhanced Artificial Neural Network," *IEEE Transactions on Electromagnetic Compatibility*, vol. 66, no. 4, pp. 1203–1212, Aug. 2024.

[62] L. Zhang, Y. Xie, Y.-R. Feng, H. Ma, J. Guo, Y. Li, D. Li, and E.-P. Li, "Active-Learning-Based Sparse Near Field Scanning with Time-Domain Current Measurement for Conductive Coupling Path Visualization," *IEEE Transactions on Instrumentation and Measurement*, vol. 73, pp. 1–8, Feb. 2024.

[63] T. Stadelmayer, Y. Hassab, L. Servadei, A. Santra, R. Weigel, and F. Lurz, "Lightweight and Person-Independent Radar-Based Hand Gesture Recognition for Classification and Regression of Continuous Gestures," *IEEE Internet of Things Journal*, vol. 11, no. 9, pp. 15 285–15 298, May 2024.

[64] M. Schierholz, Y. Hassab, C. Yang, and C. Schuster, "Evaluation of Support Vector Machines for PCB based Power Delivery Network Classification," in *Proceedings IEEE 30th Conf. Electrical Performance Electronic Packag. and Systems EPEPS*, Austin, TX, USA, Oct. 2021.

[65] M. Schierholz, Y. Hassab, and C. Schuster, "Engineering-Informed Design Space Reduction for PCB Based Power Delivery Networks," *IEEE Transactions on Components, Packaging and Manufacturing Technology*, vol. 13, no. 10, pp. 1613–1623, Oct. 2023.

[66] Y. Hassab, J. Heßling, and C. Schustter, "Machine Learning Driven Fast Prediction of Self- and Transfer-Impedance Profiles for the Modeling of PCB-Based Power Delivery Networks," unpublished.

[67] Y. Hassab, J. Heßling, M. Schierholz, I. Erdin, J. Balachandran, and C. Schuster, "Impedance Profile Prediction and Classification for PCB based PDN Decoupling Using Autoencoders," in *DesignCon 2025*, Santa Clara, CA, USA, Jan. 2025.

[68] Y. Hassab, M. Schierholz, and C. Schuster, "Application of Gaussian Process Regression for Data Efficient Prediction of PCB-Based Power

Delivery Network Impedance Features," in *2024 IEEE 28th Workshop on Signal and Power Integrity (SPI)*, Lisbon, Portugal, May 2024.

[69] Y. Hassab, H. Esmaeili, and C. Schuster, "Data-Efficient Prediction of the Specific Absorption Rate in a Human Head Model Exposed to a Plane EM Wave Using Gaussian Process Regression," in *2024 International Symposium on Electromagnetic Compatibility – EMC Europe*, Brugge, Belgium, Sep. 2024.

[70] M. Schierholz, Y. Hassab, I. Erdin, J. Balachandran, and C. Schuster, "Applying Techniques of Transfer and Active Learning to Practical PCB Noise Decoupling," in *DesignCon 2024*, Santa Clara, CA, USA, Jan. 2024.

[71] Y. Hassab, T. Stadelmayer, and F. Lurz, "Physically-Interpretable Data Augmentation for Multi-Range Hand Gesture Recognition Using FMCW Radar Time Series," *IEEE Transactions on Radar Systems*, vol. 1, pp. 571–582, Sep. 2023.

[72] Y. Hassab, T. Hillebrecht, F. Lurz, and C. Schuster, "Machine Learning Based Data Validation for Signal Integrity and Power Integrity Using Supervised Time Series Classification," *IEEE Transactions on Electromagnetic Compatibility*, vol. 66, no. 6, pp. 2150–2158, Dec. 2024.

[73] T. Hillebrecht, M. Schierholz, Y. Hassab, J. Alfert, and C. Schuster, "Generation and Application of a Very Large Dataset for Signal Integrity Via Array and Link Analysis," *IEEE Transactions on Electromagnetic Compatibility*, vol. 66, no. 6, pp. 1967–1976, Dec. 2024.

[74] D. P. Kingma and J. Ba, "Adam: A Method for Stochastic Optimization," in *3rd International Conference on Learning Representations ICLR*, San Diego, CA, USA, May 2015.

[75] C. E. Rasmussen and C. K. I. Williams, *Gaussian Processes for Machine Learning*. London, England: MIT Press, 2005.

[76] J. Snoek, H. Larochelle, and R. P. Adams, "Practical Bayesian Optimization of Machine Learning Algorithms," in *Advances in Neural Information Processing Systems*, Lake Tahoe, NV, USA, Dec. 2012.

[77] D. S. Moore, G. P. McCabe, and B. A. Craig, *Introduction to the Practice of Statistics*, 8th ed. New York City, NY, USA: W. H. Freeman, 2013.

[78] B. Settles, "Active Learning Literature Survey," University of Wisconsin–Madison, Madison, WI, USA, Computer Sciences Technical Report 1648, Jan. 2010. [Online]. Available: https://burrsettles.com/pub/settles.activelearning.pdf

[79] R. Trinchero and F. Canavero, "Use of an Active Learning Strategy Based on Gaussian Process Regression for the Uncertainty Quantification of Electronic Devices," in *1st International Electronic Conference—Futuristic Applications on Electronics*, Online, Nov. 2020.

[80] Q. Yang, Y. Zhang, W. Dai, and S. J. Pan, *Transfer Learning*. Cambridge, United Kingdom: Cambridge University Press, 2020.

[81] M. Schierholz, C. Schuster, Z. Nezhi, and M. Stiemer, "PCB Based Power Delivery Network Analysis Using Transfer Learning and Artificial Neural Networks," in *2024 IEEE 28th Workshop on Signal and Power Integrity (SPI)*, Lisbon, Portugal, May 2024.

[82] A. Dempster, F. Petitjean, and G. I. Webb, "ROCKET: Exceptionally Fast and Accurate Time Series Classification Using Random Convolutional Kernels," *Data Mining and Knowledge Discovery*, vol. 34, pp. 1454 – 1495, Jul. 2020.

[83] H. Ismail Fawaz, G. Forestier, J. Weber, L. Idoumghar, and P. Muller, "Deep Learning for Time Series Classification: A Review," *Data Mining and Knowledge Discovery*, vol. 33, pp. 917–963, Mar. 2019.

[84] S. Bai, J. Z. Kolter, and V. Koltun, "An Empirical Evaluation of Generic Convolutional and Recurrent Networks for Sequence Modeling," Apr. 2018. [Online]. Available: https://arxiv.org/abs/1803.01271

[85] H. Esmaeili, C. Yang, and C. Schuster, "Flexible Numerical Evaluation of Human Head Exposure to a Transmitter Coil for Wireless Power Transfer at 13.56MHz," in *2022 International Symposium on Electromagnetic Compatibility - EMC Europe*, Gothenburg, Sweden, Sep. 2022.

[86] H. Esmaeili, C. Yang, and C. Schuster, "SAR Prediction in Human Head Tissues with Varying Material Parameters Using an Artificial Neural Network," in *Annual Conference of BioEM*, Oxford, United Kingdom, Jun. 2023.

[87] H. Esmaeili, C. Yang, and C. Schuster, "Physics Inspired Artificial Neural Network Adaptation for SAR Prediction in Bio-EM Problems," in *2023 IEEE MTT-S International Microwave Biomedical Conference (IMBioC)*, Leuven, Belgium, Sep. 2023.

[88] S. Park, M. Kotzev, H.-D. Brüns, D. G. Kam, and C. Schuster, "Lessons from Applying IEEE Standard 1597 for Validation of Computational Electromagnetics Computer Modeling and Simulations," *IEEE Electromagnetic Compatibility Magazine*, vol. 6, no. 2, pp. 55–67, Jul. 2017.

[89] A. J. M. Martin, "Quantitative Data Validation (Automated Visual Evaluations)," Ph.D. dissertation, De Montfort University, Leicester, UK, 1999.

[90] A. P. Duffy, A. J. M. Martin, A. Orlandi, G. Antonini, T. M. Benson, and M. S. Woolfson, "Feature Selective Validation (FSV) for Validation of Computational Electromagnetics (CEM). Part I—The FSV Method," *IEEE Transactions on Electromagnetic Compatibility*, vol. 48, no. 3, pp. 449–459, Aug. 2006.

[91] A. Orlandi, A. P. Duffy, B. Archambeault, G. Antonini, D. E. Coleby, and S. Connor, "Feature Selective Validation (FSV) for Validation of Computational Electromagnetics (CEM). Part II—Assessment of FSV Performance," *IEEE Transactions on Electromagnetic Compatibility*, vol. 48, no. 3, pp. 460–467, Aug. 2006.

[92] M. R. Johnson, "FSV Versus Human Subjective Data Evaluation; An Informal Survey," in *2012 IEEE International Symposium on Electromagnetic Compatibility*, Pittsburgh, PA, USA, Aug. 2012.

[93] *Multilayer Substrate Simulator CONMLS Version 2.0.* Hamburg, Germany: TUHH - Institut für Theoretische Elektrotechnik, (Last accessed: 1-April-2025). [Online]. Available: https://www.tet.tuhh.de/wordpress/wp-content/uploads/2024/07/Manual-Conmls.pdf

[94] *ANSYS ®Electromagnetics Suite, Release 2021 R1.* Canonsburg, PA, USA: ANSYS, INC. [Online]. Available: http://www.ansys.com

[95] D. E. Coleby and A. P. Duffy, "A Visual Interpretation Rating Scale for Validation of Numerical Models," *COMPEL - The International Journal for Computation and Mathematics in Electrical and Electronic Engineering*, vol. 24, no. 4, pp. 1078–1092, Dec. 2005.

[96] I. Erdin and R. Achar, "Multipin Optimization Method for Placement of Decoupling Capacitors Using a Genetic Algorithm," *IEEE Trans. on Electromagnetic Compatibility*, vol. 60, no. 6, pp. 1662–1669, Dec. 2018.

[97] R. Rimolo-Donadio, X. Gu, Y. H. Kwark, M. B. Ritter, B. Archambeault, F. de Paulis, Y. Zhang, J. Fan, H.-D. Bruns, and C. Schuster,

"Physics-Based Via and Trace Models for Efficient Link Simulation on Multilayer Structures Up to 40 GHz," *IEEE Transactions on Microwave Theory and Techniques*, vol. 57, no. 8, pp. 2072–2083, Aug. 2009.

[98] D. Lee, D. Shin, and D. Shin, "A Finger Counting Method for Gesture Recognition," *Journal of Internet Computing and Services*, vol. 17, no. 2, pp. 29–37, Apr. 2016.

[99] H. I. Fawaz, B. Lucas, G. Forestier, C. Pelletier, D. F. Schmidt, J. Weber, G. I. Webb, L. Idoumghar, P.-A. Muller, and F. Petitjean, "InceptionTime: Finding AlexNet for Time Series Classification," *Data Mining and Knowledge Discovery*, vol. 34, no. 6, pp. 1936–1962, Sep. 2020.

[100] K. Kamycki, T. Kapuscinski, and M. Oszust, "Data Augmentation with Suboptimal Warping for Time-Series Classification," *Sensors*, vol. 20, no. 1, Dec. 2019.

[101] G. Forestier, F. Petitjean, H. A. Dau, G. I. Webb, and E. Keogh, "Generating Synthetic Time Series to Augment Sparse Datasets," in *2017 IEEE International Conference on Data Mining (ICDM)*, New Orleans, LA, USA, Nov. 2017.

[102] B. K. Iwana and S. Uchida, "Time Series Data Augmentation for Neural Networks by Time Warping with a Discriminative Teacher," in *2020 25th International Conference on Pattern Recognition (ICPR)*, Milan, Italy, Jan. 2021.

[103] M. Swaminathan and A. E. Engin, *Power Integrity Modelling and Design for Semiconductors and Systems*. Boston, MA, USA: Pearson Education, Inc., 2007.

[104] I. Sobol, "Global Sensitivity Indices for Nonlinear Mathematical Models and Their Monte Carlo Estimates," *Mathematics and Computers in Simulation*, vol. 55, no. 1, pp. 271–280, Feb. 2001.

[105] M. Schierholz, A. Sánchez-Masís, A. Carmona-Cruz, X. Duan, K. Roy, C. Yang, R. Rimolo-Donadio, and C. Schuster, "SI/PI-Database of PCB-Based Interconnects for Machine Learning Applications," *IEEE Access*, vol. 9, pp. 34 423–34 432, Feb. 2021.

[106] T. Hillebrecht, T. Weber, J. Alfert, and C. Schuster, "Relational SI/PI-Database for a Data-Driven Approach to PCB Design Automation and Performance Prediction," *IEEE Transactions on Components, Packaging and Manufacturing Technology*, vol. 15, no. 9, pp. 1847–1856, Sep. 2025.

Publications

The full printed publications are grouped according to authorship status and contribution to this cumulative dissertation. Only publications listed in the first section fulfill the formal requirements of 1st authorship and **confirmed** predominant contribution of the Hamburg University of Technology (TUHH).

First Authorship and Predominant Contribution

P1: [1] Y. Hassab, M. Schierholz, L. P. P. B. Bohl, H. Esmaeili, T. Hillebrecht, C. Yang, J. Heßling, and C. Schuster, "Developments in Machine Learning based Modeling and Design for Electromagnetic Compatibility," *IEEE Electromagnetic Compatibility Magazine*, vol. 14, no. 4, pp. 69-81, Dec. 2025.

P2: [69] Y. Hassab, H. Esmaeili and C. Schuster, "Data-Efficient Prediction of the Specific Absorption Rate in a Human Head Model Exposed to a Plane EM Wave Using Gaussian Process Regression," in *2024 International Symposium on Electromagnetic Compatibility - EMC Europe*, Brugge, Belgium, Sep. 2024.

P3: [68] Y. Hassab, M. Schierholz and C. Schuster, "Application of Gaussian Process Regression for Data Efficient Prediction of PCB-Based Power Delivery Network Impedance Features," in *2024 IEEE 28th Workshop on Signal and Power Integrity (SPI)*, Lisbon, Portugal, May 2024.

P4: [72] Y. Hassab, T. Hillebrecht, F. Lurz and C. Schuster, "Machine Learning Based Data Validation for Signal Integrity and Power Integrity Using Supervised Time Series Classification," *IEEE Transactions on Electromagnetic Compatibility*, vol. 66, no. 6, pp. 2150-2158, Dec. 2024.

P5: [71] Y. Hassab, T. Stadelmayer and F. Lurz, "Physically-Interpretable Data Augmentation for Multi-Range Hand Gesture Recognition Using FMCW Radar Time Series," *IEEE Transactions on Radar Systems*, vol. 1, pp. 571-582, Sep. 2023.

Further Publications

P6: [67] Y. Hassab, J. Heßling, M. Schierholz, I. Erdin, J. Balachandran, and C. Schuster, "Impedance Profile Prediction and Classification for PCB based PDN Decoupling Using Autoencoders," in *DesignCon 2025*, Santa Clara, CA, USA, Jan. 2025.

P7: [66] Y. Hassab, J. Heßling, and C. Schuster, "Machine Learning Driven Fast Prediction of Self- and Transfer-Impedance Profiles for the Modeling of PCB-Based Power Delivery Networks," unpublished.

Publication 1 (P1)

Title

Developments in Machine Learning based Modeling and Design for Electromagnetic Compatibility.

Publication Status

Published in peer-reviewed magazine: IEEE Electromagnetic Compatibility Magazine.

Author Contribution

Predominant involvement as a 1. author (co-author confirmation provided).

Bibliographic Information

[1] Y. Hassab, M. Schierholz, L. P. P. B. Bohl, H. Esmaeili, T. Hillebrecht, C. Yang, J. Heßling, and C. Schuster, "Developments in Machine Learning based Modeling and Design for Electromagnetic Compatibility," *IEEE Electromagnetic Compatibility Magazine*, vol. 14, no. 4, pp. 69-81, Dec. 2025.

Copyright Notice

Developments in Machine Learning based Modeling and Design for Electromagnetic Compatibility

Youcef Hassab, Morten Schierholz, Lennart P. P. B. Bohl, Hamideh Esmaeili, Til Hillebrecht, Cheng Yang, Jan Severin Hessling, Christian Schuster

***Abstract*—Machine learning (ML) has gained traction and emerged as one of most researched topics in recent years. Many engineering disciplines are taking advantage of a multitude of developed ML tools to enhance the engineering workflow, solve complicated problems or speed-up design processes. This paper presents an overview on past and present developments of ML-based modeling and design in the field of electromagnetic compatibility (EMC) and the related fields of signal integrity (SI), power integrity (PI), bioelectromagnetics (BioEM) and electromagnetic field (EMF) scans. A critical analysis of recent research on ML applications is carried out to identify the arising opportunities and challenges facing the wide adoption of ML for the modeling and design in EMC. Based on current trends, a vision for ML-based modeling and design in EMC is presented in an attempt to foresee the direction of near-future research. A set of recommendations is formulated to tackle actual challenges facing a wider adoption. ML integration in EMC engineering has a great potential to revolutionize the modeling and design processes, despite the open challenges and the rising complexities of the faced problems.**

***Index Terms*—Machine Learning, Data-Driven, electromagnetic compatibility (EMC), signal integrity (SI), power integrity (PI), bioelectromagnetics (BioEM), electromagnetic field (EMF) scans.**

I. Introduction

Electromagnetic compatibility (EMC) is becoming ever more important in the electrical engineering world with the wide spread of connected systems, high-speed connectivity, wireless communication and the rising complexity of the systems. Let's take the example of modern electric vehicles (EVs), see Fig. 1. EVs are full of interconnected electrical and electronic systems working at different voltages and frequencies, e.g., power and propulsion systems, vehicle control, communication systems and various interfaces. The proper functioning of the EVs can only be guaranteed with proper EMC considerations in the design stages. Some modern EV with the different processing units count as many as 3000 chips. Signal integrity (SI) and power integrity (PI) engineering play a crucial role in ensuring adequate signal transmission and enough qualitative power reaching the different components. The safety of the passengers of the EV is to be ensured. The interaction of the EM fields generated by the different subsystems with humans needs to be considered. Measurements and Electromagnetic field (EMF) scans are an important part of gathering information on the EM behavior of the subsystems.

The authors are with the Institut für Theoretische Elektrotechnik (TET), Hamburg University of Technology (TUHH), Hamburg, Germany.
(E-mail corresponding author: youcef.hassab@tuhh.de).

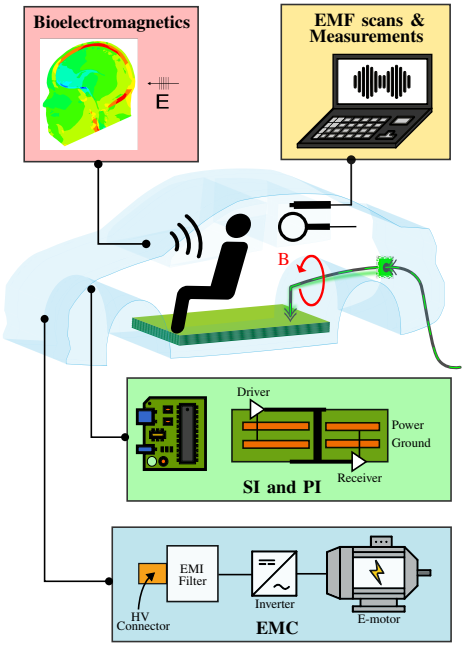

Fig. 1. Modern electric vehicles (EVs) represent a good example of the rising complexity of many electrical systems. Many subsystems are densely integrated in an EV. EMC considerations are an important aspect of the design process, e.g., HV EMI filter for compliance. SI and PI play an important role in the functioning of chips. Measurements are crucial to gather information on EM behavior. BioEM studies the interaction of EM fields and biological tissues to ensure safety.

The growing complexity of the systems demands even more efficient tools for the modeling and design. The modeling process aims at creating analytical representations of problems to correctly predict the behavior of systems. Design for EMC involves the practical implementation of techniques to ensure compliance. Machine learning (ML) has emerged as one of the most researched fields in recent years. ML is concerned with the development of computer programs that automatically improve with experience based on data [1], [2]. The evolution

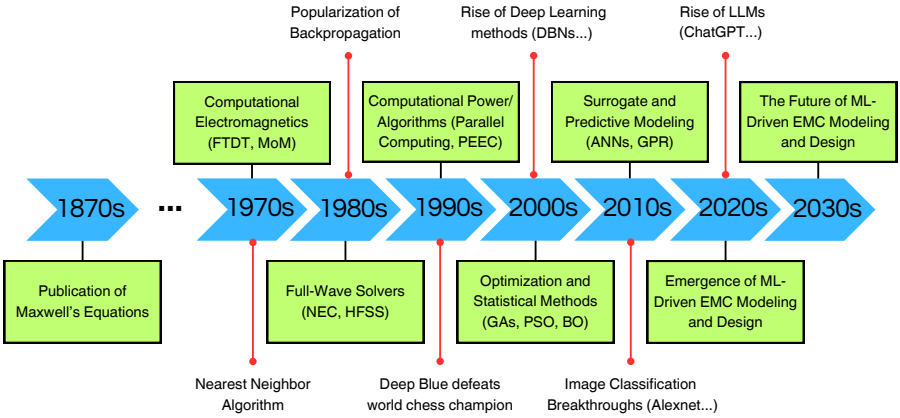

Fig. 2. The timeline of ML-based EMC engineering reflects broader advancements and milestones in modeling techniques, computational electromagnetics, data science, and AI. With the recent successes and milestones of AI and ML, the application of data-driven tools for the modeling and design in EMC has gained traction in the 2010s.

of ML-based modeling and design for EMC is a fascinating journey that reflects broader advancements in computational electromagnetics, data science, and artificial intelligence (AI), see Fig. 2. In 1865, the famous Maxwell's equations were published, laying foundations of classical electromagnetism. A century later, the finite-difference time-domain (FDTD) was proposed as a method for solving Maxwell's equations numerically. In addition to the method of moments (MoM) and the finite element method (FEM), These cornerstones of computational electromagnetics enabled the simulation of electromagnetic wave propagation in time and space, laying the groundwork for modern EMC analysis. And soon enough, the 1980s saw the emergence of softwares like numerical electromagnetics code (NEC) and high-frequency structure simulator (HFSS), which made full-wave solvers accessible to engineers. The tools enabled the simulations of electromagnetic and EMC problems in ways unimaginable before, providing accurate distributions of fields and analysis.

The era of physics-based (PB) modeling would change EMC engineering workflows and methods. This shift was helped by the increasing computational power, availability of better hardware and more established algorithms in the 1990s, e.g., parallel computing and partial element equivalent circuit (PEEC). The transformation from physical to virtual prototyping, from the reliance on intuition and experience to quantitative data, from isolated problems to system-level analysis, from trial and error to optimization allowed for major breakthroughs. The ability to efficiently simulate and visualize complex systems once thought of as impossible, have become commodity and standard practice in the 2000s, in addition to the use of computer-assisted optimization and statistical tools, e.g., genetic algorithms (GAs), Bayesian optimization (BO) and particle swarm optimization (PSO).

In the meantime, the fields of AI and ML have seen bursts of accelerated research that resulted in major breakthroughs. Many tools have seen the light of the day enabling efficient solutions, e.g., image classification or natural language processing. With the rising complexity of problems faced in the EMC domain and beyond, PB tools are either too inaccurate or too inefficient to handle the complexity of some problems. With the recent successes of AI and ML in other fields, the application of data-driven tools for the modeling and design in EMC has gained traction in the 2010s, with a particular interest in surrogate modeling, e.g., using artificial neural networks (ANNs) or Gaussian process regression (GPR). Initial investigations have shown the potential of these data-driven tools in enhancing EMC engineering with more and more emerging research looking into replacing PB-based modeling with ML-based modeling. The question that many engineers are asking themselves is how much potential does ML have to revolutionize the modeling and design processes?

In this article, the authors attempt to provide a vision for the future of ML-based modeling and design for EMC, based on the recent advancements and trends in EMC, SI, PI, bioelectromagnetics (BioEM) and measurement techniques. In Section II, a set of basic ML applications are presented to give an introduction on ML in EMC. In Section III, current trends in the research of ML for EMC are highlighted. A critical analysis of these works is carried out to identify the faced challenges and rising opportunities for ML in EMC. In Section IV, a vision for ML-based engineering is presented in an attempt to foresee the direction of near-future research in the field. In Section V, A set of recommendations is additionally provided to overcome the limitations and challenges facing a wider adoption of ML in EMC. In Section VI, a conclusion is provided.

II. Tutorial Applications

The application of ML algorithms for the modeling and design in EMC and related subfields is based on the interaction between multiple aspects. The basic components for ML application include the data acquisition, data, ML tools and users, see Fig. 3. The implementation of ML tools by trained engineers is based on data generated by acquisition methods such as simulation and measurement. This section showcases two supervised learning ML applications to give an overview on a typical and simple implementation workflow and highlights the importance of domain knowledge. A broader introduction of common ML methods for EMC is presented in [3].

A. Prediction of the SAR in Human Head Models

In this first example, a basic application is considered to present a simple ML workflow and application tutorial involving ANNs. The first important aspect to consider for any application is the problem definition, see Fig. 4. It includes a clear formulation of the problem to be solved, and the design space constraining the problem. In the considered scenario case, there is an interest in the fast determination of the specific absorption rate (SAR) in the tissues of a human head model while considering uncertainties in the electric properties (EPs) of individual tissues exposed to a plane wave at 13.56 MHz. [4], [5]. The fast prediction of the SAR presents an alternative to the time-consuming EM simulations.

When the problem is clearly defined, a needed data structure and design space is set for the training and testing of appropriate ML models. In the presented application, a human head model with 5 tissues is used. The permittivity (ε_r) and conductivity (κ) of each tissue are varied by $\pm 20\%$ around nominal values to account for the tissue uncertainty [6]. These 10 dimensions, variations in the permittivity and conductivity of each one of the 5 tissues, represent the input features. An appropriate ML algorithm and model is then chosen for the task at hand. The choice is done based on the type of problem e.g. classification, regression or clustering, the type and dimensionality of data e.g. time series, images or vectors. The relationships in the data e.g. time dependency and the computational resources play a role as well. Since the resulting SAR is a continuous value, we are faced with a regression task and choose simple feed-forward ANNs.

When the design space and ML method are set, data samples are generated for the training and testing, see Fig. 5. The data samples should be representative and cover the explored design space. The exact number of samples needed depends on many factors e.g. the complexity of the problem, the ability of the model to generalize, the amount of variability in the data, and the desired level of accuracy or robustness [7]. For the considered design space 500 data samples are set to be simulated using latin hypercube sampling (LHS).

The data is stored in a space that can be easily accessed. One important aspect is the validation of the generated and stored data. It is the important process of checking the quality of raw data. This includes i.a. the validation of simulations models, checking the physical credibility of the results and checking for missing values. Taking a look at the distribution of inputs and outputs (labels) to check if the samples are balanced and cover the desired design space is also standard practice. When the data quality is ensured, the preprocessing stage can begin. This stage brings the raw data in a format useful for ML tools and meeting the desired input/output structure. For the application at hand, the desired outputs are the mass-averaged SAR values distributed within the different tissues of the head. The SAR is calculated using the local electric field E obtained from simulations, conductivity κ and mass density ρ [8].

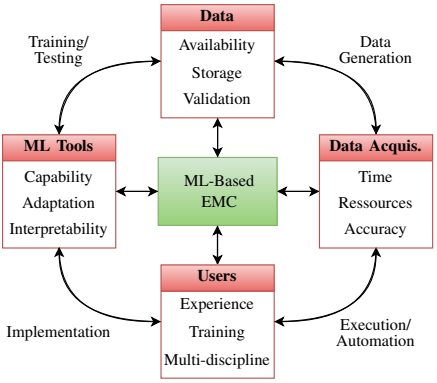

Fig. 3. Diagram highlighting the most important aspects of ML-based EMC modeling and design. All the interconnected aspects contribute to successful implementation of ML tools.

The preprocessed data is split into training and testing sets. The training sets are used to train the ML models for as many epochs as needed and the testing sets are used for the performance evaluation of the models. The 500 sample dataset is randomly divided, with 80% used for training and 20% for testing. Before the training process, data scaling is performed. Since different input features might have different scales, the different scales and outliers can impact the performance negatively. Through normalization or standardization, all values are adjusted to a single scale. The input variables are first normalized using a min-max normalization as follows:

$$\hat{X} = \frac{X - X_{\min}}{X_{\max} - X_{\min}} \tag{1}$$

where $\hat{X}$ is the scaled input, X the original input, $X_{\min}$ and $X_{\max}$ are the minimum and the maximum of the input feature, respectively. The ANN model is built during the training phase by setting the network weights and biases using an optimization routine, e.g., Adam solver. Training the neural network involves tuning and selecting optimal key hyperparameters for the training and the structure of the model such as learning rate, batch size, number of layers, and neurons per layer. Techniques like grid search or random search help explore the hyperparameter space systematically. Evaluating the performance of the neural network involves metrics that accurately reflect the model's effectiveness. For regression tasks like SAR prediction, common metrics such as root mean

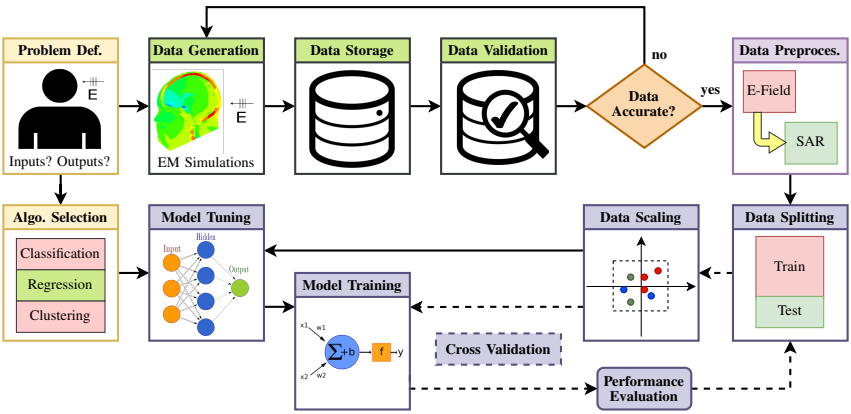

Fig. 4. Flowchart of a basic ML application workflow. The problem definition, design space setting and algorithm choice are important considerations at the start of the process. The data generation and processing represent a large part in the implementation process. Based on the pre-processed datasets, the chosen models are trained to make reliable predictions. The performance of the trained models is evaluated in the end.

squared error (RMSE) or the coefficient of determination (R^2) can be used:

$$R^2 = 1 - \frac{\sum_{i=1}^{N}(y_i - \hat{y}_i)^2}{\sum_{i=1}^{N}(y_i - \bar{y})^2} \tag{2}$$

where y_i are the original values, $\hat{y}_i$ are the predicted values, $\bar{y}$ is the mean of the original values, and N is the total number of samples. An R^2 value close to 1 indicate high prediction accuracy and a strong correlation between actual and predicted values. Additionally, K-fold cross-validation is applied to ensure robust model training and validation. It involves training and testing multiple times using a different train/test split each run. The average accuracy of multiple runs is given as a final result. K-fold cross-validation gives a more accurate estimate of the performance to mitigate the effects of an advantageous train/test split or ANN weight initialization. The ANN framework achieved an average R^2 score of 0.98 for SAR predictions on the test sets across all tissue types in the human head model. The results of the predictions in the skull tissue are shown in Fig. 6. The trained model can be used to predict the SAR for any combination of electric parameters from the defined design space.

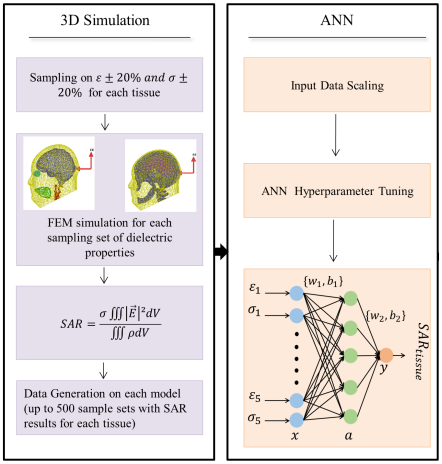

Fig. 5. To generate the training and testing datasets, the electric properties (EPs) of the tissues are varied and the head models are simulated. The SAR (output) is then calculated from the resulting fields. After preprocessing, the ANN is trained to predict SAR values from input tissue parameters. x denotes the vector of input parameters, a is the vector of hidden layer neurons, w_1 and w_2 are the weight matrices for each connection between layers, b_1 and b_2 are the bias vectors for each layer, y is the output [4].

B. Prediction of the Target Impedance Violations of PDNs

For the decoupling of power delivery networks (PDNs), many approaches of automated placement of decoupling capacitors require additional simulations during the optimization process [9]–[11]. Here, an ANN is trained to predict whether specific constellation of placed decoupling capacitors (decaps) fulfills the target impedance (TI), without the need for further simulations [12]. A simple one cavity printed circuit board (PCB) of board dimensions 12 000 mil × 10 000 mil, cavity height h_{cavity}, via radius r_{via}, antipad radius $r_{antipad}$, relative permitivity ε_r and loss tangent $tan\delta$ is investigated, see

Fig. 7. Decoupling capacitors from a defined library, are placed randomly around the IC port on 121 possible positions marked by a white grid in Fig. 7 (b). The designs are then simulated using PB via models in combination with the contour integral method and perfect magnetic conducting (PMC) boundary

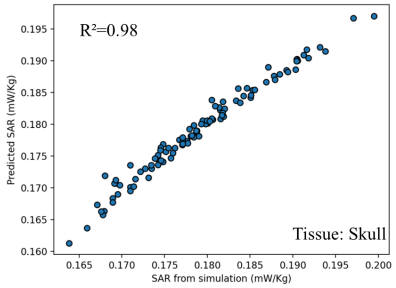

Fig. 6. The SAR prediction performance in the skull tissue is shown as an example. The predicted and simulated SAR values from the test set show good agreement with an R^2 score of 0.98 [4].

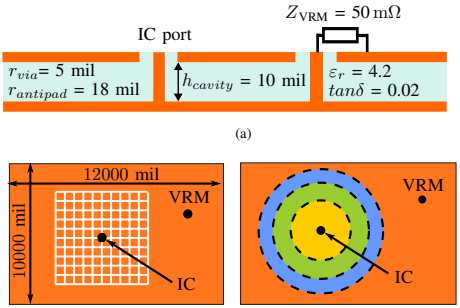

Fig. 7. Geometrical depiction of the investigated PCB. As seen in the (a) cross-section, the VRM port is terminated with a resistor and the IC port is the port under investigation. In the (b) direct preprocessing method, the value and position of decaps placed on the white grid crossing points are used as an input. In the (c) ring sector preprocessing, the decaps inside colored rings around the IC port are counted to reduce the number of input dimensions.

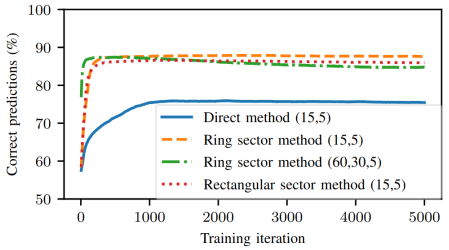

Fig. 8. Prediction accuracy of the trained ANN on the test set. Each preprocessing method is evaluated ten times. Numbers inside the brackets present the amount of neurons in each hidden layer [12].

conditions [13]. For each simulated design, the resulting PDN impedance over the frequency range of 1 MHz to1 GHz is compared with a defined TI to check for violation.

An ANN is trained to predict if a certain decap constellation violates the TI or not. A structure with two hidden layers, fifteen neurons in the first and five neurons in the second layer (15,5) is used. The neurons in the hidden layer have a ReLU activation function. For the input, two preprocessing techniques are applied. In the direct method, the exact position of a decap and its value is given using an input vector that contains the 121 possible positions, see Fig. 7 (b). In the ring sector method, sectors of equal area are defined around the IC port where decaps are counted per zone, see Fig. 7 (c). The generated 14 000 samples are split into training and testing sets. After training and testing, the direct method results in an accuracy of 75% while the ring sectors method results in an accuracy of approximately 90%, an increase of 15 percentage points, see Fig. 8. Since the distance of a decap from the IC port is a determining factor of the effect it has on the PDN impedance, decaps inside a defined sector can be assumed to have a similar effect on the impedance. This preprocessing method based on domain knowledge results in a significant performance increase, since it allows to strongly reduce the dimensionality of the problem while keeping the most important information. This shows the importance of domain knowledge in the process of applying ML techniques in problem-solving. Domain knowledge is essential for the adaptation of ML techniques for successful use. This highlights the need of trained engineers from the field that drive research of ML in EMC and beyond.

III. Current Trends and Developments

In recent years, there has been a growing interest in ML applications in EMC and related fields. In the Transactions on Electromagnetic Compatibility (TEMC), the number of ML-related publications has been increasing with a record of 19 publications in 2024, see Fig. 9. In this section, recent publications on ML-based modeling and design in EMC, SI, PI, BioEM and EMF scans are presented. The publications are analyzed to provide an overview on the relevance and benefits of the developed ML solutions and their limitations.

A. State of the Art

Many proposed applications and ML solutions in EMC aim at reducing the time and cost spent on extensive simulations. ML-based surrogate models are used to create fast predictive models to replace expensive simulations and subsequently help in optimization problems as well. Recent advances in surrogate modeling for EMC include usage of minimum amount of data from expensive 3D simulations for model construction over wide frequency bandwidths [14], [15]. ML methods offering sensitivity analysis have been investigated with regard to EMC problems, as they offer valuable insight for the design process, e.g., modeling for automotive EMC or shielded cable emission predictions [14], [16]. Using ML methods to improve existing modeling techniques has been pursued, e.g., improve PEEC modeling by integrating uncertainty quantification using ANNs or generative adversarial networks (GANs) [17], [18]. The mitigation of EMI and the optimization of EMI-filters has been improved with ML-based optimization techniques [19]–[21].

Some works successfully targeted specific applications and problems encountered in EMC using ML-based methods, such as for the assessment of shielding enclosures [22], improving the efficiency of electromagnetic susceptibility testing [23] or the prediction of lightning currents [24].

In the SI domain, many publications target the determination of the characteristics of eye diagrams, e.g., determining the shape of the inner eye using vector machine regression [25]. Similarly, the prediction of other performance metrics, inter symbol interference (ISI) and crosstalk, e.g., weighted power sums, have been pursued [26]–[28]. Many publications focused on the reconstruction of S-parameters, e.g., by using periodic Gaussian process kernels [29]. Another area of interest in link design is the optimization of equalization using i.a. BO [30], [31] and direct optimization of interconnects [32]. The SI compliant design of PCBs using ML algorithms, e.g., ANNs, decision trees and transfer learning has been investigated as well [33]–[35].

In the PI domain, the focus lies on the investigation of the capabilities of ML in enhancing the design flow. The investigations include the application of ANNs, or support vector machines (SVMs) to classify PDNs with respect to the TI [12], [36]. Different approaches to acquire sophisticated knowledge of the EM behavior using ML tools were proposed [37]–[39]. The assisted decoupling of PCBs by placement of decaps to reduce the self-impedance of the PDN using different algorithms has been investigated as well [40]–[42]. The modeling and optimization of PDNs using, e.g., reinforcement learning (RL), PSO or GA, has been of interest [43]–[45].

In BioEM, ML has been used for the estimation of tissue properties [46], prediction of SAR and exposure levels for the comparison with safety levels [7], [47], and the speed-up of design processes [48]. The effectiveness of ML methods in predicting power absorption and field-induced heating in magnetic resonance imaging (MRI) scenarios to enhance safety protocols has been demonstrated [49], [50].

ML techniques have also been investigated to support measurement and EMF techniques. The reduction of sampling points needed for accurate results is a main concern [51], [52]. Accurate modeling of radiation sources using EMF data for different investigations has been the target of many works [53], [54]. Conductive or radiative EMC problem-solving based on reduced numbers of EMF scans has been pursued [52], [55].

B. Challenges

Taking a deeper look at the latest publications on ML in EMC and related fields, there seems to be a generally common and shared set of limitations, challenges and opportunities, see Table I. In many publications, one can argue that the tackled problems and models are mostly simplified. There is still a significant gap between real-world applications and considered problems in research. This includes more often than not smaller design spaces that do not represent the full complexity of the systems. For high-dimensional models, the performances of ML tools are significantly lower, than for simpler models. To give an example, let us take a look at the complexity of PCBs used for the research of ML in PDN

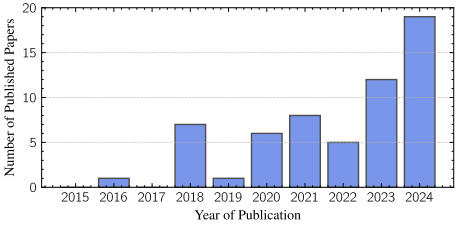

Fig. 9. Number of publications found for the search term 'Machine Learning' in the Transactions on Electromagnetic Compatibility (TEMC). The year 2024 has seen a record number of 19 publications related to ML for EMC.

design in [37]. The PCBs considered are bare boards with a maximal number of 11 varied dimensions. The number of layers and via ports is limited to 8 and 18, respectively. Real-life PCBs involve a parameter space that is usually up to 100× orders of magnitude larger with thousands of components. Depending on the application, the larger amount of layers and ports in real-life PCBs can result in simulations 10 to 100 times longer. Moreover, the presented solutions are generally valid for very specific design spaces and defined scenarios. For different design spaces and scenarios, new datasets usually have to be generated and tested. Many of the used algorithms offer very small room for interpretation of the results and processes. The latter makes scaling and applying developed solutions to different problems and design spaces difficult. Additionally, the proposed solutions often target very small portions of a design pipeline, which results in very small and incremental speed-ups of the full design pipelines. There are very few publications that share the used datasets in the studies or use openly accessible datasets. The used datasets do not show conformity and no standard benchmarking datasets are used. The latter makes the comparison of the provided ML solutions very difficult. There is also a lack of accessible parametrized models that can be used for the generation of needed data.

C. Opportunities

Tasks where the application of ML has been shown to give advantages is expanding. Despite these limitations, many works show clear advantages of ML-based solutions in contrast to conventional methods. Many commercial tools have already integrated these ML-based solutions, for example: ML-based surrogate models for the prediction of crosstalk in high-speed PCB traces. ML-based optimization methods for the automated search of EMC-compliant designs. ML-based anomaly detection in EMC testing, to name a few. The former have shown potential in speeding-up and improving design processes overall. Many of the cited works used advanced and adapted ML tools to improve the performance. On the one side, algorithms at disposition of engineers and scientists are improving, and new tools are constantly being developed. Taking the example of time series classification, newer tools have been developed with improved performances on benchmark

datasets repeatedly during the last 10 years. On the other hand, some implemented algorithms are adapted to specific domain needs and solutions, which reflects a growing experience of the involved researchers in the intersection of engineering and ML. The growing computational capabilities have made the training of models and generation of needed samples for generalization faster processes, as reported.

TABLE I
OPPORTUNITIES AND CHALLENGES FACING THE WIDE ADOPTION OF ML IN EMC MODELING AND DESIGN.

Opportunities +	**Challenges -**
Better performances than conventional tools in many areas.	Problem-specfic solutions that are hard to scale.
Development and availability of better ML tools.	Lower performances for high-dimensional problems.
Rising computational capabilities and resources.	Scarcity of accessible high-quality datasets.
Growing experience of engineers in ML domain.	ML models lacking interpretabilty and explainability.

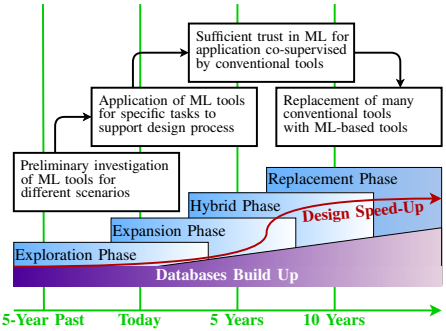

Fig. 10. Setup of the time horizon and implementation phases for different aspects of ML for the modeling and design in the EMC domain. The authors predict a shift in the next years to a hybrid application of ML and PB tools where the usage of ML tools co-supervised by conventional tools.

IV. VISION FOR FUTURE DEVELOPMENTS

In this section, a vision for the future of ML-based modeling and design for EMC engineering is presented in an attempt to foresee the direction of near-future research.

A. The Exploration and Expansion Phases

In the past few years, the research of ML-based modeling and design has been more or less led with an exploration mindset, see Fig. 10. During this phase, ML tools have been preliminarily investigated for a wide range of applications with differing degrees of complexity. It represents an important phase where more expertise is built, and the limitations and applicability of ML in EMC engineering are broadly investigated. This has resulted in the current expansion phase, where ML tools are applied to support the design and modeling processes by providing alternatives to PB and conventional tools in some parts of the design processes. New research is increasingly being conducted to expand the use of ML to a wider range of applications and parts of design processes.

B. The Hybrid Phase

Based on the exploration and expansion phase, the authors predict a shift in the next years to a hybrid application of ML and PB tools, see Fig. 10. During this phase, the rising experience in the application of ML tools in the design processes and the improving performance will be sufficient to trust the usage of ML tools co-supervised by conventional tools. This hybrid phase will result a significant speed-up in the design processes, mostly due to ML models partially replacing conventional simulation tools, e.g., PB simulations. During this phase, the integration of ML in design loops will initially run in parallel with parametric investigations using simulation models. There, active learning loops or BO will improve the performance of optimization processes and investigation of critical elements. Training a surrogate model in parallel with any investigations via parametric simulation runs and measurements will offer improved optimization. The number of simulations and measurements required for high surrogate accuracy will decrease with higher adaptation of the model to the specific problem. Furthermore, before running a simulation for a specific input parameter set, the prediction from an ML tool may be viewed including information on the uncertainty of the prediction. A major step in improvement due to ML will occur once data from previous design cycles is reused to improve the training for new problems.

Here is an example on how EMC design flow may be supported by ML tools in the near-future. The design task is as follows: A high-power EMC line filter requires design for sufficient filtering to ensure EMC compliance, adherence to thermal limits, size constraints and cost. For assessment of the EMC, a surrogate model pre-trained with data from previous design cycles and fine-tuned using some new data samples will be used to predict the EMC performance, e.g. the emissions over the whole frequency range of interest. Only few simulations will be needed to achieve sufficient accuracy of the prediction. Evaluations of the surrogate are fast which is important to speed up the global optimization task. Simultaneously, a classification algorithm will preemptively exclude all designs that will violate the thermal constants. Optimization of cost, mechanical integration and EMC will be driven by a multi-objective optimization e.g. based on BO. In addition to acquiring a global optimum, the design engineer will receive a sensitivity analysis which is inferred on the data generated during the optimization.

C. The Replacement Phase

Since more data will be generated and stored, the databases of available datasets will continue to grow. With widely available datasets and increasing trust and performance of ML tools, powerful models can be trained that generalize on past problems to provide consistent solutions for new design problems. Over time, ML-based tools may partially replace many conventional tools and overcome the reliance on PB

methods for many applications. This replacement phase will pave the way for a future where AI and ML may play a central role in the modeling and design for EMC.

PB-based simulations will be enhanced by physics-informed ML predictions for increased accuracy and speed. With growing databases, surrogate modeling and knowledge transfer will reduce the need for simulations speeding-up the design processes. The more powerful surrogate models trained on vast amounts of available data will allow the prediction of relevant outputs. For example, the radiation pattern of a device will be predicted in shorter times using available data and few new samples generated using AI accelerated simulations. Real-time EMC compliance prediction during the design phase will be possible with ML models trained on vast datasets of EMC test results and simulation data to enable rapid prototyping. The automated early recognition of failure patterns and the prediction of EMI hotspots during the design stages will reduce the need for design respins. Generative algorithms will enable the fast creation of optimized layouts, e.g., for PCBs, antennas and enclosures, to minimize EMI while maximizing the performances.

Taking the example of PCB design, AI assistants will be able to make fast design suggestions, see Fig. 11. Starting from defined design spaces or first designs, the ML tools will create surrogate models using data from available databases and a few simulations or measurements. Using the surrogate models, ML-tools will suggest trace routing, ground plane adjustments and suitable materials to minimize crosstalk and radiation. The placement of decoupling capacitors will be automated to optimize PDNs. Testing for EMC will be optimized by reducing the amount of probing needed by the generalization ability based on fewer measurements. The rise of large language models (LLMs) will allow AI assistants to be deployed and interacted with. The assistants will guide and help engineers find solutions for the modeling and design for increased efficiency and minimal interactions with programs. In addition, reports, testing evaluations and compliance reviews can be created automatically with minimal human interaction. The translation of natural language to various programming languages will help reduce the time spent on coding and creation of models. The retrieval of relevant information will be much faster to gather information on the newest regulations for example.

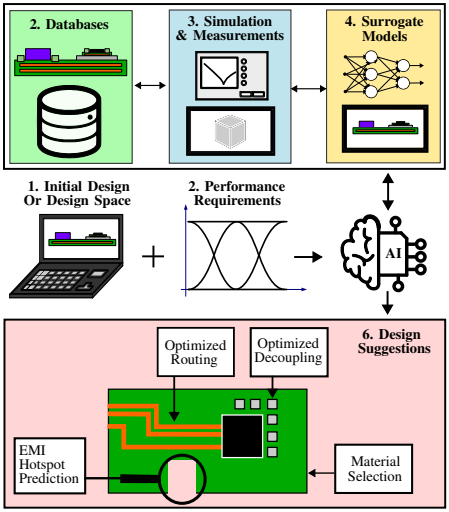

Fig. 11. The future of PCB design will involve AI assistants able to make fast design suggestions. Starting from defined design spaces or first designs, the ML tools will create surrogate models using data from available databases and a few simulations or measurements. Using the surrogate models, ML-tools will suggest trace routing, ground plane adjustments and suitable materials to minimize crosstalk and radiation. The placement of decoupling capacitors will be automated to optimize PDNs.

V. Recommendations

ML-based modeling and design involves the interplay between ML tools, data, data acquisition and engineers involved in the process, see Fig. 3. For the success and adoption of ML-based modeling and design as presented, these single components have to be developed and improved in the next years. A set of recommendations is proposed for each aspect in the following sections, summarized in Fig. 12.

A. Machine Learning Tools

With the surge of interest in the topic of ML, more performant and more varied tools have been developed recently. However, there are many drawbacks that need to be addressed either by the development of new tools or the adaptation of already existing tools. One issue is the lack of interpretability of the results and insight into the decision-making of the tools. From an engineering point of view, these aspects can be of interest to gain physical knowledge and improve the decision-making when facing design problems. Here, interpretable tools and algorithms should be investigated. Some ML tools can be coupled with data-driven algorithms to gain more insight e.g. feature importance.

Another issue is the ability to handle high-dimensional spaces. Thus, the problem of dimensionality should be a focus of future research. Since the relation between inputs and outputs is not straightforward, many models need fairly large amounts of data to generalize. Increasing the data-efficiency of the proposed algorithms and/or the ability of reusing data from previous problems should be pursued. These milestones can be reached by focusing on adapting ML tools and integrating them in frameworks based on domain knowledge. The research and development of ML tools can also be guided by more collaboration between engineers and data scientists to suit engineering needs.

B. Data Storage and Availability

The availability of high-quality and relevant datasets is very important to the development and investigation of ML tools for EMC. Additionally, data availability makes reusing previously generated datasets to optimize the learning process and reduce

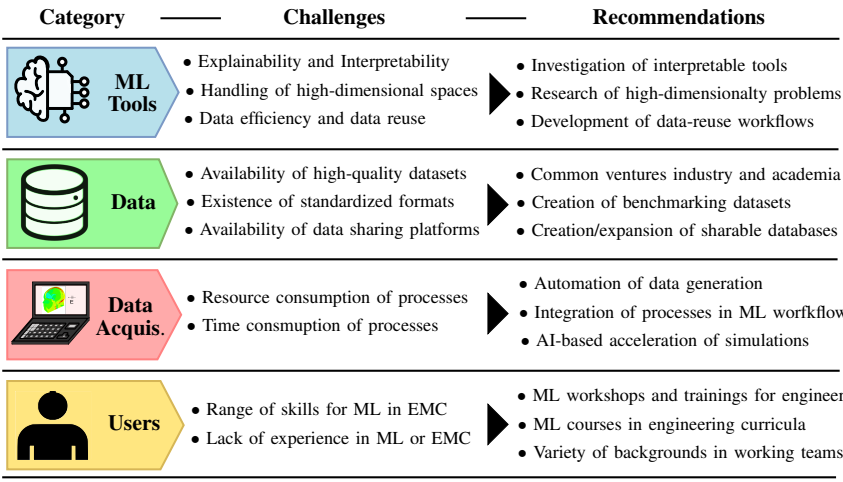

Fig. 12. A set of recommendations is provided to overcome the limitations and challenges facing a wider adoption of ML in EMC.

the need to generate new data possible. Access to high quality and relevant datasets is still a challenge. The open sharing of actual or even past design datasets is rare. Research groups are often limited by their data generation capabilities. The latter only widens the gap between industry and academia and actively creates a hindrance to research and development of ML solutions for EMC. Efforts must certainly be made to bridge the gap between industry and academia. Common ventures of industry partners and research groups for data sharing and problem-solving would be a big step towards a wide adoption of ML. Benchmarking datasets and scenarios reflecting real-life problems encountered in EMC should be made available.

The storage and management of data to be able to find, retrieve and use datasets in a meaningful way is a topic that needs to be addressed. Standards should be put in place for the preprocessing and formatting of the data for open sharing. The systematic data generation, preservation and open sharing, e.g., the SI/PI Database, is also a step forward to accelerate research in the field [56]. The SI/PI Database is a collection of PCB based structures which represent different electromagnetic aspects for signal integrity and power integrity applications. The datasets are accessible on https://www.tet.tuhh.de/en/si-pi-database.

C. Data Acquisition

Data acquisition encompasses all activities of collecting data for training and testing ML tools. More often than not, the processes of simulation and measurement are resource- and time-consuming. If the data generation is inefficient, the advantages of ML solutions will be overshadowed by the acquisition expense. It is thus imperative to find ways to increase the efficiency of these processes. Surrogate models, data-efficient tools and data reuse are capable of reducing the amount of samples that need to be generated.

However, for the successful ML-based modeling and design, the data acquisition processes need to be enhanced. One major way for a speed-up is the automation of simulation and measurement processes to reduce the need for human intervention and incurring time loss. Conventionally, data acquisition has been treated as a separate process where datasets are fully generated at the start of an ML workflow to then be processed and used for the training and testing. For the future, data acquisition should not be seen as a separate task, but an integrated task in automated workflows. These workflows should be based on intelligent sampling methods, e.g., active learning to gradually generate data samples as needed. This can be the automated simulation of determined samples or the measurement at given locations for maximum efficiency. A further solution is the use of ML-based accelerated co-simulations.

D. Engineers

The engineers behind the research and implementation of ML algorithms represent a vital resource. The skills demanded range from engineering domain-knowledge and expertise, foundations in data science, coding, ML-knowledge to creativity, communication and teamwork ability. There is noticeable increase in the experience of engineers in the application of ML tools. Many published works contain adapted and advanced algorithms that suit the type of problems faced.

However, more efforts and investments in the training of current and future engineers should be made. Developing specialized training programs that combine ML knowledge with domain-specific engineering skills is crucial. Universities and institutions should integrate ML courses into engineering curricula and offer certifications to ensure professionals stay up to date with evolving technologies. Cross-disciplinary collaboration between data scientists and engineers should be encouraged through collaborative projects, workshops and conferences. Working teams should cover a variety of backgrounds to foster knowledge exchange and accelerate the development of ML in EMC.

VI. Conclusion

EMC engineering can benefit greatly from ML. Recent publications show promising results in enhancing and speeding up the modeling and design processes, despite the simplified models, partial solutions and lack of resources e.g. relevant datasets. Helping factors for the recent progress are the improving computational capabilities and the growing experience of engineers in the adaptation of ML tools. Still, there is a long way to go to reach a wide adoption of ML in EMC. One of the major issues to be addressed are high-dimensional design spaces, data-efficiency and the generation, storage and availability of datasets. With the recent breakthroughs in some fields e.g. computer vision and language models, it is only natural to give ML the interest it deserves. The potential benefits warrant more focused research and investigations to the benefit of the EMC community at large.

References

[1] T. M. Mitchell, *Machine Learning*. New York, NY, USA: McGraw-Hill, 1997.

[2] R. Jhaveri, R. A., R. Kadiyala, R. Raut, and R. K. D, "A Review on Machine Learning Strategies for Real-World Engineering Applications," *Mobile Information Systems*, vol. 2022, pp. 1–26, 08 2022.

[3] L. Jiang, "Machine Learning for EMC/SI/PI Blackbox, Physics Recovery, and Decision Making," *IEEE Electromagnetic Compatibility Magazine*, vol. 12, no. 4, pp. 65–75, 2023.

[4] H. Esmaeili, C. Yang, and C. Schuster, "SAR Prediction in Human Head Tissues with Varying Material Parameters Using an Artificial Neural Network," in *Annual Conference of BioEM, Oxford, United Kingdom*, 2023.

[5] ——, "Physics inspired artificial neural network adaptation for sar prediction in bio-em problems," in *2023 IEEE MTT-S International Microwave Biomedical Conference (IMBioC)*, 2023, pp. 1–3.

[6] P. Hasgall, F. Di Gennaro, C. Baumgartner, E. Neufeld, B. Lloyd, M. Gosselin, D. Payne, A. Klingenböck, and N. Kuster, "IT'IS Database for thermal and electromagnetic parameters of biological tissues, Version 4.1," 2022. [Online]. Available: https://itis.swiss/virtual-population/tissue-properties/database/

[7] H. Esmaeili, C. Yang, and C. Schuster, "Efficient Iterative Data Generation Using Evaluation of Prioritized Input Parameters in ANNs for SAR Prediction in Human Head Models at 13.56 MHz," *IEEE Transactions on Electromagnetic Compatibility*, vol. 66, no. 6, pp. 1947–1957, 2024.

[8] "IEEE Standard for Safety Levels with Respect to Human Exposure to Electric, Magnetic, and Electromagnetic Fields, 0 Hz to 300 GHz," *IEEE Std C95.1-2019*, pp. 1–312, 2019.

[9] A. Kamo, T. Watanabe, and H. Asai, "An optimization method for placement of decoupling capacitors on printed circuit board," in *IEEE 9th Topical Meeting on Electrical Performance of Electronic Packaging (Cat. No.00TH8524)*, 2000, pp. 73–76.

[10] H. Park, J. Park, S. Kim, D. Lho, S. Park, G. Park, K. Cho, and J. Kim, "Reinforcement Learning-Based Optimal on-Board Decoupling Capacitor Design Method," in *2018 IEEE 27th Conference on Electrical Performance of Electronic Packaging and Systems (EPEPS)*, 2018, pp. 213–215.

[11] J. Y. Choi and M. Swaminathan, "Decoupling Capacitor Placement in Power Delivery Networks Using MFEM," *IEEE Transactions on Components, Packaging and Manufacturing Technology*, vol. 1, no. 10, pp. 1651–1661, 2011.

[12] C. M. Schierholz, K. Scharff, and C. Schuster, "Evaluation of neural networks to predict target impedance violations of power delivery networks," in *2019 IEEE 28th Conference on Electrical Performance of Electronic Packaging and Systems (EPEPS)*, 2019 IEEE 28th Conference on Electrical Performance of Electronic Packaging and Systems (EPEPS). Montreal, QC, Canada: IEEE, Oct. 2019, pp. 1–3.

[13] R. Rimolo-Donadio, X. Gu, Y. H. Kwark, M. B. Ritter, B. Archambeault, F. de Paulis, Y. Zhang, J. Fan, H.-D. Bruns, and C. Schuster, "Physics-Based Via and Trace Models for Efficient Link Simulation on Multilayer Structures Up to 40 GHz," *IEEE Transactions on Microwave Theory and Techniques*, vol. 57, no. 8, pp. 2072–2083, 2009.

[14] K. Patra, S. Cheruvalath, S. Dhar, B. P. Nayak, A. Gupta, and J. Hansen, "Surrogate modeling for predicting shielded cable emissions," *IEEE Transactions on Electromagnetic Compatibility*, vol. 65, no. 1, pp. 249–256, Feb. 2023.

[15] R. S. Rezende, J. Hansen, A. Piwonski, and R. Schuhmann, "Wideband kriging for multiobjective optimization of a high-voltage EMI filter," *IEEE Transactions on Electromagnetic Compatibility*, pp. 1–9, May 2024.

[16] A. Bingler, S. Bilicz, and M. Csornyei, "Polynomial chaos kriging metamodel for automotive EMC simulations," in *International Symposium on Electromagnetic Compatibility – EMC Europe*. Gothenburg, Sweden: IEEE, Sep. 2022.

[17] Y. Ping, Y. Zhang, and L. Jiang, "Uncertainty Quantification in PEEC Method: A Physics-Informed Neural Networks-Based Polynomial Chaos Expansion," *IEEE Transactions on Electromagnetic Compatibility*, vol. 66, no. 6, pp. 2095–2101, 2024.

[18] ——, "Uncertainty Quantification for PEEC Based on Wasserstein Generative Adversarial Network," *IEEE Transactions on Electromagnetic Compatibility*, vol. 66, no. 6, pp. 2048–2055, 2024.

[19] M. Gonzalez-Atienza, D. Vanoost, M. Verbeke, and D. Pissoort, "An Optimized Adaptive Bayesian Algorithm for Mitigating EMI-Induced Errors in Dynamic Electromagnetic Environments," *IEEE Transactions on Electromagnetic Compatibility*, vol. 66, no. 6, pp. 2085–2094, 2024.

[20] C.-P. Huang, Y.-H. Ma, Q. Q. Liu, W.-S. Zhao, B. You, X. Wang, C.-H. Yu, and D.-W. Wang, "PPO Algorithm-Assisted Design of Absorptive Common-Mode Suppression Filters," *IEEE Transactions on Electromagnetic Compatibility*, vol. 66, no. 6, pp. 2039–2047, 2024.

[21] R. S. Rezende, J. Hansen, A. Piwonski, and R. Schuhmann, "Wideband Kriging for Multiobjective Optimization of a High-Voltage EMI Filter," *IEEE Transactions on Electromagnetic Compatibility*, vol. 66, no. 4, pp. 1116–1124, 2024.

[22] R. Choupanzadeh and A. Zadehgol, "A Deep Neural Network Modeling Methodology for Efficient EMC Assessment of Shielding Enclosures Using MECA-Generated RCS Training Data," *IEEE Transactions on Electromagnetic Compatibility*, vol. 65, no. 6, pp. 1782–1792, 2023.

[23] T. Xu, Y. Chen, M. Zhao, Y. Wang, and X. Zhang, "Adaptive EMS Test Design Method on UAV Data Link Based on Bayesian Optimization," *IEEE Transactions on Electromagnetic Compatibility*, vol. 65, no. 3, pp. 716–724, 2023.

[24] P. Monferran, C. Guille-Escuret, C. Guiffaut, and A. Reineix, "Prediction of Lightning Currents on Fastening Assemblies of an Aircraft Fuel Tank With Machine Learning Methods," *IEEE Transactions on Electromagnetic Compatibility*, vol. 65, no. 3, pp. 812–822, 2023.

[25] M. Telescu, R. Trinchero, N. Soleimani, N. Tanguy, and I. S. Stievano, "Stochastic time-domain mapping for comprehensive uncertainty assessment in eye diagrams," *IEEE Transactions on Electromagnetic Compatibility*, vol. 65, no. 6, pp. 1930–1938, Dec 2023.

[26] K. Scharff, C. M. Schierholz, C. Yang, and C. Schuster, "ANN Performance for the Prediction of High-Speed Digital Interconnects over Multiple PCBs," in *2020 IEEE 29th Conference on Electrical Performance of Electronic Packaging and Systems (EPEPS)*, 2020, pp. 1–3.

[27] M. A. Dolatsara, J. A. Hejase, W. D. Becker, J. Kim, S. K. Lim, and M. Swaminathan, "Worst-case eye analysis of high-speed channels based on bayesian optimization," *IEEE Transactions on Electromagnetic Compatibility*, vol. 63, no. 1, pp. 246–258, Feb 2021.

[28] D. Shi, N. Sun, Y. Liu, C. Lian, X. Chen, X. Zhou, X. Liu, Q. Liu, and J. Zhou, "Fast Calculation Method for Crosstalk of High-Density Printed Circuit Board by Using Machine Learning," *IEEE Transactions on Electromagnetic Compatibility*, vol. 66, no. 3, pp. 971–982, 2024.

[29] F. Garbuglia, D. Spina, T. Reuschel, C. Schuster, D. Deschrijver, and T. Dhaene, "Modeling s-parameters of interconnects using periodic

gaussian process kernels," in *2023 IEEE 27th Workshop on Signal and Power Integrity (SPI)*, May 2023, pp. 1–4.
[30] M. A. Dolatsara, "Equalization optimization for serdes channels with constrained bayesian optimization," in *2022 IEEE International Symposium on Electromagnetic Compatibility and Signal/Power Integrity (EMCSI)*, Aug 2022, pp. 293–293.
[31] L. P. P. B. Bohl, K. Scharff, X. Duan, D. Kaller, and C. Schuster, "Bayesian Optimization of First-Order Continuous-Time Linear Equalization in High-Speed Links Including Crosstalk," in *2023 IEEE 27th Workshop on Signal and Power Integrity (SPI)*, 2023, pp. 1–4.
[32] Q. Chen, L. Zhang, H. Ma, D. Li, Y. Li, E.-X. Liu, and E.-P. Li, "Deep Neural Network-Based Surrogate-Assisted Inverse Optimization for High-Speed Interconnects," *IEEE Transactions on Electromagnetic Compatibility*, vol. 66, no. 6, pp. 2019–2026, 2024.
[33] E. Ecik, W. John, J. Withöft, R. Brüning, and J. Götze, "A Statistically Evaluated Decision Tree Approach for SI-Compliant PCB Design," in *2024 International Symposium on Electromagnetic Compatibility – EMC Europe*, 2024, pp. 140–145.
[34] J. Withöft, W. John, E. Ecik, and J. Götze, "AI-Based SI-Compliant PCB Design Support for DDR Technology Enhanced by Transfer Learning," in *2023 International Symposium on Electromagnetic Compatibility – EMC Europe*, 2023, pp. 1–6.
[35] J. Withöft, W. John, E. Ecik, R. Brüning, and J. Götze, "Machine Learning Methods for Elaborating the Feasible Region for Signal Integrity Analysis in Differential Pair PCB Structures," in *2024 International Symposium on Electromagnetic Compatibility – EMC Europe*, 2024, pp. 151–156.
[36] M. Schierholz, Y. Hassab, C. Yang, and C. Schuster, "Evaluation of Support Vector Machines for PCB based Power Delivery Network Classification," in *Proceedings IEEE 30th Conf. Electrical Performance Electronic Packag. and Systems EPEPS*, Austin, TX, USA, Oct. 2021.
[37] M. Schierholz, I. Erdin, J. Balachandran, and C. Schuster, "Data-Efficient Supervised Machine Learning Technique for Practical PCB Noise Decoupling," in *DesignCon 2023*, Santa Clara, CA, USA, Feb. 2023.
[38] L. Zhang, J. Juang, Z. Kiguradze, B. Pu, S. Jin, S. Wu, Z. Yang, J. Fan, and C. Hwang, "Fast impedance prediction for power distribution network using deep learning," *International Journal of Numerical Modelling: Electronic Networks, Devices and Fields*, vol. 35, no. 2, p. e2956, Oct. 2021. [Online]. Available: https://onlinelibrary.wiley.com/doi/abs/10.1002/jnm.2956
[39] Z. Nezhi, M. Stiemer, M. Schierholz, and C. Schuster, "Dimensional reduction by auto-encoders in machine learning based power integrity analysis," in *2024 IEEE 28th Workshop on Signal and Power Integrity (SPI)*. Lisbon, Portugal: IEEE, May 2024, pp. 1–4.
[40] I. Erdin and R. Achar, "Multi-objective optimization of decoupling capacitors for placement and component value," *IEEE Trans. on Compon., Packag. and Manuf. Technol.*, vol. 9, no. 10, pp. 1976–1983, Oct. 2019. [Online]. Available: https://doi.org/10.1109/tcpmt.2019.2930565
[41] Z. Xu, Z. Wang, C. Hwang, H. Delingette, and J. Fan, "Jitter-Aware Economic PDN Optimization With a Genetic Algorithm," *IEEE Transaction on Micro. Theory and Techn.*, vol. 69, no. 8, pp. 3715 – 3725, Aug. 2021. [Online]. Available: https://ieeexplore.ieee.org/document/9461629
[42] H. Park, J. Park, S. Kim, K. Cho, D. Lho, S. Jeong, S. Park, G. Park, B. Sim, S. Kim, Y. Kim, and J. Kim, "Deep reinforcement learning-based optimal decoupling capacitor design method for silicon interposer-based 2.5-d/3-d ICs," *IEEE Trans. on Compon., Packag. and Manuf. Technol.*, vol. 10, no. 3, pp. 467–478, Mar. 2020. [Online]. Available: https://doi.org/10.1109/tcpmt.2020.2972019
[43] X.-P. Zhou, D.-W. Wang, W.-S. Zhao, P. Zhang, and J.-H. Pan, "Modeling of Through-Silicon Capacitor and Its Applications for the Optimization of Power Distribution Network in 3-D Integrated Circuits," *IEEE Transactions on Signal and Power Integrity*, vol. 3, pp. 199–211, 2024.
[44] H. Vaghasiya, A. Jain, and J. N. Tripathi, "A Radial Basis Function Network-Based Surrogate-Assisted Swarm Intelligence Approach for Fast Optimization of Power Delivery Networks," *IEEE Transactions on Signal and Power Integrity*, vol. 1, pp. 140–149, 2022.
[45] J. Juang, L. Zhang, H. Manoharan, F. De Paulis, and C. Hwang, "Augmented Genetic Algorithm for Decoupling Capacitor Optimization in Power Distribution Network Design Through Improved Population Generation," *IEEE Transactions on Signal and Power Integrity*, vol. 3, pp. 186–198, 2024.
[46] E. A. Rashed, Y. Diao, and A. Hirata, "Learning-based estimation of dielectric properties and tissue density in head models for personalized radio-frequency dosimetry," *Physics in Medicine and Biology*, vol. 65, 2020.
[47] H. Esmaeili, C. Yang, and C. Schuster, "SAR Prediction for Human Head Models Considering Dependencies on Incident Angle of Exposure Using Parameter Prioritization in ANNs," in *2024 IEEE MTT-S International Microwave Biomedical Conference (IMBioC)*, 2024, pp. 152–154.
[48] C. Zheng, X. Chen, B. T. Nguyen, P. Sanpitak, J. Vu, U. Bagci, and L. Golestanirad, "Predicting RF Heating of Conductive Leads During Magnetic Resonance Imaging at 1.5 T: A Machine Learning Approach." *Annual International Conference of the IEEE Engineering in Medicine and Biology Society.*, p. 4204–4208, 2021.
[49] J. Vu, T. Nguyen, B. Bhusal, J. Baraboo, J. Rosenow, U. Bagci, G. Bright, and L. Golestanirad, "Machine learning-based prediction of MRI-induced power absorption in the tissue in patients with simplified deep brain stimulation lead models," *IEEE Trans on Electromagnetic Compatibility*, vol. 63, pp. 1757–1766, 2021.
[50] J. Chang, Q. Lan, R. Guo, J. Zheng, R. Romero, W. Kainz, S. A. Long, and J. Chen, "MRI RF-Induced Heating Prediction of Complex-Shaped Passive Implantable Medical Devices Using Mesh-Based Convolutional Neural Network," *IEEE Transactions on Microwave Theory and Techniques*, vol. 71, no. 5, pp. 2207–2214, 2023.
[51] L. Zhang, Y.-R. Feng, B. Pu, X.-D. Cai, D. Li, X.-C. Wei, B. Mutnury, J. Fan, H. Chen, J. L. Drewniak *et al.*, "A novel machine-learning-based batch selection method in sparse near-field scanning," *IEEE Transactions on Microwave Theory and Techniques*, vol. 70, no. 11, pp. 5019–5028, 2022.
[52] C. Bujard, E. Neufeld, M. Douglas, J. Wiart, and N. Kuster, "A gaussian process based approach for validation of multi-variable measurement systems: application to sar measurement systems," *IEEE Access*, 2024.
[53] J. Wen, X.-C. Wei, Y.-L. Zhang, and T.-H. Song, "Near-field prediction in complex environment based on phaseless scanned fields and machine learning," *IEEE Transactions on Electromagnetic Compatibility*, vol. 63, no. 2, pp. 571–579, 2020.
[54] Z. Gao, Y.-X. Liu, X.-C. Li, Z.-M. Wu, Z. Li, and T. Tan, "An equivalent radiation source reconstruction method based on enhanced artificial neural network," *IEEE Transactions on Electromagnetic Compatibility*, 2024.
[55] L. Zhang, Y. Xie, Y.-R. Feng, H. Ma, J. Guo, Y. Li, D. Li, and E.-P. Li, "Active-learning-based sparse near field scanning with time-domain current measurement for conductive coupling path visualization," *IEEE Transactions on Instrumentation and Measurement*, 2024.
[56] M. Schierholz, A. Sánchez-Masís, A. Carmona-Cruz, X. Duan, K. Roy, C. Yang, R. Rimolo-Donadio, and C. Schuster, "SI/PI-Database of PCB-Based Interconnects for Machine Learning Applications," *IEEE Access*, vol. 9, pp. 34 423–34 432, 2021.

Author Biographies

Youcef Hassab (Member, IEEE) was born in Oran, Algeria in 1994. He received the B.Sc. degree in General Engineering Sciences and the M.Sc. degree in Electrical Engineering with focus on high frequency, EMC and optics from the Technical University of Hamburg (TUHH), Hamburg, Germany in 2019 and 2022 respectively. His recent research focus is on radar digital signal processing, radar hand gesture recognition systems and applications of ML solutions in EMC, SI, PI and bioelectromagnetics. In November 2022, he joined the Institut für Theoretische Elektrotechnik (TET) at the TUHH to pursue a PhD degree. His thesis focuses on the application of ML and Bayesian optimization techniques for efficient EMC engineering.

Morten Schierholz (Member, IEEE) received the B.S. degree, in 2017, and the M.S. degree, in 2019, both in electrical engineering from the TUHH, Hamburg, Germany, where he is currently working toward the Ph.D. degree in analysis and decoupling of PCB-based PDNs using ML with the TET. He has authored and coauthored multiple articles with respect to ML investigations for SI and PI applications in IEEE conferences and Journals as Conference on Electrical Performance of Electronic Packaging and Systems (EPEPS) and Workshop on SI and PI (SPI). His research interests are the analysis of SI and PI of PCB-based interconnects with ML tools and techniques. Lately, he focused on the data efficient training of ML tools. Mr. Schierholz is the recipient of the DesignCon 2023 and DesignCon 2024 Early-Career Best Paper Award.

Lennart P.P.B. Bohl (Member, IEEE) received his B. Sc. in General Engineering Sciences with specialization in Electrical Engineering and his M. Sc. degree in Electrical Engineering with specialization in High Frequency Engineering, Optics and Electromagnetic Compatibility from the TUHH, Hamburg, Germany, in 2020 and 2023. During the years 2020 and 2021, Mr. Bohl worked as a student research assistant at the Institute for High-Frequency Technology at TUHH. In October 2023, he started working as a research assistant at the TET at TUHH. His current research interest focuses on electrical and thermal modeling and simulation for electric vehicle electromagnetic compatibility.

Hamideh Esmaeili (Member, IEEE) received the B.Sc. degree in electrical engineering-telecommunications from the Iran University of Science and Technology (IUST), Tehran, Iran, in 2013, and the M.Sc. degree in microwave engineering from the Amirkabir University of Technology (AUT-Tehran Polytechnic), Tehran, in 2017. She is currently working toward the Ph.D. degree with the TET, TUHH, Hamburg, Germany. Since 2016, she has been an RF and Microwave Engineer in various companies and research institutes, with experience in both active and passive microwave circuit and component design. Her research interests include EMC, BioEM, and the application of ML methods to those fields.

Til Hillebrecht (Member, IEEE) received his B. Sc. in General Engineering Sciences with specialization in Electrical/Systems Engineering and his M. Sc. degree in Electrical Engineering with specialization in High Frequency Engineering, Optics and EMC from TUHH, Hamburg, Germany, in 2019 and 2022. During the years 2019 and 2020, Mr. Hillebrecht worked as a working student at NXP Semiconductors in Hamburg, Germany. In October 2022, he started working as a research assistant at the TET at TUHH. He has authored papers in IEEE conferences Conference on Electrical Performance of Electronic Packaging and Systems (EPEPS) and Workshop on SI and PI (SPI). His current research interest focuses on the SI of printed circuit board-based interconnects. Mr. Hillebrecht received the Best Poster Paper Award at EPEPS 2023.

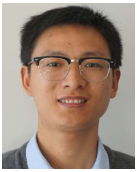

Cheng Yang (Senior Member, IEEE) received the B.S. degree in electronic science and technology from Wuhan University, Wuhan, China, in 2009, the M.S. and Ph.D. degrees in electromagnetic field and microwave technology from the National University of Defense Technology, Changsha, China, in 2012 and 2016, respectively. Since 2019, he has been a Senior Engineer with the TET, TUHH, Hamburg, Germany, where he was funded by the Chinese Scholarship Council as a joint-Ph.D. student, from 2013 to 2015. From 2017 to 2019, he was a Faculty Member of the State Key Laboratory of Millimeter Wave, Southeast University, Nanjing, China. His research interests include computational electromagnetics, microwave measurement techniques, EMC, and biology electromagnetics.

Jan Severin Hessling (Student Member, IEEE) received his B.S. degree in electrical engineering and his M. Sc. degree in Electrical Engineering with specialization in High Frequency Engineering, Optics and Electromagnetic Compatibility from the TUHH, Hamburg, Germany, in 2022 and 2025, respectively. In his Master's thesis, he investigated the application of autoencoders for the modeling of PDNs. He is currently working toward the Ph.D. degree with the TET, working on ML tools in the context of PCB and PDN design. His research interests include the application of transformer architectures and LLMs in electronic designs and the establishment of ML workflows for the design of PI compliant PCBs.

Christian Schuster (Fellow, IEEE) (S'98 - M'00 - SM'05) received the Diploma degree in physics from the University of Konstanz, Germany, in 1996, and the Ph. D. degree in electrical engineering from the Swiss Federal Institute of Technology (ETH), Zurich, Switzerland, in 2000. Since 2006 he is full professor and head of the TET at the TUHH, Germany. Prior to that he was with the IBM T. J. Watson Research Center, Yorktown Heights, NY, where he was involved in high-speed optoelectronic package and backplane interconnect modeling and signal integrity design for new server generations. His currents interests include signal and power integrity of digital systems, multiport measurement and calibration techniques, and development of electromagnetic simulation methods for communication electronics. Dr. Schuster received IEEE Transactions on EMC Paper Awards in 2002 and 2015, IEEE Transactions on CPMT Paper Awards in 2012 and 2016, DesignCon Paper Awards in 2006, 2010, 2017 and 2018, three IBM Research Division Awards between 2003 and 2005, and IBM Faculty Awards in 2009 and 2010. Also, in 2019 he received the Sustained Service to the EMC Society Award. He is a member of the German Physical Society (DPG) and several technical program committees of international conferences on signal and power integrity, and electromagnetic compatibility. He was serving as a Distinguished Lecturer for the IEEE EMC Society in the period 2012-2013, as the Chair of the German IEEE EMC Chapter in the period 2016-2019, as a member of the Board of Directors of the EMC Society in 2015 and in the period 2020-2022, and as an Associate Editor for the IEEE Transactions on EMC in the period 2019-2024. From April 2020 to March 2025 he was an Adjunct Associate Professor at the School of Electrical and Computer Engineering of the Georgia Institute of Technology, Atlanta, USA. Since February 2025 he is the President of the Northern Institute of Technology Management (NIT) at TUHH.

Publication 2 (P2)

Title

Data-Efficient Prediction of the Specific Absorption Rate in a Human Head Model Exposed to a Plane EM Wave Using Gaussian Process Regression.

Publication Status

Published in peer-reviewed conference proceedings: Proceedings of 2024 International Symposium on Electromagnetic Compatibility - EMC Europe, Brugge, Belgium.

Author Contribution

Predominant involvement as a 1. author (co-author confirmation provided).

Bibliographic Information

[69] Y. Hassab, H. Esmaeili and C. Schuster, "Data-Efficient Prediction of the Specific Absorption Rate in a Human Head Model Exposed to a Plane EM Wave Using Gaussian Process Regression," in *2024 International Symposium on Electromagnetic Compatibility - EMC Europe*, Brugge, Belgium, Sep. 2024.

Copyright Notice

Data-Efficient Prediction of the Specific Absorption Rate in a Human Head Model Exposed to a Plane EM Wave Using Gaussian Process Regression

Youcef Hassab[1], Hamideh Esmaeili[2], Christian Schuster[3]
Institut für Theoretische Elektrotechnik,
Hamburg University of Technology (TUHH),
Hamburg, Germany.
{[1]youcef.hassab, [2]hamideh.esmaeili, [3]schuster}@tuhh.de

***Abstract*— In this contribution, the specific absorption rate (SAR) in a human head model exposed to a 13.56 MHz external electromagnetic (EM) wave is predicted using Gaussian process regression (GPR). The electrical properties of the tissues are varied around the nominal values by $\pm 20\%$ to account for material uncertainties. The GPR model achieves an $\mathbf{R^2}$ regression score higher than 0.99. The maximum and the worst-case exposure over the variation space are found using a tenth of the samples needed by random sampling on average. This allows the fast comparison against standards with a high degree of confidence. A sensitivity analysis of the exposure is extracted from the GPR model to provide an insight into the effects of the different parameter variations. The proposed framework is applicable to radiated susceptibility scenarios and beyond.**

***Keywords*— Gaussian process regression, human head model, specific absorption rate, EM simulations, machine learning, wireless power transfer.**

I. Introduction

The integration of electromagnetic compatibility (EMC) analysis at the early stages of the design process is crucial for ensuring reliable operation complying with standards. Susceptibility to radiated emissions has emerged as a standard challenge in EMC. In the typical case, electromagnetic (EM) radiation emanating from an aggressor penetrates a victim system leading to induced EM fields that may cause interference, see Fig. 1 (a). These systems are often complex and composed of many subcomponents where the internal coupling mechanisms and effects are hard to retrace. EM simulations play a key role in addressing the concerns.

In recent years, there has been a surge in interest surrounding brain implants as an avenue for addressing several disorders. Many implants designs are subject to external modules using wireless power transfer (WPT) and near-field communication (NFC) for power and communication purposes. The external systems are designed with safety measures in mind and need to be aligned with established standards [1], [2]. More specifically, the EM fields associated with the external devices necessitate a comparison of the exposure levels in human head tissues against established safety standards. The average specific absorption rate (SAR) is a typical measure to assess exposure levels in biological tissues. A typical limit for uncontrolled exposure amounts to $1.6\,\mathrm{W/kg}$.

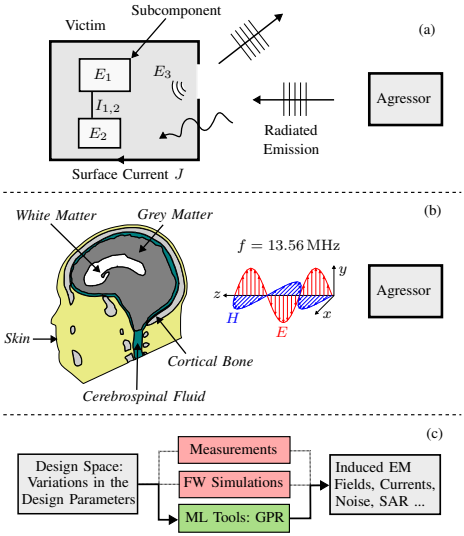

Fig. 1. Illustration of the studied problem: (a) In the typical radiated susceptibility scenario, an external EM wave may result in electric fields E_1, E_2, E_3, currents $I_{1,2}$ in and between the subcomponents of a victim system that are hard to retrace, especially with varying design parameters. (b) The case presented in this paper is a human head model with varying electrical properties of the tissues exposed to a plane EM wave. (c) GPR is applied to predict the resulting SAR in the tissues as a function of the variations in the electrical properties to replace expensive full-wave solver simulations.

Full-wave simulation of the fields in complex human head models with variations in the electrical properties of multiple tissues represents a numerical challenge [3]. The electrical properties are subject to uncertainties and vary depending on many factors, like age or size. These properties affect the field distributions and SAR. Depending on the head model complexity, a single simulation takes up from few minutes to few days on commercial PCs on average. Here, ML tools such

979-8-3503-0735-1/24/$31.00 ©2024 IEEE

as artificial neural networks (ANNs) have been successfully used for the prediction of SAR levels in human head tissues to replace EM simulations [4]–[6]. One drawback of using ML-based approaches is the need of large volume of samples for the training of the models. Gaussian process regression (GPR) is an ML-based regression algorithm. In comparison to other surrogate modeling techniques, e.g. Polynomial Chaos Expansion, it has the ability to provide uncertainty measurements on the predictions [7], [8]. This advantage allows an easy integration in active learning loops to increase the data efficiency [9].

In this work, GPR is used for the prediction of the SAR inside a human head model to reduce the number of simulations needed. The human head model includes variations of the permittivity and the conductivity in 5 different tissues. The head model is exposed to an external EM plane wave normal to the coronal plane (XY) with a frequency of $13.56\,\mathrm{MHz}$, typical for WPT and NFC systems, see Fig. 1 (b) and (c). This exposure is a simplified preliminary study case of the more complex scenario where the head model is exposed to near-fields from an external module feeding a brain implant.

The rest of the paper is structured as follows: In Section II, the simulation setup and human head model for the data generation are presented. In Section III, a brief theoretical background on GPR is presented. In Section IV, GPR is implemented for the prediction of the SAR. In Section V, the work is summarized and an outlook on future work is given.

II. Simulation Setup of Head Model Exposure

To assess the extent of exposure to EM fields in biological tissues, the SAR serves as a commonly used measure. The SAR quantifies the absorbed power per unit of mass and is directly related to field distributions and material properties. In case of plane wave exposure, many mechanisms have an influence on the distribution of fields within the tissues of a human head. Higher frequencies tend to be absorbed more superficially, while lower frequencies can penetrate deeper. Some portion of the incident wave may be reflected and refracted at tissue interfaces. The electrical properties of the tissues play thus an important role, these include the tissues' conductivity (κ_t) and permittivity (ε_t). These properties vary from subject to subject and present uncertainties that depend on many factors, like age or size [10]. The studied case involves a reduced realistic model from the Visible Human Project® (VHP) model [11]. This model contains variations to the electrical properties of five tissues, see Fig. 1 (b). Although the permittivity and conductivity exhibit a degree of correlation, the two properties are assumed to be independent for the data collection [12]. This way, the data-driven tools are investigated for cases where the correlation between inputs is not easily identifiable using physical knowledge. The tissue properties are independently varied in the $\pm 20\%$ range from the nominal values provided by the IT'IS database [13]. A uniform distribution is adopted for each property. The complete variation space and related tissues are listed in Table 1. A plane wave is radiated at the back of the head model

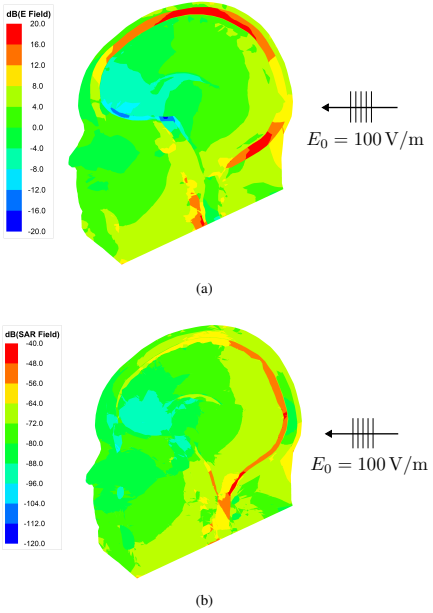

Fig. 2. The electric field and SAR distributions inside the tissues of the VHP human head model exposed to a plane wave are dependent on the electric parameters of the tissues. For a single sample from the variation space, the intensity of the (a) electric field and the (b) local SAR over the tissues of the head model are plotted in dB with reference levels $E = 1\,\mathrm{V/m}$ and $SAR = 1\,\mathrm{W/kg}$, respectively.

normal to the coronal plane with an electric field amplitude of $E_0 = 100\,\mathrm{V/m}$. A finite element method (FEM) full-wave solver is used for the simulation of the fields inside the human head model [14]. The resulting field distributions are then used to estimate the amount of power absorbed. The local SAR is calculated using the local electric field E, conductivity κ_t and mass density ρ_t [15]:

$$SAR(x,y,z) = \frac{\kappa_t |E(x,y,z)|^2}{\rho_t}. \tag{1}$$

The electric field distribution and resulting local SAR varies depending on the position, see Fig. 2. The local SAR tendentially fades from the back to the front of the head model as more energy is absorbed from the penetrating wave directed at the back of the head. A higher concentration is observed along the *Cerebrospinal Fluid* because of the much higher conductivity of the tissue. The average SAR in a tissue is calculated by integrating and averaging the local SAR over the volume V_t of a single tissue:

$$SAR_a = \frac{1}{V_t} \iiint SAR(x,y,z) \cdot dxdydz. \tag{2}$$

Table 1. FOR EACH TISSUE OF THE HUMAN HEAD MODEL, THE SAR RANGE AND THE VARIATION SPACE OF THE ELECTRICAL PROPERTIES ARE GIVEN. THE ELECTRICAL PROPERTIES ARE VARIED BY $\pm 20\%$ AROUND THE NOMINAL VALUES, WHERE ε_0 REPRESENTS THE PERMITTIVITY OF FREE SPACE.

Tissue	Average SAR (Output)		Variation Space (Input)				Index
	Min.	Max.	Electrical Property	Min.	Nominal	Max.	
Cortical Bone (CB)	$0.163\,\mathrm{mW/kg}$	$0.201\,\mathrm{mW/kg}$	*Conductivity* (κ_t)	$0.036\,\mathrm{S/m}$	$0.046\,\mathrm{S/m}$	$0.055\,\mathrm{S/m}$	1
			Permittivity (ε_t)	$24.478 \cdot \varepsilon_0$	$30.575 \cdot \varepsilon_0$	$36.679 \cdot \varepsilon_0$	2
Grey Matter (GM)	$0.173\,\mathrm{mW/kg}$	$0.241\,\mathrm{mW/kg}$	*Conductivity* (κ_t)	$0.262\,\mathrm{S/m}$	$0.327\,\mathrm{S/m}$	$0.393\,\mathrm{S/m}$	3
			Permittivity (ε_t)	$210.948 \cdot \varepsilon_0$	$263.384 \cdot \varepsilon_0$	$315.226 \cdot \varepsilon_0$	4
White Matter (WM)	$0.103\,\mathrm{mW/kg}$	$0.160\,\mathrm{mW/kg}$	*Conductivity* (κ_t)	$0.141\,\mathrm{S/m}$	$0.176\,\mathrm{S/m}$	$0.211\,\mathrm{S/m}$	5
			Permittivity (ε_t)	$122.853 \cdot \varepsilon_0$	$153.118 \cdot \varepsilon_0$	$183.738 \cdot \varepsilon_0$	6
Cerebrospinal Fluid (CF)	$1.381\,\mathrm{mW/kg}$	$1.894\,\mathrm{mW/kg}$	*Conductivity* (κ_t)	$1.611\,\mathrm{S/m}$	$2.004\,\mathrm{S/m}$	$2.405\,\mathrm{S/m}$	7
			Permittivity (ε_t)	$86.612 \cdot \varepsilon_0$	$108.263 \cdot \varepsilon_0$	$129.903 \cdot \varepsilon_0$	8
Skin (SK)	$0.201\,\mathrm{mW/kg}$	$0.277\,\mathrm{mW/kg}$	*Conductivity* (κ_t)	$0.191\,\mathrm{S/m}$	$0.238\,\mathrm{S/m}$	$0.285\,\mathrm{S/m}$	9
			Permittivity (ε_t)	$228.395 \cdot \varepsilon_0$	$285.246 \cdot \varepsilon_0$	$342.254 \cdot \varepsilon_0$	10

An automatic script calculates the SAR_a inside each tissue depending on the electrical property variations. To cover the variation space represented in Table 1, $n = 500$ data samples are generated using an latin hypercube sampling (LHS). A single full-wave simulation takes approximately 32 minutes on average on a computer equipped with a 3.7 GHz processor and 4 CPU cores. The total duration of the simulations adds up to more than 11 days. The 500 generated samples serve as the main dataset from which training samples are iteratively selected by the ML models. The 10 input dimensions are the conductivity and permittivity inside each tissue indexed in Table 1, while the 5 outputs of interest are the average SAR values inside each tissue.

III. THEORETICAL BACKGROUND ON GAUSSIAN PROCESS REGRESSION AND ACTIVE LEARNING LOOPS

GPR is a probabilistic approach to regression in which an unknown target function f is approximated by implementing a Gaussian process (GP) on a given dataset of inputs and outputs $D_t = (X_t, Y_t) = [(x_1, y_1), \cdots, (x_t, y_t)]$ [7]. This method establishes a distribution over the potential functions that could fit the provided data. To represent a distribution over a function, a distribution over the function's values at a set of points, say $f(x_1), f(x_2), \cdots f(x_t)$, is constructed. A GP assumes that any set of function values follows a joint multivariate Gaussian distribution characterized by a mean and covariance matrix:

$$f(x) \sim GP(\mu(X_t), K(X_t, X_t)) \tag{3}$$

here, $\mu(X_t)$ represents the mean function and $K(X_t, X_t)$ represents the covariance matrix whose elements are determined by a chosen kernel to impose constraints on possible function types. A commonly used kernel for EMC problems is the Matérn $5/2$ function. It is given for a pair of inputs x_i and x_j:

$$k_{\text{Matérn}}(x_i, x_j) = \left(1 + \frac{\sqrt{5}d}{\theta_l} + \frac{5d^2}{3\theta_l^2}\right) \exp\left(-\frac{\sqrt{5}d}{\theta_l}\right) \tag{4}$$

where d is the euclidean distance between the pair of inputs and θ_l the length-scale hyperparameter. This kernel has the properties of smoothness, continuity and distance-based covariance: closer points in the input space result in more correlated outputs. The hyperparameters θ of the kernel are optimized using the presented inputs to learn the patterns in the data. Since the function values are considered jointly Gaussian, the probability distribution of a function's value $y^* = f(x^*)$ at an unknown test point x^* can be obtained from the known values $Y_t = f(x_1), f(x_2), \cdots f(x_t)$ through conditioning. The results of this operation yield a mean and variance [7]:

$$\mu_\theta(x^*) = K(x^*, X_t)K^{-1}(X_t, X_t)Y_t \tag{5}$$

$$\sigma_\theta^2(x^*) = k^* - K(x^*, X_t)K^{-1}(X_t, X_t)K(X_t, x^*) \tag{6}$$

where the mean $\mu_\theta(x)$ and the variance $\sigma_\theta^2(x)$ of the trained GP represents the predicted function that fits the available data and the uncertainty in the predictions, respectively. The approximation of an example 1D target function through GPR is illustrated, see Fig. 3. A 99% confidence interval is computed using the resulting variances and the Z-score [16].

Active learning is a subset of semi-supervised machine learning. The algorithms iteratively select data points for labeling to maximize information gain while minimizing the number of labeled samples required for effective training [9]. GPR can be embedded in active learning or optimization loops to quickly find the maximum or reduce the uncertainty in the models, see Fig. 4. The predictions of the GPR on the samples of the variation spaces are used by an acquisition function to choose the next point to sample. The chosen point is labeled and added to the pool of available training data. The GPR model is retrained each iteration for better predictions. For the choice of points to sample for maximizing the knowledge about the unknown function, many acquisition functions can be chosen depending on the objective. Typical functions are i.a. maximum variance (MV), probability of improvement (PoI), expected improvement (EI) and upper confidence bound (UCB) [17]. The MV function chooses the

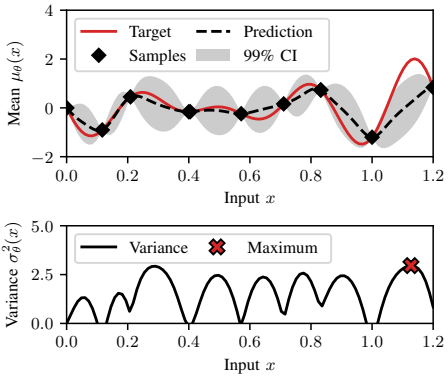

Fig. 3. In this 1D illustrative example, Gaussian process regression (GPR) is employed to approximate a target function. The mean function is predicted based on the training samples marked on the target function. The resulting variance provides insights into the uncertainty inherent in the GPR predictions, also reflected by the confidence interval (CI). The yellow cross denotes the point of maximum uncertainty in the model. As a test point deviates further from the training samples, the model expresses reduced confidence.

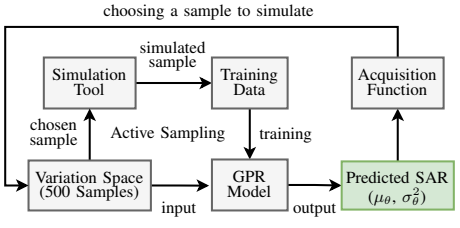

Fig. 4. A diagram of a data-efficient ML approach for SAR prediction is shown. A single data point is chosen from the variation space each iteration, simulated and added to the training dataset. The acquisition function uses the GPR predictions to choose the next point with the most information content to simulate. The GPR model is trained on all simulated training data to make predictions of the SAR over the variation space.

point with the maximal variance to sample, see Fig. 3. This allows a systematic reduction in the uncertainty and reliable predictions over the variation space. For quickly finding the maximum, the other acquisition functions, e.g. UCB, are more suitable.

IV. Data-Driven SAR Prediction Using GPR

In this section, the ML-based prediction of SAR in the tissues of the human head model is presented. The average SAR is predicted in the different tissues using separate GPR models. The maximum SAR over the variation space and the 5 tissues is tracked and the worst-case scenario identified.

Table 2. Performance evaluation of the trained models in the prediction of the average SAR in each tissue. The R^2 scores are given for each model for a training size of 10, 20, 50 and 100.

Tissue	R^2			
	10 samples	20 samples	50 samples	100 samples
CB	0.008	0.950	0.990	0.995
GM	0.002	0.956	0.995	0.996
WM	0.007	0.955	0.994	0.997
CF	0.023	0.958	0.983	0.996
SK	0.454	0.957	0.993	0.991

A. Prediction of the average SAR in tissues

GPR is implemented within an active learning loop for the prediction of the SAR_a defined in Section II inside the tissues of the head model. Finding the maximum SAR value in the tissues over the variation space with a minimal amount of iterations is the second objective. To combine these two objectives, The MV acquisition function, that aims at reducing the uncertainty over the variation space, is alternated with one of the three remaining acquisition functions PoI, EI and UCB each iteration. The parameters of the GP are optimized using a fully Bayesian approach by slice sampling [17]. The 10 input dimensions of the model are the conductivity and permittivity of each tissue, see Table 1. The average SAR in the different tissues represents the outputs to be predicted. A separate GPR model is trained and evaluated for each tissue. The training is stopped after a maximal number of 100 iterations. The accuracy is evaluated using the R^2 regression score (coefficient of determination):

$$R^2 = 1 - \frac{\sum_{i=1}^{n}(y_i - \hat{y}_i)^2}{\sum_{i=1}^{n}(y_i - \bar{y})^2} \tag{7}$$

where $\hat{y}_i$ and y_i are the predicted and true outputs, respectively, $\bar{y}$ the mean of true values and n the number of samples. The R^2 is calculated at each iteration for each tissue. The results of the evaluation show an R^2 higher than 0.99 for all tissues at the end of the training process. Starting from 20 training samples, the models achieve an accuracy score of at least $R^2 = 0.95$, see Table 2. For 50 randomly chosen sample points in the variation space, the predicted SAR in each tissue using 20 training samples is compared with the simulations, see Fig. 5. The predicted values fit the data from the simulations.

B. Tracking of the maximum SAR in tissues

The maximum SAR exposure in the human head model over the variation space is identified during the training iterations. The SAR in each tissue is dependent on the variation of the electric properties. For a single variation (sample), the highest SAR of the 5 different values in each tissue is pooled as the output. The global maximum SAR represents then the highest value over the 500 samples of the variation space. At the 17 iterations mark, the maximum SAR over the 500 samples is found by the GPR embedded in the active learning loop, see Fig. 6.

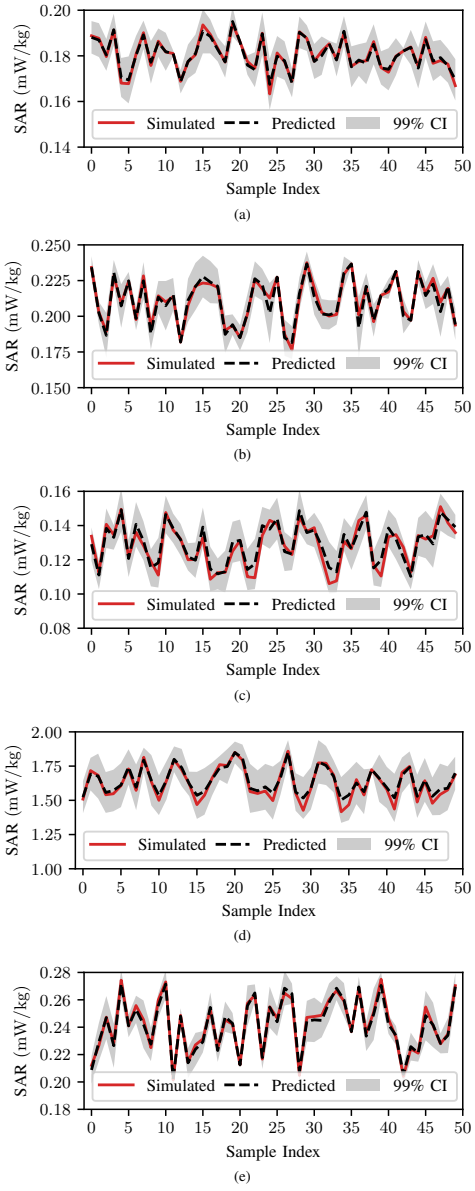

Fig. 5. The predicted average SAR values by the trained GPR models inside the tissues (a) Cortical Bone, (b) Grey Matter, (c) White Matter, (d) Cerebrospinal Fluid and (e) Skin are compared with the simulated values for 50 randomly chosen points of the variation space. 20 samples are used for the training of each model. The 99% confidence interval (CI) around the predicted values reflects the uncertainty of the trained models.

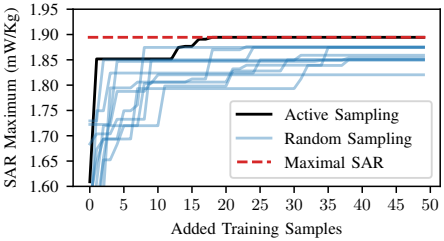

Fig. 6. The SAR maximum found through the active sampling of the GPR is compared with a random sampling approach in 10 different runs. The maximum is found after 17 iterations of the GPR. Finding the maximum using a random sampling takes 250 iterations on average.

A random sampling over the variation space would take significantly longer to find the maximum, 250 iterations on average for the 500 sample points available. Using the active sampling method coupled with the GPR results in an average reduction of the number of needed simulations to find the maximum SAR by a factor of 10.

The worst-case scenario can be calculated using the confidence interval of the model. It is equal to the maximum value of the predictions added to the 99% confidence interval over the variation space. The worst-case resulting from the trained model is equal to an SAR of approximately $1.958\,\mathrm{mW/kg}$ and $1.896\,\mathrm{mW/kg}$ after 20 and 100 iterations, respectively. Both values are higher than the variation space maximum equal to $1.894\,\mathrm{mW/kg}$. This shows that the uncertainty estimations of the trained GPR model are reliable.

C. *Sensitivity analysis of the SAR predictions*

The length-scale parameters of the kernel for each input dimension are learned by the GPR during the training process using the training inputs and outputs. A smaller length-scale of the chosen kernel indicates that the model is sensitive to localized changes in the specific dimension, in other words, the kernel is sensitive to small variations in the input feature. A larger length-scale value indicates that the model is influenced by more global trends and shows less sensitivity to local changes in the specific input dimension. The length-scale parameters can thus be used to quantify the importance of each input variable for the predictions of the GPR model. The importance of each input feature is calculated using the inverse of the length-scales θ_l in eq. (4), resulting in dimensional weights. A smaller length-scale for a specific input dimension results in a larger dimensional weight and reflects more output sensitivity. The dimensional weights allow thus the estimation of the relative feature importance for the output.

The resulting dimensional weights extracted from the trained model are given, see Fig. 7. The variation in the conductivities of the different tissues has more impact on the resulting SAR values than the variation in the permittivities of the tissues. This is an expected behavior for the SAR

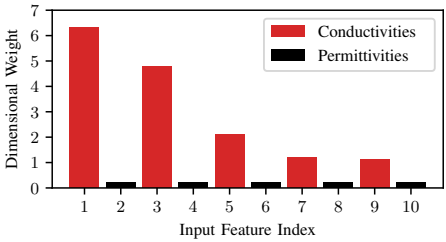

Fig. 7. The Sensitivity of the output (SAR) to variations in the input parameters is calculated using the length-scales of the GP kernel. The conductivities of the tissues show more impact on the SAR than permittivities.

as the conductivity directly impacts the heat losses and the absorbed power, see eq. (1). For the frequency of 13.56 MHz, the polarization losses are negligible, hence a much lower dependency of the SAR on the permittivities is observed.

D. Discussion of results

The GPR models embedded in active learning loops generalize well on the training data providing accurate predictions. Starting from 20 samples labeled through simulations, the prediction accuracy amounts to more than $R^2 = 0.95$ in all tissues. The prediction of SAR values in the tissues using the trained models takes a couple of milliseconds instead of the 32 minutes required on average using full-wave simulations. The predictions for all points of the variation space fall within the 99% confidence intervals calculated using the variances of the models. This shows the reliability of the uncertainty estimations of the models.

Through the active sampling, the global SAR maximum over the variation space is found in less than 20 iterations. This represents a speed-up of factor 10 in comparison to random sampling. The worst-case exposure estimation includes the uncertainty of the model to give an accurate estimate of this critical metric. Since the variances provided by the models decrease after each iteration, the estimation of the maximum exposure level is more accurate as the models are more confident in the solution with more training data available. The maximal variance through the iterations can be used for an early stopping of the active learning loop when a defined confidence in the solution is reached. Using the kernel weights of GPR model, an outlook on the importance of input features to the exposure level is extracted. The results are consistent with the physics of the problem at hand.

V. Conclusion

The generalization ability and fast predictions of the GPR model show potential in reducing the computational overhead of full-wave simulations and speeding-up the investigation of EMC problems. The integrated uncertainty estimations allow the identification of the worst-case exposure within defined confidence intervals without the need of a dense sampling over the design space. This allows i.a. the fast comparison with standards before the production stages. The gradual collection of training data with an early stopping of the loop when a defined confidence is reached solves the problem of determining the amount of needed training samples a priori, e.g. for ANNs training. The sensitivity analysis is provided with no additional computational effort to identify the important design parameters that affect the exposure levels. Future work involves the consideration of more complex scenarios towards a general framework for data-driven investigation of EMC problems.

References

[1] X. L. Chen et al. “Human Exposure to Close-Range Resonant Wireless Power Transfer Systems as a Function of Design Parameters”, in *IEEE Trans. Electromagn. Compat.*, vol. 56, no. 5, pp. 1027-1034, Mar. 2014.

[2] W. H. Bailey et al. “Synopsis of IEEE Std C95.1™-2019 “IEEE Standard for Safety Levels With Respect to Human Exposure to Electric, Magnetic, and Electromagnetic Fields, 0 Hz to 300 GHz””, in *IEEE Access*, vol. 7, pp. 171346-171356, Nov. 2019.

[3] H. Esmaeili, C. Yang, and C. Schuster, “Flexible Numerical Evaluation of Human Head Exposure to a Transmitter Coil for Wireless Power Transfer at 13.56MHz,” in *2022 International Symposium on Electromagnetic Compatibility – EMC Europe*, Gothenburg, Sweden, Sep. 2022.

[4] H. Esmaeili C. Yang. and C. Schuster, “SAR Prediction in Human Head Tissues with Varying Material Parameters Using an Artificial Neural Network”, in *Annual Conference of BioEM*, Oxford, UK, Jun. 2023.

[5] H. Esmaeili, C. Yang, and C. Schuster, “Physics Inspired Artificial Neural Network Adaptation for SAR Prediction in Bio-EM Problems,” in *2023 IEEE MTT-S Int. Microw. Biomed. Conf. (IMBioC)*, Leuven, Belgium, Sep. 2023.

[6] J. Vu et al. “Machine Learning-Based Prediction of MRI-Induced Power Absorption in the Tissue in Patients with Simplified Deep Brain Stimulation Lead Models”, in *IEEE Trans on Electromagnetic Compatibility*, vol. 63, no. 5, pp. 1757-1766, Sep. 2021.

[7] C. E. Rasmussen and C. K. I. Williams, *Gaussian Processes for Machine Learning*. London, England: MIT Press, 2005.

[8] C. Schmidt, P. Grant, M. Lowery and U. van Rienen, "Influence of Uncertainties in the Material Properties of Brain Tissue on the Probabilistic Volume of Tissue Activated," in IEEE Transactions on Biomedical Engineering, vol. 60, no. 5, pp. 1378-1387, May 2013.

[9] B. Settles, “Active Learning Literature Survey,” University of Wisconsin–Madison, Computer Sciences Technical Report 1648, 2009.

[10] C. Gabriel and A. Peyman, “Dielectric Measurement: Error Analysis and Assessment of Uncertainty”, in *Physics in Medicine and Biology*, vol. 51, no. 3, pp. 6033-6046, Oct. 2006.

[11] S. N. Makarov et al. “Virtual Human Models for Electromagnetic Studies and Their Applications”, in *IEEE Reviews in Biomedical Engineering*, vol. 10, pp. 95-121, Jun. 2017.

[12] H. P. Schwan and K. R. Foster, "RF-field interactions with biological systems: Electrical properties and biophysical mechanisms," in *Proceedings of the IEEE*, vol. 68, no. 1, pp. 104-113, Jan. 1980.

[13] P. Hasgall et al. “IT’IS Database for Thermal and Electromagnetic Parameters of Biological Tissues, Version 4.1,” Feb. 2022. [Online]. Available: https://itis.swiss/virtual-population/tissue-properties/database/

[14] High-Frequency Structure Simulator, Electromagnetics Suite 2021. ANSYS, Inc. Pennsylvania, USA. [Online]. Available: www.ansys.com/

[15] “IEEE Standard for Safety Levels with Respect to Human Exposure to Electric, Magnetic, and Electromagnetic Fields, 0 Hz to 300 GHz,” *IEEE Std C95.1-2019*, pp. 1-312, Oct. 2019.

[16] D. S. Moore, G. P. McCabe, and B. A. Craig, *Introduction to the Practice of Statistics*, 8th edition, W. H. Freeman, NY, USA, 2013.

[17] H. M. Torun, J. A. Hejase, J. Tang, W. D. Beckert, and M. Swaminathan, “Bayesian Active Learning for Uncertainty Quantification of High Speed Channel Signaling,” in *2018 IEEE 27th Conf. Electr. Perform. Electron. Packag. Syst. (EPEPS)*, San Jose, CA, USA, 2018.

Publication 3 (P3)

Title

Application of Gaussian Process Regression for Data Efficient Prediction of PCB-Based Power Delivery Network Impedance Features.

Publication Status

Published in peer-reviewed conference proceedings: Proceedings of 2024 IEEE 28th Workshop on Signal and Power Integrity (SPI), Lisbon, Portugal.

Author Contribution

Predominant involvement as a 1. author (co-author confirmation provided).

Bibliographic Information

[68] Y. Hassab, M. Schierholz and C. Schuster, "Application of Gaussian Process Regression for Data Efficient Prediction of PCB-Based Power Delivery Network Impedance Features," in *2024 IEEE 28th Workshop on Signal and Power Integrity (SPI)*, Lisbon, Portugal, May 2024.

Copyright Notice

Application of Gaussian Process Regression for Data Efficient Prediction of PCB-based Power Delivery Network Impedance Features

Youcef Hassab (youcef.hassab@tuhh.de), Morten Schierholz, Christian Schuster
Institut für Theoretische Elektrotechnik, Hamburg University of Technology (TUHH), Hamburg, Germany

***Abstract*—In this paper, a data efficient machine learning (ML)-based framework for the prediction of key-features of the power delivery network (PDN) impedance is proposed. Gaussian Process Regression (GPR) is implemented within transfer and active learning loops to explore the potential with regard to data efficiency and accuracy. For a 4 layered printed circuit board (PCB), a prediction accuracy with a normalized root mean squared error (RMSE) of 3 % is achieved for some features including the resonance frequency of the board. The use of transfer learning results in a higher data efficiency and faster convergence. It is shown that reusing data from closer problems reduces the amount of new samples that need to be generated. The higher data efficiency makes ML tools a more attractive approach to speed up PDN design by replacing the expensive electromagnetic (EM) simulations of PCBs.**

***Index Terms*—Gaussian Process Regression (GPR), machine learning (ML), PDN design, PCB, EM simulations.**

I. Introduction

The proper design of power delivery networks (PDNs) for printed circuit boards (PCBs) is critical to ensure the performance of high-speed digital integrated circuits (ICs). With increasing operating frequencies, integration density and power consumption, the PDN design is becoming a more challenging task requiring advanced simulation tools and optimization techniques. Many decoupling strategies need expensive electromagnetic (EM) simulations to collect information on the PDN impedance at each iteration e.g. [1]. Several machine learning (ML) tools have been used to replace the expensive EM simulations with a high degree of accuracy using e.g. artificial neural networks (ANNs) [2]. However, ML tools often need large amounts of data samples for the training and testing. The generation of data samples for the ML tools can cancel the computational benefit if the process is inefficient and time-consuming.

Gaussian Process Regression (GPR) is an ML method that has shown many benefits with regard to data efficiency and accuracy in the SI/PI domain [3], [4]. It has been implemented i.a. for the prediction of the resonance frequency of PCBs [5]. An increase in data efficiency by the application of two different approaches, active learning and transfer learning, has been reported. Active learning has been used to find potential data points providing the highest information content to iteratively sample. Transfer learning focuses on reusing old samples in the training process for the prediction inside new problem spaces. It has been implemented and evaluated for scenarios involving different PCBs from the same design space as well as different problems.

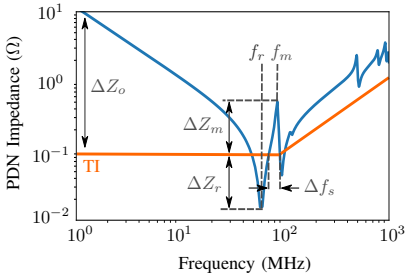

Fig. 1. Many decoupling techniques rely on information of some distinct features of the PDN and the target impedance (TI). Some of these key-features are defined here. The TI is marked with an orange line. These key-features are predicted using ML tools to replace EM simulations.

This work extends this approach by investigating the prediction of relevant PDN key-features other than the resonance frequency of PCBs, see Fig. 1. Transfer learning is implemented for variations of all relevant geometrical parameters. The effects of the amount and origin of data provided at the start of the process are assessed. A general framework for the integration of GPR in active and transfer learning loops in a data-efficient approach is also proposed. The framework uses the SI/PI database as a source of data available for reuse as a means to reduce the amount of new data that need to be generated [6]. The data generation expense is thus minimized for the prediction of relevant key-features, which speeds up the design process of PDNs.

The rest of the paper is organized as follows: In Section II, the investigated design space is presented. In Section III, a data-efficient framework for PDN feature prediction is proposed. In Section IV, GPR is implemented for the prediction of PDN key-features within active learning. In Section V, transfer learning is investigated inside the defined space. Section VI presents a conclusion with an outlook on future work.

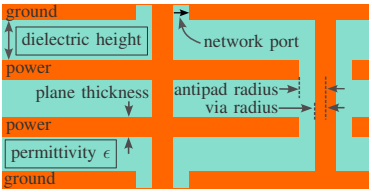

(a)

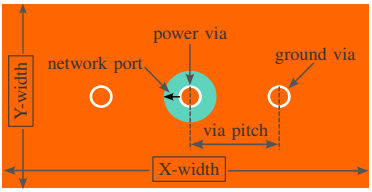

(b)

Fig. 2. Geometrical depiction of the investigated PCB seen from the (a) side and from the (b) top. The 4 variable design parameters are framed. The power via (observation point) is placed in the middle of the board.

II. Design Space Definition

PCBs serve as the main body to connect electronic components and deliver the needed power. The boards are mainly constructed by metallic planes, dielectric materials and vias. Currents passing through the vias excite EM waves in the cavities. The parallel planes and board edges form a resonator in which different modes propagate depending on the size and material parameters of the PCB and the observation point.

The design space is reduced to a feasible parameter range for a PCB. The studied case is a rectangular PCB with 4 layers (ground, power, power, ground) and a power via surrounded by two ground vias placed in the middle of the board. The geometrical and material parameters as well as the stackup and array constellation are shown in Fig. 2. The 4 varied parameters that represent the dimensions of the defined design space are given in Table I. These parameters, chosen as inputs to our model, have a significant impact on the input impedance as observed from the port at the power via location [7].

For the training and testing of the data-driven algorithms, data samples are generated to cover the defined design space. Assuming a radial wave propagation inside each cavity and ignoring fringing fields, the PCB is modeled by a contour integral method (CIM) and a physics-based (PB) via model [8]. 2000 data points are set using a latin hypercube sampling (LHS) and simulated. Fig. 3 shows the resulting magnitude of the input impedance as observed from the power via for 3 different samples. The variations of the PCB size parameters (X-width, Y-width and dielectric height) and material property (relative permittivity of the dielectric) result in variations in the observed impedance. Both the magnitude levels and frequencies of resonant peaks vary with changing input parameters.

TABLE I
Geometrical and material parameters of the defined design space of the PCB based PDN. Four parameters are varied.

Parameter	Minimum	Maximum	Value
Via Radius (mil)	–	–	5
Via Antipad (mil)	–	–	15
X-Width (mil)	1000	18000	Varied
Y-Width (mil)	1000	18000	Varied
Conductivity (S/m)	–	–	$5.8 \cdot 10^7$
Rel. Permittivity	2	6	Varied
Loss Tangent	–	–	0.02
Dielectric Height (mil)	3	80	Varied
Plane Thickness (mil)	–	–	1

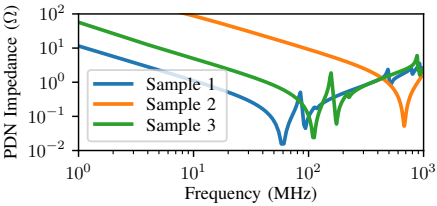

Fig. 3. The magnitude of the input impedance as seen from the port at the power via location is shown for different samples from the defined design space. The variations of the 4 design parameters result in significant changes in the impedance magnitude level and frequencies of the resonant peaks.

III. Data-Efficient Feature Prediction using GPR

For the PDN design, the frequency dependent impedance and the TI are compared. If the PDN impedance does not meet the TI specifications, decoupling capacitors (decaps) of different capacitances and locations are iteratively added to lower the impedance profile over the frequency [2]. Many methods for the placement of decaps rely on information of the EM behavior of the PDN e.g [1]. Instead of using the full frequency dependent impedance, some distinct features of the PDN and the TI can be sufficient. Some of these key-features are marked in Fig. 1 and defined as

- the resonance frequency of the board f_r,
- the overshoot at the resonance frequency ΔZ_r,
- the frequency of the first local maximum f_m,
- the overshoot at the first local maximum ΔZ_m,
- the maximum overshoot ΔZ_o, and
- the first frequency span Δf_s.

These features represent outputs that can be predicted by data-driven ML tools, e.g. ANNs, instead of using EM simulations. To increase the data efficiency, a framework is proposed using GPR as a prediction tool, see Fig. 4. For a new problem case, similar cases are found on the SI/PI

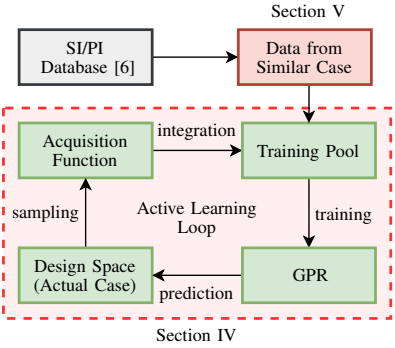

Fig. 4. A diagram of a data-efficient ML approach for key-feature prediction based on the SI/PI database is shown. Similar cases to the study case of interest are found. The data is fetched from the database to use as initial training samples. Further data points are sampled from the new design space to reach higher prediction accuracies. The new data is stored for future use.

database [6]. Similar cases refer to design spaces where the design parameters, varied dimensions and parameter ranges are close to each other e.g. proximal stackup, number of layers, size. The corresponding data are provided at the start of the GPR training. The GPR makes predictions on the new design space with integrated uncertainty estimation. Additional data points are chosen by an acquisition function to be sampled from the new space and added to training set. The acquisition function is set to reduce the uncertainty over the new design space. The GPR is retrained at each iteration for better accuracy. The prediction of key-features using the active learning loop without data reuse is shown in Section IV. The effects of reusing data through transfer learning are shown in Section V.

IV. Features Prediction using Active Learning

GPR embedded in an active learning loop is used for the prediction of the key-features. For the parameters of the gaussian process (GP), a mean function is initialized as a constant $\mu(x) = 0$ and the Matern 5/2 kernel is chosen as a covariance function. For the choice of points from the design spaces to sample, the maximal variance is set as the acquisition function. The point in the design space where the prediction is most uncertain is sampled and added to the training set [9]. A separate model is trained for each key-feature. The maximal number of iterations is set to 600, no initial data has been provided at the start of the training process. The RMSE is used as a metric to evaluate the prediction accuracy [10]:

$$RMSE = \sqrt{\frac{1}{n}\sum_{j=1}^{n}(y_j - \hat{y}_j)^2} \qquad (1)$$

where y_j and $\hat{y}_j$ are the true and predicted outputs, respectively, and $n = 600$ the number of samples used spanning the design space. The normalized RMSE is calculated using

TABLE II
Results of the prediction of key-features using GPR.

Key Feature	RMSE	RMSE/mean
Frequency First Null f_r	1.8 MHz	2.04 %
Overshoot First Null ΔZ_r	0.003 Ω	3.1 %
Frequency First Local Max f_m	66.66 MHz	54.09 %
Overshoot First Local Max ΔZ_m	14.17 Ω	>100 %
Max Overshoot ΔZ_o	60.28 Ω	>100 %
First Frequency Span Δf_s	1.58 MHz	2.24 %

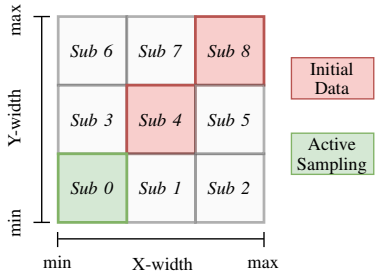

Fig. 5. For the 2D subdivision, the design space is divided into 9 subspaces depending on the X-Width and Y-Width of the board. Initial data is provided from *Sub 8* or *Sub 4* while further data points are actively sampled from *Sub 0*. The frequency f_r is predicted inside *Sub 0* using GPR.

the RMSE over the mean of the investigated key-feature. The results are given in Table II. Some key-features, related to the resonance frequency and first frequency span, are predicted with a normalized RMSE of approximately 3% or less. Other key-features, e.g. the frequency of the first local maximum f_m, are predicted by the trained model with a lower accuracy.

V. Resonance Prediction using Transfer Learning

The transfer learning approach, based on reusing data from similar cases to the study case, is investigated. The available data is integrated in the training set at the start of the learning process of the GPR. New data from the design space of the investigated case is actively sampled at each iteration as described in Section IV. To emulate similar cases the defined design space is first divided into 9 equal subspaces depending on the X-Width and Y-Width of the board, see Fig. 5. *Sub 0* represents the study case of interest, where the prediction of the resonance frequency f_r is targeted. Initial data samples are provided at the start of the training from *Sub 8* or *Sub 4*. The latter subspaces represent data from similar cases to *Sub 0*. The prediction accuracy within *Sub 0* is evaluated at each iteration, see Fig. 6. Providing initial data both from *Sub 4* or *Sub 8* results in a faster improvement in *Sub 0* than without data reuse. Providing data from the closer subspace *Sub 4* rather than *Sub 8* shows better accuracy in the first iterations, see Fig. 6c. Using a size of 50 or 100 initial samples results in a comparable improvement in the prediction accuracy.

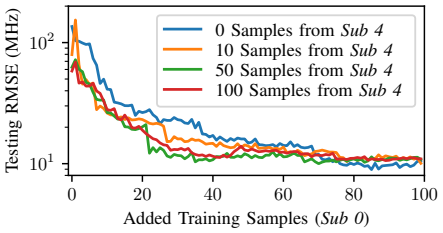

(a)

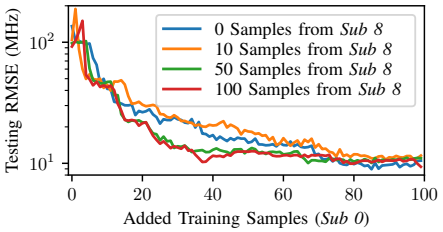

(b)

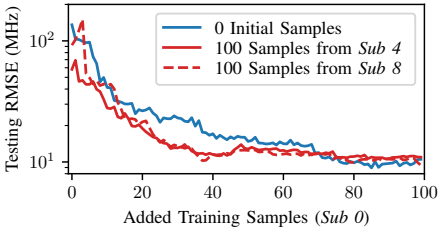

(c)

Fig. 6. For the 2D subdivision, the prediction accuracy of the resonance frequency f_r in *Sub 0* is shown for the usage of (a) initial data from *Sub 4*, (b) initial data from *Sub 8*. In (c), the two cases using data initial from *Sub 8* and *Sub 4* are directly compared for 100 samples each.

In a second experiment, the design space is divided depending on the 3 dimensions X-Width, Y-Width and Dielectric height of the board. This includes all the varied geometrical parameters. Initial data samples are provided from the furthest subspace from *sub 0*. A similar trend is observed to a less pronounced degree, see Fig. 7. Providing initial data results in an improvement of the accuracy up to 20 added *Sub 0* samples.

VI. Conclusion

GPR shows potential for the replacement of EM simulations needed for PCB decoupling. The use of GPR embedded in an active learning loop resulted in a prediction accuracy with a normalized RMSE lower than 3 % for some PDN key-

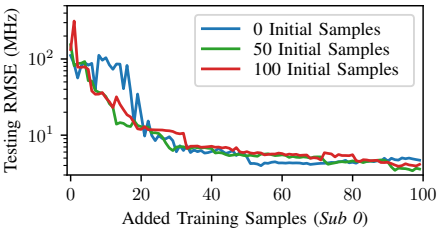

Fig. 7. For the 3D subdivision, the prediction accuracy of the resonance frequency f_r in *Sub 0* is shown for the usage of initial samples from the furthest subspace. Different initial data sizes are compared.

features. For the investigated problem, the reuse of data from different geometrical subspaces showed faster improvement and convergence in the first iterations when few new data samples are available. For effective transfer learning use, close design spaces have to be found as a source of initial data. To this aim, future work involves the development of a quantitative metric to assess the similarity of structures.

References

[1] I. Erdin and R. Achar, "Multipin Optimization Method for Placement of Decoupling Capacitors Using a Genetic Algorithm," *IEEE Transactions on Electromagnetic Compatibility*, vol. 60, no. 6, pp. 1662–1669, Dec. 2018.

[2] M. Schierholz, I. Erdin, J. Balachandran, and C. Schuster, "Data-Efficient Supervised Machine Learning Technique for Practical PCB Noise Decoupling," *DesignCon 2023*, CA, USA, Feb. 2023.

[3] F. Garbuglia, D. Spina, T. Reuschel, C. Schuster, D. Deschrijver, and T. Dhaene, "Modeling S-Pparameters of Interconnects Using Periodic Gaussian Process Kernels," in *2023 IEEE 27th Workshop on Signal and Power Integrity (SPI)*, Aveiro, Portugal, Mai. 2023.

[4] P. Manfredi and R. Trinchero, "A Nonparametric Surrogate Model for Stochastic Crosstalk Analysis Including Confidence Bounds," in *2021 IEEE 25th Workshop on Signal and Power Integrity (SPI)*, virtual online, Mai. 2021.

[5] M. Schierholz, Y. Hassab, I. Erdin, J. Balachandran, and C. Schuster, "Applying Techniques of Transfer and Active Learning to Practical PCB Noise Decoupling," in *DesignCon 2024*, CA, USA, Jan. 2024.

[6] M. Schierholz, A. Sanchez-Masis, A. Carmona-Cruz, X. Duan, K. Roy, C. Yang, R. Rimolo-Donadio, and C. Schuster, "SI/PI-Database Of PCB-Based Interconnects For Machine Learning Applications," *IEEE Access*, vol. 9, pp. 34423–34432, Feb. 2021.

[7] M. Schierholz, Y. Hassab, and C. Schuster, "Engineering-Informed Design Space Reduction for PCB-Based Power Delivery Networks," *IEEE Transactions on Components, Packaging and Manufacturing Technology*, vol. 13, no. 10, pp. 1613–1623, Oct. 2023.

[8] R. Rimolo-Donadio et al. "Physics-Based Via and Trace Models for Efficient Link Simulation on Multilayer Structures Up to 40 GHz," *IEEE Transactions Microwave Theory and Techniques*, vol. 57, pp. 2072–2083, Aug. 2009.

[9] H. M. Torun, J. A. Hejase, J. Tang, W. D. Beckert, and M. Swaminathan, "Bayesian Active Learning For Uncertainty Quantification Of High Speed Channel Signaling," in *2018 IEEE 27th Conference on Electrical Performance of Electronic Packaging and Systems (EPEPS)*, San Jose, CA, USA, Oct. 2018.

[10] D. C. Montgomery, E. A. Peck, and G. G. Vining, *Introduction to Linear Regression Analysis*. 5th ed., Wiley, NJ, USA, 2012.

Publication 4 (P4)

Title

Machine Learning Based Data Validation for Signal Integrity and Power Integrity Using Supervised Time Series Classification.

Publication Status

Published in peer-reviewed journal: IEEE Transactions on Electromagnetic Compatibility.

Author Contribution

Predominant involvement as a 1. author (co-author confirmation provided).

Bibliographic Information

[72] Y. Hassab, T. Hillebrecht, F. Lurz and C. Schuster, "Machine Learning Based Data Validation for Signal Integrity and Power Integrity Using Supervised Time Series Classification," *IEEE Transactions on Electromagnetic Compatibility*, vol. 66, no. 6, pp. 2150-2158, Dec. 2024.

Copyright Notice

Machine Learning Based Data Validation For Signal Integrity and Power Integrity Using Supervised Time Series Classification

Youcef Hassab, *Student Member, IEEE,* Til Hillebrecht, *Student Member, IEEE,* Fabian Lurz, *Senior Member, IEEE,* and Christian Schuster, *Senior Member, IEEE.*

***Abstract*—A novel approach for the validation of data in signal integrity and power integrity using machine learning is proposed. This approach presents an alternative to the feature selective validation (FSV) method outlined in the IEEE Standard 1597.1 for the validation of computational electromagnetics, computer modeling and simulations. The proposed approach focuses on replicating the human visual assessment by using data collected and labeled by expert engineers to train time series classification networks that predict the degree of agreement between two curves. The trained networks are then used for the systematic and automated validation of one-dimensional datasets. The performance and suitability of this approach for systematic data validation is evaluated and discussed. The trained network surpasses the single human subjects in predicting the expert opinion with an accuracy higher than 70%.**

***Index Terms*—data validation, time series classification, electromagnetic compatibility, signal integrity, power integrity, machine learning, feature selective validation.**

I. Introduction

IN the domain of electromagnetic compatibility (EMC) engineering, signal integrity (SI) and power integrity (PI) play an important role in the design of printed circuit boards (PCBs). The use of computational electromagnetics (CEM) and simulation tools is part of the design process. The investigation of EMC related problems relies on physics-based (PB) modeling using measurements or simulations and full-wave (FW) solvers. Since the problems faced are complex, it is important for the engineer to ensure that the used models deliver results accurate enough for the faced problems. The validation of data is the process of examining the quality and accuracy of collected data. For the SI/PI engineer, it is often about ensuring a certain confidence in the modeling techniques by comparing the simulation results with each other or with measurements and accepting some variation between the two. The knowledge and experience of the engineers involved is the major factor in deciding whether the comparison is acceptable for the use-case and field [1]. This process is conventionally subjective in nature, see Fig. 1. For instance, the SI/PI-Database, freely accessible at the homepage of the Institut für Theoretische Elektrotechnik at the Hamburg University of Technology (TUHH) (**https://www.tet.tuhh.de/en/si-pi-database/**), contains structures simulated with a PB model [2]. The data is mainly collected for machine learning (ML) applications. The generation of data is partially automated to speed up the process [3]. To ensure conformity, the engineer proceeds to validate the generated data against a FW solver before the upload, which can prove to be tedious and time-consuming.

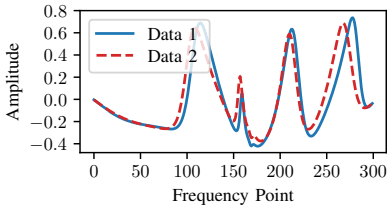

(a)

Score	1	2	3	4	5	6
Occurence	0	5	3	3	1	0

(b)

Fig. 1. Results of a survey on the subjectivity of conventional visual assessment for data validation. (a) Presented survey dataset, (b) Number of occurence of the given scores by PhD candidates with an EMC background. The given scores by the candidates are spread over a 4 scale point interval.

The feature selective validation (FSV) method, first introduced in [4], has been developed for the purpose of data validation [5]. It is outlined in the IEEE Standard 1597 for the validation of CEM, computer modeling and simulations [6], [7]. The FSV tries to mirror expert opinion when assessing datasets presented visually using analytical methods. The visual assessment follows the six-points scale developed in [8]. FSV has been used for a variety of applications including typical SI/PI design applications directly on S-parameters matrices for the validation [9]. Machine learning tools have

Manuscript received April 19, 2021; revised August 16, 2021; accepted 26 September 2023. Date of publication 29 September 2023; date of current version 10 October 2023. (Corresponding author: Youcef Hassab).
Youcef Hassab, Til Hillebrecht and Christian Schuster are with the Institut für Theoretische Elektrotechnik at the Hamburg University of Technology (TUHH), 21073 Hamburg, Germany. (emails: youcef.hassab@tuhh.de; til.hillebrecht@tuhh.de; schuster@tuhh.de).
Fabian Lurz is the Chair of Integrated Electronic Systems at the Otto von Guericke University Magdeburg (OVGU), 39106 Magdeburg, Germany. (email: fabian.lurz@ovgu.de).
Digital Object Identifier xxx

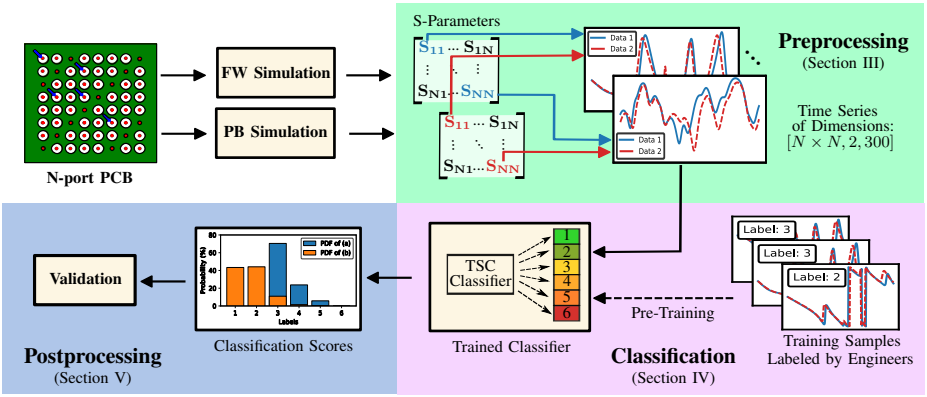

Fig. 2. Block diagram of the proposed data validation framework. The three main blocks of the pipeline are the preprocessing, classification and postprocessing. The network parameters are compiled into time series and fed to the trained classifier. The predicted scores are used for the validation.

been applied to replace FSV calculations by convolutional neural network (CNN) predictions [10]. Although the FSV does produce outputs that can be directly compared with a group response, there is no direct overlap and the scores are somewhat inaccurate for some datasets [11], [12]. Furthermore, FSV may demonstrate inconsistencies in the results when applied to the comparison of zero-crossing datasets typical in EMC domain. Although addressed in [13] and [14], the effect has only been reduced or needs extra preprocessing of data that might affect the comparison.

In this work, a new approach for the validation of data in SI/PI using time series classification (TSC) as a comparison technique is proposed. The proposed method aims at mimicking expert opinion and predicting the degree of agreement between two curves by trained time series classifiers, see Fig. 2. Time series classification, especially using deep learning, has shown very promising results in recent years [15].

For the purpose of investigation of this approach, data from different use-cases in the SI/PI domain are generated using a PB model and a commercial finite element method (FEM) solver. The simulated PCB structures and resulting network parameters are labeled by multiple domain engineers. The proposed scheme is evaluated and compared with human users.

The rest of the paper is structured as follows. In Section II, the problem and proposed approach are presented. In Section III, the data acquisition and preprocessing paradigms are highlighted. In Section IV, the classification model is presented and results evaluated. In Section V, the postprocessing block is explored while Section VI summarizes this work.

II. Validation of Data

A. Limitations of Conventional Data Validation

As mentioned in Section I, the validation of data is a crucial step in the engineering process. Conventionally, the engineer visually assesses the degree of agreement of the data to be validated. This approach has two main drawbacks. First, the assessment is subjective. There are many factors that affect the assessment e.g. domain knowledge, experience and psychological state. Different engineers give different agreement scores for the same data [16]. For instance, the pair of curves in Fig. 1 (a) has been presented to PhD candidates with an EMC background. 12 different engineers have proceeded to the assessment of the degree of agreement of the presented data following the visual assessment scale represented in table I and developed in [8]. The given scores are reported in Fig. 1 (b). It can be seen that the given scores are spread across four scale points, which is a significant spread.

The second problem with conventional validation is the need for manual input and thus the inability to be integrated in automated processing solutions. This can be a problem for the validation of large datasets. For example, the number of samples generated by the simulation of structures in the SI/PI-Database makes it particularly tedious to fully validate the data conventionally. Comparison metrics like correlation, reliability or error functions can be used for automated validation [17]. However, they usually fail to reflect expert opinion and can produce erroneous results, which motivated the development of FSV [5]. There is a need for a tool that offers better comparability and quality of comparison while overlapping with expert opinion. Moreover, the tool should also be easily integrable into automated or computer assisted frameworks. In Section II-B, such a tool is proposed.

B. Proposed Data Validation Framework

The proposed approach for the validation of data is based on TSC [18]. The main idea is the use of trained time series classifiers to predict the degree of agreement of two curves, or time series, and assign an equivalent visual scale score. The classifiers rely on user-labeled data for training. The labeling is performed by expert engineers. Expert engineers can identify

TABLE I
SIX-POINTS VISUAL ASSESSMENT SCALE FOR THE DETERMINATION OF THE DEGREE OF AGREEMENT BETWEEN TWO CURVES.

Characteristics	Quality	Description	Score
Many similarities	Perfect match	Excellent	1
	Minor variations	Very good	2
Some similarities	Good agreement	Good	3
	Reasonable agreement	Fair	4
Many dissimilarities	Minor agreement	Poor	5
	No visible agreement	Very Poor	6

important domain-relevant features, e.g. the existence and shift of resonances. The trained networks are able to mimic domain expert assessment and produce a good overlap between prediction and visual assessment of engineers. This is the main advantage of the proposed ML approach in comparison to FSV and other distance and error metrics. The second advantage of the proposed method is that it adds a layer of objectivity to the validation process. An objective assessment is defined as the average of single expert visual assessments that the network can replicate. Moreover, the trained networks can easily be implemented for automated and computer-assisted data validation frameworks. A general overview of the proposed system is presented, see Fig. 2. As a starting point, the data to be validated or compared serves as an input for the system. These can be simulation or measurement data stored as network parameters. For the presented study case, PCBs are simulated using a PB and FW solver for validation. These data have to be first preprocessed and brought into a form suitable for classification. The data is transformed into two channel time series of equal length. The two channels contain each the data to be compared with the other channel. The time series are then fed to the classifier. The classifier predicts the degree of agreement between each two curves and assigns a score for each input. The given outputs can be postprocessed for further analysis.

C. System Design of the Proposed Framework

The main three parts to be designed for a fully working system are the preprocessing, the classifier and the postprocessing blocks, see Fig. 2. These are thoroughly explored in sections Section III, Section IV and Section V, respectively. The first step is the collection of data samples from the explored domain for the training and evaluation of the TSC networks. The dataset should encompass a diverse set of examples. In SI/PI, this could be data from various models including simulation and measurement, different experiments and structures, different network parameter types in time and frequency domain. Available and generated data serve as the basis for the classifier training. Depending on data type, a preprocessing chain has to be constructed to generate time series from the original data. These time series are then plotted and labeled by expert engineers. The samples and attached labels are used to train a TSC classifier. The predictions of the trained classifier on unseen new data is used in a postprocessing step depending on the engineering needs for data validation.

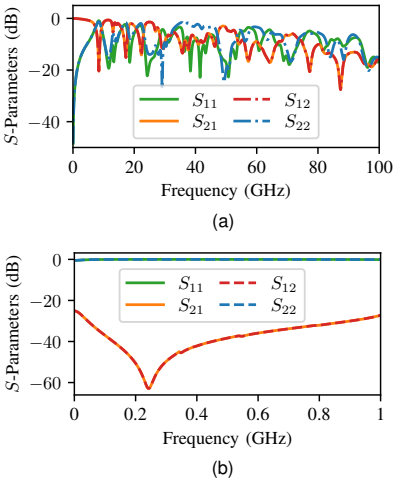

Fig. 3. The scattering parameters of two simulated structures from table II, (a) via to via link and (b) power delivery network, are shown. The structures are simulated using a full-wave (FW) finite element method (FEM) solver.

TABLE II
SIMULATED STRUCTURES FOR THE DATA GENERATION. FOR EACH STRUCTURE, THE MAXIMUM FREQUENCY, NUMBER OF FREQUENCY POINTS, PORTS, AND CAVITIES ARE GIVEN.

Structure Description	Maximum Frequency	Frequency Points	Num. of Ports	Num. of Cavities
Through vias	100 GHz	1001	4	5
Differential line	100 GHz	2000	4	4
Via to via link	100 GHz	2000	2	10
Bandpass filter	100 GHz	2000	2	11
Through via I	60 GHz	600	2	1
Through via II	60 GHz	600	2	1
PDN I	1 GHz	334	36	7
PDN II	1 GHz	334	36	7

III. Data Acquisition and Preprocessing

A. Investigated Domain and Data Generation

For the purpose of investigation of the proposed approach, the authors first limit the application area to the SI/PI domain where data is collected from realistic application cases in the SI/PI domain. For the generation of data, 8 different PCB structures are simulated using a PB model and a commercial full-wave FEM solver [19], to provide a reference for validation. The PB tool connects the components of the PCB on network parameter level. The transmission between vias is based on analytical solutions for cavity wave propagation. Considerations in the vicinity of vias are based on analytical solution provided in [21]. The simulation results for the via-ports as network parameters in frequency domain are stored as *Touchstone*® files. These simulation results are used to construct time series samples for the comparison of curves.

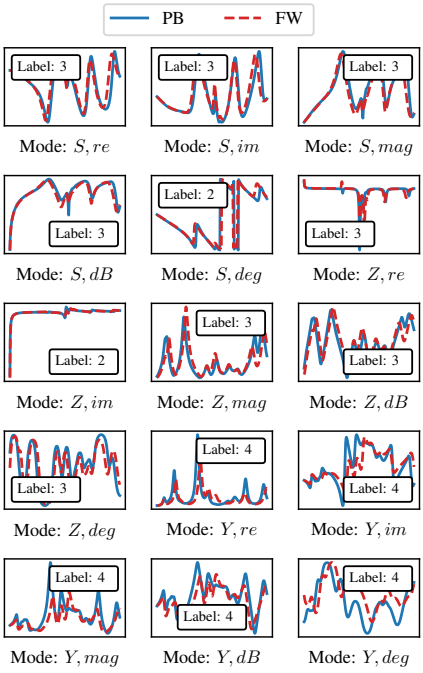

Fig. 4. Example time series generated from a single port-pair for each mode as presented for the labeling. The curves from the physics-based (PB) and full-wave (FW) simulations are shown by straight and dashed lines respectively. Labels given by a single user, *User 1*, are marked on each pair of curves.

Table II gives an overview of the PCB structures. Two different variations in the geometrical and material parameters are used for the power delivery network (PDN) and through via structures. The scattering parameters of two structures are shown to give an example on the electromagnetic behaviour, see Fig. 3.

B. Extraction of Samples from Network Parameters

All manipulations for the sample extraction are carried out using *Python* [22]. The network parameters resulting from the PB and FW simulations of the different structures are loaded using the *scikit-rf* library [23]. This facilitates the storage and manipulation of the network parameters. For each pair of ports i and j, the S-parameters S_{ij}, impedance parameters Z_{ij} and conductivity parameters Y_{ij} can be accessed and the real part (re), imaginary part (im), phase (deg), magnitude (mag) and magnitude in decibel (dB) can be represented as a function of frequency. 15 different and unique frequency dependent curves can be generated from each pair of ports. The 15 combinations of parameter type and representation are called "modes". Network reciprocity and symmetry are taken into account to avoid generating identical curves from different port-pairs. Depending on the number of frequency points for each simulated structure, the generated curves are resized into equal length time series. A common length of 300 frequency points is chosen. Curves resulting from the same port-pair and mode from the two simulation methods are stacked together to form a time series sample n. The two-channel sample has the dimensions $[n, 2, 300]$, where n represents the sample index. Each sample contains two channels of 300 timestamp series from both the PB and FW simulation tools.

A total of 1320 samples are first extracted from the simulated structures and form the main dataset. More samples are generated to provide examples with less agreement through random matching of the ports and structures. The two curves from PB and FW simulations are extracted by choosing a random structure, mode and ports for each simulation method then stacked. 280 additional samples are added to extend the dataset to 1600 samples. The time series extracted from a single ports-pair using each of the 15 possible modes show variability, see Fig. 4.

C. Labeling of Time Series Samples

Labeling is defined as the assignment of the two channel samples to a certain category or class. The labeling is based on the six-points visual assessment scale shown in table I. Following this scale, each sample can be assigned a numerical value from "1" to "6" reflecting the level of agreement between the two channels from the two different simulation methods. For the labeling, the time series are plotted and presented in a form without axis, see Fig. 4. This is done in a first step to investigate the ability of the networks to generalize on the data and reproduce an equivalent visual score. This results in a tool that globally captures the agreement of two curves. For a domain specific and fine-tuned validation tool, the data is presented with axis in a commonly used form. This allows the engineer to label the data according to domain knowledge. Overall, six different electrical engineers with an EMC/SI/PI background and years of experience have proceeded to the labeling of the available data. The histograms of the given labels vary depending on the user, see Fig. 5. The average of the given scores is marked by a white dashed line. The distribution as well as the average of the given labels vary from user to user. This reflects the subjectivity of the conventional validation as expected. These labeled time series samples are ready to be used by TSC tools.

IV. Time Series Classification for Data Validation

A. Comparison of Time Series Classification Architectures

There are many deep learning architectures specifically developed for TSC [15]. Although some tools score well in benchmarking, the performance is usually dataset-dependent with some tools performing better than others for certain datasets. In a first step, multiple tools that usually score well in benchmarking tests are preliminarily compared without hyperparameter tuning to assess the initial performance. For the training and evaluation, the *tsai* library, a deep learning package for TSC is used [24]. The full dataset is used with

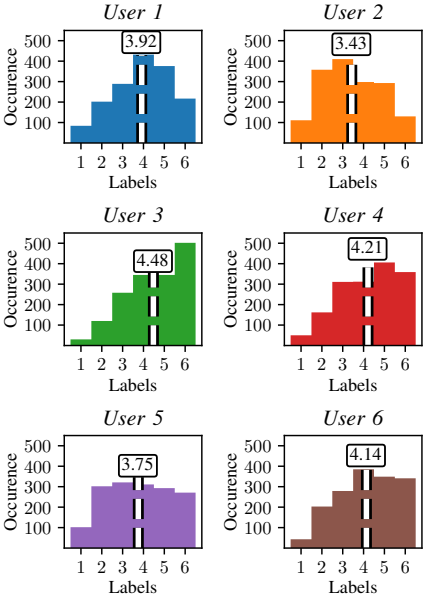

Fig. 5. The histograms of the given labels by each user are shown. The average of the given scores for each user is marked by dashed lines. The distribution as well as the average of the given labels vary from user to user.

TABLE III
COMPARISON OF TIME SERIES CLASSIFICATION DEEP-LEARNING ARCHITECTURES WITH REGARD TO THE NUMBER OF TRAINABLE PARAMETERS, TRAINING TIME, AND VALIDATION ACCURACY.

Architecture	Parameters	Time (s)	Accuracy (%)
Rocket [26]	n/a	211	77.27
InceptionTime [28]	455,685	900	71.21
ResNet [29]	479,365	70	51.89
CNN [30]	257,158	42	44.31
FCN [29]	265,605	38	43.18
LSTM [31]	42,105	43	34.09

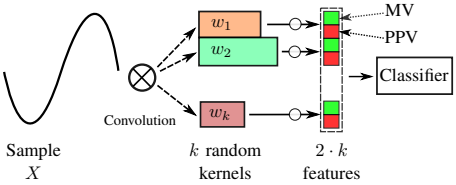

Fig. 6. In *Rocket*, a convolution operation is performed between random kernels and the time series sample. The maximum value (MV) and proportion of positive values (PPV) are extracted from each resulting feature of the convolution operations. The extracted values are concatenated to build a vector to be classified using a linear classifier.

the labels of one user, *User 1*. For training, $80\,\%$ of the available data samples are used and the other $20\,\%$ are used for testing. The samples are normalized before training. The categorical cross-entropy is used as a loss function [25]. A learning rate of 10^{-4} is used. The networks are trained for 150 epochs and validated on the test set. Table III represents an overview of the used tools and the respective test results. More information on each method and architecture can be obtained on the cited sources. The methods are ordered by decreasing validation accuracy. *Rocket* (**R**and**O**m **C**onvolutional **KE**rnel **T**ransform) provides the best score and is thus used for further experiments. *Rocket* is a state-of-the-art method for TSC with an efficient training process [26]. *Rocket* has shown both very good performances and a faster training process for a variety of benchmarking datasets [27].

B. Setup of the Time Series Classification Using Rocket

Rocket works by first transforming the time series using a large number k of random convolutional kernels, see Fig. 6. Each 1D kernel w is first generated with random length l, dilation d and bias b. The convolution performed on the time series is given for a sample X from position i in X by [32]:

$$X_i * w = \left(\sum_{j=0}^{l-1} X_{i+(j \cdot d)} \cdot w_j \right) + b. \tag{1}$$

The resulting feature maps are then used by *Rocket* to compute two aggregate values from each feature map, the maximum value (MV) (equivalent to global max pooling); and the proportion of positive values (PPV). Accordingly, for k kernels, $2 \times k$ features per sample are created. The transformed features are used to train a linear classifier. The transformations are applied on the available time series split in training and testing sets. The time series are normalized by sample in a first step. The chosen parameters are $k = 10\,000$ kernels that can take one of the three sizes $l = \{7, 9, 11\}$. The model is used to generate $20\,000$ features per sample. Each created feature is normalized again. A logistic regressor with an $l2$ penalty is chosen for the classification of features. The logistic regressor is trained using stochastic gradient descent. For the logistic regressor, an optimal inverse regularization strength of $C = 0.01$ is found and set.

The trained network is used for the prediction of the labels of the test set. For the purpose of performance comparison, two metrics are used, the accuracy and precision. The accuracy is defined as the number of correct predictions over the total number of predicted samples. The precision is defined as the number of correct predictions and false predictions adjacent to correct labels over the total number of predicted samples. In other words, the precision does not penalize prediction errors of a one score point.

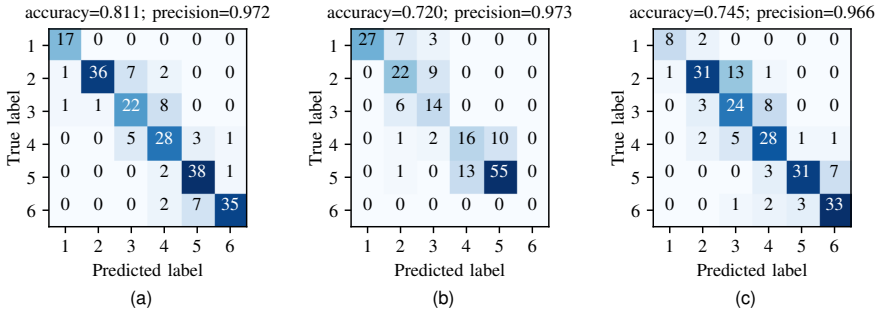

Fig. 7. The confusion matrices and classification results of the *Rocket* classifiers on the test sets are shown for the (a) single-user labels with a random train/test split, (b) single-user labels with a train/test split per structure and (c) multi-user labels. The accuracy and precision are marked on top of each matrix.

C. Classification of Single-User Labeled Samples

The performance of the *Rocket* classifier is evaluated with single-user labels. The time series with labels of *User 1* are used for the training and testing. This enables the investigation of the generalization ability of the networks and their suitability for data validation. In a first step, a random train/test split is used. In a second step a train/test split per structure is used where samples from six structures are used for training while samples from the two remaining structures are used for testing. The confusion matrices and results are shown in Fig. 7.

The models are trained using the parameters mentioned in Section IV-B. The model trained using a random train/test split reaches an accuracy of 81.1% and a precision of 97.2%. This means that 81.1% of the test samples are given the correct label by the *Rocket* classifier and 97.2% of the test samples are given either the correct label or a label adjacent to the correct label. In other words, almost all predicted labels lay in nearby classes when not correctly predicted as reflected by the confusion matrix. The probability of predicting a label with more than a one scale error is less than 3%. The model trained on a split based on structures reaches an accuracy of 72% and precision of 97.3%. The precision is as high as on the random split. A random train-test split yields a higher accuracy because of the similar data distributions in both sets, whereas splitting by structure exposes the model to new and unseen patterns that are harder to classify. In a further experiment, the model was trained and tested on a random split of data from two different commercial FW solvers on each channel [19], [20]. A time domain dataset of 8 samples has been tested as an input for the model trained on frequency domain datasets only. The curves represent step and impulse responses extracted from the structures *differential line* and *via to via link*, see Table II. The model achieved an accuracy and precision of 50% and 90%, respectively. This shows the feasibility of this framework for other input types. The input can be i.a. different simulation tools, models or measurements and not limited to PB versus FW validation.

D. Classification of Multi-User Labeled Samples

The performance of the classification is evaluated for multi-user labels. The first step is the determination of the expert labels that are considered as the objective truth. For this purpose, the average score is calculated for each sample by determining the mean over the six user labels. The mean of the given six labels by each user is then rounded to the nearest unit to get the final label. In a second step, TSC networks are trained using these new labels. The classification accuracy of the *Rocket* classifier and the different users on the same test sets are evaluated. Since the users naturally label the samples differently, their labeling can deviate from the average calculated labels. The performance of single human users can be evaluated on the same testing sets for comparison.

The confusion matrix of the classifier on the test set is shown in Fig. 7 (c). The classification metrics are of the *Rocket* classifier and the different users are represented in Fig. 8. It can be seen that the *Rocket* classifier is statistically better at finding the correct expert labels than every single user with an accuracy of approximately 75%. The classification accuracy of all human users amounts to less than 70%. The precision for both the classifier and users is comparable with values higher than 90%. The model trained on single-user labels outperforms the model trained on multi-user labels, this is due to the labeling patterns that are more easily learned by the ML model for a single user. The *Rocket* classifier and the FSV are compared with the normalized root mean square error (nRMSE) and visual score given by users. For instance, Fig. 9 (a) and Fig. 9 (b) show two samples from the test set, *Sample A* and *Sample B*, respectively. Each sample contains two curves, *Data 1* and *Data 2*, to be compared with each other. The *Rocket* score matches the average visual assessment score given by the human users. The FSV score misses the visual score by a one scale error, see Table IV. Although the nRMSE values of the two samples are very close, which would indicate the same level of similarity, the two samples show different scores of agreement, which highlights the benefits of a classifier that matches the visual assessment.

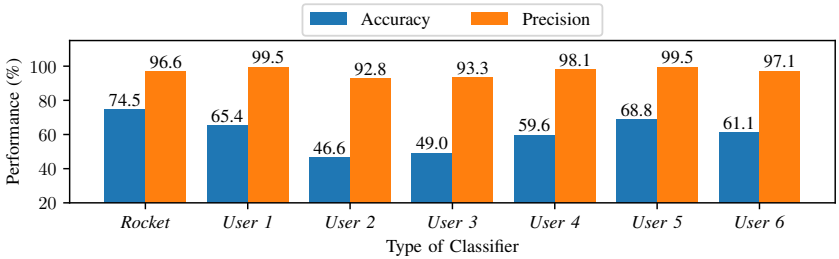

Fig. 8. Comparison of the performance of the *Rocket* classifier and the performance of the human users on the test set with multi-user labels. The accuracy and precision are both represented for the classifier and each user. The classifier surpasses all human users in terms of accuracy while the precision is comparable.

V. Postprocessing of Classification Results

A. Uncertainty-Quantified Classification of Samples

As outlined in Section IV-B, a logistic regression classifier is used in a last step to predict the agreement scores. The probabilities of an input pair having one of the six labels can be easily extracted without additional calculations. These probabilities can be used to quantify the uncertainty of the model and estimate the confidence around a prediction.

The resulting probabilities as a discrete probability density function (PDF) given by the classifier for the input pairs *Sample A* and *Sample B* are shown in Fig. 9 (c). For the first pair *Sample A*, the probability of the given label "3" by the classifier amounts to approximately 70%, which shows a relative certainty of the classifier in the given score. The label "3" is a much more probable given score than the label "4", that has a probability of approximately 25%. For the second pair *Sample B*, the probability of the given label "2" by the classifier amounts to approximately 43% only, which shows a relative uncertainty of the classifier. The label "2" is only slightly more probable than the label "1", that has a probability of approximately 42%. These probabilities serve as important information to help the engineer make decisions considering the model uncertainty.

B. Assisted Uncertainty-Aware Validation of Data

For the validation of large datasets, e.g. multi-port structures, the conventional validation of each port-pair is out of reach. The proposed framework is augmented to provide an uncertainty aware assisted validation of data. The idea is to provide confidence intervals around the predictions and notify the engineer for problematic port pairs. This is implemented first by using a discrete cumulative density function (CDF). By setting an acceptable score within a defined confidence interval, the algorithm only returns problematic cases where the probability of scoring lower than the acceptable score is higher than the confidence interval threshold. To give an example, an acceptable score of "3" and confidence interval of 95% have been defined. Taking the examples of Fig. 9 (a) and (b) again, the CDF has a value of approximately 70% and 98% at the score "3" for *Sample A* and *Sample B*, respectively.

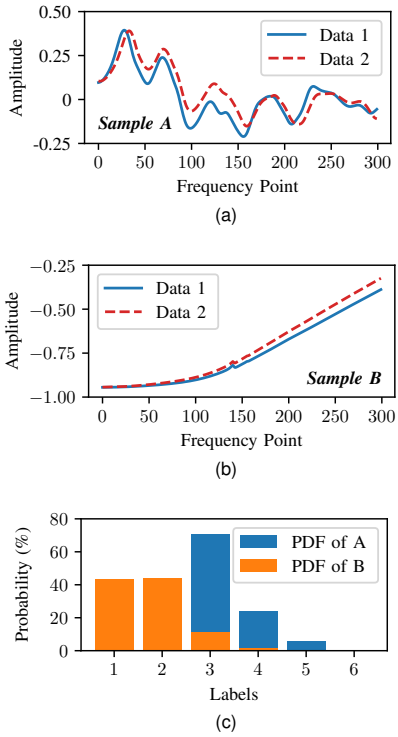

Fig. 9. For the input pairs a) *Sample A* and b) *Sample B*, the probabilities associated with the scores "1" to "6" given by the *Rocket* classifier are depicted as c) probability density functions (PDFs). The *Rocket* classifier estimates the probability of *Sample A* having a score of "3" at approximately 70%. The probabilities of *Sample B* having a score of "1" or "2" both amount to approximately 40%. The *Rocket* classifier shows a higher certainty in classifying *Sample A* than *Sample B*.

TABLE IV
DIRECT COMPARISON OF NRMSE, FSV, *Rocket* AND AVERAGE VISUAL SCORE GIVEN BY HUMAN USERS ON *Sample A* AND *Sample B*.

Test Sample	nRMSE	FSV	*Rocket*	Visual
Sample A	11%	4	3	3
Sample B	6.6%	1	2	2

This means that the probability that the pairs have a score of "3" or higher is approximately 70% and 98%, respectively. The first value is lower than the confidence interval previously defined while the second is higher. The first pair *A* fails while the second pair *B* passes the confidence test. The indices of the port-pair of *Sample A* are returned to the engineer to look into since this pair fails the confidence test. This allows a fast and systematic validation of large datasets.

VI. CONCLUSION

The trained TSC classifiers on SI/PI datasets labeled by domain engineers perform statistically better than single engineers in assessing a group average validation score. Since it provides a comparison that captures human visual assessment, very fast prediction times and integrated uncertainty quantification, this method might pave the way for automated, large scale and accurate data validation. Especially in ML frameworks where large datasets are collected and need to be validated, this tool can provide useful. The proposed framework can be fine-tuned for other domains, e.g. EMC, by using domain-relevant datasets presented and labeled by domain experts. Future work includes an extensive generation, labeling and testing on time domain datasets.

REFERENCES

[1] S. Park et al., "Lessons from applying IEEE standard 1597 for validation of computational electromagnetics computer modeling and simulations," in *IEEE EMC Magazine*, vol. 6, no. 2, pp. 55-67, Jul. 2017.

[2] M. Schierholz et al., "SI/PI-Database of PCB-Based Interconnects for Machine Learning Applications," in *IEEE Access*, vol. 9, pp. 34423-34432, Feb. 2021.

[3] T. Hillebrecht, J. Alfert, T. Reuschel and C. Schuster, "Automated Generation and Correlation of Physics-Based Via Models with Full-Wave Simulation for an SI/PI Database," in *2023 IEEE 32nd Conference on Electrical Performance of Electronic Packaging and Systems (EPEPS)*, Milpitas, CA, USA, Oct. 2023.

[4] A. J. M. Martin. *Quantitative data validation (automated visual evaluations)*, Ph.D. dissertation, De Montfort University, Leicester, UK, 1999.

[5] A. P. Duffy, A. J. M. Martin, A. Orlandi, G. Antonini, T. M. Benson and M. S. Woolfson, "Feature selective validation (FSV) for validation of computational electromagnetics (CEM). part I-the FSV method," in *IEEE Transactions on Electromagnetic Compatibility*, vol. 48, no. 3, pp. 449-459, Aug. 2006, doi: 10.1109/TEMC.2006.879358.

[6] "IEEE Standard for Validation of Computational Electromagnetics Computer Modeling and Simulations," in IEEE Std 1597.1-2008, pp.c1-41, 2008, doi: 10.1109/IEESTD.2008.4957854.

[7] "IEEE Recommended Practice for Validation of Computational Electromagnetics Computer Modeling and Simulations," in IEEE Std 1597.2-2010, pp.1-122, Feb. 2011, doi: 10.1109/IEEESTD.2011.5721917.

[8] D. E. Coleby and A. P. Duffy, "A Visual Interpretation Rating Scale for Validation of Numerical Models", in *COMPEL - The international journal for computation and mathematics in electrical and electronic engineering*, vol. 24, no. 4, pp. 1078-1092, Dec. 2005, doi: 10.1108/03321640510615472.

[9] Z. Chen, "Feature Selective Validation (FSV) Application to S-Parameter Models Directly," in *2021 IEEE 71st Electronic Components and Technology Conference (ECTC)*, San Diego, CA, USA, Jun. 2021, doi: 10.1109/ECTC32696.2021.00289.

[10] J. Bai, Y. Liu, D. Kong and K. Guo, "Credibility Evaluation of Electromagnetic Simulation Results Based on Convolutional Neural Network," in *IEEE Letters on EMC Practice and Applications*, vol. 5, no. 1, pp. 16-21, Mar. 2023, doi: 10.1109/LEMCPA.2022.3226151.

[11] A. Orlandi, A. P. Duffy, B. Archambeault, G. Antonini, D. E. Coleby and S. Connor, "Feature Selective Validation (FSV) for Validation of Computational Electromagnetics (CEM). Part II-Assessment of FSV Performance," in *IEEE Transactions on Electromagnetic Compatibility*, vol. 48, no. 3, pp. 460-467, Aug. 2006, doi: 10.1109/TEMC.2006.879360.

[12] M. R. Johnson, "FSV Versus Human Subjective Data Evaluation; An Informal Survey," in *2012 IEEE International Symposium on Electromagnetic Compatibility*, Pittsburgh, PA, USA, Aug. 2012, doi: 10.1109/ISEMC.2012.6351652.

[13] G. Zhang, A. P. Duffy, H. Sasse, L. Wang and R. Jauregui, "Improvement in the Definition of ODM for FSV," in *IEEE Transactions on Electromagnetic Compatibility*, vol. 55, no. 4, pp. 773-779, Aug. 2013, doi: 10.1109/TEMC.2012.2231416.

[14] B. Archambeault et al., "Challenges in Developing a Multidimensional Feature Selective Validation Implementation," in *2010 IEEE International Symposium on Electromagnetic Compatibility*, Fort Lauderdale, FL, USA, Jul. 2010, pp. 726-731, doi: 10.1109/ISEMC.2010.5711368.

[15] H. I. Fawaz et al., "Deep Learning for Time Series Classification: A Review," in *Data Mining and Knowledge Discovery*, vol. 33, pp. 917–963, Mar. 2019, doi: 10.1007/s10618-019-00619-1.

[16] G. Zhang, L. Wang, X. Peng and A. Duffy, "A Preliminary Study of the Influence of Experiential Backgrounds of Respondents to a Reference Survey for Verification of FSV," in *2016 IEEE International Symposium on Electromagnetic Compatibility (EMC)*, Ottawa, ON, Canada, Jul. 2016, doi: 10.1109/ISEMC.2016.7571711.

[17] B. Jiang, L. Ryder and P. Li, "Data Assessment Method Based on the Statistical Analysis," in *2023 IEEE Symposium on Electromagnetic Compatibility & Signal/Power Integrity (EMC+SIPI)*, Grand Rapids, MI, USA, Jul. 2023, doi: 10.1109/EMCSIPI50001.2023.10241365.

[18] E. A. Maharaj, P. D'Urso, J. Caiado, *Time series clustering and classification*, 1st ed, Chapman & Hall, Boca Raton, FL, USA, 2019.

[19] ANSYS® Electromagnetics Suite, Release 16.2. ANSYS, INC., Canonsburg, PA, USA.

[20] CST Studio Suite®, Dassault Systèmes, Vélizy-Villacoublay, France, [Online]. Available: https://www.3ds.com/products/simulia.

[21] R. Rimolo-Donadio et al., "Physics-Based Via and Trace Models for Efficient Link Simulation on Multilayer Structures Up to 40 GHz," in *IEEE Transactions on Microwave Theory and Techniques*, vol. 57, no. 8, pp. 2072-2083, Aug. 2009, doi: 10.1109/TMTT.2009.2025470.

[22] G. V. Rossum and F. L. Drake, *Python 3 Reference Manual*, CreateSpace, Scotts Valley, CA, USA, 2009.

[23] A. Arsenovic. *Scikit-Rf: Open Source RF Engineering*, Github, 2016, available at: https://github.com/scikit-rf/scikit-rf.

[24] I. Oguiza, *Tsai: A State-of-the-Art Deep Learning Library for Time Series and Sequential Data*, Github, 2022, available at: https://github.com/timeseriesAI/tsai.

[25] K. P. Murphy,*Probabilistic Machine Learning: An introduction*, Cambridge, MA, USA, MIT Press, 2022.

[26] D. Angus, F. Petitjean, and G. I. Webb, "ROCKET: Exceptionally Fast and Accurate Time Series Classification Using Random Convolutional Kernels," in *Data Mining and Knowledge Discovery*, vol. 34, pp. 1454–1495, Sep. 2020, doi: 10.1007/s10618-020-00701-z.

[27] B. Dhariyal, T. Le Nguyen, S. Gsponer and G. Ifrim, "An Examination of the State-of-the-Art for Multivariate Time Series Classification," in *2020 International Conference on Data Mining Workshops (ICDMW)*, Sorrento, Italy, Nov. 2020, doi: 10.1109/ICDMW51313.2020.00042.

[28] H. I. Fawaz et al., "InceptionTime: Finding AlexNet for Time Series Classification," in *Data Mining and Knowledge Discovery*, vol. 34, pp. 1936–1962, Nov. 2020, doi: 10.1007/s10618-020-00710-y.

[29] Z. Wang, W. Yan, and T. Oates, "Time Series Classification from Scratch with Deep Neural Networks: A Strong Baseline," in *2017 International Joint Conference on Neural Networks (IJCNN)*, Anchorage, Alaska, USA, May. 2017.

[30] C. Szegedy et al., "Going Deeper With Convolutions," in *2015 IEEE Conference on Computer Vision and Pattern Recognition (CVPR)*, Boston, MA, USA, 2015, doi: 10.1109/CVPR.2015.7298594.

[31] S. Hochreiter and J. Schmidhuber,*Long Short-Term Memory,* 9th ed, pp. 1735-1780, Cambridge, MA, USA, MIT Press, 1997.

[32] S. Bai, J. Z. Kolter and V. Koltun, "An Empirical Evaluation of Generic Convolutional and Recurrent Networks for Sequence Modeling," in *Computing Research Repository (CoRR)*, Apr. 2018.

Publication 5 (P5)

Title

Physically-Interpretable Data Augmentation for Multi-Range Hand Gesture Recognition Using FMCW Radar Time Series.

Publication Status

Published in peer-reviewed journal: IEEE Transactions on Radar Systems.

Author Contribution

Predominant involvement as a 1. author (co-author confirmation provided).

Bibliographic Information

[71] Y. Hassab, T. Stadelmayer and F. Lurz, "Physically-Interpretable Data Augmentation for Multi-Range Hand Gesture Recognition Using FMCW Radar Time Series," *IEEE Transactions on Radar Systems*, vol. 1, pp. 571-582, Sep. 2023.

Copyright Notice

Physically-Interpretable Data Augmentation for Multi-Range Hand Gesture Recognition Using FMCW Radar Time Series

Youcef Hassab, Thomas Stadelmayer, *Student Member, IEEE* and Fabian Lurz, *Senior Member, IEEE*.

***Abstract*—In this paper, a robust hand gesture recognition (HGR) system using a frequency modulated continuous wave (FMCW) radar and InceptionTime networks on data augmented time series is implemented. The paper proposes multiple data augmentation techniques for radar-based HGR. Since a realistic manipulation of raw radar data frames or even range-Doppler maps is a very complex challenge, we instead propose data manipulation on physically interpretable time series of range, azimuth and elevation angles extracted from the data. Due to working on physically interpretable time series data, we can on the one hand make use of well explored existing augmentation techniques for time series and on the other hand do use-case specific interpretable augmentations, such as simulating a different aspect angle or range. To investigate the system, a data recording process covering multiple ranges, angles and types of gestures is carried out. The gain in accuracy from the proposed data augmentation scheme amounts to more than 4 percentage points to reach a global prediction accuracy higher than 95% for a very diverse dataset.**

***Index Terms*—hand gesture recognition, machine learning, light-weight processing, data augmentation, InceptionTime, FMCW radar.**

I. Introduction

Technology and smart devices have taken a very important place in our lives [1]. We interact with devices such as smartphones, home appliances or the board computer in our cars on a daily basis. Keyboards, mouses and touchscreens are considered to be the most common Human computer interaction (HCI) approaches nowadays [2]. These have achieved a reliable basis for contact-based HCI. However, in some situations a touchless interaction is desirable or even necessary. During the COVID-19 outbreak a touchless interaction became essential to reduce the number of infections. But also in daily lives, when the hands are dirty or wet, e.g. during cooking, a touchless interation is required.

Y. Hassab is with the Institute of Electromagnetic Theory and with the Institute of High-Frequency Technology at Hamburg University of Technology, 21073 Hamburg, Germany (e-mail: youcef.hassab@tuhh.de).

T. Stadelmayer is with Infineon Technologies AG, 85579 Neubiberg Germany (e-mail: thomas.stadelmayer@infineon.com).

F. Lurz is with the Institute of High-Frequency Technology at Hamburg University of Technology, 21073 Hamburg, Germany (e-mail: fabian.lurz@tuhh.de).

Manuscript received March XX, 2023.

Optical sensors and cameras are heavily used in contactless HGR. Although camera based systems have proven to achieve high recognition accuracies, they suffer from a dependency on lightning conditions. Another downside are the privacy concerns around optical sensors, especially in private spaces [3]. Another technology used for alternative HGR are electronic gloves. They require the expensive and often heavy wearable devices which cause discomfort [4]. On the contrary, radar-based HGR offers many advantages. Radars are independent from lighting conditions and are in general less problematic from a privacy point of view. Radar sensors can also capture very small motions and very subtle and precise hand gestures.

Radar-based HGR has achieved very good performances using continuous wave (CW), Ultra-wideband (UWB) and FMCW radar sensors [5], [6], [7]. Implementations on resource constrained embedded devices have been also successfully carried out [8]. Recent works are mainly focused on deep learning (DL) classification, which have shown better results than signal processing methods [9]. Although many of the published works score high prediction accuracies, most only evaluate simple gestures recorded from a single defined angle and range away from the radar, which is not a realistic scenario for HGR systems. For long-range gestures, where the user can stand at different radial and angular positions, significantly more data is required. It has also been shown that in this case very large datasets are needed for representative and robust DL based HGR [8]. The collection of such large datasets is out of the capabilities of most research groups.

To solve this problem, datasets can synthetically be increased by using existing data samples to create new ones. There are well established augmentation techniques in computer vision, such as cropping, scaling brightness or rotating [10]. And although many proposed HGR systems rely on image-like representations such as spectrograms or range-Doppler images (RDIs) [8], [11]–[14], there are not yet well established data augmentation techniques for radar signals. One reason is that augmentations from computer vision, such as scaling brightness, are implausible for radar images. To model realistic data augmentation techniques for radar signals in frequency domains is challenging. Consequently, it was proposed to generate data samples by generative adversarial networks (GANs)

[15]–[17]. GANs can model complex relations, but the interpretability and quality of the output can not be guaranteed [17]. For example, in [17], the generated images are shifted by defined rules to ensure outputs that are compatible with the kinematics of human motions. The extraction of these rules is not simple. There are also further approaches to data augmentation, e.g. with physics-based RF data synthesis and skeleton-level data augmentation which provide promising results that come at the expanse of further modeling [18], [19].

In [20] and [21], it was shown that complex data representations in frequency domain are actually not required for HGR. Modeling the hand as a time series of several interpretable features leads to superior results and a better generalization capability to new users both in terms of accuracy and latency. Compared to [21] where RDIs are calculated as an intermediate step, the authors in [20] propose to extract the time series features directly from the raw radar data with the usage of a range-gating implemented by multiplying and accumulate each chirp with a complex valued sinc filter. The hands motion is consequently compressed to a one dimensional complex-valued slow-time signal from which the hand's relative change in range, azimuth, elevation and magnitude can be derived. The authors proved the concept on ten gestures executed in close range in front of the radar.

This paper extends the work in [20] and proves the concept for additional gestures and user positions up to a distance of 1.5m and at different angular positions. As the time series representation is physically interpretable, it allows us to derive simple augmentation techniques for this kind of data representation. Complex modelling techniques are not required. Instead we propose two simple augmentation techniques for the time series representation that specifically address variations of the user's position in range or angle, respectively. The advantage of the proposed data augmentation method is that it can be applied directly to the recorded and preprocessed data. Due to the relatively simple scaling and warping in the time domain, different gesture executions and motion speeds can be represented without the need for a (complex) physical model. We demonstrate on real world data the effectiveness of the proposed data augmentation techniques. The main contributions of this paper can be summarized as follows:

1) Extension of the light-weight time series based HGR scheme to a wider variety of scenarios including different ranges, angles and types of gestures.
2) Demonstration of the limitations of single point HGR systems in realistic scenarios.
3) Exploration of general and targeted data augmentation and its potential in improving the performance and robustness of time series based HGR systems in realistic settings.
4) Proposal of two purpose specific and physically-interpretable data augmentation techniques. One addresses different radial positions of the users whereas the other addresses variations in angular position. The effectiveness is demonstrated on a real recorded dataset.

The rest of the paper is structured as follows: in Chapter 2, we introduce the basic hardware hardware used with given settings and the data acquisition paradigm. In Chapter 3, the preprocessing steps that lead to samples ready for classification are highlighted. In Chapter 4, we present the machine learning based gesture classification networks and their evaluation. In Chapter 5, we explore the field of data augmentation to enhance the detection capabilities in realistic scenarios. Chapter 6 summarizes the work and provides an outlook for the future.

II. Radar System and Data Recording

The used FMCW radar hardware and its configuration are highlighted. The defined gestures set and the data recording process are presented.

A. Hardware System

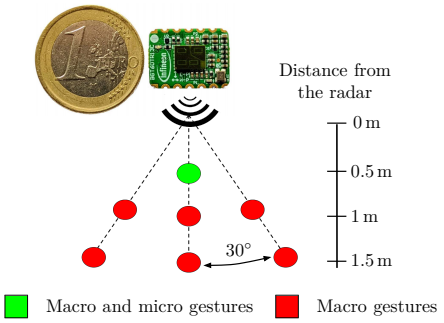

Fig. 1: Radar device and recording setup.

The 60-GHz BGT60TR13C FMCW radar chip from Infineon Technologies is used for the gesture recognition system presented in this work. The chip package of the radar has dimensions of 6.5 mm × 5.0 mm × 0.9 mm. A picture of the radar chip next to a 1€ coin for comparison is shown in Fig. 1. The radar is very compact and easily integrable in mobile and embedded systems. Its high operating frequency allows for high resolution sensing and thus makes it suitable for macro and micro HGR. The radar consists of four antennas, 1 transmit and 3 receive antennas ordered in an L-shape with half a wavelength distance to two neighboring receiving antennas. This configuration allows an angle estimation of the target in azimuth as well as elevation direction. The radar has an operational frequency range of 57 GHz to 64 GHz, a free adjustable chirp frequency and chirp duration. A phase-locked loop (PLL) with a reference frequency of 80 MHz regulates the voltage-controlled oscillator (VCO). The divider value of

the PLL and an additional tuning voltage allows the configuration of the chirp frequency bandwidth and duration. The back-scattered signal is received by each of the three antennas and mixed with the transmitted signal to get the intermediate frequency (IF) signal. The IF signal is then low pass filtered and amplified. An analog-to-digital converter with a sampling frequency of 2 MHz and a 12 bit resolution converts the signal into a digital form for further processing.

TABLE I: Radar configuration and resulting parameters.

Parameter	Value
Start frequency f_{min}	58 GHz
Stop frequency f_{max}	63 GHz
Bandwidth B	5 GHz
Samples per Chirp N_s	256
Chirps per Frame N_c	32
Number of Frames per Recording F	60
Chirp Repetition Time T_{crp}	400 µs
Frame Repetition Time T_{frp}	30 ms
Sampling Rate f_s	2 MHz
Maximum Unambiguous Range R_{max}	1.92 m
Range Resolution σ_r	0.03 m
Maximum Unambiguous Speed v_{max}	$\pm 3.2 \frac{\text{m}}{\text{s}}$
Speed Resolution σ_v	$0.2 \frac{\text{m}}{\text{s}}$

For our purposes, the chip has been configured to generate chirps swinging from the start frequency $f_{min} = 58\,\text{GHz}$ to the stop frequency $f_{max} = 63\,\text{GHz}$ within a chirp time of $T_c = 64\,\mu\text{s}$. The following radar parameters are derived using the formulas introduced in [22]. The total bandwidth of $B = 5\,\text{GHz}$ results in a range resolution of $\sigma_r = 0.03\,\text{m}$. Each chirp is sampled $N_s = 256$ times (fast-time). A maximal detectable unambiguous range of $R_{max} = 3.84\,\text{m}$ is calculated using the sampling rate of $F_s = 2\,\text{MHz}$. A sequence of $N_c = 32$ chirps (slow-time) with a repetition time of $T_{crp} = 400\,\mu\text{s}$ constitutes a single frame. This leads to a stream of chirps with equal idle time between consecutive chirps and a speed resolution of $\sigma_v = 0.2\,\frac{\text{m}}{\text{s}}$. The maximum detectable speed is calculated at $v_{max} = \pm 3.2\,\frac{\text{m}}{\text{s}}$. The frame repetition time is set to $T_{frp} = 0.03\,\text{s}$. $F = 60$ frames are compiled together to constitute a single recording of a certain gesture. This results in a window of $T_r = 1.8\,\text{s}$ where a gesture is recorded within the 60 frames. The radar configuration and resulting parameters are compiled in Table I.

B. Gesture Set

A total of 10 hand gestures have been defined. The gestures are split into 6 macro and 4 micro gestures. Macro gestures are gestures that are executed using the arms or the whole hands, while micro gestures are gestures executed using the fingers only. The 10 hand gestures used for our study are pictured in Fig. 2 and described as follows:

- Swipe up: a hand swipe using the whole arm from the bottom to the top side.
- Swipe down: a hand swipe using the whole arm from the top to the bottom side.
- Swipe left: a hand swipe using the whole arm from the right to the left side.
- Swipe right: a hand swipe using the whole arm from the left to the right side.
- Scroll up: a finger scroll from the horizontal position upwards.
- Scroll down: a finger scroll from the horizontal position downwards.
- Finger pinch: a double tap of the index and thumb fingers on a horizontal plane.
- Finger no: a fast index finger metronome motion from a side to the other.
- Push: a hand push from the body outwards in the radar direction.
- Wave: a hand wave movement in front of the body towards the radar.

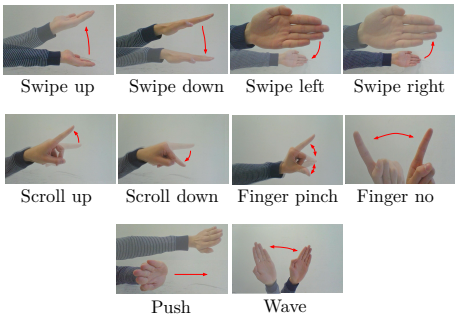

Fig. 2: Graphical representation of the defined gestures.

C. Data Acquisition

An experimental setup has been put in place in order to record subjects performing the defined gestures. The recorded gestures provide the necessary data to train the deep-learning models. A tripod containing the radar is placed on a table and brought to an adequate height. The radar is fixed at a height of 1.2 m above ground level and faced towards the subjects. A number of 7 recording positions were marked. The positions are distinguished by a unique combination of the distance from the radar and azimuth angle from the plane the radar is facing.

There are 3 different possible distances from the radar: 0.5 m, 1 m and 1.5 m. We also distinguish 3 different possible azimuth angles: 0°, −30° and 30° from the plane the radar is facing. The gestures recorded from the 0.5 m short-range were only performed in front of the radar from the 0° angle, ignoring the −30° and 30° angles. This is due to the resolution of the angle estimation that is very limited at the fringes of the field of view of the radar. The recording positions are depicted in Fig. 1. The micro gestures are only recorded from short-range since a high resolution is needed to be able to distinguish the micro motions of the fingers. The macro gestures are recorded from all the 7 positions.

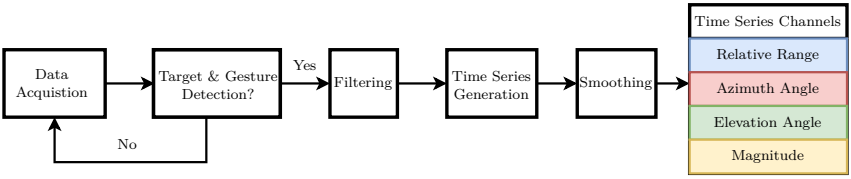

Fig. 3: Block diagram of the preprocessing pipeline.

In total, 24 subjects have taken part in the data acquisition. 20 subjects were right-handed while 4 subjects were left-handed. The number of repetitions has been set to make the recording sessions pleasant for the recorded subjects. In total, 3.852 samples and 22 GB of data have been recorded. The dataset is fully balanced as the same number of gestures has been recorded per subject and position.

III. Data Preprocessing

The raw data from the radar are passed through a series of preprocessing steps. This brings the data into a form suitable for training, classification and detection. The algorithm reduces the raw data to four 1D time signals containing information about the range, azimuth angle, elevation angle and magnitude. Fig. 3 represents an overview of the preprocessing pipeline. After a gesture performance is detected, the raw data from the radar is filtered. The resulting complex filtered signals are used to generate the time series. After smoothing, the resulting channels are used for classification. The different steps are described in more detail in the following sections.

A. Target Detection and Filtering

The very first step is a target detection in the range profile. Only if a target is detected over multiple frames in the same range bin, and therefore ensuring a standing person, the gesture recognition system gets activated. Once a person is detected, a first adaptive sinc filter is initialized at the person's position. In [23], an approach is proposed to track the target's slow-time and fast-time frequencies by a regulation loop, which progressively adjusts the filter's center frequency to the target location. All this works without the need to constantly make complex fast Fourier transformation (FFT) calculations to estimate the target's position. Only one FFT estimation is needed at the start. This approach is adapted and implemented in our work to only take into account fast-time frequencies and track the target's range. A hand gesture performance is detected when the energy of the received signals exceeds a dynamic tuned threshold level that depends on the target's range. When the start of a gesture performance is detected, a second sinc filter with a fixed bandwidth is initialized right in front of the subject. This band-pass filter is intended to filter out the human body itself and other noise sources and to only catch the hand motion, which is by nature executed shortly in front of the users body as shown in Fig. 4. If the user changes position, then the second sinc filter follows the first filter and adapts its center frequency accordingly. This means our system automatically filters noise sources out and only keeps signals from the area of interest where the hand is present during the performance.

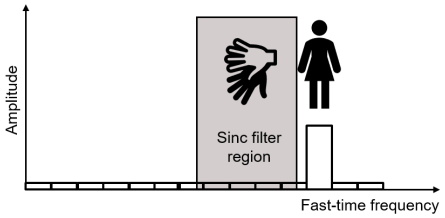

Fig. 4: Exemplary visualization of the gesture detection zone or the sinc filter right in front of the users body.

B. Time Series Generation

The generation of time series is based on the algorithm proposed in [20]. Unlike in the original paper where the range-FFT is replaced by a convolution and accumulation of each chirp signal with a low-pass filter, we use the complex valued band-pass sinc filter previously described since we do not only record gestures from short-range close to the radar. The resulting complex signal is used to extract the featured channels:

- Relative range: extracted using chirp to chirp phase difference, represents the relative change of the range between the hand and the radar from the starting position.
- Azimuth angle: extracted using an accumulation of phase differences between the signals of the two horizontal antennas, the slope represents the actual angle of arrival in azimuth direction.
- Elevation angle: extracted using an accumulation of phase differences between the signals of the two vertical antennas, the slope represents the actual angle of arrival in elevation direction.
- Magnitude: extracted using the average amplitudes of the signals from the three receive antennas, reflects the amplitude of the received signals.

TABLE II: Comparison of different preprocessing schemes using spectrograms, complex RDI and the time series processing.

Approach	Preprocessing exec. time	Network exec. time	Accuracy (full data)	Accuracy (1/3 data)
Spectrograms	475 ms	83 ms	96.7%	79%
complex RDI	160 ms	210 ms	90.4%	52.8%
Time series	101 ms	74 ms	96.9%	85.9%

C. Time Series Smoothing

The last step of the preprocessing is the smoothing of the time series using a Savitzky-Golay filter. It is a digital filter that can be applied to a set of digital data points for the purpose of smoothing the data. This serves as a noise filter basically by smoothing very small fluctuations in the time series due to noise while keeping the structure and features of the time series.

The preprocessing results in four channels time series that are interpretable and easily manipulated. Moreover, processing a data frame with N_c chirps and N_s samples per chirp has a computational complexity of only $O(N_c N_s)$ in comparison to RDI processing that has a computational complexity of $O(N_c N_s log(N_c N_s))$. When tested on close range datasets in combination with convolutional neural networks (CNNs), the time series preprocessing showed better accuracy, generalization and latency as depicted in Table II. This is translated into faster processing and prediction executions and better accuracy even on smaller datasets. We note however, that these results are dataset dependent. These advantages, among others, motivated the exploration and extension of the time series preprocessing scheme [20]. Fig. 5 represents an exemplary plot of the time series resulting from the described preprocessing for a 'push' gesture. Each color represents a different subject.

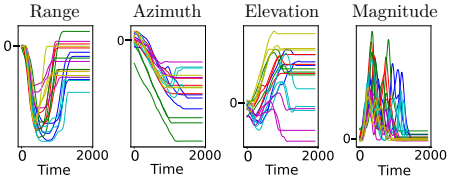

Fig. 5: Exemplary plot of the four channels of a "push" gesture recorded by multiple subjects.

IV. Evaluation of classification networks

This section describes the used InceptionTime networks, the training procedure and the results of the classification using the recorded samples.

A. Training of InceptionTime Networks

In this work, we mainly use InceptionTime models. InceptionTime has proven to be very accurate when it comes to time series classification. In comparison to other state-of-the-art models like hive-cote, InceptionTime is many folds more efficient in the training process. The fact that InceptionTime architectures use filters with different kernel sizes makes the learning of local and global dependencies in the time series possible. The introduction of InceptionTime, benchmarking, general architecture and principle are explained in depth in [24].

The first step before we proceed to fully train our models is to optimize the architecture. For the purpose of hyperparameter investigation and optimization, we use Optuna [25]. Optuna is an open source hyperparameter optimization framework to automate the hyperparameter search. The chosen architecture is an optimal trade-off between performance and complexity. Complexity refers to the number of trainable parameters and model size that directly impact the inference time. This optimal model shall be useful when investigating our datasets, where we need to train the same architecture a large number of times. Another advantage that the reduced complexity offers is a quicker prediction when subjected to an input. This can be crucial when designing a live running HGR system, where the lag between the gesture performance and prediction is important. The optimal model has the default number of filters 32 and a bottleneck layer. The default depth of 10 has been used. The kernel size has been increased to 80.

After setting the proper architectures for our model, we proceed to train and evaluate the models using different datasets in this section. An Adam optimizer has been used to update the weights for crossentropy minimization [26]. A training-validation data split of 80%/20% is performed on the datasets. The same random state generator number has been used to make the models comparable. The samples are loaded in batches of 64. The learning rate is found before each training process. The optimal learning rate is chosen after estimating the initial loss after an epoch of training for different learning rates. The learning rate that results in the fastest decrease in the loss is chosen. This results in the best outcomes according to the published paper on cyclical learning rates for training neural networks [27].

B. Evaluation of results

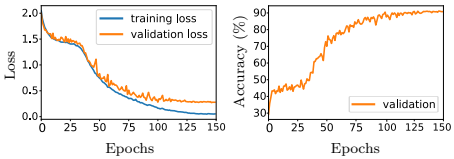

Fig. 6: Training and validation metrics of the full model.

We first train the full model using the complete dataset at our disposition. The complete dataset contains all avail-

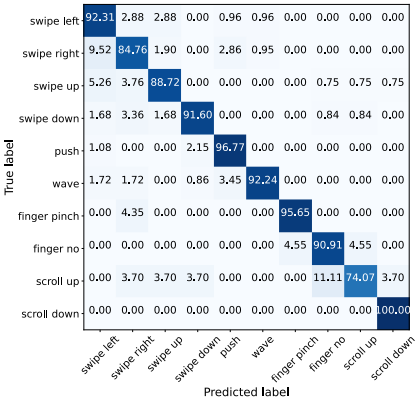

Fig. 7: Confusion matrix of the full model.

able recordings and all gestures from all defined positions. Fig. 6 represents the results of the training process using the full dataset. We can see the evolution of the training and validation losses over the epochs. When taking a more precise look at the losses in the final stages, we can see that we have reached a convergence phase where the losses no longer go down, thus we stop the training at the 150 epochs mark. The reached accuracy after 150 epochs of training is 90.79%. the overall prediction accuracy, higher than 90% is very decent and promising, considering the complex nature of having 10 micro and macro gestures recorded from different ranges and angles. Fig. 7 represents the confusion matrix of the full model. We can see that the percentage of correctly predicted labels differs depending on the gesture. Some gestures are well detected and predicted like the "push", "finger pinch" or "scroll down" gestures, all having prediction accuracies of more than 95%. Some gestures are relatively poorly categorized such as the "scroll up" or the "swipe right" gestures with prediction accuracies lower than 85%. Some gestures are often confused for each other, like the "right swipe" gesture misinterpreted as a "left swipe" gesture, or the "scroll up" misinterpreted as a "finger no" gesture in 10% of the cases. The similarity in the gesture executions explains some higher confusion rates than others.

In the next step, we are interested in the behavior of our trained models on all available samples when presented with unseen data from scenarios they were not trained upon. We take samples from our training and testing sets and split them according to the distance and angle of the recording. This results in samples from the 0.5 m, 1 m and 1.5 m ranges and samples from central 0° angle and the −30° and 30° angles. The −30° and 30° samples have been lumped together as "angular" samples. Three models are used for the following investigation. The first model is the full model previously described and trained on all available samples from all three ranges and angles. The second model is the 1 m model, trained only on samples recorded from the 1 m range. The third model is the 0° model, trained only on central samples omitting angular recordings. The three models are trained independently and tested on available test samples.

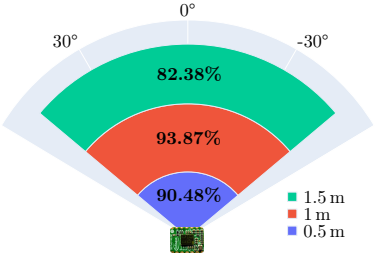

Fig. 8: Prediction accuracy of the full model on different ranges.

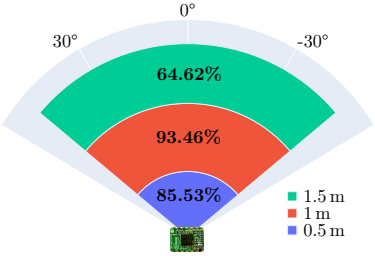

Fig. 9: Prediction accuracy of the 1m model on different ranges.

Fig. 8 represents the prediction accuracy of the full model for different ranges. We can see that the 1.5 m samples are the hardest to predict with just over 82%. This can explained by the lower magnitude of the reflected signal considering the large distance between the radar and subject. Another factor is the lower angular span or resolution when it comes to angle estimation. The 1 m samples are the easiest and most accurate to predict with an accuracy of approximately 94%. This is because they only contain the six macro gestures and the signal magnitude is 5 times higher on average than the 1.5 m range. In comparison, the 1 m model showcased in Fig. 9 suffers from a loss in prediction accuracy for both unseen samples from the 0.5 m and 1.5 m ranges. The loss in accuracy for the 1.5 m range amounts to more than 15 percentage points (pp) when compared with the more complex 10 classes full model.

Fig. 10 shows the prediction accuracy of the full model on different angular samples. The prediction accuracy

for angular samples is lower than the average accuracy with approximately 86% prediction accuracy. This can be explained by the lower azimuth angle resolution when in the fringes and edges of the field of view. Also, the relative range profile of the gestures from angular samples differs from the central samples slightly, which might lead to confusion. The 0° model suffers greatly in the prediction of angular samples not trained upon as shown in Fig. 11. The drop in accuracy in the prediction of angular samples amounts to approximately 60 pp in comparison to the full model.

The last results highlight how our models react relatively poorly to scenarios that they were not exposed to in the training process. This shows the need of an extensive and expensive data recording process containing various distances and angles. This way, the HGR can better predict gestures from different distances and angles, which is a more realistic scenario in a real life setting for most applications. To the best of the authors knowledge, the published works until now generally use recorded gestures from a fixed point away from the radar. Although very good results are found in the literature, this begs the questions of how well these systems react when the subjects deviate slightly or greatly from these experimental designed spots. In the next section, we explore and propose targeted data augmentation techniques and highlight their potential in replacing the expensive data recording process. This way, robust systems can be created with less data and without the need to cover all scenarios in the recording process.

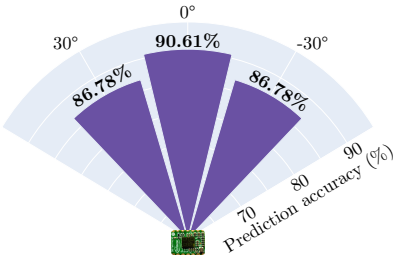

Fig. 10: Prediction accuracy of the full model on different angles.

V. Data Augmentation

In this section, the use of data augmentation techniques is explored. The usefulness of data augmentation in regard to the performance under different scenarios is investigated. Data augmentation is the process of generating synthetic samples from real recorded samples. These synthetic samples are then added to the original datasets to increase the size of available samples. This is usually done to increase the generalization ability of machine learning models, especially when the original datasets are

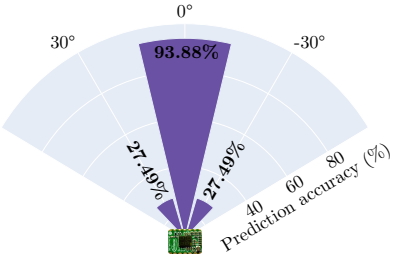

Fig. 11: Prediction accuracy of the 0° model on different angles.

small. Data augmentation can also be used to fill in gaps, missing points or to add relevant data that was not covered in the original sets. Data augmentation has shown to be an effective model-independent method of reducing overfitting and expanding the decision boundary modeled by the data [28]. Data augmentation techniques have already been successfully used on time series data with various degrees of achieved improvements depending on the datasets [29].

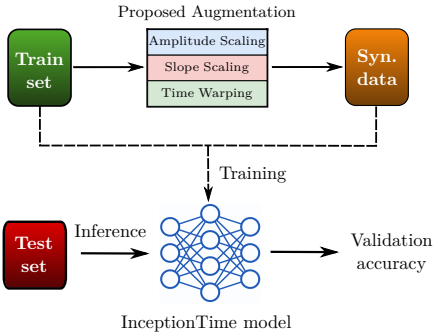

Fig. 12: Data Augmentation Framework.

The proposed data augmentation and evaluation framework is summarized in Fig. 12. First, the datasets of interest are loaded and split as usual in training and testing sets. Synthetic data is then created from the training sets only using a combination of amplitude scaling or slope scaling and time warping depending on the scenario. The choice of these three time series augmentation techniques as well as their use and hyperparameter determination are explained in the sections V-A, V-B and V-C for each scenario. These synthetic data are then added to the original training sets. The resulting samples are used to train the models. To objectively evaluate the performance, the original testing sets are fed to the trained network. The prediction accuracy is then evaluated on these test sets.

This way, it is ensured that the data tested on has not been seen by the trained network beforehand. Not only that, but training the networks using synthetic data created from the test tests is avoided. Synthetic data created from certain samples tend to show similarities to the samples they were created from. This means that if we were to use synthetic data from test sets, the test sets would become familiar to the network and the prediction accuracy would be much higher when comparing to completely unseen data.

A. Full Model

As a start, data augmentation effects on the general performance using the full dataset containing all available samples are investigated and evaluated. Different time series augmentation techniques and their outcomes are explored. Many published state-of-the-art techniques are evaluated and compared with own proposed methods. The used techniques from published sources are: Suboptimal Warped Time-Series Generator (SPAWNER) [30], Weighted Discriminative Time Warping Barycenter Averaging (wDBA) [31], Random Guided Warping (RGW) [29] and Discrimintaive Guided Warping (DGW) [29].

In addition, a data augmentation approach that is based on the analysis of available samples and rules deducted from the physics of the problem is proposed. Looking at the samples from Fig. 5 as an example, we can see a general similarity in the structure of the time series even when the subjects are different. The time series differ in their span across the time axis. They also show different scalings across the y-axis. These differences are also in accordance with the physics of the problem. The performed gestures naturally vary in their speed of execution. Some subjects are quicker than others in the performance. This is reflected by the different span in the time axis. The reach of the subjects in the radial range direction as well as in azimuth and elevation directions is also different. This is reflected by the difference in amplitude. Using these observations, we implement an algorithm to create synthetic data on the basis of time warping and amplitude scaling. For our amplitude scaling, we first draw a random number from a normal Gaussian distribution with mean μ and standard deviation σ:

$$\alpha = |z \sim N(\mu, \sigma)| \tag{1}$$

We then multiply the vectors of the four channels of a sample x with the random factor α. This results in the amplitude scaled sample x_{scaled}:

$$x_{scaled} = \left[x_{range}, x_{azimuth}, x_{elevation}, x_{magnitude}\right] \cdot \alpha \tag{2}$$

The mean and standard deviation of the Gaussian distribution are set to provide reasonable factors that result in samples in the vicinity of the real samples. We settle for a mean value of $\mu = 1$ and a standard deviation of $\sigma = 0.3$. Although most of the randomly sampled numbers are positive and in the vicinity of the mean, we still take the absolute value of these sampled numbers before multiplication. This is for the extreme case where a negative number is sampled and the time series are flipped. The latter case would result in a meaningless time series that are more confusing to our network than helping in generalization.

For the time warping, we make use of the tsaug library [32]. We use the TimeWarp function which is an implementation of the stretching or compression in time. The function takes two main parameters: the number of speed changes N_v and the maximum speed ratio R_v. The number of speed changes divides the time series into sections to be expanded or compressed. The maximum speed ratio sets the limit of the positive interval from which compression and expansion factors are chosen. We choose empirically determined number of speed changes $N_v = 2$ and maximum speed ratio $R_v = 1.8$. A synthetic sample $x_{synthetic}$ is created using the TimeWarp function on a scaled sample x_{scaled}:

$$x_{synthetic} = TimeWarp(x_{scaled}, N_v, R_v) \tag{3}$$

The hyperparameters are selected empirically to result in kinematic fidelity to real samples and hence the physical interpretable part. We mimic slight variations in the hand reach and speed of execution reflected in the span across the magnitude and time axis. By using the recorded time series of the different subjects, we try to stay within realistic bounds around the real samples. This is done by analyzing the average differences between subjects. Synthetic data from real training samples using the aforementioned algorithms are generated. The synthetic samples created by each of the introduced techniques are mixed with the original training samples. The resulting datasets are used to train the models. For the proposed augmentations, we train different models with an increasing number of synthetic samples added to the training set. The results of the evaluation are represented in Fig. 13. The prediction accuracy increases with the amount of synthetic data added until it reaches saturation for a training set 4 times larger than the original dataset. The model with a training dataset that is twice as large as the original set is referred to as the single augmentation model (SAM). The model trained with datasets that are four times as large as the original is referred to as the multiple augmentation model (MAM). The RGW, DGW, SPAWNER and wDBA models are trained using one additional synthetic sample from each real sample generated using the algorithm named after. One last model has been trained by using the samples created by the RGW and DGW together, it is referred to as the RGW+DGW model. The training samples for the last model are then thrice as large as the original. The results of the evaluation are depicted in Fig. 14.

We can see the achieved accuracies for each model and the difference in accuracy when compared with the non-augmented model. The MAM model that has been trained with the help of multiple augmentations using our proposed techniques has the best performance. This model

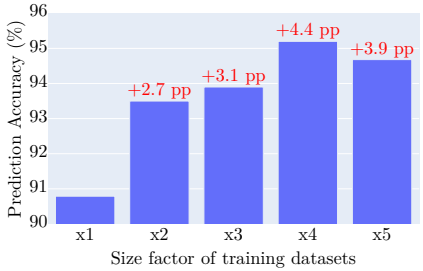

Fig. 13: Prediction accuracy of the models trained on the proposed augmented datasets as a function of the training set size. The size is marked by a factor of the original non augmented dataset size.

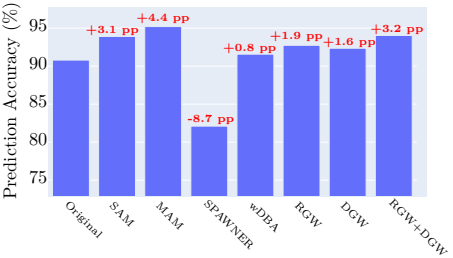

Fig. 14: Prediction accuracy of the trained models on augmented datasets.

achieved a prediction accuracy higher than 95%. This marks an increase of 4.4 pp in the accuracy when compared with the non-augmented model. The SAM model achieves a prediction accuracy of 93.5%, comparable to the RGW+DGW model augmented using samples from both RGW and DGW methods together. This marks an increase of approximately 3 pp. The RGW, DGW and wDBA models resulted in a slight increase in accuracy under 2 pp. The SPAWNER was the only model resulting in a decrease in accuracy when compared to the non-augmented model. In an other experiment, the data has been split by subject. Samples from 5 subjects has been used for the testing only and the remaining 19 subjects have been used for the training of the network. The proposed data augmentation techniques have been applied on the training set only and trained a new model equivalent to the 'MAM' model. The accuracy was then tested on the unseen test subjects only. The non-augmented model showed a prediction accuracy of 87.1429% while the augmented model showed an accuracy of 87.8571%. This represents an increase of 0.7 pp.

B. 1 m model

In this part, we are interested in enhancing the reliability of the 1 m model previously introduced using targeted physically interpretable data augmentation. For this purpose, the differences in the samples of a certain gesture from the different ranges are analyzed. The most obvious difference between the time series from the three ranges would be the difference in magnitude of the received back-scattered signals. A lower magnitude in the absolute value channel from gestures recorded from the long 1.5 m range than the 1 m recorded samples are expected. The 0.5 m samples are expected to have a higher absolute value magnitude than the 1 m samples. Since the first channel represents a relative range, recordings from a further range are expected to be smaller in scale than those from closer range. Fig. 15 shows an exemplary plot of the "push" recorded gesture of a single subject from the three different ranges. Each color represents a different range the gesture was recorded from. Three repetitions of the same gesture and position are plotted. We can clearly see that the relative range and magnitude time series follow the same trend but have a difference in the scaling between the three different ranges. The differences in the angle channels are minimal. The idea is to try and replicate these effects. We want to pick samples recorded from the 1 m range, then use them to create synthetic samples that emulate the same gesture being recorded from the 0.5 m and 1.5 m range.

To this end, similar methods to the amplitude scaling from the previous section are used. Two random factors α and β from two Gaussian distributions are sampled. The mean and standard deviation of the Gaussian distributions for the sampling of α and β are set differently:

$$\alpha = |z \sim N(\mu_\alpha, \sigma_\alpha)| \tag{4}$$

$$\beta = |z \sim N(\mu_\beta, \sigma_\beta)| \tag{5}$$

The relative range and the absolute value channels of a 1 m sample are then multiplied with the α and β factors respectively:

$$x_{synthetic}[magnitude] = x_{magnitude} \cdot \alpha \tag{6}$$

$$x_{synthetic}[range] = x_{range} \cdot \beta \tag{7}$$

The different mean and standard deviation of the distributions depend on whether we want to up-scale our sample, thus emulating a 0.5 m sample or down-scale, thus emulating a 1.5 m sample. To get a synthetic 0.5 m, values of $\mu_\alpha = 5$, $\sigma_\alpha = 0.2$, $\mu_\beta = 2$ and $\sigma_\beta = 0.3$ are chosen. To get a synthetic 1.5 m, values of $\mu_\alpha = 0.5$, $\sigma_\alpha = 0.15$, $\mu_\beta = 0.2$ and $\sigma_\beta = 0.2$ are chosen.

These values have been empirically determined after analyzing the average differences in the relative range and magnitude channels peaks of single subjects between the real 0.5 m, 1 m and 1.5 m samples. The average of the differences is used to calculate the augmentation multiplication factor to replicate these differences that would occur naturally in samples of different ranges. Fig. 16 represents

exemplary 0.5 m and 1.5 m synthetic samples created using a real 1 m sample. From each 1 m real samples from the training samples two synthetic samples emulating the 0.5 m and 1.5 m ranges are created. We shall call the model trained using the synthetic samples alongside the real samples the 'augmented 1m model'. A comparison of the prediction accuracy of the non-augmented and augmented 1 m models is depicted in Fig. 17. We can see that the augmented model outperforms the non-augmented model when predicting samples from 0.5 m, 1 m as well as the 1.5 m range. The augmented model predicts the samples from the 0.5 m, 1 m and 1.5 m ranges with accuracies of 89.81%, 96.15% and 81.94% respectively. In the 0.5 m range, the augmented model shows an increase of more than 4 pp in accuracy. In the 1.5 m range, the augmented model outperforms the non-augmented model by more than 17 pp.

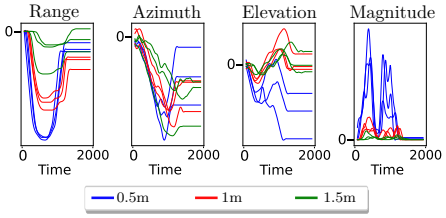

Fig. 15: Exemplary plot of a "push" gesture recorded by a single subject from the three different ranges.

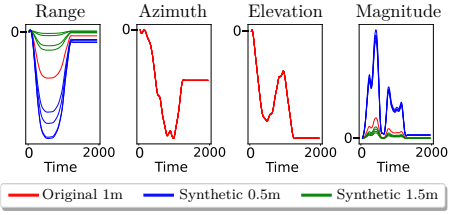

Fig. 16: Exemplary plot of synthetic data created from a real sample to account for range effects.

C. 0° model

In this part, we are interested in enhancing the 0° model trained only on samples taken from central recording positions in a way that makes a reliable prediction from the angular positions possible. We first analyse the differences in the samples taken from the 0°, −30° and 30° angles. Taking the physics of the problem at the hand into account, we expect some differences in the samples from a certain gesture recorded from different angles. We first expect a difference in the slope of the azimuth angle channel. Since the slope of the azimuth time series can be

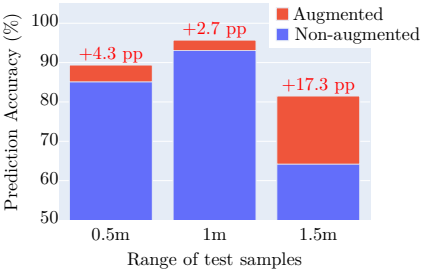

Fig. 17: Prediction accuracy of the augmented and non-augmented 1m models on test data from different ranges.

interpreted as the angle of arrival in the azimuth plane, a gesture recorded from the three different azimuth angles would result in a different slope.

Fig. 18 shows an exemplary plot of the "push" gesture. The recordings are from a single subject from a 1 m range. Each color represents a different angle the gesture was recorded from. Three repetitions of the same gesture and position are plotted. In the "push" gesture samples, we can clearly see the difference in the slope of the azimuth angle plots. No major changes are observed in the other four channels.

The idea is to try to replicate this effect. We want to pick samples recorded from the 0° angle then use them to create synthetic samples that simulate the same gesture being recorded from the −30° and 30° angles. For this purpose, we proceed as follows: first, the azimuth channel of a real 0° sample $x_{azimuth}$ is picked. The interval $x_{detected}$ with length L which represents the detected gesture is identified and extracted. This means that the constant non relevant part of the preprocessed gesture recording is excluded:

$$x_{azimuth} = [a_0, a_1, ..., a_{1919}] \tag{8}$$

$$x_{detected} = [a_0, a_1, ..., a_{L-1}] \tag{9}$$

A vector v that has the same length L as the relevant gesture interval is created. This vector has entries that form a straight line with a defined slope γ. The slope of the added vector is again set by taking the absolute value of a random number from a Gaussian distribution with mean μ_γ and standard deviation σ_γ:

$$\alpha = |z \sim N(\mu_\gamma, \sigma_\gamma)| \tag{10}$$

$$v = [\gamma \cdot 0, \gamma \cdot 1, ..., \gamma \cdot (L-1)] \tag{11}$$

This vector is added to the relevant part of the azimuth angle channel. As a last step, the last value b_{L-1} of the resulting vector x_{rel} is repeated to extend its length to the standard 1920 time stamps. This way a synthetic azimuth angle channel $x_{synthetic}[azimuth]$ with a changed slope is created:

$$x_{rel} = x_{detected} + v = [b_0, b_1, ..., b_{L-1}] \tag{12}$$

$$x_{synthetic}[azimuth] = [b_0, b_1, ..., b_{L-1}, ..., b_{L-1}] \quad (13)$$

A TimeWarp similar to the one introduced in the previous sections is also applied. μ_γ depends on whether we want to upscale a sample, thus simulating a $-30°$ sample or downscale, thus simulating a $30°$ sample. For up-scaling, a mean value of $\mu_\gamma = 0.5$ and for down-scaling, a mean value of $\mu_\gamma = -0.5$ are set. The standard deviation is set to $\sigma_\gamma = 0.2$. The mean values have been empirically determined after calculating the average change in the slope from the real $0°$ to $-30°$ and $30°$ samples of single subjects. From each $0°$ real sample from the training sets two synthetic samples simulating $-30°$ and $30°$ samples are created. Fig. 18 shows exemplary $-30°$ and $30°$ synthetic samples created using a real $0°$ sample. These synthetic samples are used to augment the $0°$ training dataset. We then train a model on these augmented sets. We shall call this model the 'augmented $0°$ model'. A comparison of the prediction accuracy of the non-augmented and augmented $0°$ models is found in Fig. 20. We can see that our augmented model outperforms the non augmented $0°$ model when predicting angular samples. The augmented model predicts the central $0°$ samples with an accuracy of 94.35% and angular samples with an accuracy of 64.12%. The non-augmented model predicts the central $0°$ samples with an accuracy of 93.88% and angular samples with an accuracy of 27.49%. This marks a small increase in central sample prediction and an increase of more than 35 pp in the prediction of angular samples. The full model where real angular samples are available scores higher than the synthetically augmented $0°$ model.

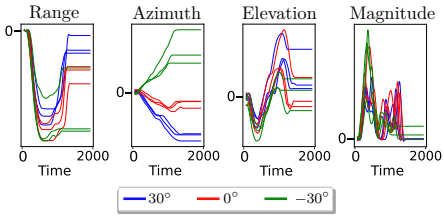

Fig. 18: Exemplary plot of a "push" gesture recorded by a single subject from the three different angles.

D. Discussion:

The performance of the 1 m and the $0°$ models highlight how our networks react relatively poorly to scenarios that they were not exposed to in the training process. This shows the importance of a data recording process containing multiple distances and angles in the design of HGR systems. This way, the models can better predict gestures from different distances and angles, which is a more realistic scenario. To the best of the author's knowledge, the works published to date generally use recorded gestures from a fixed point off the radar. Although very good

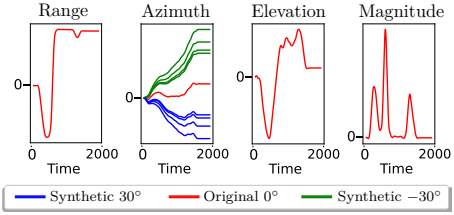

Fig. 19: Exemplary plot of synthetic data created from a real sample to account for angle effects.

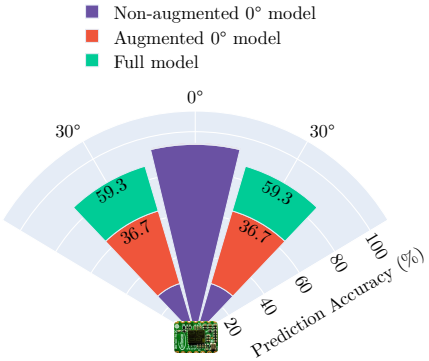

Fig. 20: Prediction accuracy of the non augmented, augmented $0°$ and full models on test data from different angles. The gain in accuracy in pp is marked on each bar.

results are reported, the question of how well these systems respond when subjects deviate from these experimental recording and testing points still stands. In our case, we showed that systems only designed for a certain range, angle or scenario suffer greatly when deviating from the designed settings.

The performance of the augmented 1 m and $0°$ models show that we can successfully create specific synthetic samples that emulate certain scenarios and recording points. This makes it possible to reinforce models without the need to cover all scenarios in the recording process. This can save tremendous costs and efforts in the data recording processes. Data augmentation also has the positive effect of boosting the performance even when real samples are available, as shown with the augmented SAM and MAM models with gains of 3.1 pp and 4.4 pp in the overall accuracy respectively. By using data augmentation, we can emulate real recordings by creating synthetic data from phantom subjects. Robust HGR systems for public use for example need to recognise the gestures performed by so many different people. Each user executes the gestures slightly differently than the other. Which means that

the HGR networks have to be exposed to gestures from as many subjects as possible to make reliable predictions. The process of recording a large amount of subjects is a time and resources consuming process. By using data augmentation, we can increase the effective number of different recorded subjects without the need to actively record every subject. This can save a lot of time and resources tied to the recording process.

VI. Conclusion

A robust HGR system using an FMCW radar, InceptionTime networks and a light-weight preprocessing scheme has been implemented. Own recorded data for training the classification models have been used. The trained models have been rigorously tested. The model trained on full dataset containing micro and macro gestures from three different ranges and angles has shown a prediction accuracy higher than 90%. We have shown the robustness of the classification in a wide variety of scenarios including different angles and distances from the radar as opposed to other works. We demonstrated the limitations of HGR systems using samples from only a single recording point. In a first, we have explored of data augmentation on HGR time series and the effects on the performance and reliability. We have successfully improved the accuracy of classification models using data augmentation with a prediction accuracy of more than 95% for a challenging dataset. Moreover, we proposed a targeted physically interpretable synthetic data creation scheme to enhance the robustness of the classification for different ranges and angles the models were not initially trained on. The combination of the time series based preprocessing and InceptionTime networks is very promising for HGR as the achieved performances show. The recording process should include as many variables as needed depending on the application for robust radar-based HGR. This process is usually very time and resources consuming. Data augmentation in conjunction with time series preprocessing can reduce the data acquisition expense. Data augmentation is also very beneficial in terms of enhancing the performances of classification networks and the reliability by covering blind spots in the recorded data.

References

[1] Sufyan Al-Janabi and Amjad Shehab, "Edge computing: Review and future directions," 09 2019.

[2] Hui-Shyong Yeo, Byung-Gook Lee, and Hyotaek Lim, "Hand tracking and gesture recognition system for human-computer interaction using low-cost hardware," *Multimedia Tools and Applications*, vol. 74, 04 2013.

[3] DoYeob Lee, Dongkyoo Shin, and Dongil Shin, "A finger counting method for gesture recognition," *Journal of Internet Computing and Services*, vol. 17, pp. 29–37, 04 2016.

[4] D.J. Sturman and D. Zeltzer, "A survey of glove-based input," *IEEE Computer Graphics and Applications*, vol. 14, no. 1, pp. 30–39, 1994.

[5] Souvik Hazra and Avik Santra, "Robust gesture recognition using millimetric-wave radar system," *IEEE Sensors Letters*, vol. 2, no. 4, pp. 1–4, 2018.

[6] Shahzad Ahmed and Sung Ho Cho, "Hand gesture recognition using an ir-uwb radar with an inception module-based classifier," *Sensors*, vol. 20, no. 2, 2020.

[7] Sruthy Skaria, Akram Al-Hourani, Margaret Lech, and Robin J. Evans, "Hand-gesture recognition using two-antenna doppler radar with deep convolutional neural networks," *IEEE Sensors Journal*, vol. 19, no. 8, pp. 3041–3048, 2019.

[8] Eiji Hayashi, Jaime Lien, Nicholas Gillian, Leonardo Giusti, Dave Weber, Jin Yamanaka, Lauren Bedal, and Ivan Poupyrev, "Radarnet: Efficient gesture recognition technique utilizing a miniature radar sensor," in *Proceedings of the 2021 CHI Conference on Human Factors in Computing Systems*, New York, NY, USA, 2021, CHI '21, Association for Computing Machinery.

[9] Shahzad Ahmed, Karam Dad Kallu, Sarfaraz Ahmed, and Sung Ho Cho, "Hand gestures recognition using radar sensors for human-computer-interaction: A review," *Remote Sensing*, vol. 13, no. 3, 2021.

[10] Connor Shorten and Taghi M Khoshgoftaar, "A survey on image data augmentation for deep learning," *Journal of big data*, vol. 6, no. 1, pp. 1–48, 2019.

[11] Thomas Stadelmayer, Avik Santra, Robert Weigel, and Fabian Lurz, "Radar-based gesture recognition using a variational autoencoder with deep statistical metric learning," *IEEE Transactions on Microwave Theory and Techniques*, vol. 70, no. 11, pp. 5051–5062, 2022.

[12] Saiwen Wang, Jie Song, Jaime Lien, Ivan Poupyrev, and Otmar Hilliges, "Interacting with soli: Exploring fine-grained dynamic gesture recognition in the radio-frequency spectrum," in *Proceedings of the 29th Annual Symposium on User Interface Software and Technology*, New York, NY, USA, 2016, UIST '16, p. 851–860, Association for Computing Machinery.

[13] Souvik Hazra and Avik Santra, "Short-range radar-based gesture recognition system using 3d cnn with triplet loss," *IEEE Access*, vol. 7, pp. 125623–125633, 2019.

[14] Wen Jiang, Yihui Ren, Ying Liu, Ziao Wang, and Xinghua Wang, "Recognition of dynamic hand gesture based on mm-wave fmcw radar micro-doppler signatures," in *ICASSP 2021 - 2021 IEEE International Conference on Acoustics, Speech and Signal Processing (ICASSP)*, 2021, pp. 4905–4909.

[15] Ibrahim Alnujaim, Shobha Sundar Ram, Daegun Oh, and Youngwook Kim, "Synthesis of micro-doppler signatures of human activities from different aspect angles using generative adversarial networks," *IEEE Access*, vol. 9, pp. 46422–46429, 2021.

[16] Ibrahim Alnujaim, Daegun Oh, and Youngwook Kim, "Generative adversarial networks for classification of micro-doppler signatures of human activity," *IEEE Geoscience and Remote Sensing Letters*, vol. 17, no. 3, pp. 396–400, 2020.

[17] Baris Erol, Sevgi Zubyede Gurbuz, and Moeness G. Amin, "Motion classification using kinematically sifted acgan-synthesized radar micro-doppler signatures," *IEEE Transactions on Aerospace and Electronic Systems*, vol. 56, no. 4, pp. 3197–3213, 2020.

[18] Jiayi Li, Aman Shrestha, Julien le kernec, and Francesco Fioranelli, "From kinect skeleton data to hand gesture recognition with radar," *The Journal of Engineering*, vol. 2019, 09 2019.

[19] Karim Ishak, Nils Appenrodt, Jrgen Dickmann, and Christian Waldschmidt, "Human motion training data generation for radar based deep learning applications," in *2018 IEEE MTT-S International Conference on Microwaves for Intelligent Mobility (ICMIM)*, 2018, pp. 1–4.

[20] Thomas Stadelmayer, Avik Santra, Robert Weigel, and Fabian Lurz, "Light-weight gesture sensing using FMCW radar time series data," 11 2021, https://doi.org/10.48550/arXiv.2111.11219.

[21] Haipeng Liu, Anfu Zhou, Zihe Dong, Yuyang Sun, Jiahe Zhang, Liang Liu, Huadong Ma, Jianhua Liu, and Ning Yang, "M-gesture: Person-independent real-time in-air gesture recognition using commodity millimeter wave radar," *IEEE Internet of Things Journal*, vol. 9, no. 5, pp. 3397–3415, 2022.

[22] Sandeep Rao Cesar Iovescu, *The fundamentals of millimeter wave radar sensors*, Texas Instruments, 2020.

[23] Thomas Stadelmayer, Avik Santra, Markus Stadelmayer, Robert Weigel, and Fabian Lurz, "Improved target detection and feature extraction using a complex-valued adaptive sine filter on radar time domain data," in *2021 29th European Signal Processing Conference (EUSIPCO)*, 2021, pp. 1745–1749.

[24] Hassan Ismail Fawaz, Benjamin Lucas, Germain Forestier, Charlotte Pelletier, Daniel F. Schmidt, Jonathan Weber, Geoffrey I. Webb, Lhassane Idoumghar, Pierre-Alain Muller, and

François Petitjean, "InceptionTime: Finding AlexNet for time series classification," *Data Mining and Knowledge Discovery*, vol. 34, no. 6, pp. 1936–1962, sep 2020.
[25] Takuya Akiba, Shotaro Sano, Toshihiko Yanase, Takeru Ohta, and Masanori Koyama, "Optuna: A next-generation hyperparameter optimization framework," 2019.
[26] Diederik P. Kingma and Jimmy Ba, "Adam: A method for stochastic optimization," 2014.
[27] Leslie N. Smith, "Cyclical learning rates for training neural networks," in *2017 IEEE Winter Conference on Applications of Computer Vision (WACV)*, 2017, pp. 464–472.
[28] Connor Shorten and Taghi Khoshgoftaar, "A survey on image data augmentation for deep learning," *Journal of Big Data*, vol. 6, 07 2019.
[29] Brian Kenji Iwana and Seiichi Uchida, "Time series data augmentation for neural networks by time warping with a discriminative teacher," in *2020 25th International Conference on Pattern Recognition (ICPR)*, 2021, pp. 3558–3565.
[30] Krzysztof Kamycki, Tomasz Kapuscinski, and Mariusz Oszust, "Data augmentation with suboptimal warping for time-series classification," *Sensors*, vol. 20, no. 1, 2020.
[31] Germain Forestier, François Petitjean, Hoang Anh Dau, Geoffrey I. Webb, and Eamonn Keogh, "Generating synthetic time series to augment sparse datasets," in *2017 IEEE International Conference on Data Mining (ICDM)*, 2017, pp. 865–870.
[32] Inc Arundo Analytics, "tsaug - augmentation methods for time series, as well as a simple api to connect," Github.

Youcef Hassab was born in Oran, Algeria in 1994. He received the B.S. degree in General Engineering Sciences and the M.S. degree in Electrical Engineering with focus on high frequency, electromagnetic compatibility and optics from Hamburg University of Technology (TUHH), Hamburg, Germany in 2019 and 2022 respectively. His recent research focus is on radar digital signal processing, radar hand gesture recognition systems and applications of machine learning solutions in electromagnetic compatibility, signal integrity, power integrity and bioelectromagnetics. In November 2022, he joined the Institute of Electromagnetic Theory at the TUHH to pursue a PhD degree. His thesis focuses on the application of machine learning and Bayesian optimization techniques for efficient electromagnetic compatibility engineering.

Thomas Stadelmayer (Student Member, IEEE) was born in Regensburg, Germany in 1994. He received the B.S. and M.S. degrees in Computational Engineering with focus on digital signal processing from the Friedrich-Alexander University Erlangen-Nuremberg in 2016 and 2019. From 2019 until 2022 he was working as a Research Assistant at the Institute of Electronics Engineering in the circuits, systems and hardware test group and working in cooperation with Infineon Technologies AG. His research focus is on digital signal processing and deep learning for mmWave radar systems. Since 2022 he is a machine learning research engineer at the Advanced Artificial Intelligence group at Infineon Technologies in Munich.

Fabian Lurz (Senior Member, IEEE) received the B.Sc. and M.Sc. degrees in information and communication technology and the Dr.-Ing. degree from the Friedrich-Alexander University Erlangen-Nuremberg (FAU), Erlangen, Germany, in 2010, 2013, and 2019, respectively. In 2013, he joined the Institute for Electronics Engineering, FAU, as a Research Assistant, and from 2017 to 2020, he was a Research Group Leader of the Circuits, Systems and Hardware Test Group. Since June 2020, he has been a Senior Engineer and a Research Group Leader at the Institute of High-Frequency Technology, Hamburg University of Technology (TUHH), Hamburg, Germany. His research interests include microwave circuits and systems, especially for low-cost and low-power metrology applications. He is a member of the IEEE Microwave Theory and Techniques Society (IEEE MTT-S) and the IEEE Instrumentation and Measurement Society (IEEE IMS). He was a recipient of the First Prize of the High Sensitivity Radar Student Design Competition of the IEEE International Microwave Symposium in 2014, 2017, and 2018, respectively, and the IEEE Microwave Theory and Techniques Society Graduate Fellowship Award in 2016.

Publication 6 (P6)

Title

Impedance Profile Prediction and Classification for PCB based PDN Decoupling Using Autoencoders.

Publication Status

Presented at peer-reviewed conference: DesignCon 2025, Santa Clara, CA, USA. (No formal proceedings).

Author Contribution

Involvement in all areas of the research, including conceptualization, methodology, implementation and writing, in a leading role (1. author).

Bibliographic Information

[67] Y. Hassab, J. Heßling, M. Schierholz, I. Erdin, J. Balachandran, and C. Schuster, "Impedance Profile Prediction and Classification for PCB based PDN Decoupling Using Autoencoders," in *DesignCon 2025*, Santa Clara, CA, USA, Jan. 2025.

Copyright Notice

DesignCon 2025

Impedance Profile Prediction and Classification for PCB-based PDN Decoupling Using Autoencoders

Youcef Hassab, Hamburg University of Technology
youcef.hassab@tuhh.de

Jan Severin Heßling, Hamburg University of Technology
jan.hessling@tuhh.de

Morten Schierholz, Hamburg University of Technology
morten.schierholz@tuhh.de

Ihsan Erdin, Celestica Inc.
ierdin@ieee.org

Jayaprakash Balachandran, d-Matrix Corp.
jayap@d-matrix.ai

Christian Schuster, Hamburg University of Technology
schuster@tuhh.de

Abstract

In this work, a machine learning (ML)-based method for fast full impedance profile prediction to bypass or speed up printed circuit board (PCB)-based power delivery network (PDN) decoupling using autoencoders is proposed. Autoencoders, a type of neural network used to learn efficient representations of data, are showcased for power integrity applications. In the proposed approach, autoencoders are trained using available datasets from previous designs to predict the full impedance profile of PDNs. For a new, unseen design space, the trained models are further tuned using few new samples to make reliable predictions of the impedance. This approach should lead to a speed-up of the decoupling process by allowing fast electromagnetic (EM) behavior prediction using autoencoders. Moreover, the autoencoders are used to find similar previous designs to apply previous decoupling strategies to bypass the design process. For this investigation, multiple cases of rectangular and irregularly shaped PCBs with up to 8 metal layers and via arrays with up to 14 ports are simulated up to a frequency of 1 GHz. The used datasets, generated using a physics-based (PB) simulation tool, are available on the SI/PI-Database from the Hamburg University of Technology (https://www.tet.tuhh.de/en/si-pi-database).

Biography

Youcef Hassab

Youcef Hassab was born in Oran, Algeria in 1994. He received the B.S. degree in General Engineering Sciences from Hamburg University of Technology (TUHH), Hamburg, Germany in 2019. He received the M.S. degree in Electrical Engineering with a focus on high frequency, electromagnetic compatibility and optics from the TUHH in 2022. During his master studies, he investigated the use of different machine learning algorithms in PCB-based PDN target impedance classification. In November 2022, he joined the Institute of Electromagnetic Theory at the TUHH to pursue a PhD degree. His project focuses on the application of machine learning and bayesian optimization techniques for efficient electromagnetic compatibility engineering.

Jan Severin Heßling

Jan Severin Hessling received his B.S. degree in electrical engineering from Hamburg University of Technology (TUHH) in 2022. He is pursuing the M.S. degree in electrical engineering at the Institute of Electromagnetic Theory at TUHH, working on machine learning tools in the context of PCB design.

Morten Schierholz

Morten Schierholz received his M.S. degree in electrical engineering from Hamburg University of Technology (TUHH) in 2019. He is pursuing the Ph.D. degree at the Institute of Electromagnetic Theory at TUHH. His focus is on the application of machine learning tools for decoupling strategies of PCB based PDNs, including the generation of training data which is collected in the SI/PI-Database.

Jayaprakash Balachandran

Jayaprakash Balachandran (JP), leads advanced packaging and system development for GenAI inference accelerator products at d-Matrix. He also leads PoC and interop workgroups at OCP-ODSA. Prior to d-Matrix, he was with Cisco Compute Server Business Unit. JP has master's from IISc Bangalore and Ph.D. from IMEC, Belgium.

Ihsan Erdin

Ihsan Erdin is a practicing engineer with over 20 years of experience in the design of high-speed data communication circuits. He has been working as an SI SME at Celestica in the design of server and networking switch systems since 2007. He is also an adjunct faculty member at Carleton U. Ottawa with research interests in electromagnetics theory and microwave engineering methods in PCB applications. He holds a Ph.D. degree in electromagnetics engineering. He is a member of the Professional Engineers Ontario and a senior member of IEEE. From 2018 to 2020, he served as a Distinguished Lecturer of the IEEE EMC Society.

Christian Schuster

Christian Schuster received the Diploma degree in physics from the University of Konstanz, Germany, in 1996, and the Ph. D. degree in electrical engineering from the Swiss Federal Institute of Technology (ETH), Zurich, Switzerland, in 2000. Since 2006 he is a full professor at Hamburg University of Technology (TUHH), Germany. Prior to that he was with the IBM T. J. Watson Research Center, Yorktown Heights, NY, where he was involved in high-speed optoelectronic package and backplane interconnect modeling and signal integrity design for new server generations. His currents interests include signal and power integrity of digital systems, multiport measurement and calibration techniques, and development of electromagnetic simulation methods for communication electronics. Since April 2020 he is an Adjunct Associate Professor at the School of Electrical and Computer Engineering of the Georgia Institute of Technology, Atlanta, USA.

1 Introduction

The effective design of power delivery networks (PDNs) for printed circuit boards (PCBs) is essential to maintain the performance of high-speed digital integrated circuits (ICs). Power integrity (PI) engineering ensures a stable voltage supply delivery over PCB components by mitigating ground bounce and simultaneous switching noise, achieved in part through strategic placement of decoupling capacitors (decaps). The PDN design usually requires detailed information on the electromagnetic (EM) behavior at each iteration step to align with the target impedance (TI). As the complexity of PCBs rises, obtaining PDN behavior data through EM simulations is becoming increasingly time- and resource-intensive, significantly prolonging the PDN design process. The application of data-driven techniques in the design of PDNs has gained more interest recently. Different data-driven techniques and algorithms have been investigated, e.g., artificial neural networks (ANNs) [1], genetic algorithms (GAs) [2] or support vector machines (SVMs) [3] to enhance or speed-up the design processes. These tools have the potential to accelerate the design process of PDNs, i.a., through the replacement of expensive EM simulations [4]. However, data-driven approaches often necessitate a substantial amount of data samples during the training phase, which can lead to significant computational overhead. This overhead may offset the benefits provided by the improved and accelerated design processes. Techniques that either reduce the number of needed data samples for a new design space or enable the reuse of previously generated data are needed.

- In DesignCon 2023, the authors have demonstrated the capability of machine learning (ML) tools to predict distinct key-features of the PDN impedance to replace conventional EM simulations [1].
- In DesignCon 2024, the authors proposed an ML approach to reuse available data to reduce the required number of samples for the prediction of key-features in a new design space [5].
- This year, the authors extend their work by proposing an ML approach for the prediction and classification of the full frequency response of PDN impedances instead of distinct key-features only.

By modelling the complete impedance profile, this method provides a deeper understanding of the PDN behavior, resulting in an enhanced design. The proposed approach uses autoencoders (AEs) building up on first investigations presented in [6]. AEs are a type of neural networks used to learn efficient representations of data. AEs compress input data into a smaller, dense format a.k.a. the ”latent space” and then reconstruct it back. A significant benefit of using AEs is their ability to not only reconstruct impedance profiles to replace EM simulations, but to evaluate the similarity among multiple impedance profiles. This allows the identification of similar datasets to be reused for new problems through transfer learning thus increasing the data-efficiency. For illustration, consider a scenario where a new PDN defined over a PCB design space requires decoupling. Datasets from previous designs along with adequate decoupling strategies are already available. This raises the question of whether similar datasets can be identified and reused to streamline the PDN design of this new case. This question will be investigated through the application of AEs for the prediction and classification of impedance profiles from four different design spaces.

The remainder of the paper is organized as follows: Section 2 discusses the challenges associated with conventional PDN design and presents ideas to improve the design process. Section 3 presents the proposed data-driven approach along with the ML tools used. Section 4 covers the defined design spaces and the associated data generation process. Section 5 highlights the investigation of the impedance profile prediction. Section 6 focuses on the classification of impedance profiles to find similar samples. Section 7 provides a discussion on the results and an outlook on future work while Section 8 concludes the paper.

2 Design of PCB-based PDNs

PCBs provide the main electrical conductivity for the signal transmission between the components. The proper design of PDNs is very important to provide a stable and reliable power supply to all components on a PCB. Without a well-designed PDN, the signal transmission at specified rates might not be ensured and in worst cases components may malfunction due to the voltage fluctuations. With the rising switching frequencies, integration densities and decreasing supply voltages, the PDN design is still a challenging process. A common approach for the design of proper PDNs is the strategic placement of adequate decaps in the vicinity of active components. These decaps lower the observed PDN impedance to fit a defined TI [7]. The decap placement process is performed by intelligently choosing the parameters, e.g., capacitance, position, amount. This is usually an iterative process where numerical simulations or calculations are performed at each step to gather information on the EM behavior of the PDN [8, 9]. The computationally costly simulations make the process time-consuming. Generally, the process is repeated for every new design space since the placement of decaps depends on the PCB and component parameters.

In this work, the use of data-efficient ML models to replace costly EM simulations is proposed. Once trained, these ML models can make very fast predictions of full impedance profiles from design parameters, see Fig. 1a. The fast and accurate predictions would result in a faster iterative decoupling process. Moreover, the used ML models provide the ability to classify impedance curves and design space parameters to identify similar EM behavior, see Fig. 1b. For a new design space, the similarity to available designs can be evaluated. Assuming that effective constellations of decaps have been found for the older problems, if the new case of interest shows similar EM behavior, the same decap constellations can be reused. The reused decap constellation either results in successful decoupling or represents a good starting point for decoupling strategies to speed up the optimization process. The prediction and classification schemes proposed here are based on two ML tools: AEs and ANNs. In the next section, a more in-depth look into these tools and how they can be used to enhance the PDN design process is presented. The investigations carried out initially focus on the prediction and classification of self-impedances of bare board without any attached decaps. This shall serve as a proof of concept of the ability to predict and classify broadband impedance curves. Direct investigations on decoupling processes are reserved for future work.

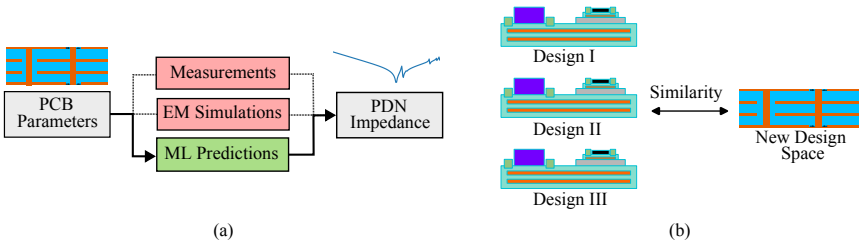

Figure 1: The two main investigated aspects in this work for the enhancement of the PDN design process are the (a) self-impedance prediction from PCB design parameters, and the (b) classification of self-impedances for the identification of similarity among different PCB design spaces.

3 Data-Driven Approach using Autoencoders

Data-driven approaches are methods for finding solutions, creating models and making predictions based on data. In contrast, physics-based approaches derive models from fundamental principles of physics or analytical approximations. Data-driven ML methods can excel in handling complex, nonlinear systems where the physical relationships are unknown, too difficult to model analytically; or where interactions between variables are hard to retrace. They can efficiently process large amounts of data and uncover hidden patterns. In this section, a short theoretical review of the used tools and concepts, ANNs, AEs and transfer learning, is provided. A data-driven approach for the enhancement of the decoupling process through the impedance prediction and classification using the presented tools is highlighted.

Artificial Neural Networks

ANNs are computational models inspired by biological neural networks. These models are first trained on data to then be used to predict an output vector $\boldsymbol{O} = [O_1 \dots O_N]$ when presented with an unseen input vector $\boldsymbol{I} = [I_1 \dots I_N]$. In other words, they can learn complex relations between inputs and outputs and model the underlying behavior. ANNs consist of multiple arranged layers of nodes (neurons) connected to each other by means of weighted connections, see Fig. 2a. The input layer neurons are connected to the input vector while the output layer neurons are connected to the output vector. Between the two layers are one or multiple hidden layers. The output a of each connected neuron, see Fig. 2b, can be determined by

$$a = f(\boldsymbol{w}^t \boldsymbol{x} + b) \tag{1}$$

where $\boldsymbol{w}$ is a vector of connected weights, b an added bias term, $\boldsymbol{x}$ a vector of inputs from connected neurons and f a set activation function to limit the output. During the training phase, the weights $\boldsymbol{w}$ are tuned to minimize a certain cost or error function. The training process is done by back-propagation using, e.g., the Adam solver [10]. The cost function is a measure of how good a neural network did with respect to training and expected outputs. Before the training process, other parameters of the ANN are set. These so-called hyperparameters can be, e.g., number of hidden layers, number of neurons in each layer, type of activation function. One practical example of ANN use in PI is the training of models to predict the resonance frequency of a PCB using design parameters as an input, e.g., size and material properties [5].

Autoencoders

AEs are a special type of neural networks often used to learn efficient representations of data. AEs consist of three main components. An encoder, a latent space and a decoder, see Fig. 3a. The encoder, which is represented by a function E_θ maps an input x to a lower dimensional output $z = E_\theta(x)$ in the latent space. The decoder, which is represented by a function D_ϕ reconstructs an output $x' = D_\phi(z)$ from the entry z of the latent space. The encoder and decoder are both neural networks, e.g., ANNs or convolutional neural networks (ConvNets). During the training phase, the set of weights (θ, ϕ) are learned to ideally result in a perfection reconstruction $x' = x$. Practically, a loss function which measures the difference between a number n of training inputs x_i and their reconstructions x_i' is minimized. One typical function to be minimized is the mean-squared error (MSE):

$$L_{AE}(\theta, \phi) = \frac{1}{n} \sum_{i=1}^{n} (x_i - x_i')^2 \tag{2}$$

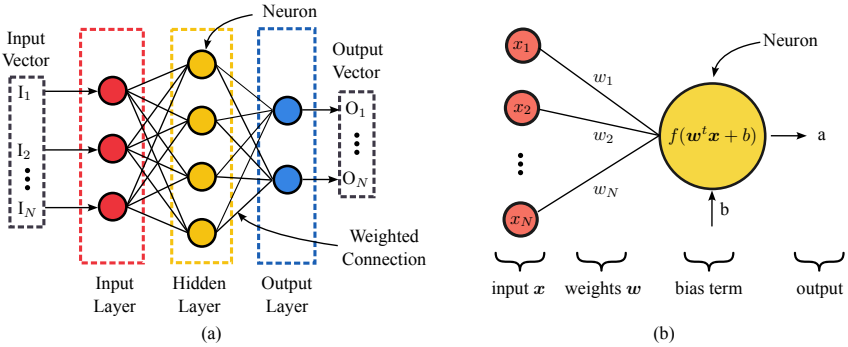

Figure 2: An overview of the (a) structure of an ANN with three layers and the (b) structure of single connected neuron from the hidden layer, are presented.

The lower dimensional latent space representation of samples contains the most important features learned from the data. The latent space has an interesting property: Samples close to each other in the original representation are close to each other in the latent space, too. This makes the analysis of data and identification of similarity an easier task. AEs can be trained to reconstruct an impedance profile presented at the input passing through the latent space, see Fig. 3a. The latent space representation allows for the analysis and comparison of profiles and datasets, as explained in Section 6.

The AEs can be tweaked to predict and build an impedance profile from a sample consisting of input design parameters. In other words, the AEs would serve as an alternative modeling technique to EM simulations. To this end, an AE is trained to be able to reconstruct impedance curves with a certain degree of accuracy as a first stage. For each impedance curve used for the training, a unique latent space representation exists. Similarly, for each impedance curve, a unique sample of design parameters exists. For the second stage, the encoder part is detached and a new ANN is trained to learn the mapping of input design parameters to the latent space, see Fig. 3b. Once the mapping is learned, the output impedance profile can be predicted passing by the trained ANN, latent space and decoder. The tweaked AE is referred to as an ANN-AE in the remainder of the paper.

Transfer Learning

Transfer learning is a method in ML where a model trained for a specific task or problem is used as a starting point to solve a new but related problem [11]. Basically, the knowledge acquired to solve a similar task is reused by a model for faster and more efficient learning to solve the new problem. The working mechanism involves two steps, see Fig. 4. The first step is the training of a model on an extensive dataset to learn how to solve a certain task, e.g., the prediction of the impedance profile for a certain design space. This is referred to as pre-training. Pre-trained models can be stored for future reuse to not repeat this stage at each new process. The second step is to start with the pre-trained model and use a new dataset from the new problem of interest to retrain the model. Retraining the model is carried out to better suit the new task and provide better performances. This is referred to as fine-tuning.

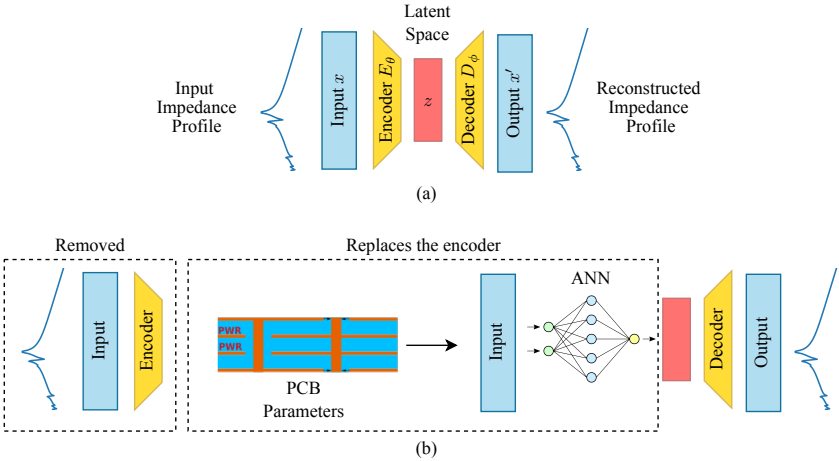

Figure 3: For the impedance profile prediction, the (a) regular AE network is trained to be able to reconstruct impedance curves presented at the input passing by the encoder, latent space and the decoder. The (b) ANN-AE is then constructed by removing the encoder and training an ANN that is able to map PCB parameters to the latent space for an accurate impedance profile prediction.

Usually, using this method successfully results in an enhanced data, time and cost efficiency. Let us consider the following scenario: The prediction of the impedance profile of a polygonal shaped PCB is targeted. If simulation results are already available for a similar case (e.g. PCB with a rectangular shape and a different number of layers), these can be reused in a transfer learning scheme. A model is pre-trained using the available data. New data samples from the polygonal PCB are generated to fine-tune the pre-trained model and make reliable predictions of the impedance for the new design space. Applying transfer learning reduces the amount of new data samples that need to be generated for the polygonal PCB. The increase in data efficiency means a reduction of the time required to solve the new problem.

Proposed Data-Driven Framework

The proposed approach for the enhancement and speed-up of the decoupling process starts with a new and unseen design space as the main problem, see Fig. 5. For this new specified design space, it is assumed that no simulation results or data are available. There are however data samples available from older designs stored in a database, e.g., the SI/PI Database [12]. These samples contain frequency-dependent impedance profiles depending on various design parameters. An AE is first trained on all available datasets. While presenting the new design space parameters as an input, similar structures can be identified. The classification and identification of similarity using a latent space analysis is investigated in Section 6. If decap constellations are available for these similar cases, they are implemented for the new problem. If the design specifications are met, no further action is required. Otherwise, the constellation can be used as a starting point for conventional iterative decoupling if the margin small. For this instance or when

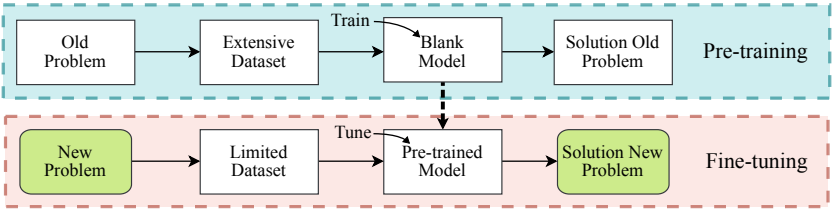

Figure 4: The transfer learning approach to increase the data efficiency is shown. The pre-training stage involves the training of a model on older available datasets. The fine-tuning stage involves the re-training of the same model using new data samples to make reliable predictions for the new problem.

no decoupling constellations are available, few data samples from the new case of interest are generated to fine-tune the AE. The tuned AE can be used to make fast and accurate predictions of the impedance profile for the whole design space without the need for additional EM simulations. The investigation of the impedance prediction from design parameters is shown in Section 5. By replacing the EM simulations with fast AE predictions, the iterative decoupling process is sped up. Investigations on the decoupling process and terminated networks to complete the pipeline are reserved for the future.

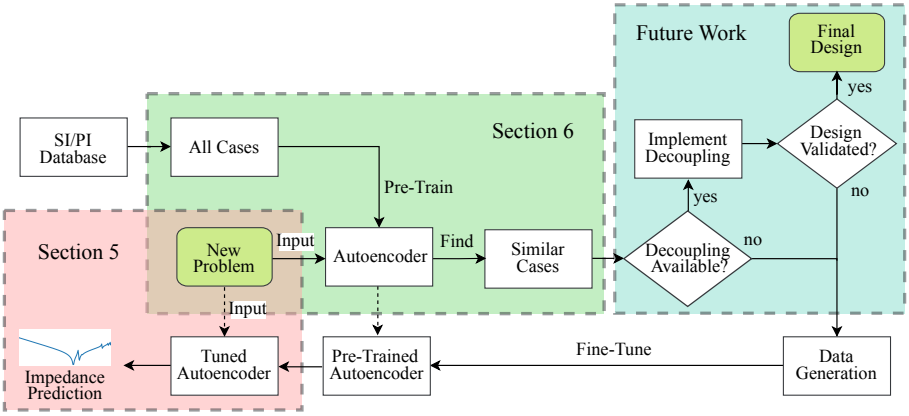

Figure 5: The proposed ML-based approach for the enhancement of the PDN design process is shown. Trained AEs are used to identify similar PCBs samples with similar EM behavior to apply available decap constellations. Alternatively, the AEs are used for the impedance profile prediction to replace computationally expensive EM simulations to speed up the PDN design.

4 PCB Design Space Definition

Since PCBs exhibit significant variability in design attributes such as geometries and material composition, the sheer number of potential parameters and their possible configurations makes it impractical to account for all conceivable PCB applications. In this work, the design spaces have been constrained to a practical subset, with parameter dimensions and ranges specifically tailored for high-speed digital systems.

Data Generation and SI/PI Database Access

For the generation of data samples, an approach combining equivalent circuit models with insights into the physical behavior of specific PCB elements, such as vias and cavities, is used. The electromagnetic interactions between PCB cavities is assumed to occur only through via antipads. Edge fringing effects are assumed to be negligible while considering 2D-radial wave propagation within each cavity. An accurate PCB model can be achieved by integrating a contour integral method (CIM) with a physics-based (PB) via model [14, 15]. A comparison of this method with a full-wave finite element method (FEM) solver is provided in Fig. 6 [13, 16]. The simulations are performed in the 1 MHz to 1 GHz frequency range in 3 MHz steps. Data samples from 4 different cases used in this work are available for download on the SI/PI-Database: **https://www.tet.tuhh.de/en/si-pi-database/** [12]. The database contains many datasets from the signal integrity (SI) and PI domains representing different PCB design spaces, shapes, stackups, and parameters. All numerical simulations for the defined cases are performed using the outlined PB approach.

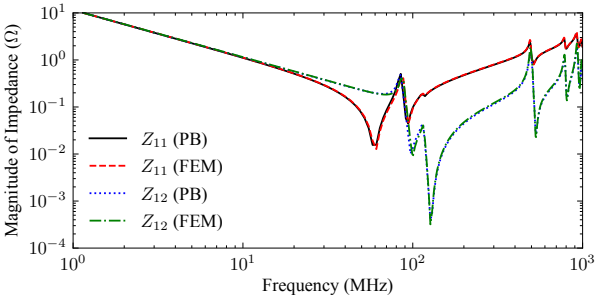

Figure 6: Comparison of the self- and transfer-impedances of a 4 layer PCB (*Case I*) observed at the board center simulated using a physics-based (PB) approach and a finite element method (FEM) solver [15, 17].

Defined PCB Cases

For the investigation of the proposed data-driven approach, 4 different PCB cases covering different design spaces are defined. These cases differ in terms of their physical layout, layer stackups, material properties, and port placements as shown in Table 1 and Fig. 7. For the generation of data, the design spaces are discretized using a latin hypercube sampling (LHS) method. The samples are then simulated to get the EM behavior and the full frequency responses of impedances.

Table 1: The full design space of the PCB-based PDNs is defined. The fixed and varied parameters as well as the covered ranges are given for *Case I*, *Case II*, *Case III* and *Case IV**. If a parameter is fixed for a given case, the specified value is given. If a parameter is varied, its value changes and covers the ranges delimited by the given minimum and maximum.

Parameter	**Minimum**	**Maximum**	**Case Variations**			
			Case I	**Case II**	**Case III**	**Case IV**
Via Radius (r_{via} mil)	5	9	5	5	5	Varied
Via Pitch ($pitch$ mil)	40	80	80	60	40	40
Antipad Radius ($r_{antipad}$ mil)	15	24	15	19	15	Varied
PCB X-Width (mil)	1000	18000	Varied	Varied	Fig. 7e	Varied
PCB Y-Width (mil)	1000	18000	Varied	Varied	Fig. 7e	Varied
Conductivity (δ_c S/m)	$4.5 \cdot 10^7$	$5.8 \cdot 10^7$	$5.8 \cdot 10^7$	$5.8 \cdot 10^7$	$5.8 \cdot 10^7$	Varied
Rel. Permittivity (ϵ_r)	2	6	Varied	Varied	Varied	Varied
Loss Tangent ($\tan\delta$)	0.005	0.025	0.02	0.02	0.02	Varied
Dielectric Height (t_{diel} mil)	3	80	Varied	Varied	Varied	Varied
Plane Thickness (t_{met} mil)	1	4	1	1	1	Varied
Observation X Position (A_Ix mil)	0	PCB X Width	PCB Center	Random on PCB	5100	Random on PCB
Observation Y Position (A_Iy mil)	0	PCB Y Width	PCB Center	Random on PCB	1412	Random on PCB
Stackup Order	–		Ground 2·Power Ground	3·Ground 2·Power 3·Ground	Ground 2·Power Ground	Ground 2·Power Ground
EXT1 (mil)	−5000	5000	–	–	Varied	–
EXT2 (mil)	−1000	5000	–	–	Varied	–
Shape	–	–	Rect.	Rect.	Irregular	Rect.
Varied Dimensions	4	11	4	6	4	11
Generated Samples	500	18000	3000	10000	500	18000
Top View	–	–	Fig. 7b	Fig. 7d	Fig. 7e	Fig. 7g
Stackup View	–	–	Fig. 7a	Fig. 7c	Fig. 7a	Fig. 7f
Reference	–	–	[5]	[1]	[13]	–

**Case III* has an irregular shape with two extensions EXT1 and EXT2 to change the size of the board while all other cases have rectangular shaped boards. For *Case II* and *Case IV*, two via arrays are present on the board with only one power via on one array used as an observation point.

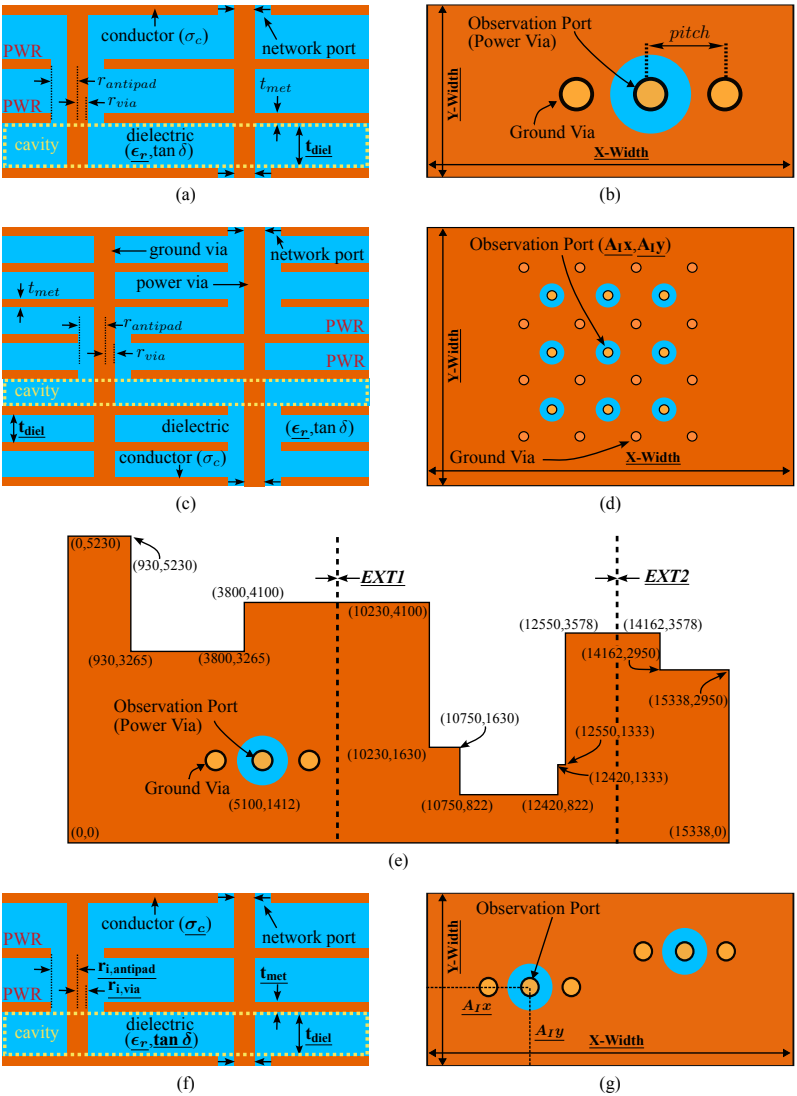

Figure 7: The defined PCBs are presented as a (a) stackup view of *Case I* and *Case III*, (b) top view of *Case I*, (c) stackup view of *Case II*, (d) top view of *Case II*, (e) top view of *Case III*, (f) stackup view of *Case IV* and (g) top view of *Case IV*. The varied parameters are marked in **bold**. Figures adapted from [5].

5 Impedance profile prediction

In this section, investigations with regard to the prediction of PDN impedance profiles from design parameters are shown. The training setups of the AEs for impedance reconstruction and ANN-AEs for impedance prediction are presented. The results of this approach are evaluated. Transfer learning for increased data efficiency is implemented for a chosen use-case.

Training Setup

The training of the AEs for impedance reconstruction is based on datasets of self-impedance curves stored as complex arrays with dimensions $(2, 334)$. The first two dimensions represent the magnitude and phase sampled at 334 points in the frequency range from 1 MHz to 1 GHz. As a pre-processing step, a natural logarithm is applied to the magnitude vectors. Both magnitude and phase are then standardized. The 2D arrays are combined to a 1D array of length 668 containing both the magnitudes then the phases at each frequency point. For each experiment, the used dataset is divided into training, validation and testing sets in a $(70, 20, 10)$ split. The hyperparameters are determined before the training stage, see Table 2. For the decoder and encoder, hidden layers of dimensions $(150, 50)$ and a latent space size of 12 are used. An Adam optimizer with MSE as a loss function is used for the optimization. The training and validation sets are used as a basis for the optimization while the performance of the AE in the reconstruction of curves is evaluated on the unseen test set, see Fig. 8.

Once an AE is trained, the second stage is the training of an ANN that predicts the latent space representation of a sample from design space parameters. The trained ANN then replaces the encoder, see Fig. 3b. The same trained decoder of the first stage is then used for the reconstruction of impedance curves for any point in the latent space. Since the number of varied design parameters differs from case to case, the datasets are pre-processed to be brought in a uniform format with the same input dimensions. This enables the training and prediction on data from multiple cases. The 11 defined input design dimensions are: via radius, antipad radius, pitch, conductivity, permittivity, loss tangent, height of the PCB, area of the PCB, distance of observation point to the farthest board edge and power plane distance from the outside board layers. These input dimensions are normalized between 0 and 10. The outputs of the ANN represent the associated 12D points on the latent space. The hyperparameters and training setup are listed in Table 2.

For the performance evaluation, the original simulated impedance magnitude profiles x_i from an unseen test set are compared with the reconstructed or predicted output impedance profiles x_i' of the trained networks. Multiple metrics are computed to evaluate the accuracy: the root mean squared error (RMSE), mean absolute error (MAE) and normalized mean absolute error (nMAE). The nMAE represents a percentage error relative to the absolute impedance and makes a better comparison metric between cases:

$$\text{RMSE} = \sqrt{\frac{1}{m}\frac{1}{n}\sum_{i=1}^{n}\sum_{f=1}^{m}(x_i(f) - x_i'(f))^2} \tag{3}$$

$$\text{MAE} = \frac{1}{m}\frac{1}{n}\sum_{i=1}^{n}\sum_{f=1}^{m}|x_i(f) - x_i'(f)| \tag{4}$$

$$\text{nMAE} = \frac{1}{m}\frac{1}{n}\sum_{i=1}^{n}\sum_{f=1}^{m}\left|\frac{x_i(f) - x_i'(f)}{x_i(f)}\right| \tag{5}$$

Table 2: The list of hyperparameters and training setup for the full AE and ANN is shown.

Parameter	Description	AE	ANN
Data Split	Train	70%	70%
	Validation	20%	20%
	Test	10%	10%
Layer Sizes	Input layer	668	11
	Hidden layers	(150, 50)	(32, 950, 800, 870, 840, 600)
	Latent space	12	-
	Output layer	668	12
Training Setup	Loss Function	MSE	MSE
	Optimizer	Adam	Adam
	Learning rate	5e-4	5e-4
	Batch size	8	16
	Early stopping	35 epochs	35 epochs
	Max. epochs	1000	1000
Data Type	Input	Original Impedance	Design Parameters
	Output	Reconstructed Impedance	Latent Space Vector

where f is the frequency index, $m = 334$ the number of frequency points, i the sample index, n the number of samples in the test set.

Performance Evaluation

Using the aforementioned training setup, initially AEs then ANN-AEs are trained in two steps for impedance reconstruction and impedance prediction, respectively. The networks are trained and evaluated using data samples from the four defined cases, see Section 4. The four cases differ in complexity, varied parameters and number of available data samples. The results of the performance evaluation on the test set after the training show a dependency of the accuracy on the use case, see Table 3. The accuracies of the reconstruction and prediction for *Case IV* and *Case III* are relatively lower than the other two cases, as reflected by higher nMAE values around 15%. This is due to the high dimensionality of *Case IV* and low number of training samples used for *Case III*. The accuracy of the impedance reconstruction (AE) is slightly higher than the impedance prediction (ANN-AE). This is due to the imperfect mapping of the design parameters to the latent space by the additional ANN during the second stage. The training times for a machine equipped with a 2.23 GHz, 24 GB RAM and 16384 core graphics card show a dependency on the amount of training samples. The AEs of the first stage take longer to train than the ANNs of the second stage. The prediction of impedance curves takes less than 30 ms. For all cases, the ANN-AE is able to predict the impedance profiles from design parameters. A comparison of the original simulated, reconstructed and predicted impedance profiles show good agreement, see Fig. 9. Some resonant peaks are sometimes not reproduced by the trained networks. The slopes for the capacitive and inductive parts of the profiles are well predicted.

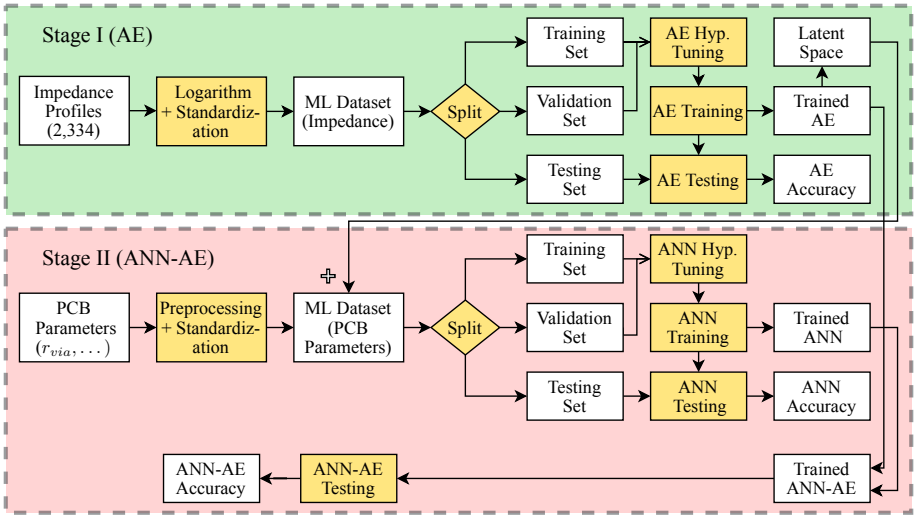

Figure 8: The training and evaluation setup for the impedance prediction is shown. The first stage involves the training and testing of AEs for impedance profile reconstruction. In the second stage, ANNs are trained to predict the latent space representation from PCB parameters. The trained ANN replaces the encoder part of the AE for impedance prediction. The resulting ANN-AE is tested on datasets of PCB parameter inputs and associated impedance profile outputs.

Table 3: The performance of the AE impedance reconstruction and the ANN-AE impedance prediction from design parameters are shown. Three different metrics are used to compare the simulated impedance profiles with the predicted and reconstructed impedance profiles: RMSE, MAE and nMAE.

Case	**Samples**	**Evaluation**	**RMSE (Ω)**	**MAE (Ω)**	**nMAE (%)**	**Training (s)**
Case I	3000	AE	1.539	0.113	6.31	144
		ANN-AE	2.199	0.488	7.5	177
Case II	10000	AE	0.414	0.168	2.4	462
		ANN-AE	0.488	0.199	2.89	562
Case III	500	AE	1.008	0.482	15.54	22
		ANN-AE	1.133	0.572	18.93	32
Case IV	18000	AE	4.865	0.612	13.63	516
		ANN-AE	4.686	0.719	16.97	696

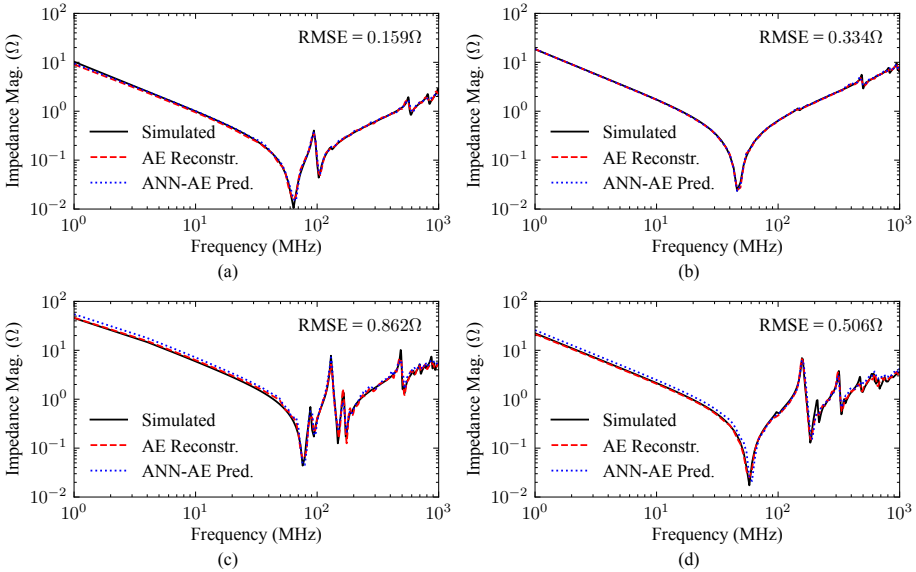

Figure 9: Exemplary predicted curves from PCB parameters using an ANN-AE are compared with simulated and reconstructured curves using an AE on a sample from (a) *Case I*, (b) *Case II*, (c) *Case III* and (d) *Case IV*. The RMSE between the predicted and simulated curves is shown.

Transfer Learning

Data efficiency is key to the success of data-driven algorithms as an alternative to conventional tools. As previously described, transfer learning can be used to increase data-efficiency, when similar data and tasks exist. In the following, transfer learning is investigated by comparing the latter with a classical non-transfer learning approach, see Fig. 10. The polygonal shaped PCB and design space of *Case III* is considered to be a new problem with no data samples available at the start. Here, the reconstruction the impedance curves from design parameters for *Case III* is targeted. Let us assume that a certain amount of data samples from *Case I*, *Case II* and *Case IV* are available. Using a transfer learning approach, a blank AE is first pre-trained using 3000 data samples from each of the three cases. The trained AE is then fine-tuned (retrained) using an increasing number of data samples from *Case III*, as the case of interest. In the classical non-transfer learning approach, an AE is trained from a blank state using an increasing number of data samples from *Case III* only. The performances of both these approaches are evaluated on the same unseen 50 *Case III* samples from the test set. A 10-fold cross-validation is performed to mitigate the effects of training sample choice. Reusing available samples from other cases results in a better accuracy and faster convergence, see Fig. 10c and Fig. 10d. Especially for the first iterations, where few training samples from *Case III* are used for the training, the improvement is noticeable, see Fig. 10d. Using 20 samples from *Case III* for the training results in an RMSE of approximately 1.5 Ω and 1.9 Ω, by using AE transfer learning and not using

transfer learning, respectively. To reach an RMSE lower than 1.6 Ω, Only 15 samples from *Case III* are needed if a pre-trained AE is used. Otherwise, for a blank AE, approximately five times as much training samples from *Case III* are needed. For a larger amount of 450 training samples from *Case III*, the transfer learning approach reaches an RMSE lower than 1 Ω, surpassing the non transfer learning approach.

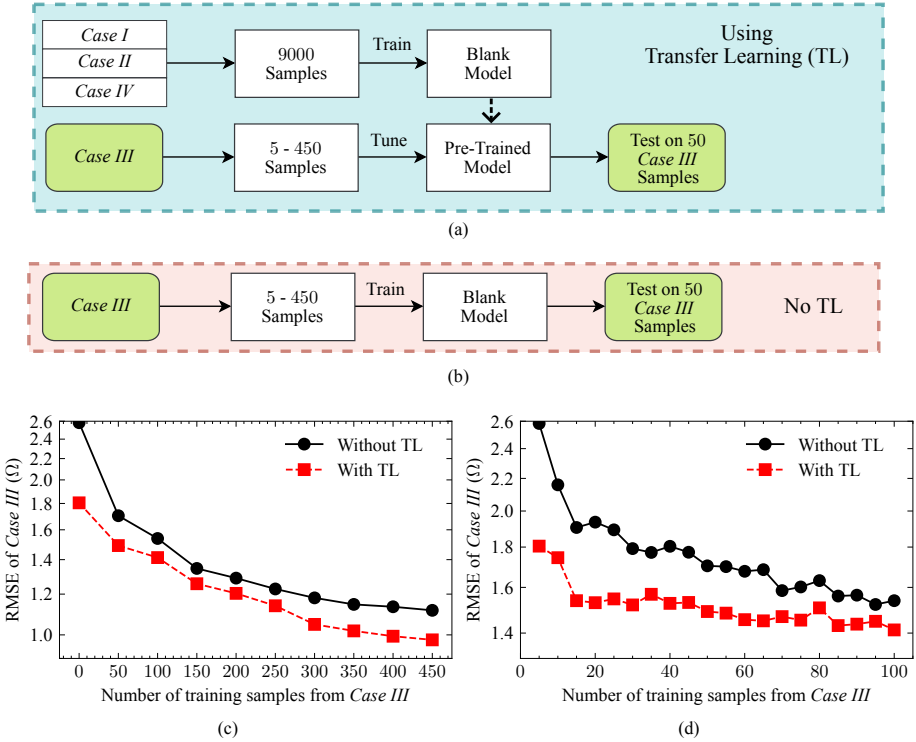

Figure 10: The reconstruction of the impedance profiles of *Case III* is evaluated using a (a) transfer learning approach where an AE is pre-trained on data samples from other cases and (b) classical approach without transfer learning use. The performance is compared for a (c) broad sampling in steps of 50 added training samples and (d) fine sampling in steps of 5 added training samples. It can be seen that TL usage results in improved performances and faster convergence.

6 Impedance Profile Classification

The AE and the latent space structure can be used for the analysis of features and identification of similarity between samples and cases. This step is important as it allows for finding similar samples to either apply existing decoupling or use transfer learning more effectively for impedance prediction and thus speeding up PDN design processes. The latent space stores the most important features of the data samples in a lower dimensional space. Samples close in the latent space tend to showcase a certain similarity in the original space. This property is called regularity. Hence, the analysis of the latent space allows the identification of important features learned by the AE as well as an easier analysis of similarity.

Latent Space Analysis

To show the property of regularity, an AE is trained on all impedance samples from the four available cases. For each impedance sample, a unique latent space representation is learned during the training process. This representation has 12 coordinates, since a 12D latent space is used. A 3D principal component analysis (PCA) is performed to make the visual representation of the latent space possible [18]. The latent space representation of the test samples from the four cases is shown, see Fig. 11. The different cases occupy different regions of the latent space. However, there is a noticeable overlap between the cases and a clear separation is not identifiable in the 3D visuals. From the original latent space, 15 samples are randomly chosen and the associated impedance profiles extracted. The average euclidean distance between the chosen points amounts to 4.124. Another 15 very close samples from a dense latent area are chosen and the associated impedance profiles are likewise extracted. The average euclidean distance between the chosen points amounts to 1.491. The random and close chosen samples are marked by blue and red dots in the latent space representation in Fig. 12a, respectively. The impedance profiles associated with the samples close to each other and the randomly chosen samples are shown in Fig. 12b and Fig. 12c, respectively. The same color coding is used for better comparison. The samples near to each other in the latent space show a high agreement and similarity, with an average RMSE of $1.563\,\Omega$ between the fifteen impedance profiles. The samples randomly chosen show much less agreement and more divergence with an average RMSE of $10.554\,\Omega$ between the fifteen impedance profiles. The property of regularity makes the identification of similar impedance profiles in the latent space possible, without the need for a direct comparison of profiles in the original space. Regardless of the source case, two close samples in the latent space exhibit a certain degree of similarity.

Identification of Similarity

Using the property of regularity, one interesting application is finding similar available cases and samples. Let us assume that *Case III* is an unseen new case of interest. An AE is trained on the remaining impedance samples from the three available cases: *Case I*, *Case II* and *Case IV*. For each impedance sample, a unique latent space representation is learned. Unseen samples from *Case III* are presented as an input to the trained AE and mapped to the latent space, see Fig. 13. The samples of *Case III* cover a certain region of the latent space that can be delimited. The samples of other cases overlapping this region can be assumed to be similar to *Case III* samples. As a case study, two samples from *Case III* are chosen. One sample is chosen from a dense region of the latent space with many samples from other cases in the vicinity. The second sample is chosen from a region where samples from other cases are further away, see Fig. 14a.

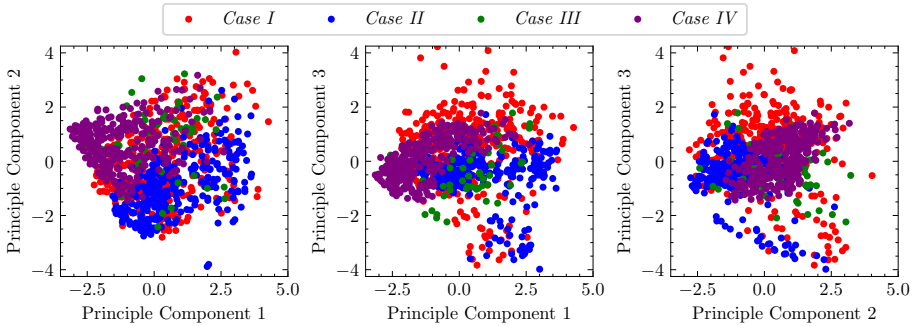

Figure 11: An AE is trained on all available cases. The 3D PCA visualization of the latent space representation of all test samples is shown. Each case is represented by a single color.

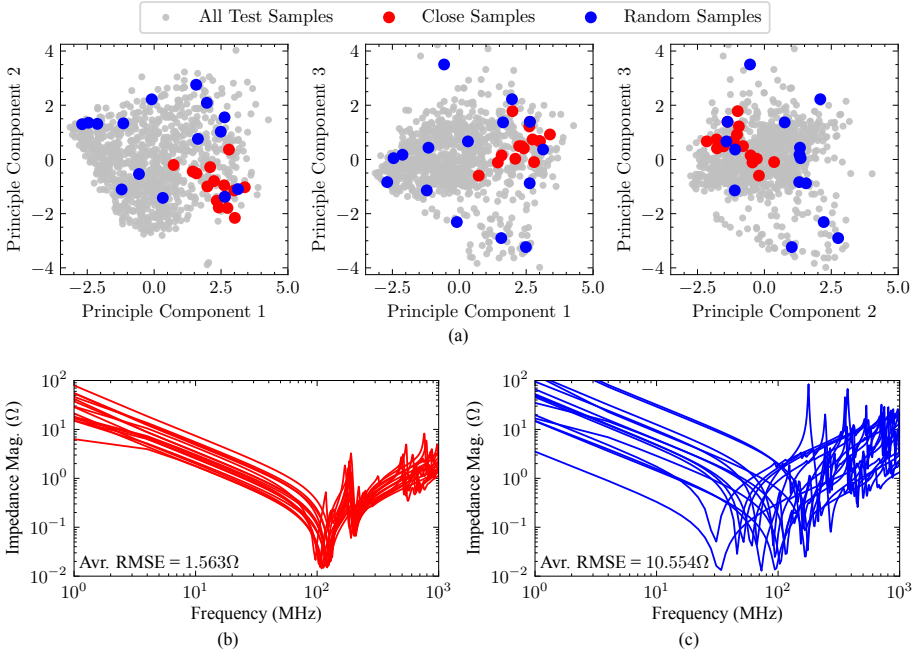

Figure 12: An AE is trained on all available cases. The (a) 3D PCA visualization of the latent space representation of all the test samples is shown, as well as the (b) impedance profiles associated with samples close to each other in the latent space and (c) impedance profiles from randomly chosen point in the latent space. Samples close to each other in the latent space result in similar impedance profiles.

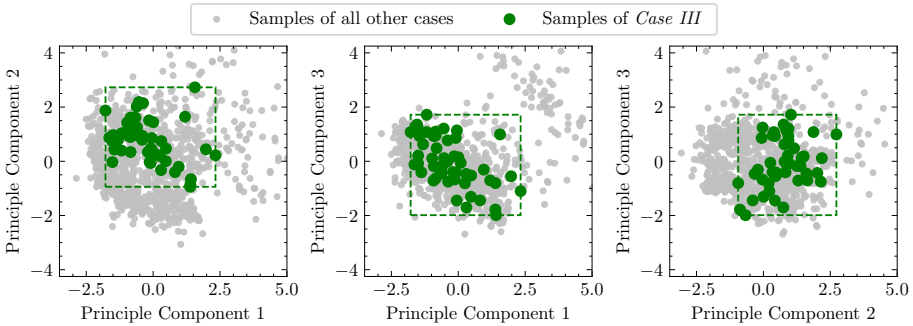

Figure 13: An AE is trained on data from *Case I*, *Case II* and *Case IV* while data points from *Case III* are used as an input. A 3D PCA visualization of the latent space representation is shown.

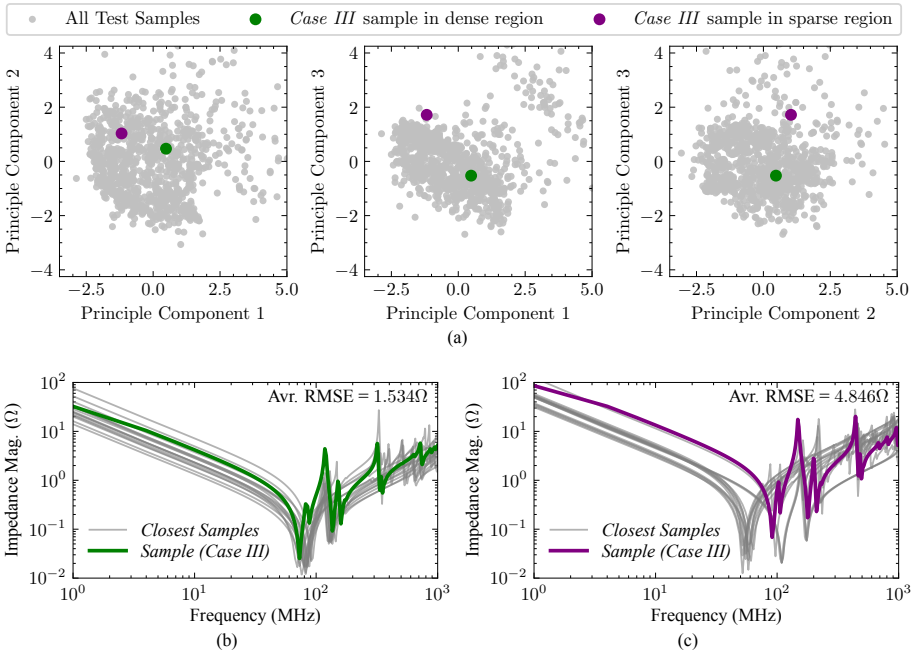

Figure 14: An AE is trained on data from *Case I*, *Case II* and *Case IV* while data points from *Case III* are used as an input. A (a) 3D PCA visualization of the latent space representation is shown. For two *Case III* samples, the (b) impedance profiles of the 15 nearest samples in a dense latent space region, and the (c) impedance profiles of the 15 nearest samples in a sparse region are shown.

For the dense area, the average euclidean distance between the *Case III* sample and the closest 15 samples amounts to 1.374. For the sparse area, the average euclidean distance between the *Case III* sample and the closest 15 samples amounts to 1.896. The nearest 15 samples from other cases to the chosen *Case III* samples are identified and the associated impedance profiles are extracted. The 15 nearest impedance profiles to the two *Case III* samples from the dense and sparse region are compared, see Fig. 14b and Fig. 14c, respectively. It can be seen that the samples from the other cases that are close to the *Case III* sample exhibit a certain degree of agreement with an average RMSE of 1.534 Ω, see Fig. 14b. Samples further apart from the *Case III* sample exhibit much less agreement with an average RMSE of 4.846 Ω, see Fig. 14c. This shows that even for unseen and new problems, similar profiles can be identified by only looking at the distance in the latent space. Since it has been shown that PCB parameters can directly be mapped to the latent space The trained ANN-AE can be used to map these input samples to the latent space, without any simulations needed.

7 Discussion and Outlook

In Section 5, the ability of ANN-AEs in the prediction of self-impedance profiles from design space parameters has been shown. The accuracy of the prediction depends on many factors including the complexity, dimensionality and amount of available samples. The dimension of the latent space influences the accuracy as high dimensions mean more important features can be stored and learned. A latent space analysis shows that many features, e.g., direct current impedance level, initial impedance slope and frequency of resonant peaks are deemed important for impedance reconstruction. The one-port input impedance in a resonator model of a power ground plane structure consists of a static impedance (plane capacitance) and an infinite number of modal impedances (parallel conductances and inductances) [19]. For a full-mode representation in the frequency range of interest, more degrees of freedom and modes have to be considered for more accurate modeling [20]. This is also observed in the AE model where high dimensional latent spaces allow for storing more information about higher frequency resonant peaks to capture the full behavior. In Section 6, the ability to find similar samples in the latent space for unseen design spaces has been shown. These similar samples in the latent space showcase similar output impedance profiles. Meaning, for any input sample, the output impedance can be approximated if similar samples exist. With more and more available datasets of various design spaces and possible impedance profiles, the probability of finding similar impedance profiles increases. In other words, the need to generate new data will decrease with the availability of more data. Moreover, regions in the latent space where not many similar samples are available can be identified to generate new data in order to cover these regions for future use.

These two shown abilities of AEs can help speed up the decoupling process and design of PDNs in two ways: by replacing slow EM simulations needed in existing decoupling algorithms, e.g., GAs. With growing databases, even less data needs to be generated for new problems making the process even more efficient. The second way involves the ability of reusing available decoupling strategies. If a successfully used decap constellation for a certain PDN impedance behavior is available, using the same constellation for a very similar sample should result in an adequate design meeting the TI or at least a good starting point for further optimization. Finding this similar impedance behavior is done rapidly without any EM simulations needed. To achieve the promised speed-up, the proposed approach needs to be extended to multi-port systems in future work. The extension would allow the prediction of the self- and transfer-impedances which can represent a port of interest and other open via locations where decaps can be placed. The PDN impedance with attached decaps can be quickly calculated such that the matrix of the bare impedance is

predicted by AEs while the impact of attached decaps is determined by a simple post-processing matrix multiplication. Similar design spaces can be found in the same manner and available decoupling constellations can be quickly applied to evaluate their effects. Another aspect that needs to be taken into account is a unified pre-processing for the design spaces and data. PCB design spaces need to have the same format using and same design dimensions for successful data reuse. These dimensions should be carefully elaborated to be able to cover at least very large portions of conventional PCB designs.

8 Conclusions

AEs are able to predict the full impedance profile of PDNs from PCB design parameters. The accuracy of the prediction depends on the complexity and volume of available samples for training. Reusing older datasets results in an increased data-efficiency and performance, this is especially advantageous for small datasets when simulations are time-costly. The amount of training samples from older datasets for efficient transfer learning has to be chosen carefully to avoid overfitting. The prediction of AEs is very fast with durations lower than 30 ms for the used cases. The training times can be reduced if models are apriori pre-trained then fine-tuned on new datasets. For trained and accurate AEs, similar impedance profiles and datasets can be found by a latent space analysis. The similarity identification is a result of the regularity property of AEs and does not necessitate further independent training.

The prediction and classification has been demonstrated for self-impedances on a bare board. For the enhancement of the decoupling process the prediction of transfer-impedances is likewise needed. The impedance matrices enable the consideration of termination decaps needed for the decoupling of PDNs. This approach has the potential to speed up the design of PDNs by either replacing the slow EM predictions with fast ANN-AE predictions or finding similar design spaces and samples to reapply available decoupling strategies. With more data available and larger databases, the speed-up and efficiency will keep increasing. This is due to both less new data needed for accurate prediction and the availability of more designs for comparison. The databases should have a unified format and dimensions for all considered design spaces and problems to enable data reuse.

References

[1] M. Schierholz, I. Erdin, J. Balachandran, and C. Schuster, "Data-Efficient Supervised Machine Learning Technique for Practical PCB Noise Decoupling," in *DesignCon 2023*, (Santa Clara, CA, USA), Feb. 2023.

[2] F. de Paulis, R. Cecchetti, C. Olivieri, and M. Buecker, "Genetic Algorithm PDN Optimization based on Minimum Number of Decoupling Capacitors Applied to Arbitrary Target Impedance," in *2020 IEEE International Symposium on Electromagnetic Compatibility & Signal/Power Integrity (EMCSI)*, (Reno, NV, USA), July 2020.

[3] M. Schierholz, Y. Hassab, C. Yang, and C. Schuster, "Evaluation of Support Vector Machines for PCB based Power Delivery Network Classification," in *Proceedings IEEE 30th Conf. Electrical Performance Electronic Packaging and Systems EPEPS*, (Austin, TX, USA), Oct. 2021.

[4] W. Zhang, F. Feng, J. Jin, and Q.-J. Zhang, "Parallel Multiphysics Optimization for Microwave Devices Exploiting Neural Network Surrogate," *IEEE Microwave and Wireless Components Letters*, vol. 31, pp. 341–344, Apr. 2021.

[5] M. Schierholz, Y. Hassab, I. Erdin, J. Balachandran, and C. Schuster, "Applying Techniques of Transfer and Active Learning to Practical PCB Noise Decoupling," in *DesignCon 2024*, (Santa Clara, CA, USA), Jan. 2024.

[6] Z. Nezhi, M. Stiemer, M. Schierholz, and C. Schuster, "Dimensional Reduction by Auto-Encoders in Machine Learning Based Power Integrity Analysis," in *2024 IEEE 28th Workshop on Signal and Power Integrity (SPI)*, (Lisbon, Portugal), May 2024.

[7] M. Swaminathan and A. E. Engin, *Power Integrity Modelling and Design for Semiconductors and Systems*. Boston, MA, USA: Pearson Education, Inc., Nov. 2007.

[8] J. Y. Choi and M. Swaminathan, "Decoupling Capacitor Placement in Power Delivery Networks Using MFEM," *IEEE Transactions Components, Packaging and Manufacturing Technology*, vol. 1, pp. 1651–1661, Oct. 2011.

[9] S. Han, O. W. Bhatti, and M. Swaminathan, "A Knowledge Based Method for Optimization of Decoupling Capacitors in Power Delivery Networks," *IEEE Transactions on Components, Packaging and Manufacturing Technology*, vol. 12, no. 5, pp. 828–838, 2022.

[10] D. P. Kingma and J. Ba, "Adam: A Method for Stochastic Optimization," in *3rd International Conference on Learning Representations ICLR*, (San Diego, CA, USA), May 2015.

[11] S. Bozinovski, "Reminder of the First Paper on Transfer Learning in Neural Networks, 1976," *Informatica, An Interational Journal of Computing ad Informatics*, vol. 44, pp. 291–302, Sept. 2020.

[12] M. Schierholz, A. Sanchez-Masis, A. Carmona-Cruz, X. Duan, K. Roy, C. Yang, R. Rimolo-Donadio, and C. Schuster, "SI/PI-Database of PCB-Based Interconnects for Machine Learning Applications," *IEEE Access*, vol. 9, pp. 34423–34432, Feb. 2021.

[13] X. Duan, R. Rimolo-Donadio, H.-D. Brüns, B. Archambeault, and C. Schuster, "Special Session on Power Integrity Techniques: Contour Integral Method for Rapid Computation of Power/Ground Plane Impedance," in *DesignCon 2010*, (Santa Clara, CA, USA), Feb. 2010.

[14] P. D. T. Okoshi, *Planar Circuits For Microwaves ad Lightwaves*. Springer-Verlag Berlin Heidelberg New York, 1985.

[15] R. Rimolo-Donadio, X. Gu, Y. Kwark, M. Ritter, B. Archambeault, F. de Paulis, Y. Zhang, J. Fan, H.-D. Brüns, and C. Schuster, "Physics-Based Via and Trace Models for Efficient Link Simulation on Multilayer Structures Up to 40 GHz," *IEEE Transactions Microwave Theory and Techniques*, vol. 57, pp. 2072–2083, Aug. 2009.

[16] S. Müller, X. Duan, M. Kotzev, Y.-J. Zhang, J. Fan, X. Gu, Y. H. Kwark, R. Rimolo-Donadio, H.-D. Brüns, and C. Schuster, "Accuracy of Physics-Based Via Models for Simulation of Dense Via Arrays," *IEEE Transactions on Electromagnetic Compatibility*, vol. 54, pp. 1125–1136, Oct. 2012.

[17] *ANSYS ®Electromagnetics Suite, Release 16.2*. Canonsburg, PA, USA: ANSYS, INC.

[18] I. T. Jolliffe and J. Cadima, "Principal Component Analysis: A Review and Recent Developments," *Philosophical Transactions of the Royal Society A: Mathematical, Physical and Engineering Sciences*, vol. 374, April 2016.

[19] G.-T. Lei, R. Techentin, and B. Gilbert, "High-Frequency Characterization of Power/Ground-Plane Structures," *IEEE Transactions on Microwave Theory and Techniques*, vol. 47, pp. 562–569, May 1999.

[20] G.-T. Lei, R. Techentin, P. Hayes, D. Schwab, and B. Gilbert, "Wave Model Solution to the Ground/Power Plane Noise Problem," *IEEE Transactions on Instrumentation and Measurement*, vol. 44, pp. 300–303, Apr. 1995.

Publication 7 (P7)

Title

Machine Learning Driven Fast Prediction of Self- and Transfer-Impedance Profiles for the Modeling of PCB-Based Power Delivery Networks.

Publication Status

In preperation for resubmission to peer-reviewed journal: IEEE Transactions on Signal and Power Integrity. This version was accepted for publication but withdrawn by the authors to further improve and include updated results.

Author Contribution

Involvement in all areas of the research, including conceptualization, methodology, implementation and writing, in a leading role (1. author).

Bibliographic Information

[66] Y. Hassab, J. Heßling, and C. Schuster, "Machine Learning Driven Fast Prediction of Self- and Transfer-Impedance Profiles for the Modeling of PCB-Based Power Delivery Networks," unpublished.

Machine Learning Driven Fast Prediction of Self- and Transfer-Impedance Profiles for the Modeling of PCB-Based Power Delivery Networks

Youcef Hassab, Student Member, IEEE, Jan Hessling, Student Member, IEEE, and Christian Schuster, Fellow, IEEE

***Abstract*—In this work, a machine learning (ML)-driven method is employed for the prediction of broadband impedance profiles enabling fast modeling of printed circuit board (PCB)-based power delivery networks (PDNs). Extending its scope beyond prior applications on self-impedances, the approach now predicts both self- and transfer-impedance profiles on bare-board ports, using a combination of feedforward neural networks (FNNs) and autoencoders (AEs). The ML approach leverages datasets from existing designs to ensure fast and data-efficient prediction of N-port impedance behavior of a new PCB case, based on 2-port training data. In the future, this approach could lead to a speed-up of the PDN design process by replacing expensive simulations with fast predictions over large design spaces. In order to demonstrate robustness and scalability, 55500 samples of an extended collection of previous and new cases of rectangular and irregularly shaped PCBs with up to 14 layers and arrays with up to 25 power vias, simulated up to a frequency of 1 GHz, are proposed and simulated. The datasets are available for download on the SI/PI-Database from the Hamburg University of Technology (https://www.tet.tuhh.de/en/si-pi-database).**

***Index Terms*—Machine learning (ML), printed circuit board (PCB), power delivery network (PDN), autoencoder (AE), electromagnetic (EM) modeling.**

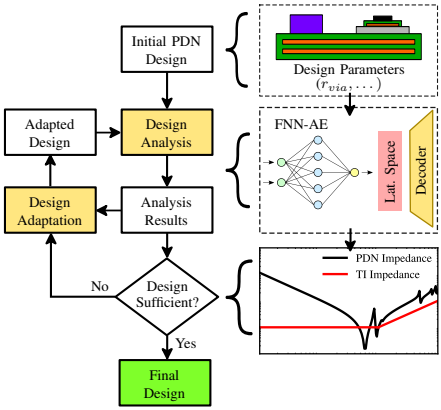

Fig. 1. Flowchart of a PDN design process: Starting from an initial design, the PDN is optimized in an iterative process where the design is alternately analyzed and adapted until target criteria are met. In the proposed ML-based approach, a combination of feedforward neural network (FNN) and autoencoders (AEs) predicts the self- and transfer-impedances from design parameters to fully model the PDN. The fast modeling of the PDN as opposed to slow full-wave simulations should lead to a speed-up of the design process.

I. Introduction

THE design of power delivery networks (PDNs) is an integral part of printed circuit board (PCB) design to ensure the proper functioning of high-speed digital integrated circuits (ICs). The task of designing PCB based PDNs is showing an increasing complexity due to higher switching frequencies, higher integration density of components, and lower supply voltages With higher currents flowing through the systems, even lower PDN impedances have to be achieved [1]. The reduction of the PDN impedance is partially attained through the iterative design adaptation and placement of decoupling capacitors (decaps), see Fig. 1. There are many methods for the strategic placement of decaps including conventional guidelines [2], [3], gradient based methods [4], [5], genetic algorithms (GAs) [6], [7], and ML based methods [8], [9]. These methods require detailed information on the electromagnetic (EM) behavior of the PDN at each iteration step to align with the target impedance (TI). The design analysis for the acquirement of impedance characteristics of PDNs is a time- and resource-consuming procedure that can delay the design process. This is especially a relevant problem for large design spaces, variable PCB structures and ports, where full-wave simulations are needed and analytical models are not sufficient. The application of machine learning (ML) techniques in the modeling and optimization of PDNs has been a topic of interest in recent years. ML methods have been used to classify PDNs with respect to the TI [10], [11], to automate the placement of decaps [12], [13] and the modeling and optimization of PDNs [14]–[16].

One major research topic is the replacement of the expensive EM simulations with fast ML predictions and surrogate models to speed up the design process. The prediction of distinct key-features of the PDN impedance on bare PCBs has been first investigated by the authors in [17]–[19]. Moreover, the prediction of broadband PDN impedance profiles using ML techniques has been pursued, as they offer a more sophisti-

The authors are with the Institut für Theoretische Elektrotechnik (TET) of Hamburg University of Technology (TUHH), Hamburg, Germany. (E-mail corresponding author: youcef.hassab@tuhh.de).

cated knowledge on the PDN behavior [20], [21]. Autoencoders (AEs) have been investigated for PCB classification and design by utilizing a compressed representation in the latent space [22], [23]. However, these approaches need a substantial amount of data samples for the training of the ML models, often leading to a significant computational overhead overshadowing any ML benefits. To tackle these issues, a combination of feedforward neural networks (FNNs) and AEs embedded in a data reuse scheme has been proposed and tested by the authors for the data-efficient prediction of self-impedance profiles in a first proof of concept [24]. In this work, the prediction of the self-impedances is extended to transfer-impedances for a full characterization of the PDN behavior. The approach is investigated using the original AEs based on FNNs and a new AE architecture based on convolutional neural networks (CNNs). The data preprocessing, based on domain knowledge, is extended to enable the accurate prediction of transfer-impedance profiles. The performance of the ML networks is tested on additional more complex multi-port PCBs for a total of six different PCB cases with increased complexities for reliable evaluation. The used datasets are validated to ensure quality and statistically analyzed for a full characterization of the complexity of the problem.

The investigated ML-based approach enables the fast full modeling of PDNs on N-port bare PCBs, instead of predicting self-impedances only, allowing the consideration of terminated ports with decaps for PDN decoupling processes. The resulting PDN impedance as observed from a port of interest can be calculated by simple matrix operation between the modeled bare-board impedance matrix and the decap terminations. Since this method leverages existing datasets for enhanced data-efficiency, the growing databases and systematic data generation [25], e.g., the SI/PI-Database, should lead to a speed-up in the design of PDNs. The SI/PI-Database (Access: **https://www.tet.tuhh.de/en/si-pi-database/**) contains many datasets from the signal integrity (SI) and power integrity (PI) domains representing different PCB cases, shapes, stackups, and parameters [26], [27].

The remainder of the paper is organized as follows: The defined PCB cases alongside the data generation and analysis of the used datasets are covered in Section II. The setup and evaluation of ML methods for the prediction of PDN impedances are highlighted in Section III. An application and discussion of the proposed ML methods for PDN modeling is provided in Section IV, while Section V concludes the paper.

II. Benchmark Design and Data Evaluation

For the investigation of the proposed ML-based impedance prediction approach, datasets are generated by the simulation of PCBs from a defined design space. The overall design space covers an explorable bounded subset balancing physical realism with computational tractability. This allows for the generation of representative datasets for the training and evaluation. The chosen dimensions and parametric ranges are suitable for practical high-speed digital systems, see Table I and Fig. 2. The design dimensions include parameters that are known to influence the PCB-based PDN impedances [28].

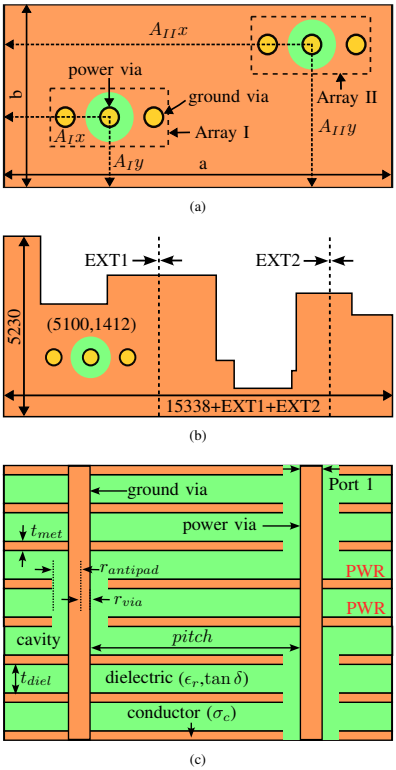

Fig. 2. The varied geometry and material properties of the defined PCBs are shown as (a) top view for the rectangular cases, (b) top view for irregular-shaped *Case III* and (b) side view of the stackups. Adapted from [24].

Six different PCB cases are defined exhibiting variability in design attributes, including geometric configurations and material composition. The chosen benchmark cases have an increasing number of varied parameters and include canonical rectangular boards as well as an irregular shape, and range from single-via topologies to realistic via arrays commonly found in voltage regulator module (VRM) layouts. While the test cases are simplified compared to full-scale commercial boards, they retain the core physical mechanisms govering impedance behavior. Moreover, the defined cases possess two ports on two via arrays, which allow to initially demonstrate the feasibility of the proposed approach for transfer-impedances. However, the method is inherently scalable and can be extended to more complex scenarios with N ports, see Section IV-C. In the rest of this section, the defined cases as well as the data generation and validation processes are presented.

TABLE I
THE OVERALL DESIGN SPACE OF THE PCB-BASED PDNS IS DEFINED THROUGH MAXIMUM AND MINIMUM VALUES CONSTRAINING THE DESIGN DIMENSIONS DEFINED IN FIG. 2. THE FIXED, VARIED PARAMETERS AND THE COVERED RANGES ARE GIVEN FOR SIX DEFINED APPLICATION CASES.

Parameter	**Overall Design Space**		**Case Variations**					
	Minimum	**Maximum**	**Case I**	**Case II**	**Case III**	**Case IV**	**Case V**	**Case VI**
Via Radius (r_{via} mil)	5	9	5	5	5	Varied	5	Varied
Via Pitch ($pitch$ mil)	40	80	80	60	40	40	40	40
Antipad Radius ($r_{antipad}$ mil)	15	24	15	19	15	Varied	18	Varied
PCB X-Width (a mil)	1000	18000	Varied	Varied	Varied	Varied	12000	Varied
PCB Y-Width (b mil)	1000	18000	Varied	Varied	5230	Varied	10000	Varied
Conductivity (δ_c S/m)	$4.5 \cdot 10^7$	$5.8 \cdot 10^7$	$5.8 \cdot 10^7$	$5.8 \cdot 10^7$	$5.8 \cdot 10^7$	Varied	$5.8 \cdot 10^7$	Varied
Rel. Permittivity (ϵ_r)	2	6	Varied	Varied	Varied	Varied	Varied	Varied
Loss Tangent ($\tan\delta$)	0.005	0.025	0.02	0.02	0.02	Varied	0.02	Varied
Dielectric Height (t_{diel} mil)	3	80	Varied	Varied	Varied	Varied	Varied	Varied
Plane Thickness (t_{met} mil)	0.7	4	1	1	1	Varied	1	Varied
Array I Type (Power Vias)	1	26	Type B	Type C	Type B	Type B	Type E	Type B
Array I X-Position (A_Ix mil)	0	X-Width	Center	Random	5100	Random	Varied	Random
Array I Y-Position (A_Iy mil)	0	Y-Width	Center	Random	1412	Random	Varied	Random
Array II Type (Power Vias)	1	5	–	Type D	–	Type B	Type A	Type B
Array II X-Position ($A_{II}x$ mil)	0	X-Width	–	Random	–	Random	10000	Random
Array II Y-Position ($A_{II}y$ mil)	0	Y-Width	–	Random	–	Random	9000	Random
Extension I (EXT1 mil)	-5000	5000	–	–	Varied	–	–	–
Extension II (EXT2 mil)	-1000	5000	–	–	Varied	–	–	–
Stackup Order (layers)	2	14	Ground 2·Power Ground	3·Ground 2·Power 3·Ground	Ground 2·Power Ground	Ground 2·Power Ground	Ground Power –	6·Ground 2·Power 6·Ground
PCB Shape	–	–	Rect.	Rect.	Irregular	Rect.	Rect.	Rect.
Variable Dimensions	4	13	4	8	4	13	4	13
Available Samples	500	20000	3000	10000	500	20000	2000	20000

A. PCB Test Case Definitions

1) Case I: Features a rectangular geometry with a 4-layer, symmetric stackup: [ground, 2×power, ground], introduced in [18]. A single via array of type B (Fig. 3b) is positioned at the center of the PCB. A total of 3000 samples are generated using numerical simulations, with variations in the cavity height, relative permittivity, and the two dimensions of the board X-Width, and Y-Width.

2) Case II: Features a rectangular shape with an 8-layer, symmetric stackup: [3×ground, 2×power, 3×ground] [18]. Two via arrays are placed on the PCB. The first via array of type C (Fig. 3c) and the second via array of type D (Fig. 3d) are placed randomly on the PCB. A total of 10 000 samples are generated using numerical simulations, with variations to the cavity height, relative permittivity, X-Width, and Y-Width of the PCB.

3) Case III: Features a polygonal shape with a 4-layer, symmetric stackup: [ground, 2×power, ground], see Fig. 2b [18]. A single via array of type B (Fig. 3b) is fixed at the coordinates $(5100, 1412)$. A total of 500 numerical simulations are carried out, varying the cavity height, relative permittivity and the extensions *EXT1*, and *EXT2* that allow for extending the PCB at two specific horizontal points.

4) Case IV: Features a rectangular geometry with a 4-layer, symmetric stackup: [ground, 2×power, ground] [24]. Two identical via arrays of type B (Fig. 3b) are placed randomly on the PCB. A total of 20 000 numerical simulations are conducted, with variations to most parameters listed in Table I.

5) Case V: Features a rectangular geometry with a 2-layer stackup: [ground, power]. Two via arrays are placed on the PCB. The position of the first via array of type E (Fig. 3e) is varied while the second via array of type A (Fig. 3a) is fixed. A total of 2000 numerical simulations are conducted, with variations in the cavity height, relative permittivity, and the two coordinates of the first array.

6) Case VI: Features a rectangular geometry with a 14-layer, symmetric stackup: [6×ground, 2×power, 6×ground]. Two identical via arrays of type B (Fig. 3b) are placed randomly on the PCB. A total of 20 000 numerical simulations are conducted, with variations to most parameters, see Table I.

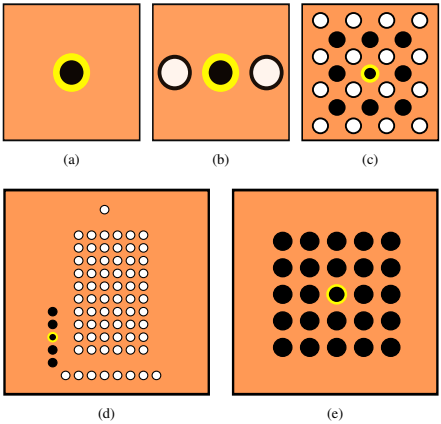

Fig. 3. The different via arrays placed on the PCBs are shown from a top view: (a) type A, (b) type B, (c) type C, (d) type D and (e) type E. The power and ground vias are depicted in black and white, respectively. The central power via used as an observation point is highlighted in yellow.

B. Data Generation and Access

A physics-based (PB) modeling tool is used for the generation of data samples [29]. A 2D-radial wave propagation in the cavities of a PCB is assumed. The PCB models are created by the combination of the parallel plane impedance calculated using a contour integral method (CIM) and a PB via model within each cavity [30], [31]. The partial models for each cavity are then concatenated on a network parameter level. A perfect magnetic conductor (PMC) is assumed at the borders of the PCBs and fringing effects are assumed to be negligible. The ports for the network parameters are placed within the antipad regions of power vias. The ports on the top side of the PCB on the observation power vias are indexed "1" and "2" for Array I and Array II, respectively. A validation of this method with a full-wave finite element method (FEM) solver is provided in [32], [33]. To cover the defined design spaces, sampling points are selected using a latin hypercube sampling (LHS) method for simulation. The PCBs are simulated in the 1 MHz to 1 GHz frequency range in 3 MHz steps. The simulation of the PB models is factors of magnitude faster than full-wave FEM solvers on the same machine, see Table II. The speed-up factor is more pronounced for more complex cases with more ports. The generated and used datasets in this work from the six defined cases are available for download on the SI/PI-Database of the Technical University of Hamburg (TUHH) [26]: **https://www.tet.tuhh.de/en/si-pi-database/**.

C. Data Analysis and Validation

The generated datasets using the aforementioned PB modeling tool are validated using a commercial FEM solver. For selected samples from the defined PCB cases, the resulting self- and transfer-impedances (Z_{11} and Z_{12}) are compared, see Fig. 4. The simulated impedance profiles using the PB modeling tool and the FEM solver show good agreement.

TABLE II
COMPARISON OF SIMULATION AND PREDICTIONS TIMES FOR SAMPLES (334 FREQUENCY POINTS) FROM CASE V (2-LAYER) AND CASE VI (14-LAYER) USING AN FEM SOLVER, PB AND ML-BASED MODELS*

Case	FEM Sim.	PB Sim.	ML Pred.
Case V	9 min	40 s	50 ms
Case VI	30 min	4 min	50 ms

*Simulations performed on a machine equipped with an Intel®Core i5-6500 CPU and 64 GB DDR4 Memory.

In total, 55500 samples from six different cases are available as a main dataset. The distribution of the input dimensions of all available samples shows that a wide range of PCB designs with varying geometric and material properties are covered, see Fig. 5 (a) to (i). The resulting EM behavior of the simulated samples exhibits variability: The output bare-board PDN impedances vary in the number, amplitude and frequency of the resonances as well as the profiles, see Fig. 6. To quantify the variability of the impedance profiles, the magnitude at 1 MHz frequency Z_1, the first resonance frequency f_r and the amount of resonances N_r are extracted. The distribution of these key-features is given in Fig. 5 (j) to (l).

The transfer-impedances exhibit less smooth and more complex profiles with sharper and more numerous resonances than self-impedance profiles, see Fig. 6. The cavity resonator model gives an analytical expression to explain the impedance characteristics of rectangular plane pairs based on the solution of a 2D-Helmholtz equation using Green's function. It is used to obtain insights on the behavior of the more complex multilayer structured that are investigated in this work. The frequency-dependent impedance $Z_{ij}(\omega)$ between two ports i and j in a cavity model can be expressed as a summation over eigenmodes, weighted by a product f of the mode shapes at the source and observation points [30]:

$$Z_{ij}(\omega) = \frac{j\omega\mu \cdot t_{diel}}{ab} \sum_{m=0} \sum_{n=0} g(m,n) \cdot f(x_i, y_i, x_j, y_j) \quad (1)$$

where

$$f(x_i, y_i, x_j, y_j) = \cos\left(\frac{m\pi x_i}{a}\right) \operatorname{sinc}\left(\frac{m\pi t_{x_i}}{2a}\right) \cos\left(\frac{n\pi y_i}{b}\right) \operatorname{sinc}\left(\frac{n\pi t_{y_i}}{2b}\right) \times \cos\left(\frac{m\pi x_j}{a}\right) \operatorname{sinc}\left(\frac{m\pi t_{x_j}}{2a}\right) \cos\left(\frac{n\pi y_j}{b}\right) \operatorname{sinc}\left(\frac{n\pi t_{y_j}}{2b}\right)$$

$g(m,n)$ is a mode-dependent function, (x_i, y_i) and (x_j, y_j) are the coordinates of the center of the ports, (t_{xi}, t_{yi}) and (t_{xj}, t_{yj}) represent the widths of the ports, m and n represent the mode numbers, μ the permeability of the dielectric. For self-impedances ($i = j$), only the squared magnitude of mode shapes at one port location contributes to the impedance, resulting in smoother profiles due to the consistently additive effect of the modes, see $f(x_i, y_i, x_j, y_j)$ in Eq. (1). In contrast, transfer-impedance ($i \neq j$) involves cross-terms between two spatial locations, which can interfere with each other.

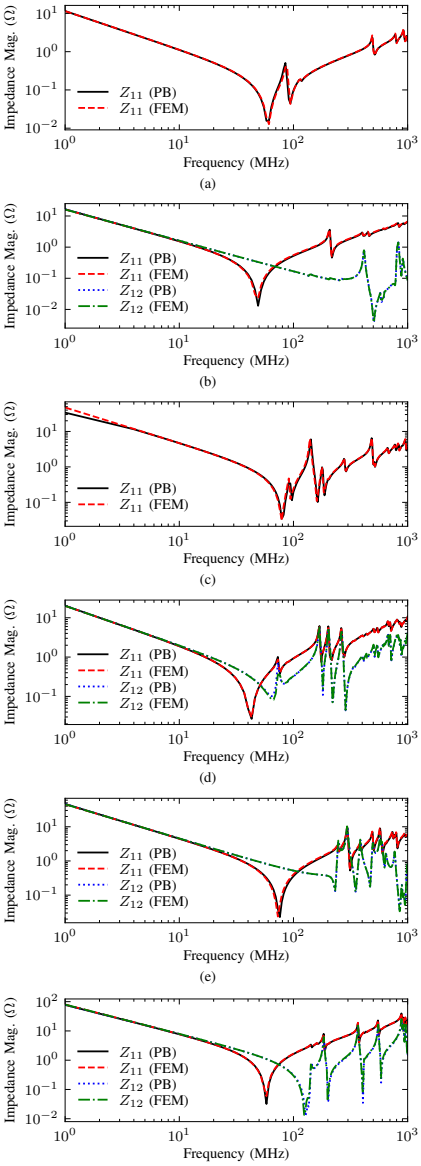

Fig. 4. Comparison of the self- and transfer-impedances between the observation ports of via arrays in example samples from (a) *Case I*, (b) *Case II*, (c) *Case III*, (d) *Case IV*, (e) *Case V* and (f) *Case VI*, simulated using the described PB approach [29] and a commercial FEM solver [34].

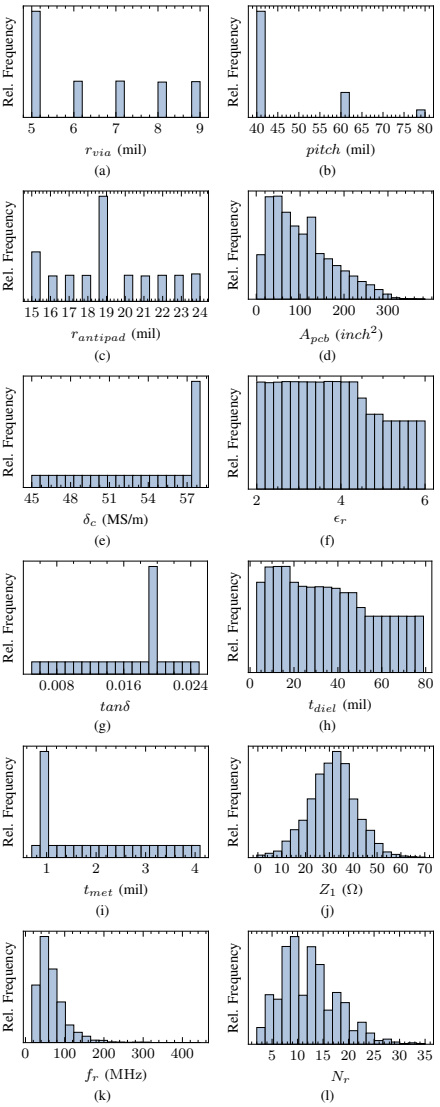

Fig. 5. Histograms of the distribution of input design parameters (a) r_{via}, (b) $pitch$, (c) $r_{antipad}$, (d) A_{pcb}, (e) δ_c, (f) ϵ_r, (g) $\tan\delta$, (h) t_{diel} and (i) t_{met}, and the output impedance features (j) Z_1, (k) f_r and (l) N_r of the main dataset. A wide range of PCB designs with varying geometric and material properties are covered. The resulting output impedances vary in the number, amplitude and frequency of the resonances as well as the profiles.

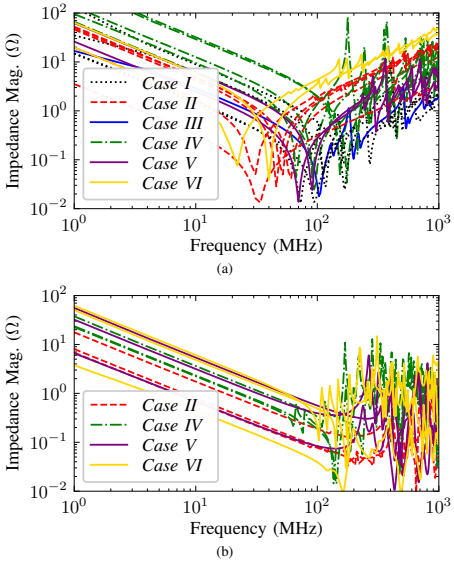

Fig. 6. Plots of a randomly chosen set of (a) 20 self-impedance profiles and (b) 12 transfer-impedance profiles from different cases show a variability in the number, amplitude and frequency of the resonances as well as the general trends of the profiles. In contrast to self-impedances, the transfer-impedances exhibit more irregular profiles with sharper and more irregular resonances.

The constructive or destructive interference depends on the relative phase and polarity of the modal fields. This results in more irregular profiles with sharper and more irregular resonances. These characteristics make transfer-impedances more sensitive to the geometric and electrical configuration of the structure and more challenging to predict accurately. The setup of suitable ML models for impedance prediction is introduced in the next section.

III. ML Setup for Impedance Prediction

In this section, investigations of the proposed ML-based approach for the prediction of PDN impedance profiles from design parameters are presented. The data is first preprocessed to allow efficient training and optimal results. The training and testing setups of the ML models for the profile prediction are summarized. The results of this approach are evaluated.

A. Impedance Profile Prediction Methodology

Autoencoders, consisting of encoder/decoder networks and a latent space, can be trained to reconstruct impedance profiles presented at the input, e.g., 1D self- and transfer-impedance magnitude profiles. In the proposed approach, the AE structure is tweaked to be able to predict and generate an impedance profile from an input sample consisting of design parameters, e.g., geometry, material properties and observation point on

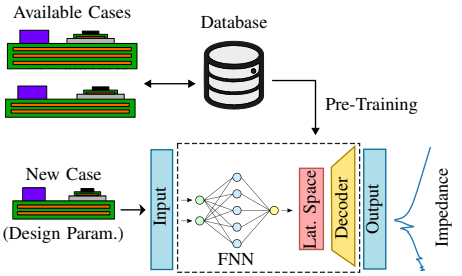

Fig. 7. In the proposed approach, regular autoencoder (AE) networks are trained to be able to reconstruct impedance profiles presented at the input passing by the encoder, latent space and the decoder in the first stage. For the modeling of power delivery networks (PDNs), a feedforward neural network (FNN) is combined with the latent space and decoder parts of the trained AE to predict the impedance profiles. Using previous datasets by transfer learning allows the prediction of the impedance profiles with a higher data-efficiency. Partially adapted from [24].

the PCB [21]. After the training of the AE for impedance reconstruction in a first stage, the encoder part is removed and replaced by an FNN, see Fig. 7. The FNN is trained in a second stage to predict the latent space representation of any sample of design parameters. This is possible, since a unique latent space representation learned by the AE corresponds to a known design parameter sample from the training set. The training set consists of samples from the defined design space of a case of interest. Once the training is done, an output profile can be predicted from a design parameter sample passing by the trained FNN, latent space and decoder. The tweaked AE is referred to as an FNN-AE in the remainder of the paper. In case of a transfer learning (TL) approach, the FNN-AE is trained on all available and previously generated datasets in a pre-training step. A sample of interest from the new case that need to be modeled can be approximated by the pre-trained FNN-AE for a fast evaluation. For more accurate predictions, few new samples from the case of interest are simulated and used to retrain the available pre-trained model. The retraining is referred to as fine-tuning, see Section IV-A.

B. Feature Engineering and Data Preprocessing

The description of the PCBs has to be reduced to a feasible amount of input features for the neural network. Those features need to describe the different cases while also maintaining the physically necessary information. For this purpose, new input features are created and selected based on physics and engineering domain knowledge [35]. This process is referred to as feature engineering. It is assumed that the impedance at the observation point is correlated to the cavity model impedance, see Eq. (1) [30]. Therefore, important features can be constructed from that representation. The static capacitance, calculated using the PCB Area (A_{pcb}), t_{diel} and ϵ_r, is especially relevant to determine low-frequency impedance level. The PCB Area (A_{pcb}) is thus defined to measure the area of the board for both regular and irregular shapes. Additionally,

TABLE III
TUNED HYPERPARAMETERS FOR THE TWO DIFFERENT AEs ARCHITECTURES (FIRST STAGE) AND THE CORRESPONDING FNNs (SECOND STAGE).

Type	Parameter	AE (FNN)	FNN for AE (FNN)	AE (CNN)	FNN for AE (CNN)
Layers	Input	334	15/16	334	15/16
	Hidden	(512, 512)	(32, 500, 950, 800, 870, 840)	(128, 64)	(32, 500, 950, 800, 870, 840, 1000, 1024)
	Latent	25	–	25	–
	Output	334	25	334	25
	Trainable Parameters	447 310	2 692 364	131 000	4 573 921
Training	Activation Function	ReLU	ReLU	ReLU	ReLU
	Loss Function	MSE	MSE	MSE	MSE
	Optimizer	Adam	Adam	Adam	Adam
	Learning Rate	$7e^{-4}$	$5e^{-4}$	$5e^{-4}$	$10e^{-4}$
	Max. Epochs	500	1000	500	1000
Kernels	Size	–	–	(15, 5)	–
	Stride	–	–	5	–
	Padding	–	–	3	–
Data	Input	Impedance	Design Parameters	Impedance	Design Parameters
	Output	Impedance	Latent Space	Impedance	Latent Space

the boards have a differing number of concatenated layers, the PCB height (t_{pcb}) is thus given for each sample to simplify the total capacitance estimation. For multiple concatenated layers, the vertical distance of the vias from observation port on the top of the board to the closest power plane delimits the inductance loop [28]. This value is defined as the power plane distance (d_{pp}). Additionally, the coordinates of the observation points relative to the PCB edges are needed, as they determine the local coupling to cavity resonant modes and the spatial distribution of electromagnetic fields within the structure. For irregular-shaped boards, these edges are not constant and cannot be simply given by the length and width of the PCB [35]. The distance between the observation point and the closest left, right, top and bottom edges of board (d_{LE}, d_{RE}, d_{TE}, d_{BE}) are thus calculated. For the determination of transfer-impedances, the euclidean distance between the two observation ports (d_{array}) is additionally given. d_{array} is a compact parameter that directly influences the inductance levels between two ports [36].

As a result of the feature engineering process, the used input design parameters for the FNNs are: r_{via}, $r_{antipad}$, $pitch$, δ_c, ϵ_r, $\tan\delta$, t_{diel}, t_{met}, t_{pcb}, A_{pcb}, d_{LE}, d_{RE}, d_{TE}, d_{BE} and d_{pp}, in addition to d_{array} for transfer-impedances. These input parameters are normalized between 0 and 10. The raw output impedance profiles are stored as magnitude vectors of size 334, representing the sampling points in the frequency range from 1 MHz to 1 GHz. For the impedance profiles, a natural logarithm is applied to the magnitude vectors before standardization. The resulting inputs of 334 are used as an input for the training of AEs.

C. Training and Testing Setup

The ML setup for the prediction of impedance profiles is based on the methods presented in [24]. The preprocessed datasets are divided into training, validation and testing sets in a 70%, 20%, 10% split for each experiment. Two main types of architectures are used for the first stage: AEs with encoders and decoder networks composed of FNNs or CNNs, referred to as AE (FNN) or AE (CNN), respectively. At this stage, the inputs and outputs used are preprocessed impedance profiles to train the AEs in the reconstruction of curves, see Fig. 8. The hyperparameters of the networks are optimized before the training stage, see Table III for the chosen parameters. An Adam optimizer with an mean squared error (MSE) loss function is used for the optimization. The training and validation sets are used for the optimization while the performance of the AEs in the reconstruction of curves is evaluated on the unseen test set. Once an AE is trained, the second stage involves the training of an FNN that predicts the latent space representation of a sample from design space parameters. The trained FNN replaces the encoder in the final two-stage model, see Fig. 7. The same trained decoder of the first stage is then used for the reconstruction of impedance curves for any point in the latent space. This enables the two-stage FNN-AE architecture to predict impedance profiles directly from design parameters.

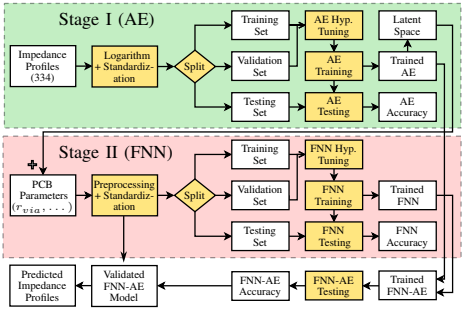

Fig. 8. Flowchart of the training and testing setup of the two-stage FNN-AE. The first stage involves the training and testing of AEs for impedance profile reconstruction. In the second stage, FNNs are trained to predict the latent space representation from PCB parameters. The trained FNN replaces the encoder part of the AE. The resulting and validated FNN-AE can be used to predict impedance profiles from unseen PCB parameters. Adapted from [24].

For the performance evaluation, the original simulated magnitude profiles x_i from an unseen test set are compared with

TABLE IV
PERFORMANCE COMPARISON FOR THE PREDICTION OF THE SELF- AND TRANSFER-IMPEDANCE PROFILES OF SAMPLES FROM THE TEST SETS.

Type	Model	RMSE	MAE	nMAE	Train.	Pred.
Z_{11}	AE (FNN)	4.28 Ω	0.72 Ω	12%	5.9 min	54 ms
	AE (CNN)	4.21 Ω	0.75 Ω	13%	5.3 min	267 ms
Z_{12}	AE (FNN)	4.13 Ω	0.64 Ω	38%	8.4 min	40 ms
	AE (CNN)	4.23 Ω	0.58 Ω	35%	8.5 min	274 ms

TABLE V
PERFORMANCE COMPARISON FOR THE PREDICTION OF THE SELF-IMPEDANCE (Z_{11}) ON DIFFERENT USE CASES USING AN AUTOENCODER (AE) WITH FEEDFORWARD NEURAL NETWORKS (FNNS).

Case	Samples	Dim.	RMSE	MAE	nMAE
Case I	3000	4	4.54 Ω	0.16 Ω	11%
Case II	10 000	8	1.05 Ω	0.36 Ω	8%
Case III	500	4	1.45 Ω	0.65 Ω	17%
Case IV	20 000	13	5.22 Ω	0.74 Ω	18%
Case V	2000	4	0.46 Ω	0.21 Ω	7%
Case VI	20 000	13	5.38 Ω	1.01 Ω	9%
All Cases	55 500	–	4.28 Ω	0.72 Ω	11%

the predicted output magnitude profiles x_i' of the trained networks. Multiple metrics are computed to evaluate the accuracy: the root mean squared error (RMSE), mean absolute error (MAE) and normalized mean absolute error (nMAE). Since the absolute impedance magnitude values vary depending on the case and predicted parameter, a normalized MAE metric is defined. The nMAE represents a percentage error relative to the average magnitude values to make the comparison between cases and parameters:

$$\text{RMSE} = \sqrt{\frac{1}{m}\frac{1}{n}\sum_{i=1}^{n}\sum_{f=1}^{m}(x_i(f) - x_i'(f))^2} \tag{2}$$

$$\text{MAE} = \frac{1}{m}\frac{1}{n}\sum_{i=1}^{n}\sum_{f=1}^{m}|x_i(f) - x_i'(f)| \tag{3}$$

$$\text{nMAE} = \frac{\frac{1}{m}\frac{1}{n}\sum_{i=1}^{n}\sum_{f=1}^{m}|x_i(f) - x_i'(f)|}{\frac{1}{m}\frac{1}{n}\sum_{i=1}^{n}\sum_{f=1}^{m}|x_i(f)|} \tag{4}$$

where f is the frequency index, $m = 334$ the number of frequency points, i the sample index, n the number of samples in the test set of interest.

D. Evaluation of Performance

Using the aforementioned training setup, the two different variants of AEs coupled with FNNs are trained in two stages for the impedance prediction. The networks are trained and evaluated using the main dataset containing samples from all available cases simultaneously. A comparison of the prediction accuracy of the self- and transfer-impedance profiles using the two different architectures is provided in Table IV. Both self- and transfer-impedance profiles are predicted accurately with an average MAE lower than 0.75 Ω. In relative terms, the self-impedances are predicted with a slightly higher degree of accuracy than transfer-impedances. This is reflected by the nMAE values around 13% and 35% for the prediction the self- and transfer-impedances, respectively. This is partially due to the less smooth and more complex nature of transfer-impedance profiles, as discussed previously. Both the AE (FNN) and AE (CNN) architectures provide similar performances in the prediction of impedance profiles. On a machine equipped with a 2.23 GHz processor, 24 GB memory and 16384 core graphics card, the training times vary between 5 min and 9 min. The prediction of output impedance profiles takes around 50 ms using the AE (FNN) and a bit less than 300 ms using the AE (CNN). The AE (FNN) yields thus faster inferences. Since the cases differ in complexity, number of varied parameters and number of available data samples, the accuracy is evaluated on the test sets of each case separately. The results show a comparable prediction accuracy with a nMAE lower than 20% across the different cases, see Table V. Additionally, two separate FNN-AEs are trained from a blank state using an increasing number of samples from *Case IV* (13 dimensions) only and *Case V* (4 dimensions) only, respectively. Both models converge using less than 150 training samples, see Fig. 9. The latter shows the ability of the trained networks to generalize on a limited amount of training samples.

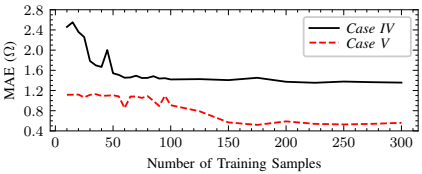

Fig. 9. Prediction accuracies of two separate FNN-AEs trained from a blank state using data from *Case IV* (13 dimensions) only and *Case V* (4 dimensions) only, respectively, are compared as a function of added training samples. Both models converge using less than 150 training samples.

The comparison of the original simulated and ML predicted impedance profiles from the test sets show good agreement, see Fig. 10. Examples with an MAE close to the average prediction accuracy of each have been chosen to give an accurate visual representation of average predictions, compare with Table V. Overall, the predicted impedance profiles closely follow the simulated curves across the full frequency range, reflecting strong generalization performance of the ML model. Particularly in the low- and mid-frequency bands, the slopes in both the capacitive and inductive regions are accurately reproduced. This indicates that the model successfully learns the global structural behavior of the PDN over several decades of frequency. Most resonant peaks, typically lower in magnitude and sharper in the case of transfer-impedances, are reproduced and match both the frequency and amplitude. Since the impedance profiles are plotted on a logarithmic scale, discrepancies tend to be more visible at low-magnitude peaks. This is expected, as small absolute deviations at lower magnitudes correspond to larger relative errors in the log domain. The low MAE values and close visual alignment indicate that the model generalizes well and provides high-fidelity predictions suitable for PDN modeling.

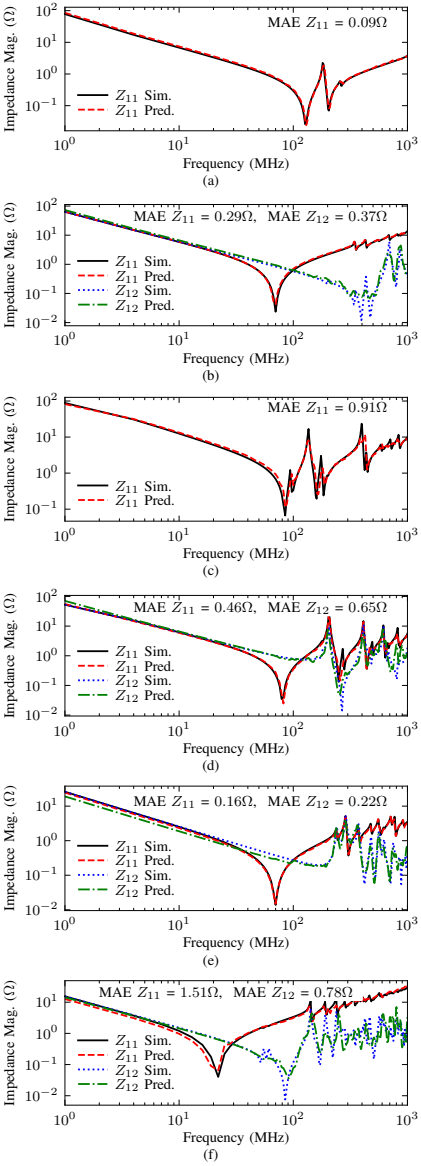

Fig. 10. Simulated and predicted self- and transfer-impedances are compared for example samples from (a) *Case I*, (b) *Case II*, (c) *Case III*, (d) *Case IV*, (e) *Case V* and (f) *Case VI*. The MAE between the simulated and predicted profiles is given at the top of each plot.

IV. Applications for PDN Modeling

In this section, three applications of the proposed ML-based PDN modeling approach are provided. In the first application, the impedance profiles of a new case of interest are modeled using a transfer learning method. The second application involves the modeling of a 3-port PCB case using previously trained ML models trained on 2-port systems. The third application covers the modeling of a more complex 10-port PCB sample. The results are discussed with regard to the application of the ML-based approach to speed up the PDN modeling and design process.

A. Efficient PDN Modeling Using Transfer Learning

To increase the data-efficiency and make the proposed approach applicable to practical PDN design, transfer learning is implemented in a data reuse scheme. The PCB of *Case V* is assumed to be an application example, where the task is the modeling of PDN impedance using a limited amount of generated samples. Data samples from the remaining 5 cases (*Case I-IV* and *Case VI*) are assumed to be available and can be used for training. In the transfer learning method, a pre-trained AE on available samples from the other cases is fine-tuned using an increasing number of samples from *Case V*. This method is compared with a classical non-transfer learning method where a blank state AE is trained using an increasing number of samples from *Case V* only. The two trained networks are tested by the prediction of the same unseen 200 *Case V* samples then compared, see Fig. 11.

Reusing available samples from other cases results in a better accuracy in the modeling of *Case V*, see Fig. 11c. Using 50 generated samples from *Case V*, the TL method reaches an MAE of less than 0.6 Ω while a training from a blank state in a classical method results in an MAE twice as high around 1.2 Ω. For a chosen unseen sample, the predictions of the self-impedance by both models from the two methods are compared, see Fig. 12. Starting from 10 new *Case V* training samples only, the TL method can model the impedance accurately. In the non-TL method, a larger number of new samples from *Case V* have to be used to improve the accuracy. Thus, fewer data samples need to be generated to accurately model *Case V* by reusing available data from other cases in a TL scheme.

B. Impedance Prediction in a 3-Port Case

For the application of the proposed approach in the modeling of PDNs, an additional case with 3 via arrays is used. The *Case IV-b* has the same stackup and design space as *Case IV* with 10 000 variations to input parameters. Three, instead of two identical via arrays of type B (Fig. 3b), are placed randomly on the PCB, see Fig. 13a. The previously trained FNN-AE on available samples (*Case I-VI*) is used to predict the self- and transfer-impedances of showcased 3-port system. The trained FNN-AE is used for the modeling of *Case IV-b* without further training. In other words, no additional training samples from the new *Case IV-b* have been used. The new 10 000 samples are used for the testing and evaluation of the prediction accuracy.

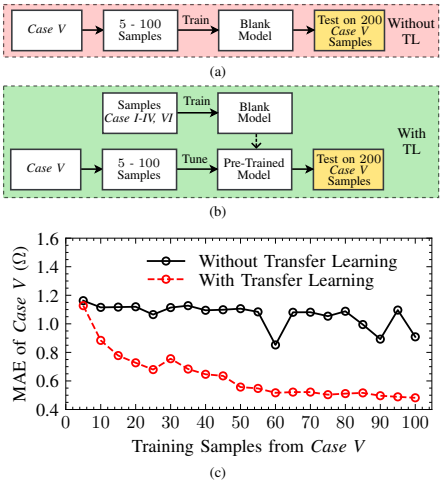

Fig. 11. Prediction of self-impedance profiles of *Case V* evaluated using (a) classical method without transfer learning (TL) where a blank FNN-AE is trained using an increasing number of *Case V* samples only and (b) TL method where an FNN-AE is pre-trained on data samples from other cases then fine-tuned using an increasing number of *Case V* samples. (c) The performance of both methods is compared in steps of 5 added training samples from *Case V*. It can be seen that TL usage results in improved performances (lower MAE) and a faster convergence.

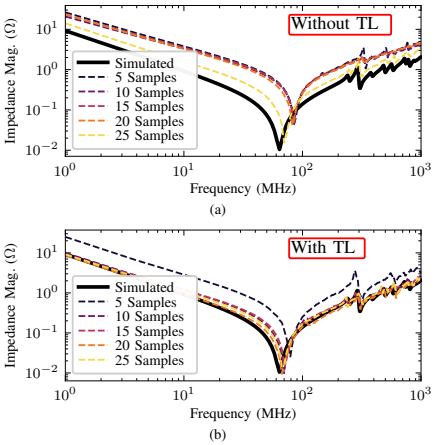

Fig. 12. Effect of transfer learning (TL) is shown using an unseen sample from *Case V*. The simulated (black) and predicted (colored) self-impedance are compared for models trained using (a) classical method without transfer learning where a blank FNN-AE is trained with an increasing number of *Case V* samples only and (b) TL method where an FNN-AE is pre-trained on data samples from other cases then fine-tuned using an increasing number of *Case V* samples. The TL method results in accurate prediction of the simulated sample starting from 10 new samples of *Case V* used for the training.

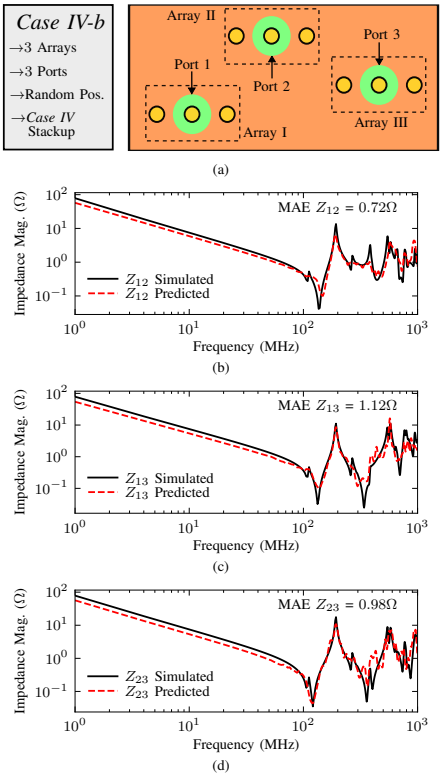

Fig. 13. Prediction of transfer-impedances of a 3-port case (*Case IV-b*) using a trained FNN-AE is shown. *Case IV-b* adds an extra port to the design space of *Case IV*. Instead of two, three different arrays and ports are used as seen on the (a) top view of the PCB. For a chosen sample, the simulated and predicted (b) transfer-impedance between port 1 and 2 (Z_{12}), (c) transfer-impedance between port 1 and 3 (Z_{13}) and (d) transfer-impedance between port 2 and 3 (Z_{23}), are compared. The used FNN-AE for the prediction has been trained on data from 2-port systems only.

The accuracy of the trained FNN-AE in the prediction of the transfer-impedances between the 3 ports amounts to an MAE of 0.72 Ω, similar to *Case IV*. For a chosen sample *Case IV-b*, the transfer-impedances between the 3 ports are predicted, see Fig. 13b, Fig. 13c and Fig. 13d. The simulated and predicted impedance profiles show good agreement, despite an MAE above the average of 0.72 Ω for the shown profiles. The networks, trained to be able to predict the self- and transfer-impedances in a 2-port system can thus be used for the modeling of systems with 3 ports. This enables the modeling of more complex systems while training using simulation data from 2-port systems only. This approach is evaluated on a more complex sample with 10 ports in the next application.

C. Impedance Prediction in a 10-Port Sample

To investigate the applicability of the proposed approach for N-port systems, a PCB sample with 10 ports is generated. The generated example is sampled from the *Case IV* design space and has the same stackup. Instead of 2 via arrays, 10 arrays of type B (Fig. 3b) are placed strategically on the PCB, see Fig. 14a. The placement of the ports is as follows: 5 via arrays are placed randomly, 4 via arrays are placed very close to each other in a cluster and the last array is placed close to one edge of the board. The previously trained FNN-AE on available samples (*Case I-VI*) are used to predict the self- and transfer-impedances to fully model the bare-board PDN of the new and unseen PCB. No data samples of 10-port PCBs have been additionally generated and used for training or tuning.

The self- and transfer-impedances between the 10 ports are predicted with an average MAE of $0.43\,\Omega$. For 3 different chosen ports, including a via at the edge of board (index: 10), a via in a cluster (index: 4) and a via in the middle of the board (index: 8), the self- and transfer-impedances are shown, see Fig. 14b to Fig. 14e. The simulated and predicted self- and transfer-impedances show good agreement. The self-impedances are predicted with a higher degree of fidelity, see Fig. 14b. For transfer-impedances, some discrepancies tend to be more visible at low-magnitude peaks as previously mentioned, see Fig. 14e. Nonetheless, the self- and transfer-impedances on a 10-port system are accurately modeled, despite having used training data from 2-port systems only. In other words, the modeling of more complex N-port systems can be performed while using training data from 2-port systems. The generation of data samples for 2-port systems is much faster than for more complex systems with more ports. Coupled with the higher data-efficiency achieved through TL, this method has the potential to enhance the efficiency of the PDN modeling through fast prediction times, less and simpler simulations needed for the training. Speeding up the design analysis bottleneck in the PDN design process should lead to faster design loops, see Fig. 1 in Section I.

V. Conclusion

The two-stage FNN-AE architecture can accurately model PCB based PDNs by predicting broadband self- and transfer-impedance profiles from input design parameters. The prediction accuracy is influenced by the complexity and size of the training dataset for a specific design case. Leveraging existing datasets enhances the data-efficiency and model performance, enabling accurate results with fewer simulations needed. With growing databases, the need to generate new and large datasets for the training of the ML models will decrease. Moreover, the ML models are able to model more complex N-port systems using easier to generate training data from 2-port systems. The fast modeling can significantly accelerate the design of PDNs by replacing slow EM simulations in existing decoupling and optimization strategies. Future work includes the application of the ML-based approach for the practical decoupling in PCB-based PDNs and the consideration of terminated boards.

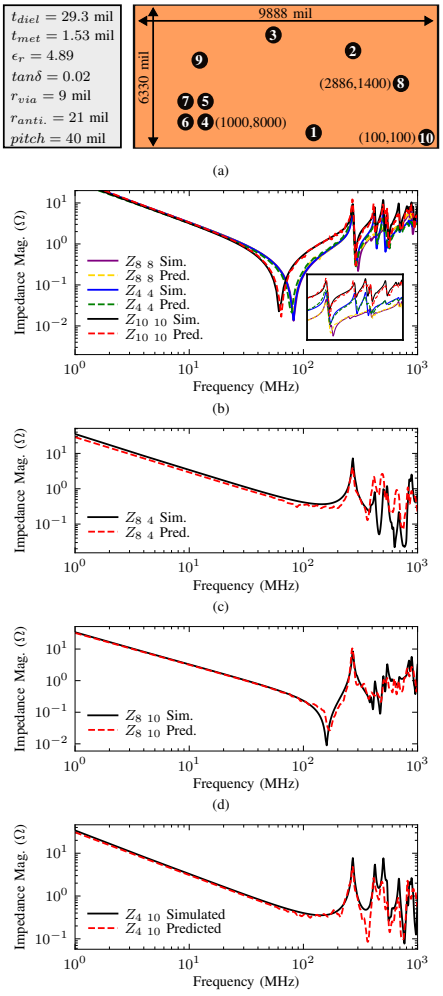

Fig. 14. Modeling of an N-port sample using a trained FNN-AE is shown. The considered example is sampled from the design space of *Case IV* with ten different arrays and ports instead of two ports only, as seen on the (a) top view of the PCB. The ports are numbered from 1 to 10 and the PCB parameters are given. For 3 chosen ports with marked coordinates, the simulated and predicted (b) self-impedances of the ports 4, 8 and 10 (with a zoom-in in the frequency range 300 MHz to 900 MHz), (c) transfer-impedance between port 4 and 8 ($Z_{8\ 4}$), (d) transfer-impedance between port 10 and 8 ($Z_{8\ 10}$) and (e) transfer-impedance between port 10 and 4 ($Z_{4\ 10}$), are compared. Despite the FNN-AE being trained on 2-port systems only, the predicted and simulated impedance of the 10-port PCB sample show good agreement.

REFERENCES

[1] M. Swaminathan and A. E. Engin, *Power Integrity Modelling and Design for Semiconductors and Systems*. Boston, MA, USA: Pearson Education, Inc., Nov. 2007.

[2] J. L. Knighten, B. Archambeault, J. Fan, G. Selli, and S. Connor, "PDN Design Strategies: I. Ceramic SMT Decoupling Capacitors - What Values Should I Choose?" *IEEE Electromagnetic Compatibility Magazine*, pp. 46–53, 2005.

[3] J. L. Knighten, B. Archambeault, J. Fan, S. C. Giuseppe Selli, Liang Xue, and J. L. Drewniak, "PDN Design Strategies: II: Ceramic SMT Decoupling Capacitors - Does Location Matter?" *IEEE Electromagnetic Compatibility Magazine*, pp. 56–67, 2006.

[4] J. Wang, Z. Xu, X. Chu, J. Lu, B. Ravelo, and J. Fan, "Multiport PDN Optimization With the Newton–Hessian Minimization Method," *IEEE Transactions on Microwave Theory and Techniques*, vol. 69, no. 4, pp. 2098–2109, 2021.

[5] I. Erdin and R. Achar, "MCB-DPO: Multiport Constrained Barrier Method-Based Decoupling Capacitor Placement Optimization on Irregularly Shaped Planes," *IEEE Transactions on Components, Packaging and Manufacturing Technology*, vol. 12, no. 4, pp. 665–675, 2022.

[6] ——, "Multipin Optimization Method for Placement of Decoupling Capacitors Using a Genetic Algorithm," *IEEE Transactions on Electromagnetic Compatibility*, vol. 60, no. 6, pp. 1662–1669, Dec. 2018. [Online]. Available: https://doi.org/10.1109/temc.2018.2803047

[7] ——, "Multi-Objective Optimization of Decoupling Capacitors for Placement and Component Value," *IEEE Transactions on Components, Packaging and Manufacturing Technology*, vol. 9, no. 10, pp. 1976–1983, Oct. 2019. [Online]. Available: https://doi.org/10.1109/tcpmt.2019.2930565

[8] H. Park, J. Park, S. Kim, K. Cho, D. Lho, S. Jeong, S. Park, G. Park, B. Sim, S. Kim, Y. Kim, and J. Kim, "Deep Reinforcement Learning-Based Optimal Decoupling Capacitor Design Method for Silicon Interposer-Based 2.5-D/3-D ICs," *IEEE Transactions on Components, Packaging and Manufacturing Technology*, vol. 10, no. 3, pp. 467–478, Mar. 2020. [Online]. Available: https://doi.org/10.1109/tcpmt.2020.2972019

[9] S. Han, O. W. Bhatti, and M. Swaminathan, "A Knowledge Based Method for Optimization of Decoupling Capacitors in Power Delivery Networks," *IEEE Transactions on Components, Packaging and Manufacturing Technology*, vol. 12, no. 5, pp. 828–838, 2022.

[10] M. Schierholz, K. Scharff, and C. Schuster, "Evaluation of Neural Networks to Predict Target Impedance Violations of Power Delivery Networks," in *Proceedings IEEE 28th Conf. Electrical Performance Electronic Packaging and Systems EPEPS*, Montreal, CA, Oct. 2019.

[11] M. Schierholz, Y. Hassab, C. Yang, and C. Schuster, "Evaluation of Support Vector Machines for PCB based Power Delivery Network Classification," in *Proceedings IEEE 30th Conf. Electrical Performance Electronic Packaging and Systems EPEPS*, Austin, TX, USA, Oct. 2021.

[12] I. Erdin and R. Achar, "Decoupling Capacitor Placement on Resonant Parallel-Plates Via Driving Point Impedance," *IEEE Transactions on Microwave Theory and Techniques*, vol. 67, no. 6, pp. 2162–2171, Jun. 2019. [Online]. Available: https://doi.org/10.1109/tmtt.2019.2906621

[13] Z. Xu, Z. Wang, C. Hwang, H. Delingette, and J. Fan, "Jitter-Aware Economic PDN Optimization With a Genetic Algorithm," *IEEE Transactions on Microwave Theory and Techniques*, vol. 69, no. 8, pp. 3715 – 3725, Aug. 2021. [Online]. Available: https://ieeexplore.ieee.org/document/9461629

[14] X.-P. Zhou, D.-W. Wang, W.-S. Zhao, P. Zhang, and J.-H. Pan, "Modeling of Through-Silicon Capacitor and Its Applications for the Optimization of Power Distribution Network in 3-D Integrated Circuits," *IEEE Transactions on Signal and Power Integrity*, vol. 3, pp. 199–211, 2024.

[15] H. Vaghasiya, A. Jain, and J. N. Tripathi, "A Radial Basis Function Network-Based Surrogate-Assisted Swarm Intelligence Approach for Fast Optimization of Power Delivery Networks," *IEEE Transactions on Signal and Power Integrity*, vol. 1, pp. 140–149, 2022.

[16] J. Juang, L. Zhang, H. Manoharan, F. De Paulis, and C. Hwang, "Augmented Genetic Algorithm for Decoupling Capacitor Optimization in Power Distribution Network Design Through Improved Population Generation," *IEEE Transactions on Signal and Power Integrity*, vol. 3, pp. 186–198, 2024.

[17] M. Schierholz, I. Erdin, J. Balachandran, and C. Schuster, "Data-Efficient Supervised Machine Learning Technique for Practical PCB Noise Decoupling," in *DesignCon 2023*, Santa Clara, CA, USA, Feb. 2023.

[18] M. Schierholz, Y. Hassab, I. Erdin, J. Balachandran, and C. Schuster, "Applying Techniques of Transfer and Active Learning to Practical PCB Noise Decoupling," in *DesignCon 2024*, Santa Clara, CA, USA, Jan. 2024.

[19] Y. Hassab, M. Schierholz, and C. Schuster, "Application of Gaussian Process Regression for Data Efficient Prediction of PCB-Based Power Delivery Network Impedance Features," in *2024 IEEE 28th Workshop on Signal and Power Integrity (SPI)*, Lisbon, Portugal, May 2024.

[20] W. Zhang, F. Feng, J. Jin, and Q.-J. Zhang, "Parallel Multiphysics Optimization for Microwave Devices Exploiting Neural Network Surrogate," *IEEE Microwave and Wireless Components Letters*, vol. 31, no. 4, pp. 341–344, Apr. 2021. [Online]. Available: https://doi.org/10.1109/lmwc.2021.3053600

[21] Z. Nezhi, M. Stiemer, M. Schierholz, and C. Schuster, "Dimensional Reduction by Auto-Encoders in Machine Learning Based Power Integrity Analysis," in *2024 IEEE 28th Workshop on Signal and Power Integrity (SPI)*, Lisbon, Portugal, May 2024.

[22] I. Cahani and M. Stiemer, "Autoencoders in the Machine Learning Supported Design of PCBs," in *2023 Kleinheubach Conference*, Miltenberg, Germany, Sep. 2023.

[23] ——, "Mathematical Optimization and Machine Learning to Support PCB Topology Identification," *Advances in Radio Science*, vol. 21, pp. 25–35, 2023. [Online]. Available: https://ars.copernicus.org/articles/21/25/2023/

[24] Y. Hassab, J. Heßling, M. Schierholz, I. Erdin, J. Balachandran, and C. Schuster, "Impedance Profile Prediction and Classification for PCB based PDN Decoupling Using Autoencoders," in *DesignCon 2025*, Santa Clara, CA, USA, Jan. 2025.

[25] T. Hillebrecht, J. Alfert, T. Reuschel, and C. Schuster, "Automated Generation and Correlation of Physics-Based Via Models with Full-Wave Simulation for an SI/PI Database," in *2023 IEEE 32nd Conference on Electrical Performance of Electronic Packaging and Systems (EPEPS)*, Milpitas, CA, USA, Oct. 2023.

[26] M. Schierholz, A. Sánchez-Masís, A. Carmona-Cruz, X. Duan, K. Roy, C. Yang, R. Rimolo-Donadio, and C. Schuster, "SI/PI-Database of PCB-Based Interconnects for Machine Learning Applications," *IEEE Access*, vol. 9, pp. 34 423–34 432, 2021.

[27] T. Hillebrecht, M. Schierholz, Y. Hassab, J. Alfert, and C. Schuster, "Generation and Application of a Very Large Dataset for Signal Integrity Via Array and Link Analysis," *IEEE Transactions on Electromagnetic Compatibility*, vol. 66, no. 6, pp. 1967–1976, 2024.

[28] M. Schierholz, Y. Hassab, and C. Schuster, "Engineering-Informed Design Space Reduction for PCB Based Power Delivery Networks," *IEEE Transactions on Components, Packaging and Manufacturing Technology*, vol. 13, no. 10, pp. 1613–1623, 2023.

[29] *Multilayer Substrate Simulator CONMLS Version 2.0*. Hamburg, Germany: TUHH - Institut für Theoretische Elektrotechnik, (Last accessed: 1-April-2025). [Online]. Available: https://www.tet.tuhh.de/wordpress/wp-content/uploads/2024/07/Manual-Conmls.pdf

[30] T. Okoshi, *Planar Circuits For Microwaves and Lightwaves*. Springer-Verlag Berlin, Heidelberg, 1985.

[31] R. Rimolo-Donadio, X. Gu, Y. Kwark, M. Ritter, B. Archambeault, F. de Paulis, Y. Zhang, J. Fan, H.-D. Brüns, and C. Schuster, "Physics-Based Via and Trace Models for Efficient Link Simulation on Multilayer Structures Up to 40 GHz," *IEEE Transactions on Microwave Theory and Techniques*, vol. 57, no. 8, pp. 2072–2083, Aug. 2009.

[32] X. Duan, R. Rimolo-Donadio, H.-D. Brüns, B. Archambeault, and C. Schuster, "Special Session on Power Integrity Techniques: Contour Integral Method for Rapid Computation of Power/Ground Plane Impedance," in *DesignCon 2010*, Santa Clara, CA, USA, Feb. 2010.

[33] S. Müller, X. Duan, M. Kotzev, Y.-J. Zhang, J. Fan, X. Gu, Y. H. Kwark, R. Rimolo-Donadio, H.-D. Brüns, and C. Schuster, "Accuracy of Physics-Based Via Models for Simulation of Dense Via Arrays," *IEEE Transactions on Electromagnetic Compatibility*, vol. 54, no. 5, pp. 1125–1136, Oct. 2012. [Online]. Available: https://doi.org/10.1109/temc.2012.2192123

[34] *ANSYS ®Electromagnetics Suite, Release 16.2*. Canonsburg, PA, USA: ANSYS, INC. [Online]. Available: http://www.ansys.com

[35] M. Schierholz, C. Schuster, Z. Nezhi, and M. Stiemer, "PCB Based Power Delivery Network Analysis Using Transfer Learning and Artificial Neural Networks," in *2024 IEEE 28th Workshop on Signal and Power Integrity (SPI)*, Lisbon, Portugal, May 2024.

[36] J. Kim, L. Ren, and J. Fan, "Physics-Based Inductance Extraction for Via Arrays in Parallel Planes for Power Distribution Network Design," *IEEE Transactions on Microwave Theory and Techniques*, vol. 58, no. 9, pp. 2434–2447, Sep. 2010. [Online]. Available: https://doi.org/10.1109/tmtt.2010.2058278